

MICROMAGNETIC MODELING OF WRITE HEADS  
FOR HIGH-DENSITY AND HIGH-DATA-RATE  
PERPENDICULAR RECORDING

A dissertation submitted to

Department of Electrical and Computer Engineering  
Carnegie Institute of Technology  
Carnegie Mellon University

in partial fulfillment of the requirements  
for the degree of

DOCTOR OF PHILOSOPHY

by

DANIEL ZHIGANG BAI

Pittsburgh, Pennsylvania

August, 2004

# CARNEGIE MELLON UNIVERSITY

CARNEGIE INSTITUTE OF TECHNOLOGY

## THESIS

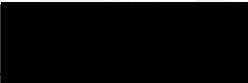
SUBMITTED IN PARTIAL FULFILLMENT OF THE REQUIREMENTS


FOR THE DEGREE OF DOCTOR OF PHILOSOPHY

TITLE Micromagnetic Modeling of Write Heads for High-density  
and High-data-rate Perpendicular Recording

PRESENTED BY Zhigang Bai

ACCEPTED BY THE DEPARTMENT OF Electrical and Computer Engineering

  
\_\_\_\_\_  
MAJOR PROFESSOR  
DATE 7/26/04

  
\_\_\_\_\_  
DEPARTMENT HEAD  
DATE 9/14/04

APPROVED BY THE COLLEGE COUNCIL

  
\_\_\_\_\_  
DEAN  
DATE 9/14/04

## Abstract

In this dissertation, three dimensional dynamic micromagnetic modeling based on Landau-Lifshitz equation with Gilbert damping has been used to study the magnetic processes of the thin film write heads for high density and high data rate perpendicular magnetic recording.

In extremely narrow track width regime, for example, around or below 100 nm, the head field is found to suffer from significant loss from the ideal  $4\pi M_s$  value for perpendicular recording. In the meantime, remanent head field becomes significant, posing potential issue of head remanence erasure.

Using micromagnetic modeling, various novel head designs have been investigated. For an overall head dimension around one micron, the shape and structure of the head yoke have been found to greatly affect the head magnetization reversal performance, therefore the field rise time, especially for moderate driving currents. A lamination of the head across its thickness, both in the yoke and in the pole tip, yields excellent field reversal speed, and more importantly, it suppresses the remanent field very well and thus making itself a simple and effective approach to robust near-zero remanence. A single pole head design with a stitched pole tip and a recessed side yoke can produce significantly enhanced head field compared to a traditional single pole head. Various head design parameters have been examined via micromagnetic modeling.

Using the dynamic micromagnetic model, the magnetization reversal processes at data rates beyond 1 Gbit/s have been studied. The excitation of spin wave during the head field reversal and the energy dissipation afterwards were found important in dictating the field rise time. Both the drive current rise time and the Gilbert damping constant affect the field reversal speed.

The effect of the soft underlayer (SUL) in both the write and the read processes have been studied via micromagnetic modeling. Although it is relatively easy to fulfill the requirement for the magnetic imaging in writing, the SUL deteriorates the readback performance and lowers the achievable recording linear density. Various parameters have been investigated and solutions have been proposed.

The effect of stress in magnetostrictive thin films has been studied both analytically and by simulation. The micromagnetic model has been extended to incorporate the stress-induced anisotropy effect. Simulation was done on both a magnetic thin film undergoing stresses to show the static domains and a conceptual write head design that utilizes the stress induced anisotropy to achieve better performance.

A self-consistent model based on energy minimization has been developed to model both the magnetization and the stress-strain states of a magnetic thin film.

## Acknowledgments

I would like to express my sincerest gratitude to my thesis advisor, Professor Jian-Gang Zhu. Without his inspiration, guidance, support and encouragement this thesis would not have been possible.

I am also grateful to my other committee members: Professor James A. Bain, Dr. Robert E. Rottmayer, and Professor Robert M. White.

I would like to thank the Data Storage Systems Center (DSSC) at Carnegie Mellon University, its former director Professor Robert M. White, and the support team of the DSSC, especially Kathy Miskinis, for making an excellent research environment, which I enjoyed throughout my Ph.D. research at the DSSC and CMU. I would also like to thank the computing facilities support team of the Department of Electrical and Computer Engineering at Carnegie Mellon for a lot of help in computing related issues.

I would like to thank Dr. Chris Mao, Dr. Tzuning Fang, Dr. Gang Li, and Dr. Rick Shi for their help in the early stage of the thesis work. I have also enjoyed many discussions with Dr. Lijie Guan, which have been very fruitful.

Special thanks go to the following persons for the discussions and help in respective chapters: Dr. Sharat A. Batra and Dr. Robert E. Rottmayer for Chapter 3 and 4; Dr. Adam F. Torabi for Chapter 6; Professor James A. Bain and Winnie Yu for Chapter 7 and 8; Dr. Zhaohui Fan for Chapter 8; Xun Zhang for Chapter 8 and on Latex; and Dr. Joshua Schare for the FEM results in Section 2.7.1.

Finally, I would like to thank my parents, my wife Jingxu, and my whole family for their constant love and support.

## Table of Contents

Abstract	i
Acknowledgments	iii
Table of Contents	iv
List of Tables	ix
List of Figures	x
<b>1 INTRODUCTION</b>	<b>1</b>
1.1 Overview of magnetic recording . . . . .	1
1.2 Issues with write heads at high density and high data rate . . .	5
1.3 Motivation and approach . . . . .	7
1.3.1 Analytical models . . . . .	9
1.3.2 Transmission line models . . . . .	12
1.3.3 Finite element and boundary element methods . . . . .	13
1.3.4 Micromagnetic models . . . . .	14
1.4 Outline of the thesis . . . . .	16
<b>2 MICROMAGNETIC MODEL</b>	<b>19</b>
2.1 Overview . . . . .	20
2.2 System energy expression . . . . .	22
2.2.1 Magnetostatic energy . . . . .	22
2.2.2 Exchange energy . . . . .	25
2.2.3 Anisotropy energy . . . . .	26
2.2.4 Zeeman energy . . . . .	27
2.3 Effective Field . . . . .	27

2.4	Spin Dynamics . . . . .	29
2.4.1	Landau-Lifshitz-Gilbert equation . . . . .	29
2.4.2	Damping constant . . . . .	30
2.5	Numerical Solution . . . . .	31
2.6	Miscellaneous . . . . .	32
2.6.1	Mesh cell size and grain size . . . . .	32
2.6.2	Magnetic imaging . . . . .	33
2.6.3	Removal of surface charges . . . . .	36
2.7	Validation of the micromagnetic model . . . . .	37
2.7.1	Comparison with FEM . . . . .	37
2.7.2	Thin film magnetization . . . . .	39
<b>3</b>	<b>IMPACT OF TRACK WIDTH REDUCTION</b>	<b>43</b>
3.1	Model and geometry . . . . .	44
3.2	Results and Discussions . . . . .	46
3.2.1	Analytical results . . . . .	46
3.2.2	Maximum Head Field vs. Track Width . . . . .	50
3.2.3	Field Gradient vs. Track Width . . . . .	53
3.2.4	Impact of Track Width Reduction on Remanent Head Field	55
3.3	Conclusions . . . . .	60
<b>4</b>	<b>NOVEL PERPENDICULAR WRITE HEAD DESIGNS</b>	<b>63</b>
4.1	Micromagnetic Model . . . . .	64
4.2	Laminated- and Detached-Pole Tip Head Design . . . . .	66
4.2.1	Head A . . . . .	66
4.2.2	Head B . . . . .	69
4.2.3	Head C . . . . .	75
4.2.4	Head D . . . . .	80

4.2.5	Remanent head field in laminated and detached pole tip heads . . . . .	82
4.3	Stitched Pole Tip Head Design . . . . .	86
4.3.1	Micromagnetic model and head geometry . . . . .	87
4.3.2	Head field . . . . .	88
4.3.3	Throat height . . . . .	91
4.3.4	Flare angle . . . . .	92
4.3.5	ABS-SUL separation . . . . .	92
4.3.6	Induced anisotropy . . . . .	93
4.4	Conclusions . . . . .	94
<b>5</b>	<b>HIGH FREQUENCY HEAD FIELD DYNAMICS</b>	<b>97</b>
5.1	Introduction . . . . .	98
5.2	Micromagnetic modeling . . . . .	99
5.3	Results and discussions . . . . .	99
5.3.1	Magnetization reversal processes . . . . .	99
5.3.2	Effect of damping constant . . . . .	101
5.3.3	Effect of current rise time . . . . .	102
5.3.4	Limit of field reversal speed . . . . .	107
5.4	Conclusions . . . . .	110
<b>6</b>	<b>SOFT UNDERLAYER IN READ AND WRITE IN PERPENDICULAR RECORDING</b>	<b>111</b>
6.1	Introduction . . . . .	111
6.2	Micromagnetic modeling . . . . .	114
6.3	SUL micromagnetics and transition response . . . . .	115
6.4	High density readback rolloff and $-20\text{dB}$ -density $D_{20\text{dB}}$ . . . . .	119
6.5	$D_{20\text{dB}}$ maximization . . . . .	123



6.6	Conclusions . . . . .	130
<b>7</b>	<b>EFFECT OF STRESS IN MAGNETIC THIN FILMS</b>	<b>132</b>
7.1	Introduction . . . . .	132
7.2	Stress induced in-plane anisotropy: Analytical derivation . . . .	134
7.3	Micromagnetic modeling . . . . .	138
7.3.1	Effective field due to magnetoelastic energy . . . . .	139
7.3.2	Effect field of cubic anisotropy . . . . .	140
7.4	Thin film magnetization rearrangement under stress . . . . .	141
7.5	Conceptual design of a voltage-assisted magnetostrictive perpen- dicular write head . . . . .	146
7.5.1	The head design . . . . .	147
7.5.2	Micromagnetic modeling analysis . . . . .	149
7.5.3	Summary and remarks . . . . .	152
7.6	Conclusions . . . . .	155
<b>8</b>	<b>MAGNETOELASTIC RELAXATION OF MAGNETIC THIN FILMS</b>	<b>157</b>
8.1	Model construction/Derivation . . . . .	158
8.1.1	Elastic energy and force . . . . .	159
8.1.2	Magnetoelastic energy and force . . . . .	161
8.1.3	The solution algorithm . . . . .	165
8.2	Simulation results . . . . .	166
8.2.1	Fe <sub>65</sub> Co <sub>35</sub> thin film . . . . .	166
8.2.2	Arbitrary materials . . . . .	170
8.2.3	Discussions . . . . .	174
8.3	Conclusions . . . . .	181

<b>9 SUMMARY</b>	<b>183</b>
<b>List of References</b>	<b>188</b>
<b>A Magnetostatic interaction matrix calculations: for calculating field from magnetization</b>	<b>197</b>
<b>B Magnetostatic interaction matrix calculations: for calculating field from surface charge density</b>	<b>201</b>
<b>C Calculation of the driving field from the coil</b>	<b>205</b>
<b>D Coordinate transform matrices and magnetoelastic energy averaging for different textures</b>	<b>208</b>
D.1 Random texture . . . . .	208
D.2 100 texture . . . . .	208
D.3 110 texture . . . . .	209
D.4 111 texture . . . . .	209

## List of Tables

4.1	Parameters of different head designs. All values are in unit of $\mu\text{m}$ .	65
6.1	Default simulation parameters for Chapter 6. . . . .	114
7.1	Effective in-plane anisotropy constants for different textures. The numbers in last two columns are the anisotropy constant values, in unit of $10^4 \text{ erg/cm}^3$ , for films under a 1 GPa stress. . . . .	139

## List of Figures

1.1	Schematic drawing of the longitudinal recording configuration .	3
1.2	Schematic drawing of the perpendicular recording configuration	4
1.3	Schematic illustration of the Karlqvist head and the magnetic potential . . . . .	10
1.4	Schematic of the Karlqvist head used for the trailing edge head field of a single pole head with SUL in perpendicular recording .	11
2.1	Imaging of (a) electric charges and (b) magnetic moments. . . .	34
2.2	The modeled head structure for the FEM-micromagnetic comparative case study . . . . .	38
2.3	The perpendicular field profiles along $z$ direction . . . . .	39
2.4	Domain configurations during a magnetization switching process in a permalloy thin film . . . . .	40
2.5	Domain configurations during a magnetization switching process in a permalloy thin film, continued . . . . .	41
3.1	Schematic of the single pole head and SUL modeled in this chapter.	44
3.2	Illustration of the write pole and the image pole due to the SUL.	46
3.3	Maximum perpendicular head field $H_y$ vs. the track width for different aspect ratios of the pole tip footprint. . . . .	47
3.4	Maximum perpendicular head field $H_y$ vs. the aspect ratios of the pole tip footprint for a track width of 100 nm. . . . .	48
3.5	Illustration of the written track width with (a) zero head skew and (b) non-zero head skew . . . . .	49
3.6	The percentage increase of the actual written track width with respect to the zero-skew track width as a function of the pole tip footprint aspect ratio . . . . .	50

3.7	The down-track field profiles for different track widths . . . . .	51
3.8	Micromagnetic results of the maximum head field versus track width . . . . .	53
3.9	Down-track gradient of the perpendicular field component versus the field magnitude . . . . .	54
3.10	Dependence of the maximum field gradient on the track width .	55
3.11	The remanent state magnetization of two heads with different track widths . . . . .	57
3.12	Dependence of the remanent field and its percentage to the max- imum field on the track width, for $l_x/l_z = 1$ . . . . .	58
3.13	Maximum remanent perpendicular field versus the throat height	59
3.14	3-D view of the remanent state magnetization of the pole tips with different throat heights . . . . .	60
3.15	Remanent state magnetization of a head with track width of 80 nm and pole/yoke thickness of 160 nm . . . . .	61
4.1	Write current waveform used in the simulations in this chapter .	65
4.2	Schematic of head A with all dimensions marked in unit of micron	66
4.3	Temporal profiles of the maximum perpendicular head field at two different driving currents for head A. . . . .	68
4.4	Head field rise time and field magnitude vs. driving current for head A. . . . .	68
4.5	Domain structures of head A during a flux reversal process . . .	69
4.6	Remanent state magnetic domain structures of head A after writ- ing with two different drive currents . . . . .	70
4.7	Schematic of head B with all dimensions marked in unit of micron	71
4.8	Temporal profiles of the maximum perpendicular head field at different driving currents for head B. . . . .	72

4.9	Head field rise time and field magnitude vs. driving current for head B. . . . .	72
4.10	The magnetic domain structures in head B during a flux reversal process . . . . .	73
4.11	The magnetization relaxation process of head B after writing with a large current . . . . .	74
4.12	Schematic of head C with all dimensions marked in unit of micron	76
4.13	Temporal profiles of the maximum perpendicular head field at different driving currents for head C. . . . .	77
4.14	Head field rise time and field magnitude vs. driving current for head C. . . . .	77
4.15	Magnetization configurations of head C during a field reversal .	78
4.16	Magnetization configurations of head C with drive current on and off . . . . .	79
4.17	Head field rise time vs. the driving current for head A, B and C.	81
4.18	Head field magnitude vs. the driving current for head A, B and C.	81
4.19	Schematic of head D with all dimensions marked in unit of micron	82
4.20	Remanent magnetization of head D after driven by a large current.	83
4.21	The head field relaxation with time for head A, B, C, and D. . .	83
4.22	Head field magnitude dependence on pole tip-yoke separation for two different driving currents. . . . .	84
4.23	Remanent head field dependence on the throat height for an unlaminated head and a laminated head . . . . .	85
4.24	Vector plot of the remanent state pole tip magnetization of the two layers of the laminated head with two throat heights . . . .	85
4.25	Schematic of the stitched pole tip head with all dimensions marked in unit of micron . . . . .	87

4.26	The down-track field profile of the stitched-pole-tip head . . . . .	89
4.27	Maximum perpendicular head field and maximum down-track field gradient versus the throat height . . . . .	90
4.28	Cross-track field profiles for different throat heights . . . . .	90
4.29	Cross-track field profiles for different flare angles . . . . .	93
4.30	Dependence of the maximum perpendicular field and down-track field gradient on the media thickness . . . . .	94
4.31	Head field relaxation for different longitudinal induced anisotropy fields. . . . .	95
4.32	Maximum perpendicular head field versus write current for dif- ferent induced longitudinal anisotropy fields. . . . .	95
5.1	Head field versus time for current rise time $\tau_c = 100$ ps and damping constant $\alpha = 0.01$ . . . . .	100
5.2	Magnetization configurations of the head during the flux reversal corresponding to point A, B, C, and D in Figure 5.2. . . . .	100
5.3	Temporal profile of the head field for different damping constants. The current rise time is 100 ps. . . . .	102
5.4	Temporal profile of the head field for different damping constants. The current rise time is 20 ps. . . . .	103
5.5	Temporal profile of the head field for different damping constants. The current rise time is 500 ps. . . . .	103
5.6	The magnetization configuration of the head at the “knee” point of the field reversal for current rise time of 20 ps. . . . .	105
5.7	The magnetization configuration of the head at the “knee” point of the field reversal for current rise time of 500 ps. . . . .	105
5.8	Hysteresis loops of the head field versus the normalized driving current for current rise time of 20 ps and 500 ps, respectively. . .	106

5.9	Field rise time versus current rise time for different values of damping constant. . . . .	107
5.10	Temporal profile of the head field for damping constant $\alpha = 0$ , current rise time $\tau_c = 100$ ps, and data rate of 1 Gbit/sec. . . .	108
5.11	Temporal profile of the head field for damping constant $\alpha = 0.004$ , current rise time $\tau_c = 20$ ps, and data rate of 2 Gbit/sec. . . .	108
5.12	The critical frequency versus the damping constant for two different current rise times. . . . .	109
6.1	The magnetization states of the free layer, the shields, and the SUL, for two linear densities . . . . .	116
6.2	Transition response for different values of the SUL thickness . .	117
6.3	Transition response for different values of the SUL saturation magnetization . . . . .	118
6.4	Examples of the simulated readback waveforms at different linear densities . . . . .	119
6.5	A comparison of the rolloff curves of the readback amplitude with linear density for the cases with and without SUL . . . . .	120
6.6	The ratio of the readback voltage with SUL, $V_d$ , to that without SUL, $V_s$ , as a function of the linear density for two medium thickness values. . . . .	121
6.7	Normalized rolloff curves of the readback power with linear density for the cases with and without SUL . . . . .	122
6.8	Dependence of $D_{20dB}$ and the write field on the SUL thickness. .	124
6.9	The dependence of $D_{20dB}$ and write field on the SUL saturation magnetization. . . . .	124
6.10	The dependence of $D_{20dB}$ and write field on the anisotropy field of the SUL. . . . .	125



6.11	Rolloff curves of the readback power with linear density for different values of medium thickness. . . . .	126
6.12	Dependence of $D_{20dB}$ on the medium thickness and the head-medium magnetic spacing HMS. . . . .	126
6.13	Dependence of $D_{20dB}$ on the reader gap (SSS) . . . . .	128
6.14	Normalized rolloff curves of the readback power with linear density for different spin valve reader stripe heights . . . . .	128
6.15	Dependence of $D_{20dB}$ and the write field on the interlayer thickness.	130
7.1	Illustration of the two coordinate systems . . . . .	136
7.2	The micromagnetic simulation results of the magnetic domains of a $\text{Fe}_{65}\text{Co}_{35}$ thin film element . . . . .	143
7.3	The simulated magnetic domains of a Fe thin film element under a 5 GPa uniaxial horizontal tensile stress . . . . .	144
7.4	The simulated magnetic domains of a $\text{Fe}_{65}\text{Co}_{35}$ thin film element with a uniform strain of 0.6% . . . . .	145
7.5	The simulated magnetic domains of a $\text{Fe}_{65}\text{Co}_{35}$ thin film element under a 1 GPa biaxial compressive stress . . . . .	145
7.6	Schematic of the voltage-assisted perpendicular write head design and the drive current and voltage waveforms . . . . .	148
7.7	Illustration of the head operating mechanism. . . . .	149
7.8	Simulated on-track maximum head field as a function of the applied stress . . . . .	150
7.9	Simulated on-track maximum head field as a function of the write current amplitude for a stress amplitude of 3 GPa and zero, respectively . . . . .	151
7.10	Cross-track field profiles of the head with and without stress assist. The drive currents are different. . . . .	152

7.11	Cross-track field profiles of the head with and without stress assist. The throat heights are different. . . . .	153
7.12	Simulated on-track field waveform at 1 Gbit/sec data rate . . .	154
8.1	Different energy terms in the relaxation process. . . . .	167
8.2	Colormaps of the magnetization and the spontaneous strain-stress distribution of a $\text{Fe}_{65}\text{Co}_{35}$ thin film under 2-D constraint .	168
8.3	Colormaps of the spontaneous strain-stress distribution of a $\text{Fe}_{65}\text{Co}_{35}$ thin film without constraint . . . . .	169
8.4	The equilibrium state magnetization configuration of the thin film element with low magnetostriction . . . . .	171
8.5	The equilibrium state distribution of the horizontal strain component in the film with low magnetostriction . . . . .	171
8.6	Different terms of the energy density averaged over all the cells in the relaxation process for the low-magnetostriction case . . .	172
8.7	The equilibrium state magnetization configuration of the thin film element with high magnetostriction . . . . .	173
8.8	The equilibrium state distribution of the horizontal strain component in the film with high magnetostriction . . . . .	173
8.9	Different terms of the energy density averaged over all the cells in the relaxation process for the high-magnetostriction case . . .	174
8.10	Dependence of simulated values of different terms of the energy density at equilibrium state on the saturation magnetostriction of the material . . . . .	176
8.11	Simulated initial magnetization curves for different values of Young's modulus for an arbitrary material. . . . .	177
8.12	Simulated initial magnetization curves for different values of Young's modulus for FeCo alloy with constraint. . . . .	178

8.13	Magnetic domain configurations corresponding to 25 Oe field on the three curves in Figure 8.12. . . . .	179
8.14	Simulated domain configurations of a constrained film with a uniform initial horizontal magnetization for different values of Young's modulus. . . . .	180
C.1	Illustration of the current coil and the field . . . . .	205

# 1 INTRODUCTION

## 1.1 Overview of magnetic recording

Magnetic hard disk recording technology has been invented in 1956 by IBM. The first hard disk drive was called RAMAC (Random Access Method of Accounting and Control), which had a total capacity of 5 MB with an areal density of about 2 kb/in<sup>2</sup> and a data rate of 8.8 kB/s. Since then the magnetic recording technology has been experiencing amazing advancement in the past half century. The areal recording density has increased by more than 10<sup>7</sup> times- the latest demonstrated hard drive recording densities were 130 Gbit/in<sup>2</sup> [1] and 170 Gbit/in<sup>2</sup> [2] for longitudinal and perpendicular recording, respectively. In the first three decades, the recording density had been increasing at a rate of about 30% per year. In 1990s, the annual growth rate of the recording density went up to about 60%, and this number had even reached 100% in late 1990s and early 2000s.

In the history of the hard drive technology, there have been a number of technological breakthroughs not only in head and media, but also in other aspects such as mechanical control, channel, etc. that made the aforementioned growth possible. Among those advancements, the scale-down of the dimension of the write and read heads is rather essential, as they basically define the track width of the recorded bits. In the early years, the recording heads were ring heads made of ferrite, which were used both as the writer and the reader. In 1979, IBM first introduced the thin film head, which was fabricated using the thin film processing techniques similar to that used in silicon based integrated

circuits. The thin film technology enabled batch fabrication of heads and lowered the cost. More importantly, it became possible to significantly reduce the dimension of the head pole tip, hence enabling smaller track widths and higher recording density. In early 1990s, the use of the magnetoresistive (MR) head and the giant magnetoresistive (GMR) head as the reader further increased the recording density at a higher rate and finally brought the technology beyond 100 Gbit/in<sup>2</sup> recording density.

Despite the tremendous success that has been achieved in the hard drive industry, it becomes more and more difficult to further increase the recording density. Due to the signal-to-noise ratio (SNR) constraint posed by the bit error rate (BER) requirement and the capability of the channel, in continuous thin film media, the number of the grains across a track should be maintained reasonably large, which means that the media grain size needs to be reduced with decreasing track width. As a result, eventually, the grain size will be so small that superparamagnetism will occur in the medium, i.e., the recorded bits will be spontaneously switched due to thermal agitation [3]. The thermal stability factor is given by

$$\zeta_{th} = \frac{K_u V}{k_B T} \quad (1.1)$$

where  $K_u$  is the anisotropy energy constant of the medium,  $V$  is the grain volume,  $k_B$  is the Boltzmann constant, and  $T$  is the temperature in Kelvin. For a lifetime of 10 years for the recorded bits, the condition is  $\zeta_{th} > 40$ . For high density recording, with high- $K_u$  hence high-coercivity medium being used, higher write field is needed to be able to write on the media. However, in longitudinal recording, the write field in the medium is the fringing field due to the flux leaking from the deep gap between the two poles of the ring head, P1 and P2, as shown in Figure 1.1. The maximum achievable field will therefore be limited to about half of the saturation induction of the pole material, i.e.,  $4\pi M_s$ , where

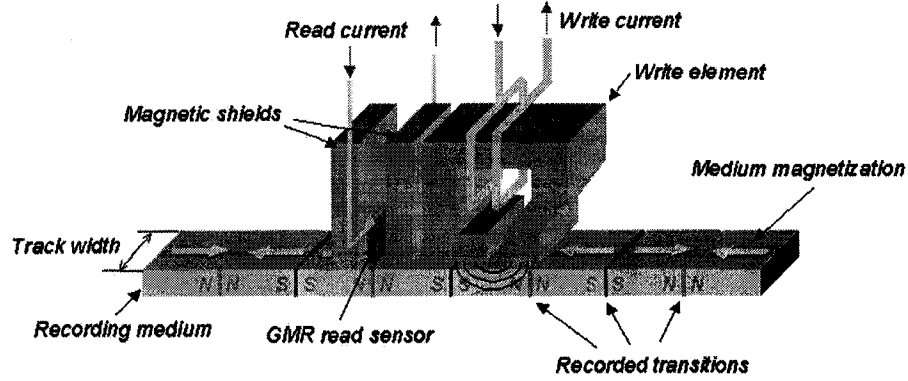


Figure 1.1: Schematic drawing of the longitudinal recording configuration (not in scale, from [4]).

$M_s$  is the saturation magnetization of the head pole tip material. This will no longer be enough for high-coercivity media at high densities. For example, even with  $\text{Fe}_{65}\text{Co}_{35}$ , the material with highest known saturation induction of 2.45 Tesla, the maximum write field will still be limited to below 1.2 Tesla. To ensure good overwrite, the head field typically needs to be about twice the media coercivity. Therefore, with longitudinal recording, the media coercivity will be limited to below 6000 Oe [4]. Another fundamental shortcoming that prevents longitudinal recording from going to ultra-high density is that the magnetic poles at the transition generates a demagnetizing field, which tend to broaden the transition, causing partial erasure at high densities [5].

Perpendicular recording has long been proposed as a candidate for replacing the current longitudinal recording technology [6]. The way the medium stores information in perpendicular recording avoids the problems encountered by longitudinal recording at high density. Since the medium is magnetized perpendicular to the plane, it intrinsically favors high density, which minimizes the magnetostatic energy thanks to the highly localized fringing field from the media. Unlike the ring head used in longitudinal recording, in perpendicular

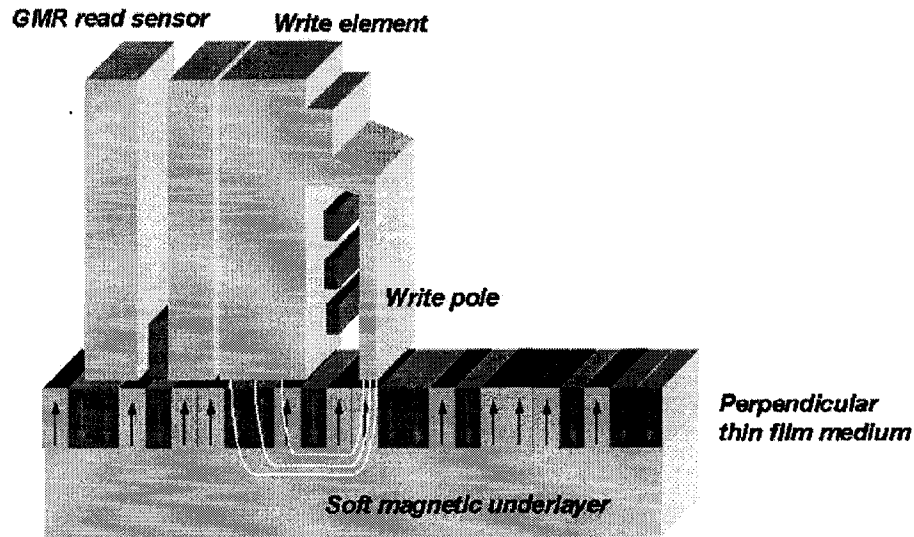


Figure 1.2: Schematic drawing of the perpendicular recording configuration (not in scale, from [4])

recording scheme, a single pole type (SPT) head is suggested to be used together with a soft magnetic underlayer (SUL) that is deposited underneath the recording layer, as shown in Figure 1.2. During writing, the SUL plays a role of magnetically imaging the head magnetization, effectively creating an “image head” that enhances the perpendicular field. The medium layer is therefore effectively in the deep gap between the real head pole tip and its image, hence experiencing the deep gap field, as opposed to the fringing field in longitudinal recording. Ideally, the write field could be as large as  $4\pi M_s$ . As a matter of fact, longitudinal recording has reached a point where further increasing the areal density becomes very difficult. Therefore, the hard drive recording technology has begun the transition from longitudinal to perpendicular recording, and tremendous research effort has also been invested in perpendicular recording in the past several years, more than 20 years after

the introduction of the perpendicular recording concept by Iwasaki.

## 1.2 Issues with write heads at high density and high data rate

The main focus of this thesis research will be micromagnetic modeling of the write head for high density, high data rate perpendicular recording. For these applications the requirements for a write head include the following:

1. *Sufficiently high on-track field.* To be able to switch all the medium grains, the on-track field needs to be at least greater than the saturation field of the medium hysteresis loop. This is also the primary motivation to move from longitudinal recording to perpendicular. However, as will be shown in Chapter 3, even in perpendicular recording using a single pole head and an SUL, the head field magnitude still decreases rapidly as the track width is made narrower and narrower, e.g., below 100 nm. This is one of the major challenges for high density perpendicular write head design.
2. *High field gradient.* In the down-track direction, the written magnetization gradient at the transition in the medium is determined by

$$\begin{aligned} \frac{dM}{dx} &= \frac{dM(H)}{dH} \frac{dH}{dx} \\ &= \frac{dM(H)}{dH} \left( \frac{dH_h}{dx} + \frac{dH_d}{dx} \right) \end{aligned} \quad (1.2)$$

where  $dM(H)/dH$  is the slope of the medium hysteresis loop at coercivity,  $dH_h/dx$  is the head field gradient down the track at media coercivity, and  $dH_d/dx$  is that of the media demagnetizing field [7]. Therefore, to write sharp transitions, a medium with high squareness and a head with sharp field gradient are needed. To optimally utilize the head field, it should be chosen to work in such a way that the sharpest head field gradient occurs



at the position where the head field is equal to the media coercivity. In reality, as the perpendicular media hysteresis loops are usually “sheared” due to the demagnetizing field, there is usually a relatively large switching field distribution. Therefore, in order to ensure the writeability, the actual transition may not be written with the maximum head field gradient. Nevertheless, a sharp head field gradient is always desirable.

As far as the cross-track direction is concerned, a reasonably sharp field gradient is also needed with the off-track field small enough not to erase the data on adjacent tracks. This in fact is another challenge for high density perpendicular write head design.

3. *Short field rise time.* The transition time for the head field to change from one polarity to the opposite should be small enough compared to the bit duration. Otherwise it will cause broadening of written transitions. This was not an issue for drives working at data rate range up to hundreds of MHz, where the bit interval is several nanoseconds, and the field rise time requirement is also at the order of nanosecond. In those cases, the dynamic micromagnetic behavior of the head magnetization does not need to be considered, rather, simply reducing the rise time of the drive current is sufficient. However, as the recording data rate goes beyond 1 GHz, the head field rise time has to be shortened to a fraction of a nanosecond. In this regime, the dynamics of the head magnetization reversal, including the spin gyromagnetic motion, has to be taken into account. In fact, Kaiser *et al.* recently did some experiments on very high data rate recording subsystems running up to 2.6 Gbits/s [8], and indication of the head field not able to follow the driving current has been observed. Therefore,

detailed micromagnetic study of the magnetization dynamics is very important for the understanding and design of write heads for high data rate applications.

4. *Zero remanence.* For ultra-high density recording, the write head pole tip is so small that there will still be a significant no-zero residual magnetization remaining in the pole-tip, after the write current is turned off. This is due to the ferromagnetic exchange coupling as it does to make small particles single domain. This means that a non-zero field will be sweeping over the media after the writing process. If this is the case, it will present a danger of erasing some of the previously written bits. Therefore, a zero remanence has to be produced in high density recording heads.

The above issues are the fundamental ones for high density and high data rate recording head design. Therefore, the majority of this thesis work will focus on these issues.

### 1.3 Motivation and approach

As mentioned above, there are a number of challenges for the write head design at ultra-high densities. Furthermore, up to date, it still remains a difficulty to measure the head field directly, simply due to the extremely small dimension in the vicinity of the write pole. Therefore, all experimental approaches of measuring head field are indirect. One way to measure the head field is through recording on a standard “calibrated” media and then measuring the readback waveform or the media magnetization through magnetic force microscopy (MFM). Even the media property is perfectly known, the readback waveform is only the convolution of the read sensor response and the media magnetization, thus limited by the sensitivity of the read sensor. While the

resolution of the MFM, which is typically about 20-30 nm [9, 10]. The resolution of the two approaches is not even able to resolve the magnetization transition, therefore it is impossible to capture the spatial profile of the head field. Kerr microscopy has also been used to image the write head magnetization, in particular, it is used to map the temporal profile of the head yoke magnetization, which is somewhat a reflection of the head field dynamics, at high frequency. The problem with this approach is the imaging resolution due to the optical diffraction limit, which is at the order of hundreds of nanometers, much larger than the dimension of today's writer pole-tips, the latter being the real interesting part that directly determines the head field.

As opposed to the difficulty of measuring head field experimentally, it is much easier to compute the head field with a correctly built model via numerical computations. One other motivation for modeling is from the standpoint of the head design. Properly built models could enable the simulation of heads with different materials, structures, geometries etc., before actually fabricating the heads. In fact, modeling has been used as a very important tool to guide the design and study the performance of heads in the industry.

There have been various head models developed over years, including analytical models with simplified geometries and assumptions, such as Karlqvist 2-D head field model [11], which was later extended to 3-D by Lindholm [12]. Another analytical model more accurate than Karlqvist model is by Westmijze [13]. Transmission line models can also provide some insights into the head geometry and head material selection, but they are of limited use nowadays for high density write heads with very sophisticated structures. Some numerical methods such as finite element method (FEM) and boundary element method (BEM) are now widely used to model the write heads. They have the advantage of being able to model complicated head structures. The

approach we employed in this research is micromagnetic modeling, which, together with aforementioned methods, will be reviewed below.

### 1.3.1 Analytical models

A very simple, yet very widely used head field model was one by Karlqvist published in 1954 [11]. In this model, the following assumptions were made:

1. The head magnetic material has infinite permeability.
2. The sizes of the head in both the down-track direction and the cross-track direction are infinity, so is the depth of the deep gap region. This essentially makes it a 2-D problem where the head field is restricted only in the  $x$ - $y$  plane, as shown in Figure 1.3(a).
3. The magnetic potential across the gap follows a linear drop from  $gH_g/2$  to  $-gH_g/2$ , while the deep gap field,  $H_g$ , is constant inside the gap down to  $y = 0$ .

Based on the above assumptions, the magnetic potential for  $y > 0$  is given by

$$\phi(x, y) = \frac{y}{\pi} \int_{-\infty}^{\infty} dx' \frac{\phi_s(x')}{(x - x')^2 + y^2} \quad (1.3)$$

The  $x$ - and  $y$ -components of the Karlqvist head field in this region then follow

$$\begin{aligned} H_x(x, y) &= -\frac{\partial \phi}{\partial x} \\ &= \frac{H_g}{\pi} \left[ \tan^{-1} \left( \frac{x + g/2}{y} \right) - \tan^{-1} \left( \frac{x - g/2}{y} \right) \right] \end{aligned} \quad (1.4)$$

$$\begin{aligned} H_y(x, y) &= -\frac{\partial \phi}{\partial y} \\ &= -\frac{H_g}{2\pi} \ln \frac{(x + g/2)^2 + y^2}{(x - g/2)^2 + y^2} \end{aligned} \quad (1.5)$$

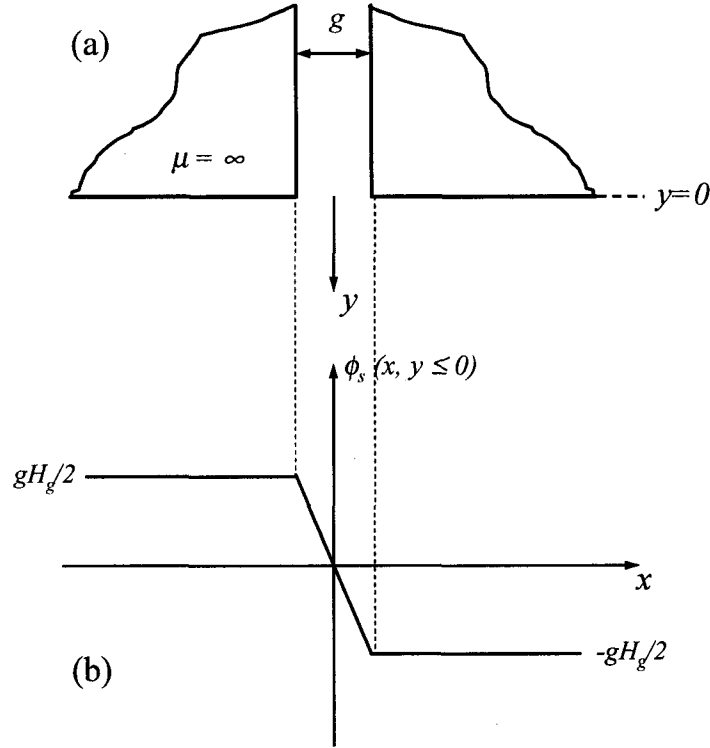


Figure 1.3: (a) Schematic illustration of the Karlqvist head. (b) The magnetic potential  $\phi_s$  for the region  $y \leq 0$ .  $x$  is the down-track direction,  $z$  is the cross-track direction, and  $y$  is the direction perpendicular to the air-bearing surface (ABS). (Redrawn from [14])

In fact, Karlqvist head field model can be used not only for a ring head for longitudinal recording, it is also used to approximate the trailing edge head field of a single pole head with SUL in perpendicular recording. As mentioned earlier in this chapter, the effect of the SUL to the recording media is a magnetic image of the write pole magnetization, or an “image” head. Therefore, assuming the thickness of the write pole in down-track direction is very large, the total head field from both the write pole and the image head will be that of a Karlqvist head turned sideways by  $90^\circ$  [15, 16], as shown in Figure 1.4.

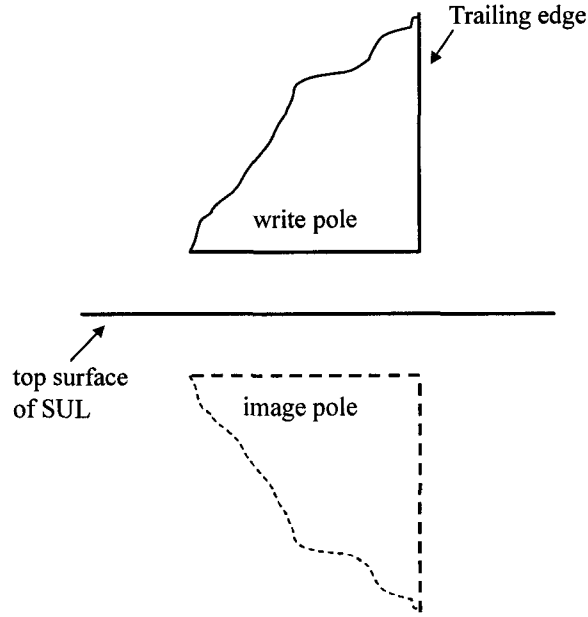


Figure 1.4: Schematic illustration of the Karlqvist head used for calculating the trailing edge head field of a single pole head with SUL in perpendicular recording. The head field is defined in the half plane at the right of the trailing edge.

The Karlqvist head field gives a good approximation to that of a thin film head at locations far away from the corners of the write gap. However, there are limitations inherent to the assumptions based upon which this field is derived. First of all, Eqs. (1.4) and (1.5) only give the expression of the field components as functions of the deep gap field  $H_g$ , the gap length  $g$ , and the location. It does not tell how  $H_g$  is calculated. The latter could be obtained from magnetic circuit analysis, which itself introduces errors when a real inductive head is treated as an effective magnetic circuit. Secondly, Karlqvist field is only a 2-D field, hence it does not contain the information about the head field at track edge. Lindholm [12] has extended the Karlqvist field into 3-D, starting with the same assumptions taken by [11], which gives the head field with half-infinite track width and finite track width. Finally, Eqs. (1.4) and (1.5) are not very accurate

close to the gap corner, as the actual magnetic potential around the gap corner is not as simple as that assumed here. For high density recording, the shape of the field profile around the edge of the write pole is of great importance. Therefore, a more accurate model is needed in this case. A model by Westmije [13] using conformal mapping gives more accurate field than the Karlqvist head field. Clearly, the analytical models only assumed very simple geometries of the head, which are over-simplification for today's state-of-the-art heads with sophisticated structures. In addition, they do not account for the magnetic flux conduction details, nor the micromagnetics of the head magnetization.

### 1.3.2 Transmission line models

Transmission line models are essentially based on magnetic circuit analysis, which is the counterpart to electric circuit in magnetics. In a magnetic circuit, the magnetic flux flows in the path formed by the magnetic material of the head and the air gap, each of them having its own value of reluctance, counterpart to resistance in electric circuits. The original transmission line head model was developed by Paton [17] in 1971. A more frequently used one was later introduced by Jury *et. al.* [18] in 1978.

The simple form of the transmission line models assumes a 2-D structure of the head, i.e., the head is infinitely wide in the cross-track direction. It also assumes a quasi-static current in the coil. Although this could give some insight into the estimation of the head efficiency, it is an over-simplification to the real 3-D structure of the head. The 3-D version of the transmission line models can provide more accurate information about the head structure by dividing the head into segments with various gaps and widths [19]. Static transmission line models are only valid for low frequencies, as the permeability

of the head reduces, and the eddy current effect becomes more significant at high frequencies. In those cases, models accounting for high-frequency effects [20, 21] are needed.

In general, transmission line models are useful to calculate head efficiency and the effect of head geometry and head material such as permeability. The assumptions these models usually make include linear property of the material with a fixed permeability. This assumption was reasonably good when the model was used for inductive heads as readers. However, for write heads, especially those used at high densities, magnetization saturation occurs frequently, at least in regions close to the corners of the pole tip or the neck region between the pole tip and the yoke. In these cases, the nonlinear behavior of the head magnetization invalidates the transmission line models. Furthermore, same as the analytical models, transmission line models can not provide any information about the domain structure in the head, nor its dynamics when driven by a write current that varies in time.

### 1.3.3 Finite element and boundary element methods

As discussed above, both the analytical models and the transmission line models have the shortcoming of inability to deal with complicated structure and/or geometries. Finite element method (FEM) and boundary element method (BEM) are very powerful numerical methods that are able to fulfill this functionality. In fact, nowadays, there are numerous commercially available FEM and BEM packages, not only for magnetic problems, but for other fields such as structural mechanics *etc.*. In the hard drive industry, FEM- and BEM-based models are widely used as design tools.

For electro-magnetic problems, FEM models [22] are usually based on



Maxwell's equations. The model generates finite element meshes for the entire structure of the head to be modeled. The magnetic potential at each of the vertices of the meshes is solved in a self-consistent manner for given boundary conditions. Once the potential at each point is known,  $\mathbf{B}$ ,  $\mathbf{H}$ , and  $\mathbf{M}$  at each point of the magnetic system are determined. BEM method is similar to FEM, except that instead of solving for potential, it finds equivalent source located on the boundaries and interfaces by forcing it to satisfy given boundary conditions [23].

Although FEM and BEM methods are very powerful, there are still problems they are unable to deal with, in particular, some of them are those that are important for high density and high data rate applications. For these issues, micromagnetic models are the perfect candidate, as shown in the next section.

#### 1.3.4 Micromagnetic models

As seen in previous sections, none of those head models capture the micromagnetic details of the pole tip and/or the yoke, which are very important at high density, where the head pole tip dimension is in deep sub-micron region. At such a dimension, the micromagnetic features of the head, such as the crystal and/or induced anisotropy field, the ferromagnetic exchange coupling effect, and the microstructure of the thin film, may all affect the head field. These factors, though impossible to be accounted for in other models, could be readily dealt with in micromagnetic modeling.

Micromagnetic modeling, as a simulation tool, typically is a blend of Brown's micromagnetic theory [24] and the Landau-Lifshitz-Gilbert (LLG) equation that describes the dynamic evolution of magnetization with time. Due to very intense

computation needed, micromagnetic modeling was first used only in 2-D cases, for instance, the thin-film recording media [25], and it has been a tremendous success in modeling the thin film media [26]. However, the application of micromagnetic modeling on thin-film heads with 3-D structure had been limited, due to the prohibitive computation intensity. With the continuous advancement of computers and the shrinkage of the head dimension, it has become viable to simulate thin-film heads using micromagnetic models [27, 28]. Though the simulation is still limited within the pole tip region or a head with highly miniaturized dimension, it provides significant insight into understanding of the head at such dimensions, as it has the following major advantages, in addition to those mentioned earlier in this section.

1. Magnetic domain structures in the head can be modeled using micromagnetic modeling. The dependence of the domains, therefore the head field performance, on the head structure, geometry and other parameters such as induced anisotropy, can be readily investigated. Of particular interest is the remanent head field, i.e., the head field after the drive current is turned off, which may no longer be zero for heads with extremely narrow track width, thus presenting a potential remanence erasure problem. This phenomenon will be studied in Chapter 3 and Chapter 4 using micromagnetic modeling, as none of the other models have this capability.
2. The dynamics of the magnetization motion in the head could be simulated, as most micromagnetic models utilize LLG equation, which gives the dynamic data of the magnetization evolution with time. This is particularly important, as the recording data rate is moving beyond 1 Gbit/sec. In this frequency regime, the drive current is reversed in

the time scale of sub-nanosecond, which is comparable to the characteristic time of the gyromagnetic motion of the spins. Therefore, the dynamic micromagnetic features have to be taken into account. The LLG-equation-based micromagnetic models enable us to perform this investigation. A detailed study on this will be presented in Chapter 5.

#### 1.4 Outline of the thesis

The rest of the dissertation is organized as follows.

Chapter 2 presents the micromagnetic model that is utilized in this research. Different energy terms and the effective magnetic field are discussed. Landau-Lifshitz-Gilbert equation that describes the magnetization evolution is presented. Some important parameters of this model and their physical meaning and constraints are discussed.

In Chapter 3, effects of track width reduction, as an immediate result of increasing the areal density, will be studied. The effect of the pole-tip foot print aspect ratio on the head field and head skew induced loss of track density will first be discussed. The impact of track width reduction will then be investigated, especially on the maximum on-track field magnitude and on the down-track field gradient, the two critical measures of the head field. Finally, the remanent head field is studied. The factors affecting the remanent head field are identified and investigated in detail.

In Chapter 4, several head designs are proposed and investigated. A head with a double-layer lamination in the yoke is found to have excellent high frequency magnetization reversal performance at low drive current. Furthermore, laminating the pole tip will solve the non-zero remanent field problem at extremely narrow track widths. A stitched pole-tip head design will also be presented, which shows significant enhancement of the head field compared to a

conventional single pole head. Effects of various head design parameters will be investigated as well.

Chapter 5 focuses on the head magnetization reversal behavior at very high frequency (GHz range), in which the gyromagnetic precession of spins and the energy dissipation process play an important role. In this chapter, the details of the magnetization reversal processes will first be studied, followed by an investigation of the effects of the Gilbert damping constant and the drive current rise time on the magnetization reversal hence the field rise time. The phenomenon observed from the simulation results in this chapter provides insight into potential limits of high frequency magnetization reversal speed, therefore relevant to high data rate applications.

Chapter 6 deals with the SUL, essentially part of the head in perpendicular recording, thus a very important component of the recording system. The effect of the SUL on both the write process and the readback process will be studied via micromagnetic modeling. The SUL material properties as well other parameters are investigated in detail. Specially emphasized is the linear density limitation posed by the existence of the SUL.

In Chapter 7, the effects of stress on the magnetic properties of soft magnetic thin film with non-zero magnetostriction will be studied. An analytical derivation will be presented first, based on which the currently used micromagnetic model is extended by incorporating the magnetoelastic energy. Some example cases are studied using the extended model, including domain rearrangement in a thin film element under stress, and a conceptual write head design that utilizes a stress induced in-plane anisotropy to improve the head performance.

In Chapter 8, we will develop a model that is able to compute the stress and strain in a magnetic thin film, as a result of minimizing the total energy,

including magnetic energy (all the energy terms discussed in Chapter 2), magnetoelastic energy, and elastic energy. Several case studies will be presented using this model.

Chapter 9 concludes the entire dissertation.

In this thesis, *cgs* units are used unless otherwise noted.

## 2 MICROMAGNETIC MODEL

In this chapter, we will discuss the 3-D micromagnetic model that is used for the simulations in most chapters of this thesis work. Although there are extension of functionality of the model in later part of the thesis, the core of the model is covered in this chapter. In section 2.2, we will discuss the energy terms based upon which this model is built. The energy terms include magnetostatic energy, exchange energy, anisotropy energy and Zeeman energy due to the external magnetic field. There are other possible energy terms, such as magnetoelastic energy, when magnetostriction and stress are considered, which will be discussed in Chapter 7, as in most cases that effect is not considered. Having set the energy terms, Section 2.3 presents the effective magnetic field exerted on the magnetization for a given magnetization configuration of the system, which will be used in LLG equation to solve for the dynamic magnetization evolution. Section 2.4.1 presents the LLG equation, which is the underlying equation of this model governing the magnetization dynamics. An important phenomenological parameter, the Gilbert damping constant, will be discussed in Section 2.4.2. The rest of the chapter discusses some other aspects of this model, such as the numerical solution of the model, the selection of the mesh size, the treatment of magnetic imaging, as well as the removal of surface charges in the model. Several cases validating the model are presented at the end of this chapter.

## 2.1 Overview

The theory behind micromagnetic was first formulated by Landau and Lifshitz [29]. It was then further developed by Brown [24] into a self-consistent framework. Before the micromagnetic theory came out, the only theory to describe the magnetization of a magnetic system was the domain theory [30]. In domain theory, the magnetization in a material is described by the domains and the domain walls. In a magnetic domain, the magnetization is uniform, while the magnetization direction varies from one domain to another. The transition region between two domains is the domain wall. The domain configuration, i.e., the domain magnetization direction and the wall thickness, positions *etc.*, can be solved by minimizing the total system energy. In contrast, in micromagnetic theory, there is no such clear definition of domain and domain wall. The magnetization of the material at any point  $i$  is described by a vector  $\mathbf{M}_i$ :

$$\mathbf{M}_i = M_s \cdot \mathbf{m}_i \quad (2.1)$$

where  $M_s$  is the saturation magnetization of the material, and  $\mathbf{m}_i$  is the direction of the magnetization at that point. To get the magnetization configuration of a given magnetic entity, one has to solve for  $\mathbf{M}_i$  at every point in the region of interest. Once  $\mathbf{M}_i$  is known everywhere, the domains and domain walls can be naturally found from the resulting magnetization distribution, the former being the regions where the spatial magnetization change is very little, whereas the latter corresponding to those where the magnetization direction varies rapidly in space. Early application of the micromagnetic theory was limited to cases with simple geometry and problems with symmetry [31]. In order to use this theory to solve more realistic problems with more complication, the magnetic system needs to be discretized to facilitate the use of computers for numerical computations. Obviously, the amount of computation required depends upon

the total number of discretization units, which is determined by the dimension of the magnetic system and that of the discretization cells, while the latter can not be arbitrarily chosen due to some physical constraints, as will be discussed in Section 2.6.1. As a result, over years the micromagnetic modeling had been limited to two-dimensional (2-D) problems, such as a thin-film recording media, where only one layer of cells is needed, though the magnetization still is solved with possible orientations in 3-D space [25]. The rapid advancement of computers in recent years had made it possible to do micromagnetic modeling of a three-dimensional (3-D) system, such as a thin film head [27].

The construction of the micromagnetic model includes the mesh generation, the expression of energy terms and/or the effective field, and the solution process to find the magnetization of the system under certain conditions. As opposed to triangular mesh cells (with variable size) in most FEM packages, most micromagnetic models employ a regular array of cells with identical shapes and dimensions to generate the mesh, primarily due to the way it calculates the magnetostatic energy (see Section 2.2.1). In 2-D cases, a hexagonal close-packed array of cells in the plane is usually used. Whereas in the case of a 3-D model here, the mesh cells are chosen to be identical fine rectangular parallelepipeds. After the total energy of the system is expressed as functions of  $\mathbf{M}_i$ , the problem could be solved either statically by minimizing the total system energy, or dynamically by using LLG equation (Section 2.4.1), as many micromagnetic models do. The advantage of using LLG equation is that it provides information about the dynamic process of the magnetization evolution, which is extremely important for modeling the head field reversal time at high frequency.



## 2.2 System energy expression

As discussed above, the first stage of building the model is the mesh generation. After having all cells, the magnetization vector of each cell will be represented by  $\mathbf{M}_i$ . As in Eq. (2.1), the magnetization vector of each cell is assumed to have a constant magnitude, equal to the saturation magnetization of the material, whereas its direction is to vary in space. Here we will calculate the energy density of each cell, based on which the effective field will be derived. The energy terms considered include the magnetostatic energy, the anisotropy energy (uniaxial and/or cubic), the ferromagnetic exchange energy, and the Zeeman energy. These are the basic terms for this general head model. Other energy terms for extension of the model, for example, the magnetoelastic energy, will be presented in later chapters.

### 2.2.1 Magnetostatic energy

The magnetostatic energy is the energy of the magnetization in the field it produces:

$$U = -\frac{1}{2} \int \mathbf{M} \cdot \mathbf{H}_d d^3r \quad (2.2)$$

where  $\mathbf{H}_d$  is the demagnetization field. In the discrete form, the magnetostatic energy density is essentially the interaction energy between the magnetic dipole moments. This energy density associated with  $i^{th}$  moment is:

$$E_{mag}(\mathbf{r}_i) = -\mathbf{M}_i \cdot \mathbf{H}_d(\mathbf{r}_i) \quad (2.3)$$

where  $\mathbf{H}_d(\mathbf{r}_i)$  is the demagnetization field produced by all the dipole moments in the system at the location of the  $i^{th}$  moment,  $\mathbf{r}_i$ , which is given by:

$$\mathbf{H}_d(\mathbf{r}_i) = \sum_{j=1}^N \mathbf{H}_d^j(\mathbf{r}_i) \quad (2.4)$$

where  $\mathbf{H}_d^j(\mathbf{r}_i)$  is the demagnetizing field of the moment of  $j^{th}$  cell at the location of  $i^{th}$  cell,  $N$  is the total number of discrete cells in the system. Since the magnetization of the discrete cells is assumed uniform, the demagnetizing field is only due to the magnetic poles, or charges, on the surface of the cells [32]. Therefore we have  $\mathbf{H}_d^j(\mathbf{r}_i)$  given by this surface integral over  $j^{th}$  cell:

$$\mathbf{H}_d^j(\mathbf{r}_i) = \int_{s_j} \frac{(\mathbf{r}_i - \mathbf{r}_j)\mathbf{n}_j \cdot \mathbf{M}_j}{|\mathbf{r}_i - \mathbf{r}_j|^3} d^2r_j \quad (2.5)$$

where  $\mathbf{n}_j$  is the surface normal vector of the  $j^{th}$  cell. Combining Eqs. (2.4) and (2.5), we have:

$$\mathbf{H}_d(\mathbf{r}_i) = \sum_{j=1}^N \mathbf{D}_{ij} \cdot \mathbf{M}_j \quad (2.6)$$

where  $\mathbf{D}_{ij}$  is called the demagnetization matrix and is defined as follows:

$$\mathbf{D}_{ij} = \int_{s_j} \frac{(\mathbf{r}_i - \mathbf{r}_j)\mathbf{n}_j}{|\mathbf{r}_i - \mathbf{r}_j|^3} d^2r_j \quad (2.7)$$

As seen from Eq. (2.7),  $\mathbf{D}_{ij}$  is only dependent on the relative positions of the two cells and the geometries of the  $j^{th}$  cell, it can be pre-calculated once the system geometry is fixed. The magnetostatic energy will then be determined once the magnetization distribution is given at any moment. In our 3-D micromagnetic model case, since the cells are of rectangular parallelepiped shape,  $\mathbf{D}_{ij}$  can be analytically calculated. The detailed derivation of  $\mathbf{D}_{ij}$  is given in Appendix A.

It must be noted that, as the magnetostatic energy is the result of the long-range dipole-dipole pair interaction, for each of the cells, the computation involves the contribution from all  $N$  cells. It is therefore very computationally demanding to compute this energy. Assuming the total number of cells in the system is  $N$ , the amount of numerical computations is at the order of  $N^2$ , which easily becomes prohibitive as  $N$  increases. This is the main reason limiting the size of 3-D system we can model. Fortunately, Eq. (2.6) has the form of a

discrete convolution of the demagnetization matrix and the magnetization - if we expand them into the 3-D component form:

$$\mathbf{H}_d(i_x, i_y, i_z) = \sum_{i=0}^{N_x-1} \sum_{j=0}^{N_y-1} \sum_{k=0}^{N_z-1} \mathbf{D}(i_x - j_x, i_y - j_y, i_z - j_z) \mathbf{M}(j_x, j_y, j_z) \quad (2.8)$$

where the short index  $i$  and  $j$  used earlier are replaced by the indices  $(i_x, i_y, i_z)$  and  $(j_x, j_y, j_z)$ , and  $N_x, N_y, N_z$  are the number of cells in the three dimensions, respectively. Therefore, according to the property of the Fourier transform [33], with proper manipulation (see [27] for details), we have:

$$\mathcal{F}\{\tilde{\mathbf{H}}_d\} = \mathcal{F}\{\tilde{\mathbf{D}}\} \mathcal{F}\{\tilde{\mathbf{M}}\} \quad (2.9)$$

where  $\tilde{\mathbf{H}}_d$ ,  $\tilde{\mathbf{D}}$  and  $\tilde{\mathbf{M}}$  are the Fourier transform of the periodic version of  $\mathbf{H}_d$ ,  $\mathbf{D}$ , and  $\mathbf{M}$ , respectively. Having done with Eq. (2.9), taking an inverse Fourier transform of  $\mathcal{F}\{\tilde{\mathbf{H}}_d\}$  will yield  $\tilde{\mathbf{H}}_d$  and therefore  $\mathbf{H}_d(\mathbf{r}_i)$ .

The employment of the Fourier transform technique is implemented in the form of 3-D fast Fourier transform (FFT) in the model. This process is crucial for the model to be viable. The amount of the computation of the demagnetizing field using FFT algorithm is reduced to the order of  $N \log_2 N$ , compared to  $N^2$  for direct multiplication and summation. Nevertheless, among the calculations of different energy terms, the magnetostatic energy is the most intense one, due to its nature of long-range interaction. It is noticed that the magnitude of the magnetostatic interaction decays very fast as the relative distance of the two cells increases due to the inverse-squared-distance nature. Therefore, there might be ways to reduce the computation for the demagnetizing field [34], although this is beyond the scope of this thesis.

### 2.2.2 Exchange energy

The source of exchange energy is from the quantum mechanical exchange coupling effect between neighboring spins. In a ferromagnetic material, this exchange interaction favors neighboring spins to be aligned in the same direction. The treatment of the exchange energy in micromagnetic models [24] is based on Heisenberg's model [35]. For a continuous magnetization distribution in a material, the exchange energy density is given by:

$$E_{exc}(\mathbf{r}) = 2A [(\nabla\alpha)^2 + (\nabla\beta)^2 + (\nabla\gamma)^2] \quad (2.10)$$

where  $A$  is the exchange constant of the magnetic material, which is dependent on the Heisenberg exchange integral and the material structure [36], and  $\alpha$ ,  $\beta$ , and  $\gamma$  are the continuous directional cosines of the magnetization vector  $\mathbf{m}$ . Eq. (2.10) can be rewritten as:

$$E_{exc}(\mathbf{r}) = 2A \left[ \left( \frac{\partial \mathbf{m}}{\partial x} \right)^2 + \left( \frac{\partial \mathbf{m}}{\partial y} \right)^2 + \left( \frac{\partial \mathbf{m}}{\partial z} \right)^2 \right] \quad (2.11)$$

In the case of a discrete system here, Eq. (2.11) is replaced by the finite difference form, leading to the expression of the exchange energy density of the  $i^{th}$  cell:

$$E_{exc}(\mathbf{r}_i) = \frac{2A}{a^2} \sum_{n.n.} (1 - \mathbf{m}_i \cdot \mathbf{m}_j) \quad i = 1, 2, \dots, N \quad (2.12)$$

where  $a$  is the center-to-center distance between neighboring cells, assuming the cell shape is cubic, which is the case in our model. The summation is only over the nearest neighbors, consistent with the nature of the short-range interaction of exchange coupling. By dropping the first term in Eq. (2.12), which is a constant, we can rearrange Eq. (2.12) to the following form, which will make

the later calculation of the effective field easier:

$$\begin{aligned} E_{exc}(\mathbf{r}_i) &= -\frac{2A}{a^2} \mathbf{m}_i \cdot \sum_{n.n.} \mathbf{m}_j \\ &= -\frac{2A}{M_s^2 a^2} \mathbf{M}_i \cdot \sum_{n.n.} \mathbf{M}_j \quad i = 1, 2, \dots, N \end{aligned} \quad (2.13)$$

where  $M_s$  is the saturation magnetization of the material.

### 2.2.3 Anisotropy energy

Anisotropy energy is the term that is dependent on the magnetization orientation relative to the direction of the anisotropy easy axes. The anisotropy could be crystalline anisotropy or some induced anisotropy in the material. The crystalline anisotropy can be divided into uniaxial anisotropy and cubic anisotropy. The former usually exists in materials with hexagonal structure, whereas the latter in cubic materials. In this section, we will describe the case of uniaxial anisotropy. It doesn't matter whether it is crystalline or induced, as it has exactly the same mathematic form. In most cases of interest in this thesis, the effect of cubic anisotropy is very small and therefore not considered, although there are problems where cubic anisotropy can not be neglected [37]. The treatment of cubic anisotropy is slightly more complex, as it involves three orthogonal easy axes. Details of incorporating the cubic anisotropy in the model is given in Section 7.3.2.

For uniaxial anisotropy, with only  $K_1$  considered, the anisotropy energy density is given by:

$$E_{ani}(\mathbf{r}_i) = K_1 \sin^2 \theta_i \quad i = 1, 2, \dots, N \quad (2.14)$$

where  $K_1$  is the anisotropy constant,  $\theta_i$  is the angle between the magnetization of the  $i^{th}$  cell and the anisotropy easy axis, and  $N$  is the total number of cells

in the system. Eq. (2.14) can be rewritten as:

$$\begin{aligned} E_{ani}(\mathbf{r}_i) &= K_1 |\mathbf{k}_i \times \mathbf{m}_i|^2 \\ &= K_1 [1 - \mathbf{k}_i \cdot \mathbf{m}_i]^2 \quad i = 1, 2, \dots, N \end{aligned} \quad (2.15)$$

where  $\mathbf{k}_i$  is the unit vector along the direction of the easy axis of the  $i^{th}$  cell, and  $\mathbf{m}_i$  is the unit vector of the magnetization of the  $i^{th}$  cell.

#### 2.2.4 Zeeman energy

Zeeman energy is the energy of a magnetic moment in an externally applied magnetic field. The Zeeman energy density of the  $i^{th}$  cell is:

$$E_{ext}(\mathbf{r}_i) = -\mathbf{M}_i \cdot \mathbf{H}_a(\mathbf{r}_i) \quad i = 1, 2, \dots, N \quad (2.16)$$

where  $\mathbf{H}_a(\mathbf{r}_i)$  is the applied external field at the location of the  $i^{th}$  cell, which, in the case of a write head model, is the driving field produced by the write current in the coil. The calculation of this driving field for a given geometry of the current coil sheet is given in Appendix C. Since our model is a dynamic one,  $\mathbf{H}_a$  also varies with time, as all other terms of the effective field do, as shown in the next section.

### 2.3 Effective Field

The total energy density of the  $i^{th}$  cell is the sum of the contributions from different energy terms:

$$E_{tot}(\mathbf{r}_i) = E_{mag}(\mathbf{r}_i) + E_{exc}(\mathbf{r}_i) + E_{ani}(\mathbf{r}_i) + E_{ext}(\mathbf{r}_i) \quad (2.17)$$

The effective magnetic field exerting on the magnetization of the  $i^{th}$  cell is then given by taking the partial derivative of the total energy density with

respect to the magnetization vector:

$$\begin{aligned}\mathbf{H}_{eff}(\mathbf{r}_i) &= -\frac{\partial E_{tot}(\mathbf{r}_i)}{\partial \mathbf{M}_i} \\ &= -\frac{\partial E_{tot}(\mathbf{r}_i)}{\partial M_x^i} \hat{\mathbf{e}}_x - \frac{\partial E_{tot}(\mathbf{r}_i)}{\partial M_y^i} \hat{\mathbf{e}}_y - \frac{\partial E_{tot}(\mathbf{r}_i)}{\partial M_z^i} \hat{\mathbf{e}}_z\end{aligned}\quad (2.18)$$

where  $\hat{\mathbf{e}}_x$ ,  $\hat{\mathbf{e}}_y$ , and  $\hat{\mathbf{e}}_z$  are the unit vectors along the three axes of the Cartesian coordinate system used here. Substituting Eqs. (2.3), (2.6), (2.13), (2.15) and (2.16) into (2.17) and (2.18) yields:

$$\mathbf{H}_{eff}(\mathbf{r}_i) = \sum_{j=1}^N \mathbf{D}_{ij} \cdot \mathbf{M}_j + \frac{2A}{M_s^2 a^2} \sum_{n,n} \mathbf{M}_j + \frac{2K_1}{M_s} (\mathbf{m}_i \cdot \mathbf{k}_i) \mathbf{k}_i + \mathbf{H}_a(\mathbf{r}_i) \quad (2.19)$$

In the first term at the right hand side of Eq. (2.19), the quantity  $2K_1/M_s$  is defined as the anisotropy field, denoted by  $H_k$ , which is a measure of the strength of anisotropy for a given material. From Eq. (2.19) it is seen that at any moment, with the external field given, the effective field is completely described by the magnetization configuration. From Eq. (2.18), the meaning of the effective field is that it is the direction the magnetization  $\mathbf{M}_i$  tends to rotate towards to lower its energy. How exactly  $\mathbf{M}_i$  rotates toward  $\mathbf{H}_{eff}(\mathbf{r}_i)$  depends on what the model assumes about the magnetization relaxation mechanism. In a model based on energy minimization, at each step of calculation,  $\mathbf{M}_i$  could be set to simply rotate towards  $\mathbf{H}_{eff}(\mathbf{r}_i)$  by some small amount, until the total system energy reaches a minimum. While in our model, the magnetization dynamics is described by the LLG equation, which is discussed in the next section.

•

## 2.4 Spin Dynamics

### 2.4.1 Landau-Lifshitz-Gilbert equation

The dynamic motion of the magnetization of the cells is determined by the Landau-Lifshitz equation, which, combined with Gilbert damping, has the form:

$$\frac{d\mathbf{M}_i}{dt} = -\gamma\mathbf{M}_i \times \mathbf{H}_i - \frac{\alpha\gamma}{(1+\alpha^2)M_s}\mathbf{M}_i \times (\mathbf{M}_i \times \mathbf{H}_i) \quad i = 1, 2, \dots, N \quad (2.20)$$

where  $\gamma = 1.76 \times 10^7 \text{ s}^{-1}\text{Oe}^{-1}$  is the electron gyromagnetic ratio,  $\alpha$  is a phenomenological damping constant, which will be discussed in more detail in section 2.4.2. The first term at the right hand side of Eq. (2.20) describes the gyromagnetic precession of the magnetization around the axis of the field acting on it,  $\mathbf{H}_i$ , which is calculated from Eq. (2.19). The precession frequency is  $\gamma\mathbf{H}_i$ . The first term alone will never align  $\mathbf{M}_i$  with the direction of  $\mathbf{H}_i$ . In reality, there is always energy dissipation mechanisms, which is phenomenologically described by the second term at the right hand side of Eq. (2.20). From the equation it can be seen that this term brings the magnetization towards the axis of the field direction at a rate proportional to  $\alpha\gamma$ . Also note that the entire right hand side is a vector that is orthogonal to  $\mathbf{M}_i$ . Therefore, during the process of motion, the magnetization vector always maintains its magnitude, which is consistent with the assumption we made about the rotation of magnetization of the cells. In Section 2.6.1, the condition for the uniform magnetization of cells to be physically valid will be discussed.

Eq. (2.20) can be written in the reduced form as follows, by defining  $\tau = \gamma M_s t$  and  $\mathbf{h}_i = \mathbf{H}_i / M_s$ :

$$\frac{d\mathbf{m}_i}{dt} = -\gamma\mathbf{m}_i \times \mathbf{h}_i - \frac{\alpha}{(1+\alpha^2)}\mathbf{m}_i \times (\mathbf{m}_i \times \mathbf{h}_i) \quad i = 1, 2, \dots, N \quad (2.21)$$

Eq. (2.21) tells how the magnetization of each cell changes its direction at any moment with a given magnetization configuration of the system. We



now essentially have  $N$  coupled ordinary differential equations. The final task is to solve these  $N$  coupled equations numerically by integrating it over time. Therefore, we have not only the final state of the magnetization of the system, but the solution process towards the final state also gives the dynamic evolution of the magnetization.

#### 2.4.2 Damping constant

We have briefly mentioned the damping constant in the second term at the right hand side of Eq. (2.20). This is the only phenomenological parameter in LLG equation. As a phenomenological constant, it basically does not tell what the mechanism of the damping is, though there are multiple mechanisms for the damping in a magnetic system [38]. The constant  $\alpha$  is assumed to be a quantity that accounts for the overall energy damping. There have been experimental efforts measuring the damping constant by high-frequency permeability measurements or ferromagnetic resonance. Both soft materials [39, 40, 41] and hard materials [42], such as a recording media, have been measured, and the results showed that the damping constant ranges from 0.0045 to 0.06.

For a single spin, the damping constant determines the energy dissipation rate. The larger the damping constant, the faster the magnetization approaches the axis of the field direction. On the other hand, for a collective system of spins, such as a magnetic thin film where all spins are interacting with one another through the short range and long range interactions, the effect of the damping constant is not as straightforward.

Previous micromagnetic simulations have shown that, in a soft magnetic thin film, the magnetization can be switched under an applied reversed field, even with zero damping [27], which is not possible for an isolated single spin

as discussed in Section 2.4.1. In the case of zero damping, there is no way the energy can be dissipated, therefore, the initial Zeeman energy actually transformed into exchange energy that is stored in the excited spin wave. In fact, this process has been found quite often in our simulations of the magnetization reversal of a write head, which will be discussed in more detail in Chapter 5.

Micromagnetic simulations of recording media [43] also showed that under certain conditions, such as an applied field with very short rise time, a small damping constant actually yields a faster switching of the media magnetization and requires lower field. This is due to the precessional switching, in which the precessional motion of the magnetization is favored, which will otherwise be suppressed by a large damping.

In a word, the damping constant is a very important parameter and has significant implications to the magnetization switching process of both the recording head [44] and the recording media [45] at very high frequencies.

## 2.5 Numerical Solution

The last step of the modeling is to solve the coupled differential equations that we got in Section 2.4 for the magnetization of the system at any time instants. Eq. (2.21) basically is a set of first order ordinary differential equations (ODE) of time with the initial conditions known, the latter being the initial magnetization distribution. There are many packages of ODE solvers freely available. The one we choose is a predictor-corrector method that uses the Adams-Bashforth-Moulton schemes [46]. This method uses the solution at the present and previous steps to extrapolate for the solution at next step, it then corrects the extrapolation using the derivative information obtained at the new point. This algorithm is suitable for high precision requirements with

complicated form at the right hand side of the ODE, such as Eq. (2.21).

## 2.6 Miscellaneous

In this section we will discuss some other aspects of the micromagnetic model, which, although not the core of the model, are important in order to have the model work correctly with reasonable speed.

### 2.6.1 Mesh cell size and grain size

This micromagnetic model actually needs to not only characterize the magnetics correctly, but it often has to take into account the crystal structural information, as the crystal anisotropy energy depends differently on the magnetization due to the different orientations of the crystal grains in the material. Therefore, we need to have the model keep the information of the crystal orientation of the grains, which will be used to calculate the anisotropy energy (and any other energy terms that are crystal orientation dependent, see Chapter 7). Consequently, we have two sizes: the size of the mesh cell that is used to do the discretization, and the physical grain size of the material. In most cases of interest here, the latter is larger than the former, hence a crystal grain may span several mesh cells. Those cells assigned to the same grain will have exactly the same crystal orientation data.

As to the discretization cell size, it has to be properly chosen too, in order to have the model make physical sense. From the view point of computation intensity, fewer cells are desirable. However, this means large cell size for a given overall dimension of the system. The immediate consequence is that too large cell size may cause loss of spatial resolution and accuracy of the result. In fact, what is worse is that, if the cell size is too big, the model will no longer yield

physically meaningful results. The reason is that the fundamental assumption of the model, when doing discretization, is that the magnetization of each cell is always uniform and only changes its direction by rotation. This assumption puts a strong condition on the cell size - it has to be smaller than or about the size of the exchange length of the magnetic material,  $l_{ex}$ , which is defined as:

$$l_{ex} = \sqrt{\frac{A}{2\pi M_s^2}} \quad (2.22)$$

where  $A$  is the exchange constant,  $M_s$  is the saturation magnetization of the material. The physical meaning of  $l_{ex}$  is the length over which the magnetization is highly exchange coupled together in the same direction.  $l_{ex}$  is a measurement of the strength of exchange coupling relative to the magnetostatic energy. Mao [27] showed that the critical single domain size of a magnetic cube is around  $8.7l_{ex}$ . For a material such as  $\text{Fe}_{65}\text{Co}_{35}$ , the exchange length is about 3 nm, corresponding to a single domain size of about 30 nm. In our simulation of write heads, a cell size of 10 nm is typically used. In those cases where an even smaller cell size is needed, for example, in order to resolve the inner structure of a domain wall at a nano-contact [47], the model itself has no constraint on it. The only possible issue is that the exchange energy term might dominate other energy terms by orders-of-magnitude difference and may cause numerical instability. The smallest cell size we have used is 1 nm without numerical crash.

### 2.6.2 Magnetic imaging

One of the major differences between longitudinal and perpendicular recording is that the latter has a high-permeability layer underneath the recording media - the SUL. The effect of SUL on the write pole is that it will be magnetized by the field from the write pole, hence the write pole will experience the

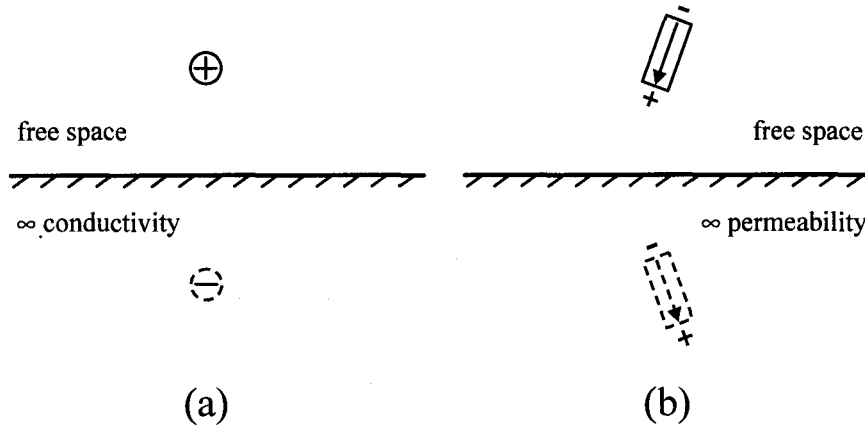


Figure 2.1: Imaging of (a) electric charges and (b) magnetic moments.

field produced by the magnetic charges in the SUL. Therefore, when modeling the write pole, this effect need to be considered. Ideally, this should be done by modeling both the write pole and the SUL together self-consistently. However, the amount of computation needed will be prohibitively large compared to that for the pole head only. Fortunately, the magnetic imaging effect shown below allows us to greatly simplify the computation while still correctly treating the effect of the SUL.

Magnetic imaging is the effect that when a magnetic moment is near the flat surface of an infinitely large magnetic material with infinite permeability, the effect of the induced magnetization in the latter, at any place outside the large permeable(soft) material, will be exactly the same as that from a moment that is a “mirror image” of the original moment. This “imaging” effect is only true when the flat surface is infinitely large with infinite permeability. In the case of finite permeability, the strength of the image magnetization will be multiplied by a factor of  $(\mu - 1)/(\mu + 1)$ , where  $\mu$  is the permeability of the soft material.

According to Jackson [32], the image charge of an electric charge close to the

surface of a large flat perfect conductor is at the location of the mirror image of the charge about the surface, with opposite polarity, as shown in Figure 2.1(a). For magnetic imaging, if treating the magnetic moment as a dipole with magnetic “charges” on its ends, the image of the magnetic moment will have the form as shown in Figure 2.1(b) [48]. Therefore, for a given discretization cell in the head with magnetization

$$\mathbf{M} = (M_x, M_y, M_z) \quad (2.23)$$

its image magnetization will be

$$\mathbf{M}' = (-M_x, M_y, -M_z) \quad (2.24)$$

where  $y$  is the direction normal to the surface of the SUL.

Similar to the calculation of the demagnetization matrix for the head magnetization on itself, the matrix for the interaction due to the image magnetization on the head can be calculated, with the only difference of an offset of the position of the image head. With the new demagnetization matrix and Eq. (2.24), the magnetostatic field due to the image head on the real head can be calculated the same way as in Section 2.2.1 using the FFT technique. By doing this imaging, the computation needed for the demagnetizing field of the SUL is only the same as that of the demagnetizing field of the head to itself, which is tremendously less than that with an actual micromagnetic modeling of the SUL. Comparisons of the results using the imaging technique to that from actual micromagnetic modeling of the SUL have also shown negligible difference on the resulting head field.

### 2.6.3 Removal of surface charges

In certain cases of the simulation, we may want to have a boundary condition such that the magnetic charges on a boundary surface of the region simulated is set to zero. This is to eliminate the artificial demagnetizing field arising from the charges at the boundary surface of the modeled region, which in reality should not be there if the modeled region is only a small part of the actual material. This technique has been used in Chapter 3 when simulating a finite region of SUL, which essentially is infinitely large in-plane. Part of the simulations in Chapter 4 also used this technique. To be discussed here is how to deal with this removal of charges in the model when calculating the demagnetizing field.

One straightforward way to do this is, at each time step, calculate the demagnetizing field as usual with the method in Section 2.2.1, then based on the magnetization of the cells at the boundary surface, calculate the demagnetizing field due to the surface charges and subtract it from the former one. However, the calculation of the field from the surface charges at each of the  $N$  cells turned out to be even more time-consuming than that of the field from the magnetization of all cells, making the model very inefficient. The solution to this issue is that, we can calculate the field directly from the charges at the interfaces between two neighboring cells using the following formula:

$$\mathbf{H}_d(\mathbf{r}_i) = \sum_j \mathbf{D}'_{ij} \cdot \sigma_j \quad (2.25)$$

where the three components of  $\sigma_j$  are defined as follows:

$$\begin{aligned} \sigma_x(j_x, j_y, j_z) &= M_x(j_x, j_y, j_z) - M_x(j_x + 1, j_y, j_z) \\ \sigma_y(j_x, j_y, j_z) &= M_y(j_x, j_y, j_z) - M_y(j_x, j_y + 1, j_z) \\ \sigma_z(j_x, j_y, j_z) &= M_z(j_x, j_y, j_z) - M_z(j_x, j_y, j_z + 1) \end{aligned} \quad (2.26)$$

and  $\mathbf{D}'_{ij}$  is the demagnetization matrix for the surface charge form, which is derived in Appendix B. Note that the number of surface charge elements are

$N_x+1$ ,  $N_y+1$ , and  $N_z+1$ , respectively, in the three dimensions, where  $N_x$ ,  $N_y$  and  $N_z$  are the number of discretization cells in the three directions, respectively.

Now at any moment, with all  $\mathbf{M}_j$  known, all the surface charge elements are given by Eq. (2.26). The nice thing is that to remove the charges at any of the six boundary surfaces (for  $j_x=0$ ,  $N_x$ , or  $j_y=0$ ,  $N_y$ , or  $j_z=0$ ,  $N_z$ ), just simply set the value of those charge elements to zero. The rest steps will be the same as that in Section 2.2.1, and the 3-D FFT can be used here as well. Then the amount of calculation of the demagnetizing field from charges will be essentially the same as that from magnetization in the case of a real boundary as in Section 2.2.1. Therefore, using this calculation technique, negligible computation overhead is introduced while treating the “free” boundary conditions, in the sense of removing the artificial charges at the boundary surfaces of the finite region modeled.

## 2.7 Validation of the micromagnetic model

In this section, we will present some test cases to show the validation of the micromagnetic model. The first case is a head field comparison with that from a FEM model. The second case is a comparison of the calculated magnetic domains with that measured from a magnetic thin film during a magnetization switching process.

### 2.7.1 Comparison with FEM

In this section, we present a comparison of the head field calculation result using our micromagnetic model with that from a FEM simulation. Although the latter does not include the effect of the exchange energy and anisotropy energy, it is not expected to cause much difference, as in this case the head is driven



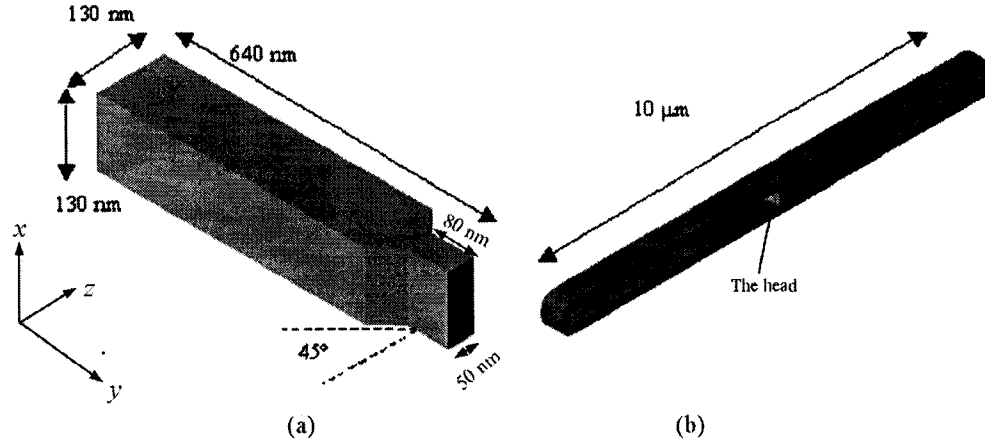


Figure 2.2: The modeled head structure for the FEM-micromagnetic comparative case study. (a) The geometry of the head. (b) the full structure used in FEM, the tiny light region at the center is the head, with a coil carrying current around it.

by a large current and therefore is in a state near saturation. The structure simulated is shown in Figure 2.2(a). In the micromagnetic modeling, cubic mesh cells with 10 nm edges are used for the discretization. No anisotropy was assumed in the head. The saturation magnetization of the material was assumed  $1830 \text{ emu/cm}^3$ . The driving current density was  $2 \times 10^8 \text{ A/cm}^2$ . The soft underlayer was 26 nm from the ABS and was modeled as a perfectly imaging structure. The coil shown in Figure 2.2(b) was that used in the FEM model to simulate an infinite coil structure as is done in the micromagnetic simulation.

The corresponding profile of the perpendicular field component  $H_y$  along the  $z$  direction, calculated from both models, is shown in Figure 2.3. The maximum perpendicular field for the FEM is about 3% lower than that of the micromagnetic model, whereas there is no difference in other parts of the field profile.

The possible reasons for the maximum field discrepancy might be the following. First, due to the cubic discretization, in the micromagnetic model,

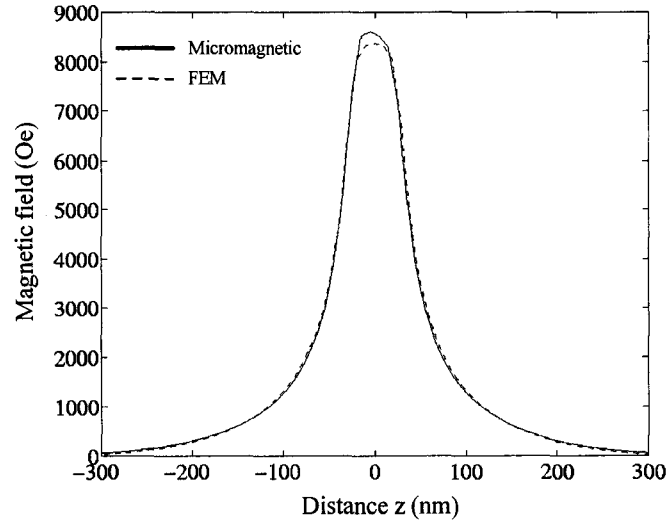


Figure 2.3: The perpendicular field profiles along  $z$  direction, calculated 13 nm from the ABS, from FEM and micromagnetic model, respectively.

in the sloped region, there will be artificial “stairs” along the surface which, in the case where the cell size is much smaller than the overall dimension, will not matter, but in this case that region only span a few cells. Secondly, the FEM model was based on a bulk B-H loop which goes through the origin, i.e., zero coercivity of bulk material. Nevertheless, the two models agrees with each other reasonably well, especially, in terms of the field profile.

### 2.7.2 Thin film magnetization

In this section we compare the micromagnetic modeling results of the domain configurations of a thin film element during a magnetization switching with the experimental results from MFM imaging [27]. Experimentally measured was a patterned rectangular permalloy thin film element. The dimension of the element is  $10\text{ }\mu\text{m}$  by  $20\text{ }\mu\text{m}$  with a thickness of 30 nm. In micromagnetic modeling, a  $1\text{ }\mu\text{m}$  by  $2\text{ }\mu\text{m}$  permalloy element with thickness of 25 nm was assumed, and the mesh cell used was 10 nm by 10 nm with a height of 12.5 nm.

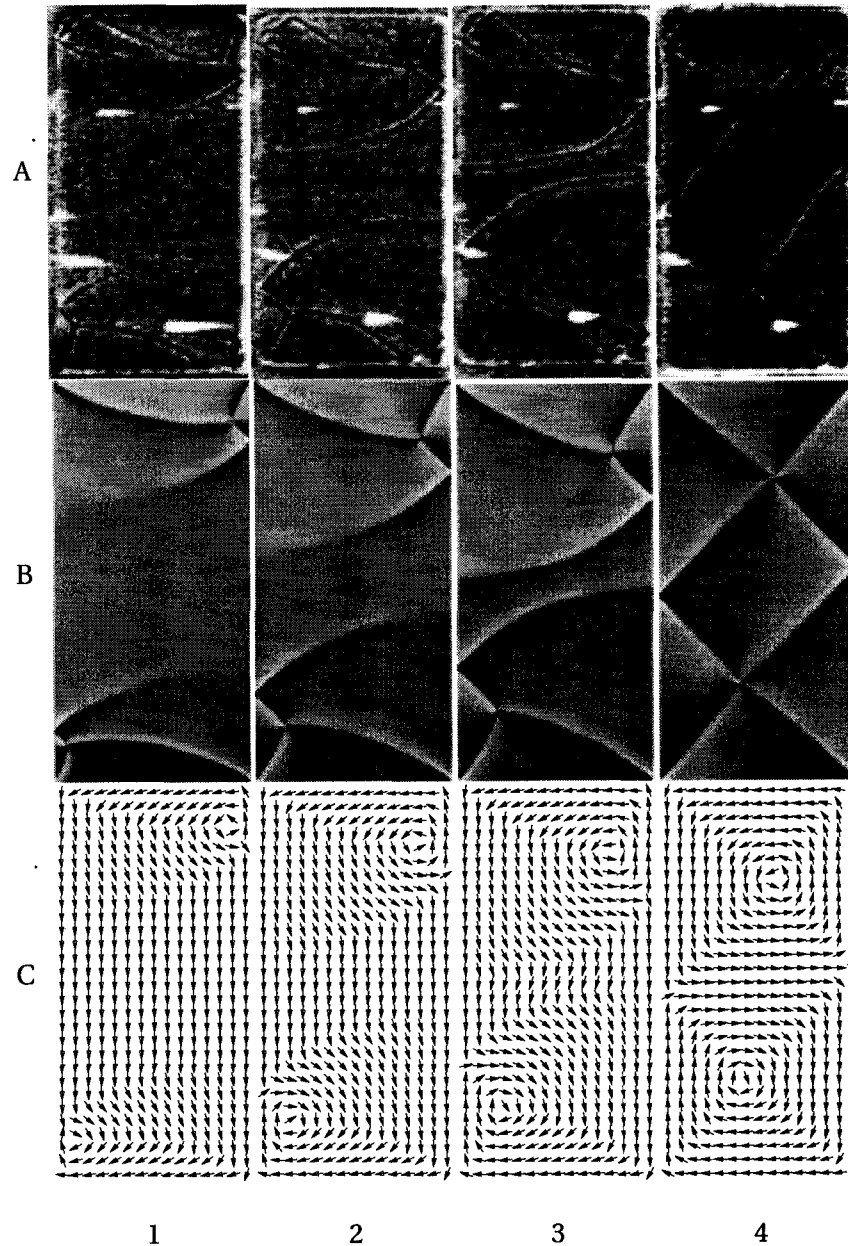


Figure 2.4: Domain configurations during a magnetization switching process in a permalloy thin film. Row A is the MFM images, row B is the calculated magnetic charge density from the micromagnetic simulation, and row C is the vector plot of the simulated magnetization patterns. To be continued in Figure 2.5. From [27].

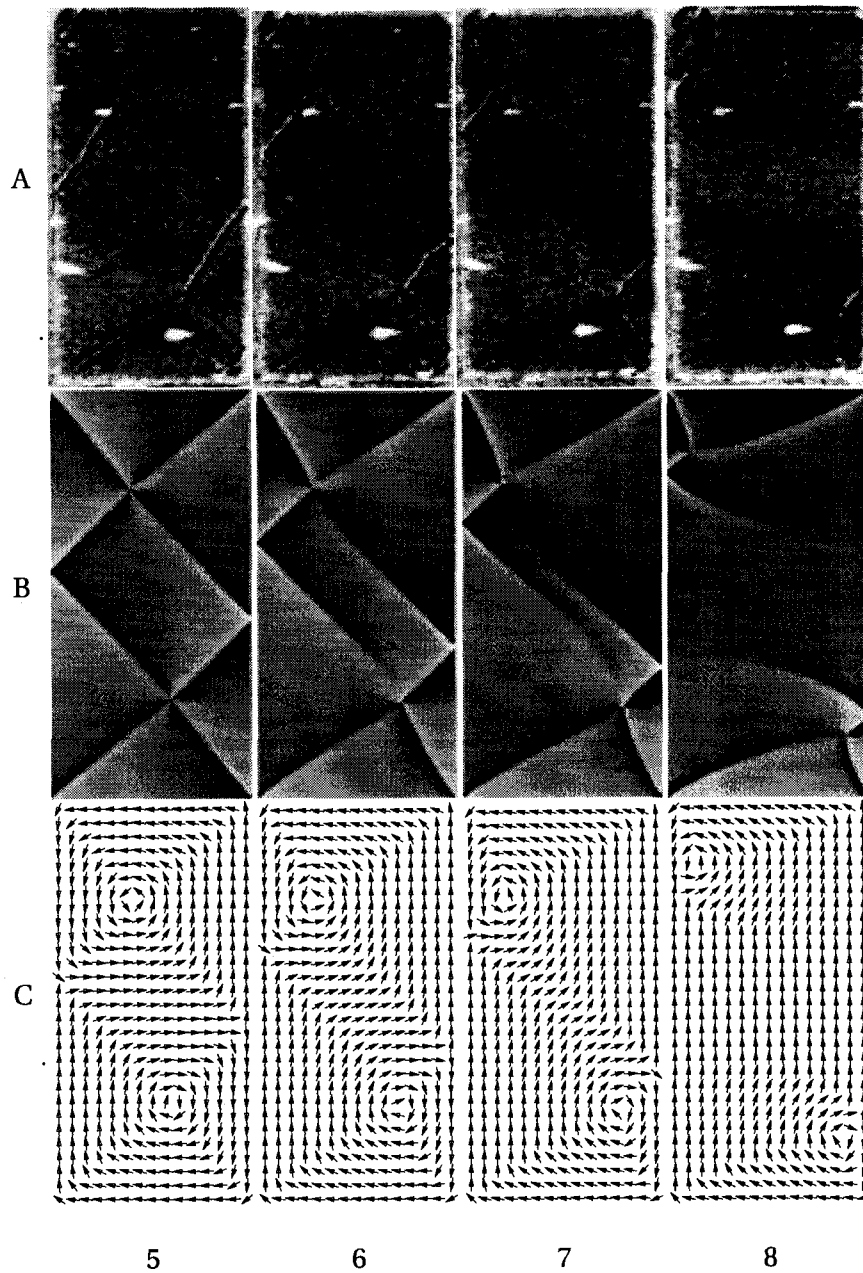


Figure 2.5: Domain configurations during a magnetization switching process in a permalloy thin film, continuing from Figure 2.4. Row A is the MFM images, row B is the calculated magnetic charge density from the micromagnetic simulation, and row C is the vector plot of the simulated magnetization patterns. From [27].

Figures 2.4 and 2.5 show the comparison of the domain configurations from MFM measurements and that from the micromagnetic modeling. A field up to 110 Oe in both directions was applied during the magnetic switching process. Excellent agreement was found between the patterns in the MFM images and the magnetic charge density plot from the simulation. In both cases, the bright and dark lines represent the domain walls in the film.

### 3 IMPACT OF TRACK WIDTH REDUCTION

To increase the areal recording density, both the linear density and the track density have to be increased accordingly, the former usually requires higher field gradient in order to write sharper transitions to facilitate smaller bit length, whereas the latter presents an immediate requirement on the write head - the physical track width of the head has to be reduced. In principle, as the recording density goes up, all geometric dimensions have to be shrunk in proportion, i.e., the track width, the head-media magnetic spacing (the distance between the head ABS to the center of the media layer). In reality, however, it is becoming more and more difficult to keep them in scale while shrinking down their sizes as going towards high density. Even though the lateral dimension (down-track and cross-track) of the head could be made smaller, it is no longer the case for the head-media spacing, simply because that the head flying height and the media thickness can not be arbitrarily reduced. This will present some issues, which are the main focus of study of this chapter [49]. Specifically, in this chapter, we will first show the model and the geometry of the head that is being studied. In the results section, a simple analytical analysis will be presented to give an idea about how the head field depends upon the geometric factors. The effect of the aspect ratio of the head pole-tip footprint will be discussed, which is followed by the impact of track width reduction on the head field magnitude and the field gradient. Finally, the remanent head field will be studied for heads with extremely small pole tips.

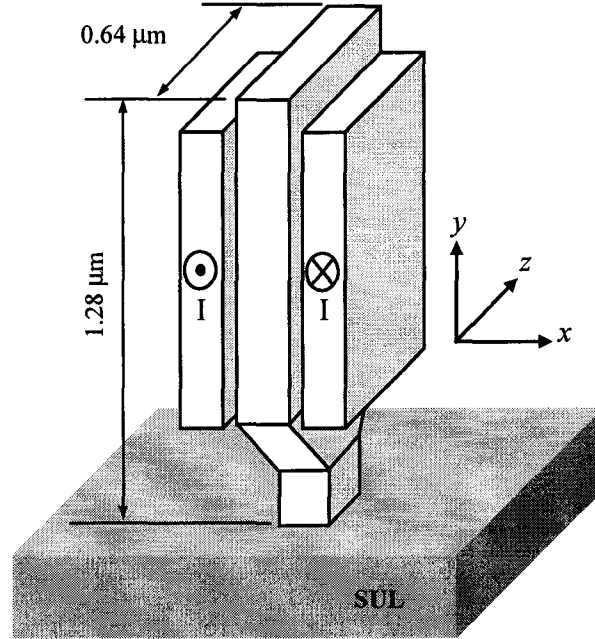


Figure 3.1: Schematic of the single pole head and SUL modeled in this chapter.

### 3.1 Model and geometry

The model used here is a 3-D micromagnetic model. In this study, the SUL is also included and simulated micromagnetically. This makes the simulation very computationally intensive. A schematic of the system being modeled is shown in Figure 3.1. The single pole head is driven by a single turn coil. The coordinate system is chosen such that  $x$  is the down-track direction,  $z$  is the cross-track direction and  $y$  is the direction perpendicular to the medium plane. This convention of the coordinate system will be used throughout the thesis unless otherwise noted. The single pole head and the SUL are first discretized into identical cubes with a side length of 10 nm. Landau-Lifshitz-Gilbert Equation is then utilized to solve for the magnetization of both the single pole head and the SUL, given an initial condition of the system. As discussed in last chapter, the computation is too intense for a simultaneous dynamic simulation

of both the head and the SUL. Therefore, we have employed a quasi-static modeling. Specifically, at any step, the head magnetization is first computed assuming perfect imaging. The magnetic field from the head magnetization is then applied on the SUL to solve for the SUL magnetization. From this point on, iterations are performed with the field from the two pieces applied on one another at each iteration, until a convergence is reached. Therefore, this is essentially a static modeling. To account for the fact that the SUL is infinitely large in plane compared with the pole tip footprint, the area of the simulated region of the SUL is much larger than the pole tip footprint. Furthermore, the four boundary surfaces of the simulated SUL region that are perpendicular to  $x$  and  $z$  directions are also assumed to abut to flux sinks that have infinite permeability. This is implemented by removing the magnetic charges on these four surfaces when calculating the demagnetizing field due to the SUL, as discussed in Section 2.6.3. In the present simulations, the head material is  $\text{Ni}_{45}\text{Fe}_{55}$  with saturation magnetization  $M_s = 1280 \text{ emu/cm}^3$ , and the SUL is Fe with  $M_s$  of  $1700 \text{ emu/cm}^3$ . A weak anisotropy field of 8 Oe is assumed in the head along  $z$  direction and no anisotropy in the SUL. The throat height of the head is kept constant at 90 nm for all cases. The flare angle of the head in the slanted region is  $45^\circ$ . The spacing between ABS and SUL is 30 nm, assuming a head flying height of 10 nm and a total thickness of 20 nm for the medium (including the non-magnetic overcoat layer, the lubricant layer, and the interlayer between the hard layer and the SUL). The head field is calculated from the resulting magnetization of the head and the SUL, in the plane that is 20 nm underneath the ABS, i.e., the center of the medium layer. The drive current in the single turn coil was 100 mA if not otherwise noted.



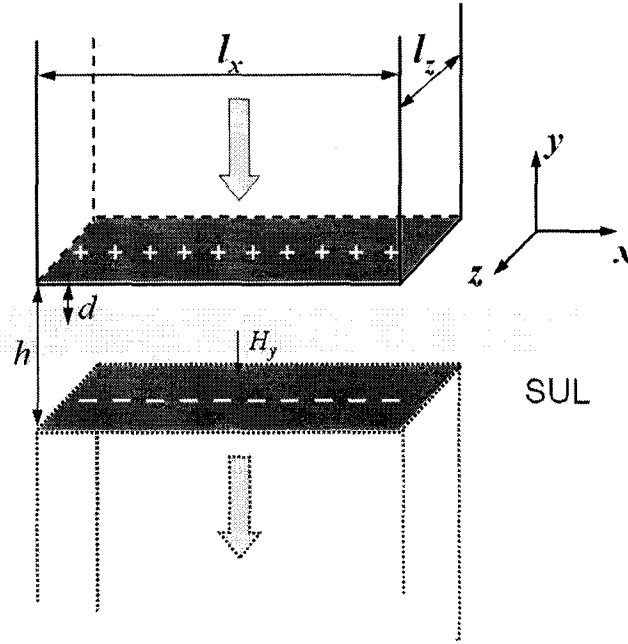


Figure 3.2: Illustration of the write pole and the image pole due to the SUL.

## 3.2 Results and Discussions

### 3.2.1 Analytical results

For a single pole head in perpendicular recording, the head field is mainly from the magnetic charges at the ABS of the pole-tip (In reality, however, the slanted region behind the pole tip also contributes to the field. This effect will be shown later). Therefore, simple analytical calculations could be performed to estimate the maximum field that could be produced from a pole-tip for given geometries. Let's consider a write pole tip with a rectangular footprint and magnetic charges only on the ABS, with the dimensions shown in Figure 3.2. At a plane that is a distance of  $d$  away from the ABS, the maximum perpendicular field component  $H_y$  occurs at the point right underneath the center of the footprint. Assuming the magnetic charge density at the ABS of the pole tip is equal to  $M_s$ , where  $M_s$  is the saturation magnetization of the material, i.e., a full saturation. The maximum  $H_y$  that the pole tip alone produces is then

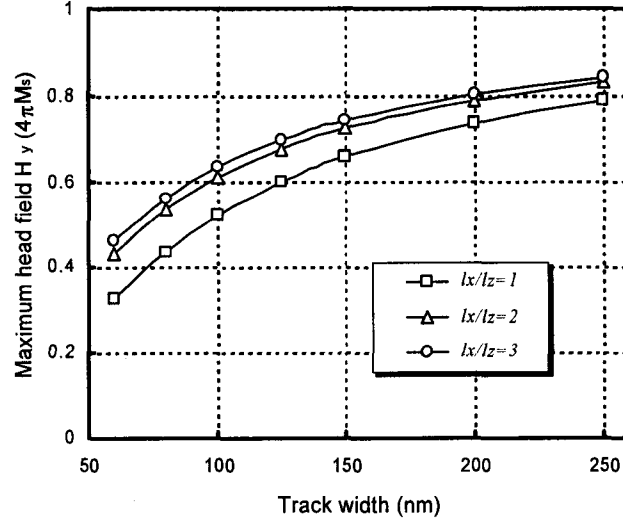


Figure 3.3: Maximum perpendicular head field  $H_y$  vs. the track width for different aspect ratios of the pole tip footprint.

given by the following formula:

$$H_y^{max} = 4M_s \tan^{-1} \left( \frac{l_x l_z}{2d \sqrt{l_x^2 + l_z^2 + (2d)^2}} \right) \quad (3.1)$$

In the case of a single pole head with SUL in perpendicular recording, the media layer experiences the field both from the pole tip and from the image of the head due to the SUL imaging effect. Assuming the distance between ABS and the center of the recording layer is  $d$ , and the ABS-to-SUL distance is  $h$ , the total maximum  $H_y$  the media sees will then be:

$$H_y^{max} = 4M_s \left[ \tan^{-1} \left( \frac{l_x l_z}{2d \sqrt{l_x^2 + l_z^2 + (2d)^2}} \right) + \tan^{-1} \left( \frac{l_x l_z}{2(h-d) \sqrt{l_x^2 + l_z^2 + (2(h-d))^2}} \right) \right] \quad (3.2)$$

The physical meaning of the above equation is that the maximum perpendicular field component is proportional to the solid angle extended from the center of the medium layer to the pole-tip foot print. The immediate consequence of this

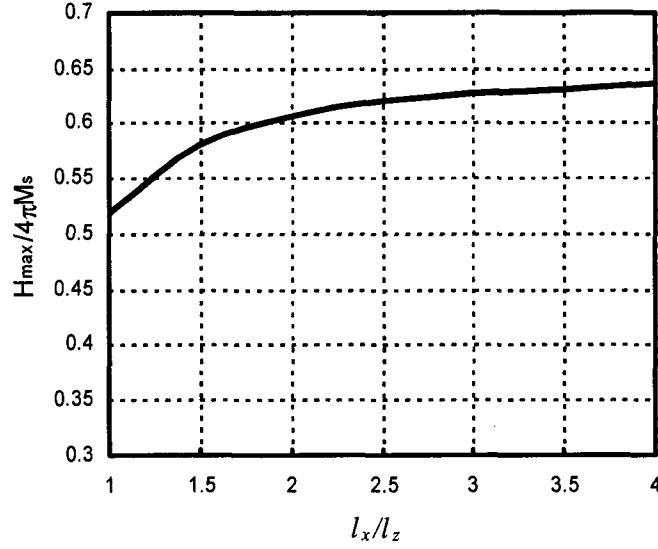


Figure 3.4: Maximum perpendicular head field  $H_y$  vs. the aspect ratios of the pole tip footprint for a track width of 100 nm.

is that for given values of  $h$  and  $d$ , reducing the lateral dimension of the pole tip  $l_x$  and/or  $l_z$  will decrease the solid angle hence lower the head field. Figure 3.3 shows the maximum  $H_y$  as a function of  $l_z$ , i.e., the track width, according to Eq. (3.2), for three different values of the aspect ratio,  $l_x/l_z$ , of the pole tip, for  $d = 20$  nm and  $h = 30$  nm. Significant loss of field magnitude can be seen as the track width is reduced into the region where  $l_z$  becomes comparable with  $h$ .

The dependence of the maximum field on the pole-tip footprint aspect ratio is shown in Figure 3.4 for a track width of 100 nm. It is noticed that the head field is significantly higher for  $l_x/l_z = 2$  compared to that for  $l_x/l_z = 1$ . However, further increasing the aspect ratio only yields very little field increase. On the other hand, in perpendicular recording with single pole head, the side erasure at inner diameter (ID) and outer diameter (OD) due to the head skew could cause significant broadening of the written track width hence TPI (track per

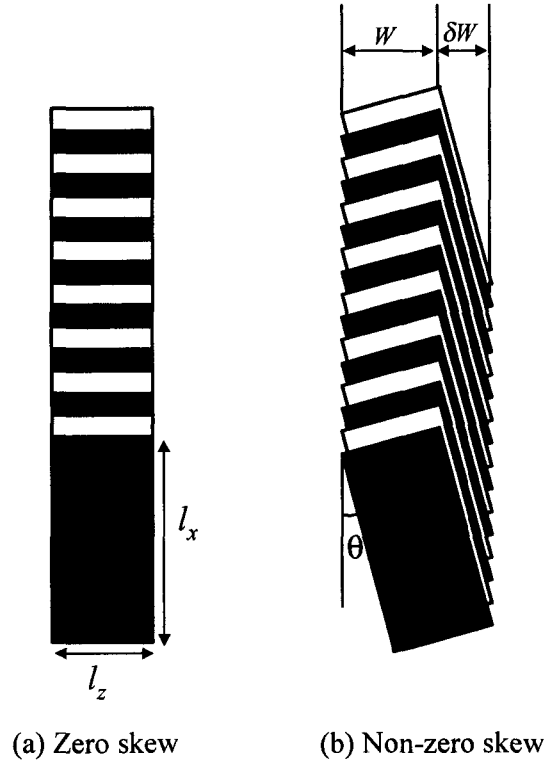


Figure 3.5: Illustration of the written track width with (a) zero head skew and (b) non-zero head skew with a pole tip footprint aspect ratio of  $l_x/l_z = 2$  and a skew angle of  $15^\circ$ .

inch) loss [50, 51], as illustrated in Figure 3.5. The percentage increase of the written track width is given by:

$$\frac{\delta W}{W} = \frac{l_x}{l_z} \tan \theta \quad (3.3)$$

where  $\theta$  is the skew angle, and  $W$  and  $\delta W$  are the usable written track width and its broadening due to the skew, respectively. The dependence of this track width broadening upon  $l_x/l_z$  is shown in Figure 3.6 for several skew angles. As the pole-tip footprint aspect ratio increases from 2 to 4, the maximum field increases by only about 6%, however, the head skew caused write track width increases by 100%. This effect is much faster than that of the increase of field magnitude for  $l_x/l_z$  greater than, say, 2. Therefore, a low aspect ratio pole tip,

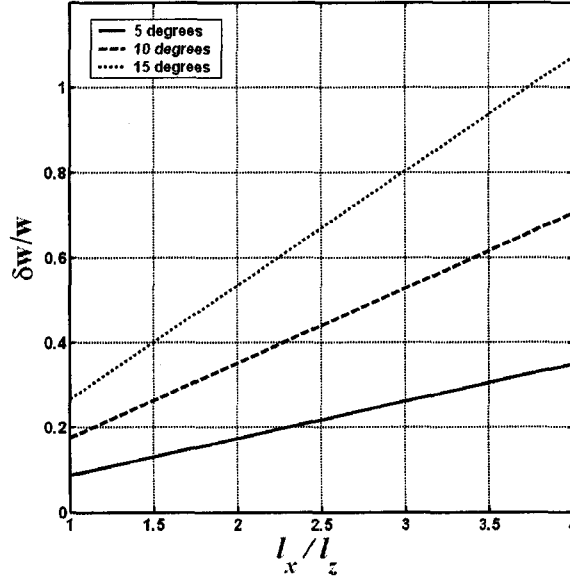


Figure 3.6: The percentage increase of the actual written track width with respect to the zero-skew track width as a function of the pole tip footprint aspect ratio,  $l_x/l_z$ , for different head skew angles.

e.g., 2, should be used unless the several percent field increase is critical. In that latter case, other techniques such as a trapezoidal pole tip footprint [52] should be used, in order to minimize the TPI loss caused by the head skew.

The rest of the results in this chapter are all micromagnetic modeling results obtained using the model and parameters shown in Section 3.1. In particular, the head pole tip aspect ratio is 1 for all cases.

### 3.2.2 Maximum Head Field vs. Track Width

As shown in the previous section, the maximum achievable head field inside the medium will be greatly limited by the geometric factors as the pole tip dimensions in both cross-track and down-track directions become comparable to the ABS-SUL separation. For a track width of 200 nm, the maximum possible field is about 70% of  $4\pi M_s$ . However, as the track width is reduced to below

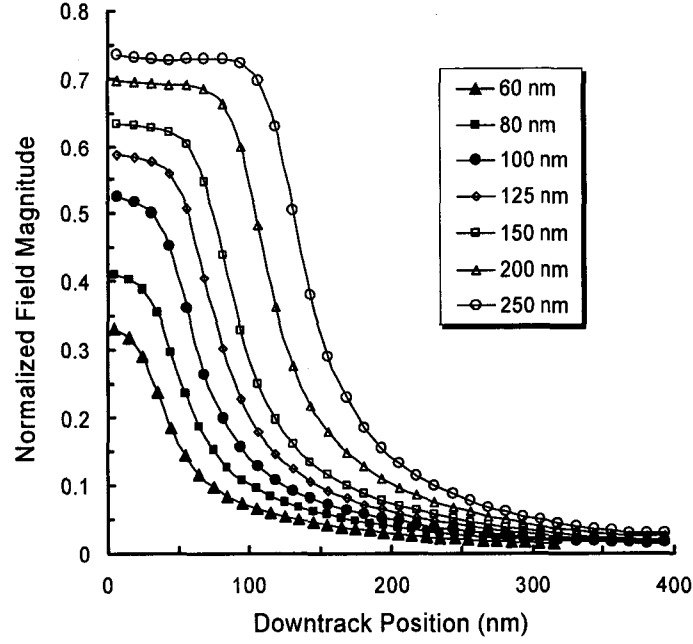


Figure 3.7: The down-track field profiles for different track widths with all heads having a square footprint, i.e.,  $l_x/l_z = 1$ . The field magnitude is normalized to  $4\pi M_s$ .

100 nm, the upper limit of the maximum field is even less than 50% of  $4\pi M_s$ . In this case, the advantage of using SUL to achieve large field is impaired simply by the geometry.

Figure 3.7 shows the simulation results of the down-track field profile evaluated at the track center for the single pole head with different track widths. The profiles for narrow track widths are more rounded due to relatively large ratio of head-medium spacing to the pole tip footprint size. The reduction of the maximum field is clearly shown with decreasing track width. Figure 3.8 plots the simulation results of the maximum field as a function of the track width, along with the analytical result from Figure 3.3 for the same pole-tip footprint dimensions. Remember that the analytical results were based on the assumption that the pole tip is fully saturated and it is the only source of field.

This is not true in a real head. First of all, the pole tip is never fully saturated in a head, due to the strong demagnetizing field at the ABS. This leads to a lower field compared to the analytical result. The charge distribution on the ABS of the pole tip is not uniform either, which should lead to a different field profile in the space. On the other hand, however, there is a slanted region at the bottom of the yoke, which will be magnetized as well. In other words, there will be magnetic charges on that surface, contributing to the total field. How large the field from this side region is depends on how hard the head is driven by the current as well as the throat height and the flare angle, and the total field in this case could be higher than that from a saturated pole tip alone. This will be dealt with in detail in Chapter 4. In the case shown here, the drive current is moderate, and the two mechanisms discussed above together give a maximum head field close to the analytical value. Anyway the analytical results are only used here to show the geometry dependence of the head field, and the trend it gives matches the micromagnetic results very well here. The deviation of the micromagnetic result at large track width from the analytical value might be due to the higher demagnetizing field from the surface charges at the ABS, therefore lower charge density at the ABS.

It has been shown that if the  $M_s$  and/or the thickness of the SUL are not sufficiently large, SUL saturation may occur thus affecting the head field [53]. In this study, both of these parameters are chosen such that no SUL saturation occurs. In fact, as far as the imaging effect alone is concerned, the micromagnetic result shows that the field from the SUL is practically the same as that from an ideal imaging effect. Therefore, in later chapters, the SUL effect will be replaced by a simple imaging of the head magnetization in the simulation, except Chapter 6, in which the SUL itself will be micromagnetically modeled for other purposes.

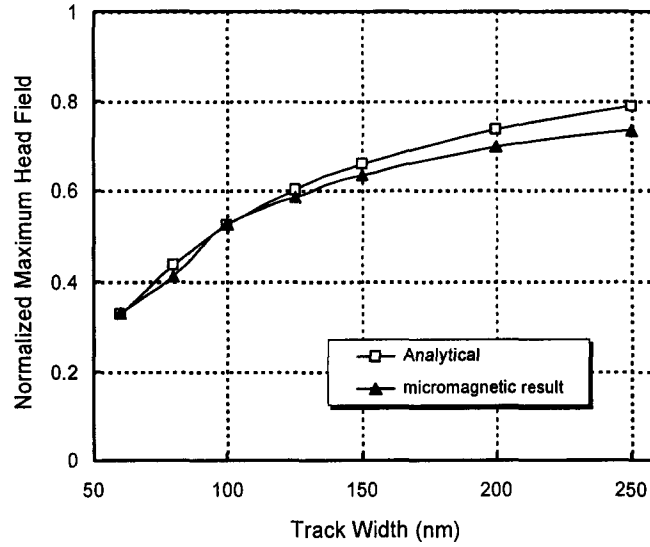


Figure 3.8: Maximum head field (normalized to  $4\pi M_s$ ) versus track width for  $l_x/l_z = 1$  from micromagnetic modeling with moderate driving current. The analytical result from Figure 3.3 is shown here for comparison.

### 3.2.3 Field Gradient vs. Track Width

Not only is the maximum head field affected by the track width reduction, but the field gradient also degrades with decreasing track width. Figure 3.9 shows the field gradient vs. field magnitude as going down the track from the center of the pole tip. The maximum head field gradient occurs at the field value about 70% of the maximum field for all track widths. This value is much greater than that of longitudinal recording heads. If the maximum field-gradient is used to write transitions, i.e., the head field at maximum gradient position is equal to the media coercivity, then the media switching field distribution has to be small enough so that the maximum switching field is still smaller than the maximum head field, in order to ensure the writability of the head on the media. Otherwise, the writable media coercivity will have to be lowered and the writing



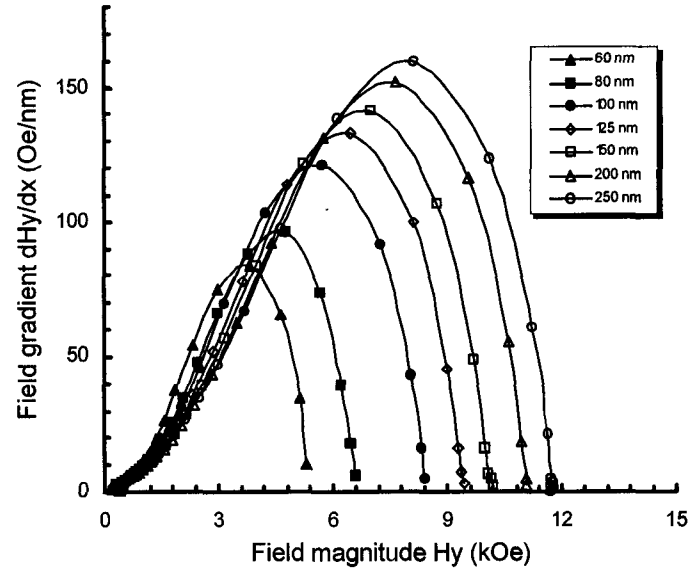


Figure 3.9: Down-track gradient of the perpendicular field component,  $dH_y/dx$ , versus the field magnitude,  $H_y$ , for different track widths. The pole tip footprint is square for all cases.

will not happen at the optimum field gradient. The maximum field gradient also degrades with decreasing track width very quickly from about 160 Oe/nm for 250 nm track width to about 85 Oe/nm for 60 nm track width. Figure 3.10 plots more clearly the dependence of the down-track and the cross-track maximum field gradient upon the track width for square pole-tips. The cross-track field gradient is slightly lower than that down-track, although the pole-tip is square shaped. This is because of the field from the flared neck region has a much more broadened distribution over a wide range across the track.

It has also been noticed that though the SUL imaging effect enhances the perpendicular field component, it actually suppresses the longitudinal field component. A sufficiently large longitudinal component effectively makes the total field at an angle with respect to the perpendicular direction to the media plane, i.e., the media easy axis direction. This is essential for making

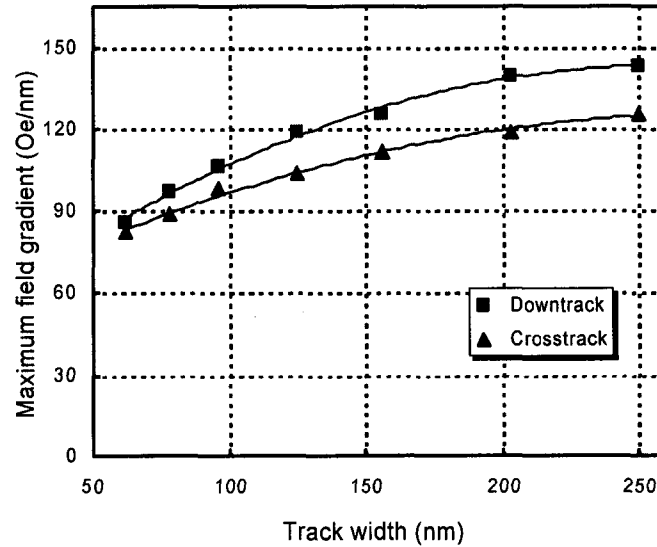


Figure 3.10: Dependence of the maximum field gradient, both down-track and cross-track, on the track width. The pole tip footprint is square for all cases.

perpendicular media reversal easier [54]. Our simulations show that the maximum longitudinal field occurs at about the same position as the maximum field gradient  $dH_y/dx$ , where the total field is at an angle of about  $10^\circ$  with respect to the perpendicular direction, which is much smaller than that of a ring head. To increase the field angle, a shield-pole head [55] may be used in perpendicular recording, which shows not only larger field angle, but also higher field gradient than that of a single pole head.

#### 3.2.4 Impact of Track Width Reduction on Remanent Head Field

One other important issue that is associated with write heads at extremely small track width is the remanent head field, which results from the pole tip that did not relax to a demagnetized state when the driving current is turned off. This used to be not a concern in conventional write heads with track width at

the order of micrometers. In those cases, the magnetostatic energy is dominant compared to the exchange energy. Therefore, after the drive current turned off, the pole tip will relax to a demagnetized state with negligible remanent field. However, for deep sub-micron track widths, the pole tip dimension is so small that the increase of the exchange energy will overwhelm the decrease of the magnetostatic energy if the magnetization tries to form a multi-domain state. As a result of energy minimization, a single domain may stay in the pole tip, yielding high remanent head field. The mechanism behind the formation of the single-domain-like remanent state magnetization in the pole is exactly the same as that for the formation of single domain in small particles. For a soft magnetic material, the critical size of the single domain state is related to the exchange length, which is defined by Eq. (2.22). This exchange length actually characterizes the strength of the exchange coupling relative to the magnetostatic interaction and gives the length scale over which the magnetization maintains its coherence in spatial orientations.

The model used in this work enables us to investigate the micromagnetic behavior of the head. In the simulation, the heads were first driven by the write current into a steady state, and then the current is turned off to let the head magnetization relax. Figure 3.11 shows a comparison of the remanent state head magnetization for track widths of 60 nm and 200 nm, respectively. In both cases, the pole tip ABS aspect ratio is 1:1. Although the entire yoke is relaxed to a demagnetized state by forming a flux closure in both cases, the magnetization in the pole tip region is quite different. In the 60 nm track width head, the pole tip remains in a single domain state after being saturated during a writing process. Whereas for the 200 nm track width one, the pole tip is sufficiently large to allow the magnetization to follow the surface of the pole tip to minimize magnetostatic energy without increasing exchange energy too

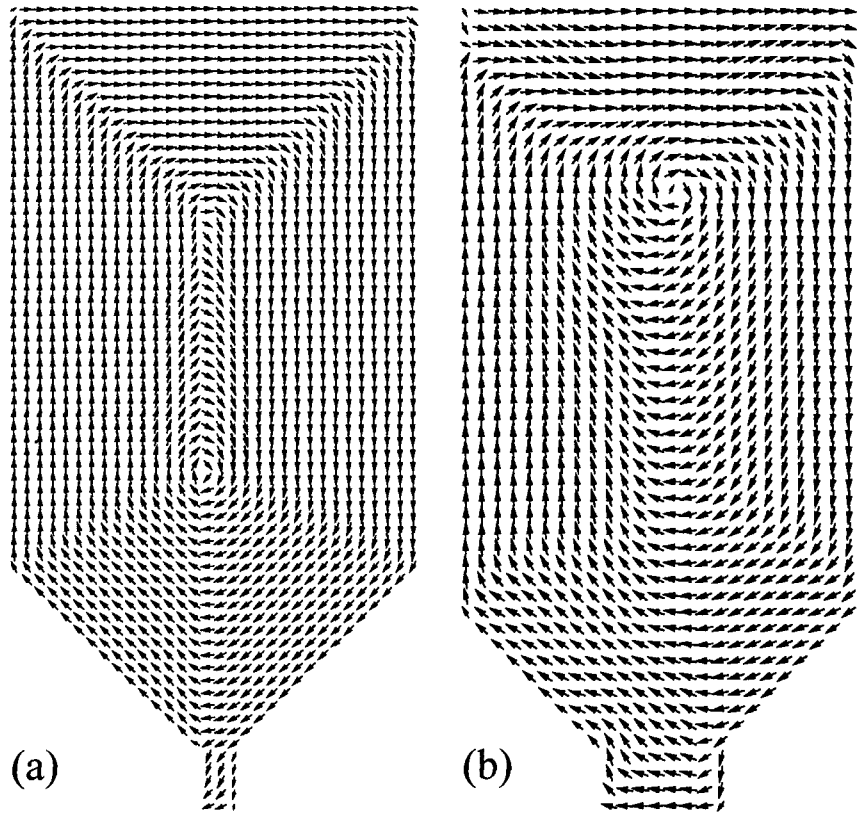


Figure 3.11: The remanent state magnetization of two heads with track widths of (a) 60 nm and (b) 200 nm, respectively. The pole tip footprint is square for both cases.

much. This leads to a much smaller remanent field.

Figure 3.12 shows the dependence of the remanent field as a function of the track width for a pole tip ABS aspect ratio of 1:1. Clearly, as the track width goes below 100 nm, the remanent head field increases dramatically. The ratio of the remanent field to the maximum field for each track width is also shown in the same figure, which shows that a much more significant portion of the head field remains in small track width heads than that with wider track widths.

At a given pole tip footprint size where a single domain tends to form, say, below 100 nm, the remanent field actually also depends on the length of

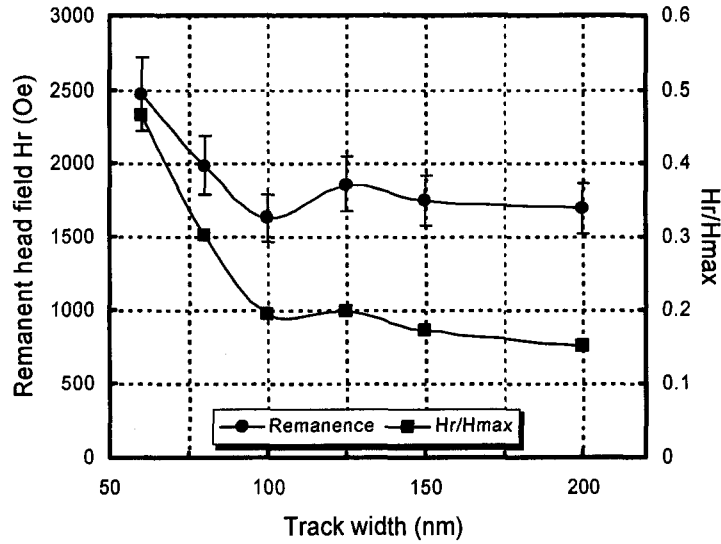


Figure 3.12: Dependence of the remanent field and its percentage to the maximum field on the track width, for  $l_x/l_z = 1$ .

the throat height. In other words, due to the shape anisotropy, a long pole tip will produce more remanent field than a short one. Figure 3.13 shows the simulation result for a pole tip with 60 nm by 60 nm footprint with different throat heights. The magnetization pattern shown in Figure 3.14 clearly reveals the shape anisotropy effect [56].

It has also been found that, for those heads with track widths of 100 nm or less and a pole tip ABS aspect ratio of 2:1, the remanent field may not necessarily be smaller than that of a squared pole tip with same track width, though the overall cross section area of the pole tip is larger. A close look at the remanent state magnetization pattern of the thick pole tip head reveals that the yoke magnetization pattern could be much more complex and vortices could form across the head thickness, which can lead to residual flux from the yoke still driving the pole tip, as shown in Figure 3.15. This actually makes the behavior of the remanent head field at extremely narrow track width much more complicated than that of a small free-standing magnetic cube or a rectangular

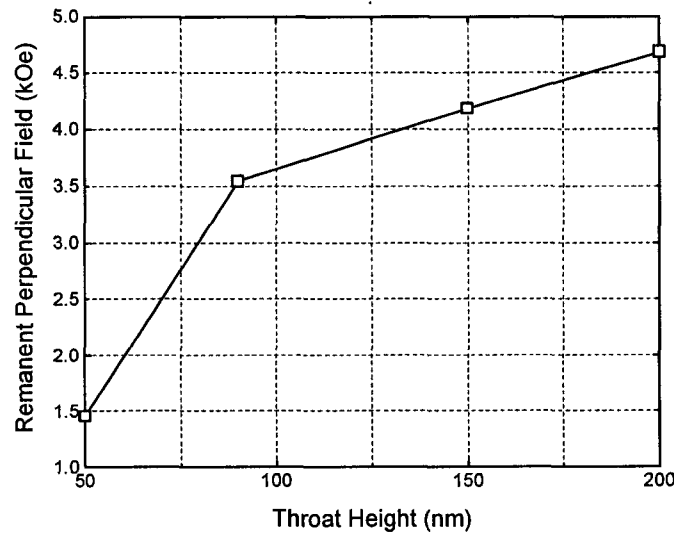


Figure 3.13: Maximum remanent perpendicular field versus the throat height. The pole-tip footprint size is 60 nm by 60 nm.

parallelepiped. As a result, the remanent field could vary over a wide range as well. A detailed study on controlling the remanent field will be presented in Chapter 4.

Finally, it is worthwhile mentioning the effect of the induced anisotropy field in the narrow track heads. Traditionally, in the head with pole tip at micron scale, a weak anisotropy field induced in the transverse direction is usually sufficient to orient the major domains in the yoke and the pole tip to the direction orthogonal to the flux conduction direction. This will favor a magnetization rotation rather than domain wall motion mechanism, which is desirable for high frequency field reversal and for the stability of the head field performance [57]. However, in the heads of interest here with such small dimensions, our simulation shows that, the transverse anisotropy even up to a few hundred Oersteds essentially has no appreciable effect on the domains in the yoke and the pole tip, as the demagnetizing field and the exchange coupling field are much stronger than the induced anisotropy field, for the deep

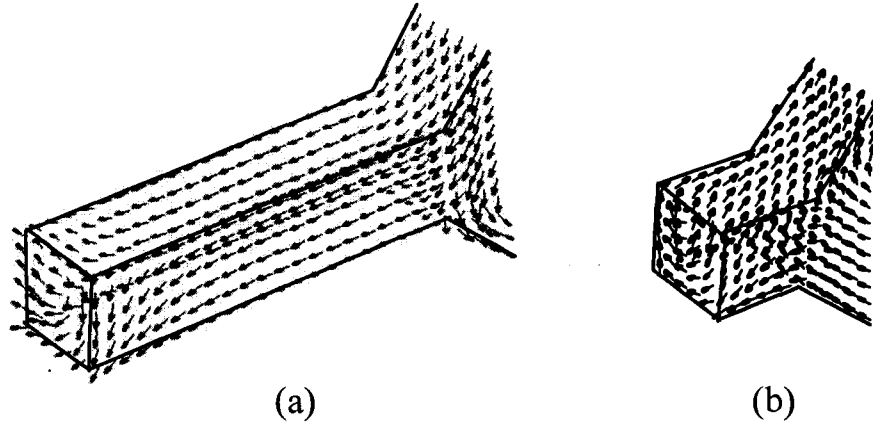


Figure 3.14: 3D view of the remanent state magnetization of the pole tip with same footprint size of 60 nm by 60 nm and different throat height of (a) 200 nm and (b) 50 nm.

sub-micrometer dimensions.

### 3.3 Conclusions

In this chapter, the effects of the track width reduction for single pole heads with deep sub-micron dimension have been studied using 3-D micromagnetic modeling. It has been found that at deep submicron track widths, due to the geometric effect, the maximum head field inside the medium is significantly smaller than the ideal  $4\pi M_s$  value. The field gradient degrades with decreasing track width as well at a given ABS-to-SUL spacing. At small pole-tip dimensions (around or below 100 nm), significant remanence in the pole-tip will develop after writing, due to the ferromagnetic exchange coupling effect, presenting a danger of erasing previously written bits. The remanent head field also depends on the throat height of the pole tip and the micromagnetic state at the neck region between the yoke and the pole tip. More sophisticated head designs are needed to ensure robust zero remanence, as will be discussed in Chapter 4. In

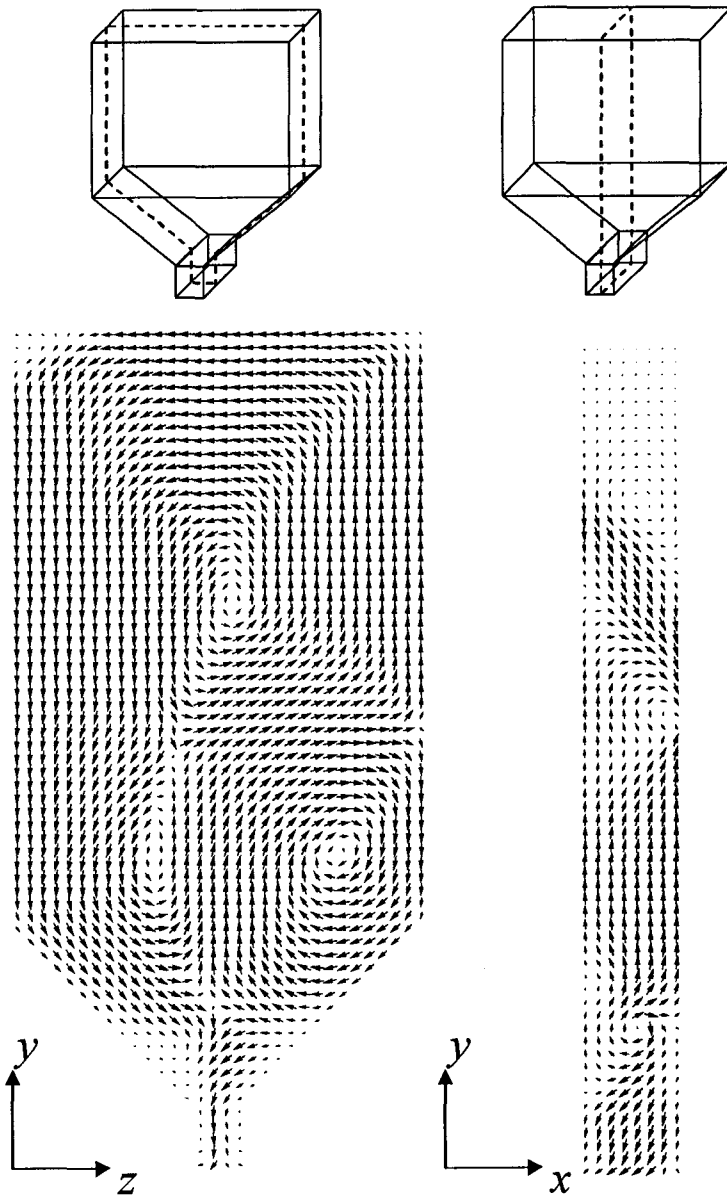


Figure 3.15: Remanent state magnetization of a head with track width of 80 nm and pole/yoke thickness of 160 nm. Left:  $y$ - $z$  plane view. Right:  $x$ - $y$  plane view. The drawing on the top shows the planes where the magnetization is plotted.



contrast to longitudinal recording, the maximum field gradient of the single pole perpendicular head with SUL occurs much closer to the maximum field position, implying that a perpendicular media with narrow switching field distribution, or higher coercive squareness is required to write transition at maximum field gradient, for optimized transition sharpness. The longitudinal component of the head field is suppressed by the image head due to the SUL.

## 4 NOVEL PERPENDICULAR WRITE HEAD DESIGNS

As discussed in Chapter 3, the reduction of the track width for high density has posed a number of issues on the write head design. In this chapter, several novel head designs will be presented based on the understanding of the micromagnetics of the heads through simulation. To meet the requirement for high data rate recording, the write head need to be made small to minimize its inductance, as the drive current rise time is determined by the time constant of the write driver circuit. The time constant of the write current rise time, to the first order approximation, is simply  $L/R$ , where  $L$  is the head inductance and  $R$  is the open circuit resistance of the write driver circuit. Nowadays, the typical head inductance value is several nanoHenry, and it will be further made smaller for high data rates. This necessitates the study of the heads with overall dimension at the scale of a micron or even submicron. It will be shown in this chapter that, at such a scale, the magnetization configuration, both at static state and during a dynamic reversal process, is highly dependent on the overall shape of the yoke as well as some structural features such as a lamination of the yoke and the pole tip. Therefore, it is very important to investigate the performance of single pole heads with different yoke and pole tip designs.

This chapter is organized as follows. In section 4.1 the micromagnetic model is presented. In section 4.2, we will compare four heads with different structures and/or dimensions and show the performance differences. A head with a short yoke and a lamination of both the yoke and the pole tip has been found to have the best field rise time performance. More importantly,

the lamination of the pole tip guarantees a near-zero remanence, regardless of the throat height. In section 4.3, a stitched pole-tip head is presented, which produces much higher head field than a conventional single pole head with the same pole-tip footprint size, while maintaining a near-zero remanence. Other design parameters, such as the throat height, the flare angle, and the induced anisotropy field, will be investigated as well.

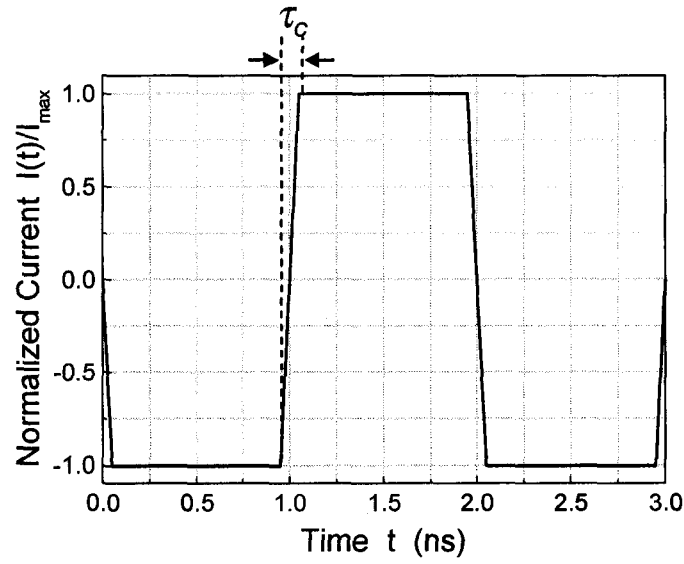
#### 4.1 Micromagnetic Model

In this chapter, all the simulations were done using the 3-D dynamic micromagnetic model, as the dynamic magnetization reversal processes is of great interest here. For all cases, the head is discretized into cubic cells with the edge length of 10 nm. Landau-Lifshitz equation with Gilbert damping is applied to each of the cubic cells to solve dynamically the head magnetization. The Gilbert damping constant used here is  $\alpha = 0.05$ . The head material was assumed to have  $M_s = 1930 \text{ emu/cm}^3$ . The SUL is treated as a perfect image in the computations, i.e., the demagnetizing field from the SUL is treated as that from the image magnetization of the head, dynamically in real time in the computation. This is actually a very good approximation as long as a high moment material is chosen for the SUL, so that the response of SUL magnetization to the field produced by the head is only a slight rotation upward or downward with respect to the plane of the media film, which does not slow down the head field dynamic reversal. The spacing between the ABS and the SUL is assumed 30 nm, and the head field is calculated at a plane 20 nm below the ABS, assumed to be the center plane of the media, from both the head magnetization and the image magnetization.

All the heads modeled in this chapter are driven by the coil current at

Table 4.1: Parameters of different head designs. All values are in unit of  $\mu\text{m}$ .

Head	Length	Width	Thickness	Laminated?	Pole-tip detached?
A	1.28	0.64	0.08	No	No
B	0.64	0.64	0.08	No	No
C	0.64	0.64	0.08	Yes	No
D	0.64	0.64	0.08	Yes	Yes

Figure 4.1: Write current waveform used in the simulations in this chapter.  $\tau_c = 0.1$  ns is the current rise time.

a data rate of 1 Gbit/sec. The current waveform was assumed to follow a linear ramp at the rising and falling edges between the two polarities, with an interval of the transition period of 0.1 ns, which is referred to as the current rise time here, as shown in Figure 4.1. The field produced by the drive current is calculated analytically (see Appendix C) and assumed to follow the same rise time as the current. The head field rise time calculated from the head magnetization is defined to be the time for the field to reverse from +90% to -90% of the maximum field magnitude.

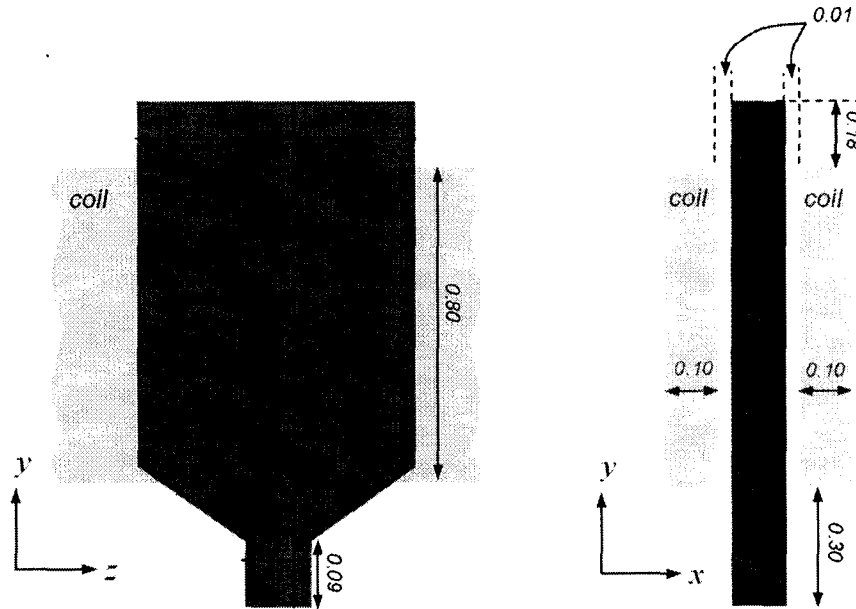


Figure 4.2: Schematic of head A with all dimensions marked in unit of micron. Left: the  $y$ - $z$  plane view. Right: the  $x$ - $y$  plane view, where the currents in the two coil sheets flow in the directions into and out of the paper, respectively.

## 4.2 Laminated- and Detached-Pole Tip Head Design

In this section, four different head designs will be compared. The dependence of the head magnetization reversal behavior upon the shape and/or structure of the yoke and the pole tip will be analyzed, based on the micro-magnetic modeling results. The parameters of the heads are tabulated in Table 4.1.

### 4.2.1 Head A

Figure 4.2 shows the schematic of head A. In this head, the length of the head is twice as much as its width, and the head is a single piece with same

thickness for both the yoke and the pole tip. It will be shown that the overall geometry of the head significantly affects its domain structure, both at quiescent state (remanent state) and during the dynamic field reversal.

Figure 4.3 shows the temporal profiles of the maximum perpendicular head field component under two different drive currents of 256 mA and 64 mA, respectively. Clearly, a larger current produces not only a higher field, but also a shorter field rise time. This is because with the same current rise time, a higher driving field is reached at the end of current reversal, therefore more driving flux is delivered. The dependence of the head field magnitude and the field rise time upon the drive current amplitude is shown more clearly in Figure 4.4. Although the field magnitude still slowly increase with increasing driving current, the field rise time levels off beyond a current value of around 130 mA. In the low current region, the field rise slows down very drastically with decreasing driving current amplitude. This can be understood by Figure 4.5, which shows the curl of the head magnetization during a dynamic magnetization reversal process. The bright and dark lines indicate the curling of local magnetization with opposite senses, and the small fluctuation of the contrast shows the deviation of the local magnetization from a saturation state. In this head, because the length of the yoke is much longer than its width, during the writing process, the yoke magnetization is easily saturated along the head length, i.e.,  $y$  direction. This configuration requires the nucleation of reversed magnetization in the yoke for each head field reversal, and this process is rather slow for small driving current. Furthermore, what really matters the most, as far as the field rise time is concerned, is how much time it takes for the reversed yoke flux to propagate to the pole-tip to reverse the pole tip magnetization. This process could be very long in this head.

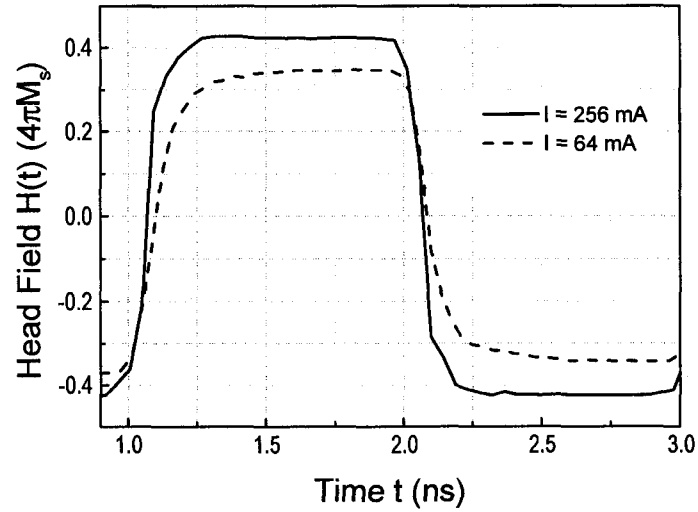


Figure 4.3: Temporal profiles of the maximum perpendicular head field at two different driving currents for head A.

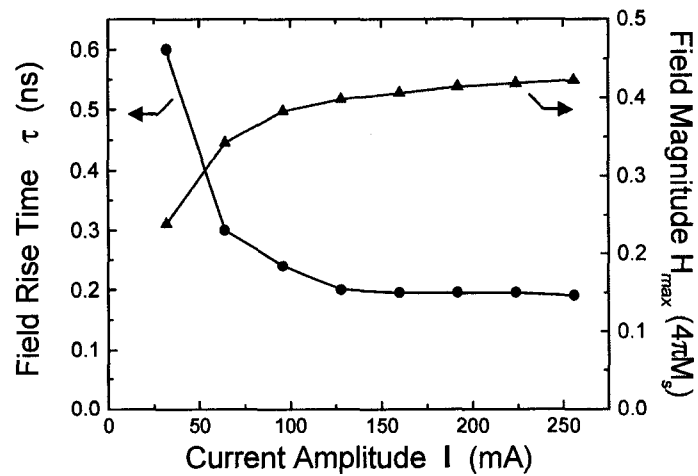


Figure 4.4: Head field rise time and field magnitude vs. driving current for head A.

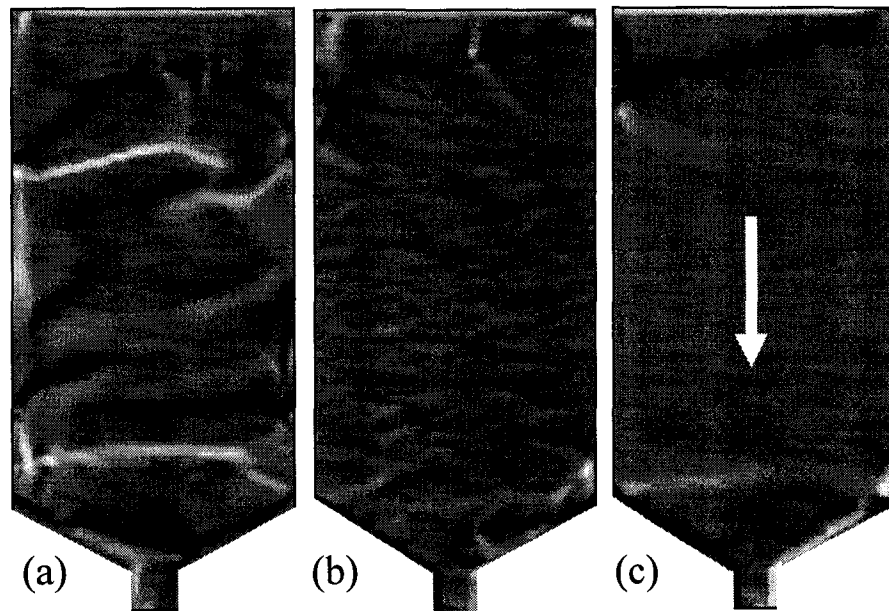


Figure 4.5: Domain structures of head A during a flux reversal process. The head fields are (a) zero, (b) close to full magnitude, and (c) full magnitude.

It is noticed in head A that during a head field reversal, the head magnetization pattern is rather complicated, as seen in Figure 4.5(a). This transient state magnetization is also quite different from the remanent state magnetization. The latter itself actually varies dramatically too, as shown in Figure 4.6. This is primarily due to the relatively long yoke, which does not favor well repeatable domain configurations in the head. Instead, it always involves dramatic domain rearrangements. As seen in Figure 4.6, the apparently different remanent yoke magnetization could also yield different remanent head fields.

#### 4.2.2 Head B

The only difference between head B and head A is that the length of the head B is half that of head A. Therefore, the shape of the yoke is closer to a square, as shown in Figure 4.7. This shape difference significantly affects the domain



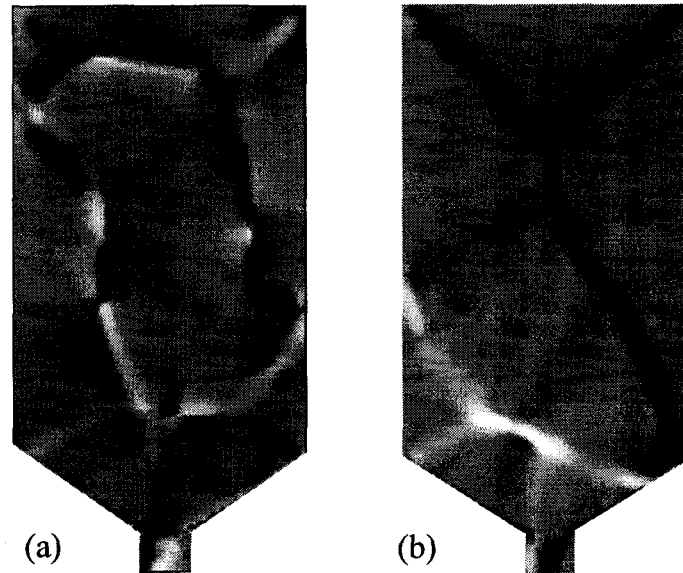


Figure 4.6: Remanent state magnetic domain structures of head A after writing with a drive current of (a) 250 mA and (b) 160 mA. The contrast represents the curl of the magnetization.

structure in the yoke and the flux reversal mechanism and, therefore, the head field rise time performance. As will be discussed in detail in this section.

Figure 4.8 shows the temporal profiles of the maximum perpendicular field under three different values of the driving current for head B. The dependence of the head field magnitude and the field rise time upon the drive current amplitude is shown in Figure 4.9, which has the same trend as that of head A, except a subtle difference in the head field rise time curve, where there is a minimum at 80 mA position. This point actually is the one that differentiates head B from head A, in terms of the behavior of the domains and, therefore, the head field rise time performance. This will be readily seen from the following discussion of the domain structures of head B.

Figure 4.10 shows the magnetic domain structures of head B during a flux

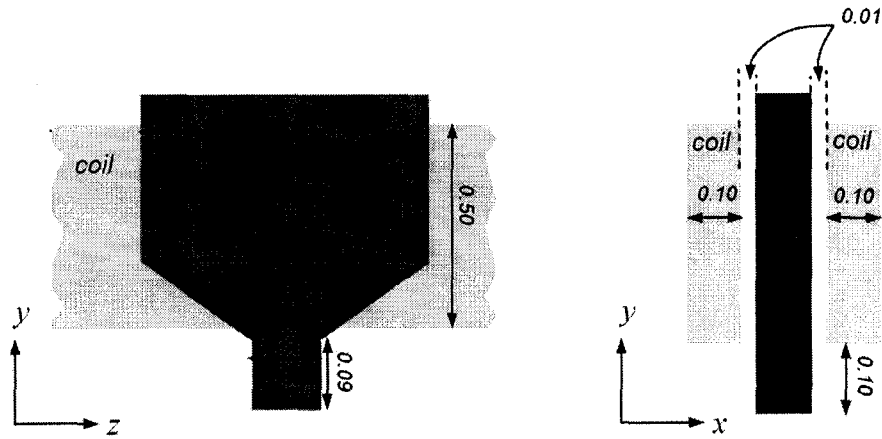


Figure 4.7: Schematic of head B with all dimensions marked in unit of micron. Left: the  $y$ - $z$  plane view. Right: the  $x$ - $y$  plane view, where the currents in the two coil sheets flow in the directions into and out of the paper, respectively.

reversal process under a moderate driving current of 60 mA. The contrast represents the magnetization component in  $y$  direction (perpendicular to the ABS). It has been found that in this head, the flux reversal at small and moderate driving current is through the motion of the center of the vortex that stays in the yoke. The vortex center (denoted by the dashed ellipse) is slightly elongated, because the width of the yoke is actually larger than its height. During the field reversal, the vortex center is moved from the right to the left in the yoke. As a result, the major domain magnetization is reversed from downward to upward, as highlighted by the thick arrows in Figure 4.10(a) and (c), which provide the driving flux to the pole tip. This domain configuration is very well repeatable, as the vortex is always in the yoke, unless the driving current is so large that it is driven out of the yoke during writing.

In small and moderate current region (below about 80 mA), the field rise time decreases monotonically with increasing driving current amplitude. However, for currents higher than 80 mA, the vortex center is driven out of the yoke,

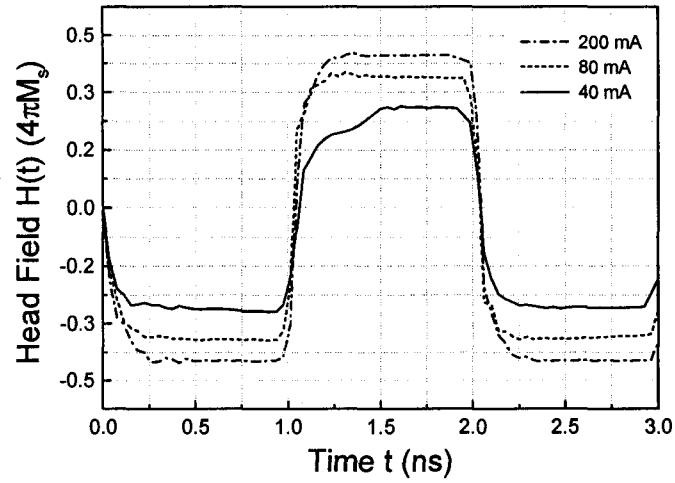


Figure 4.8: Temporal profiles of the maximum perpendicular head field at different driving currents for head B.

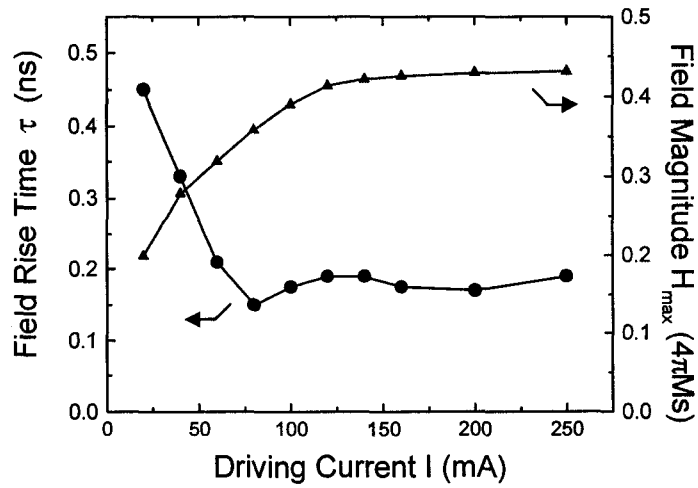


Figure 4.9: Head field rise time and field magnitude vs. driving current for head B.

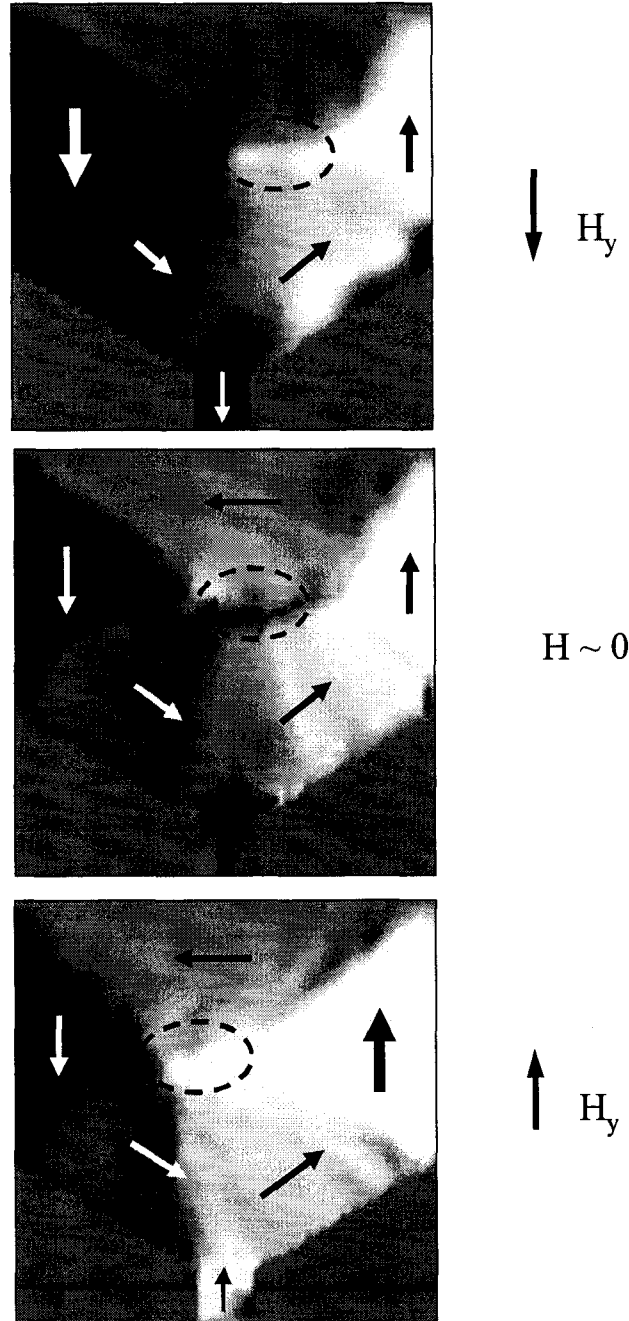


Figure 4.10: The magnetic domain structures in head B during a flux reversal process. The driving current is 60 mA. The contrast represents the vertical component of the magnetization  $M_y$ .

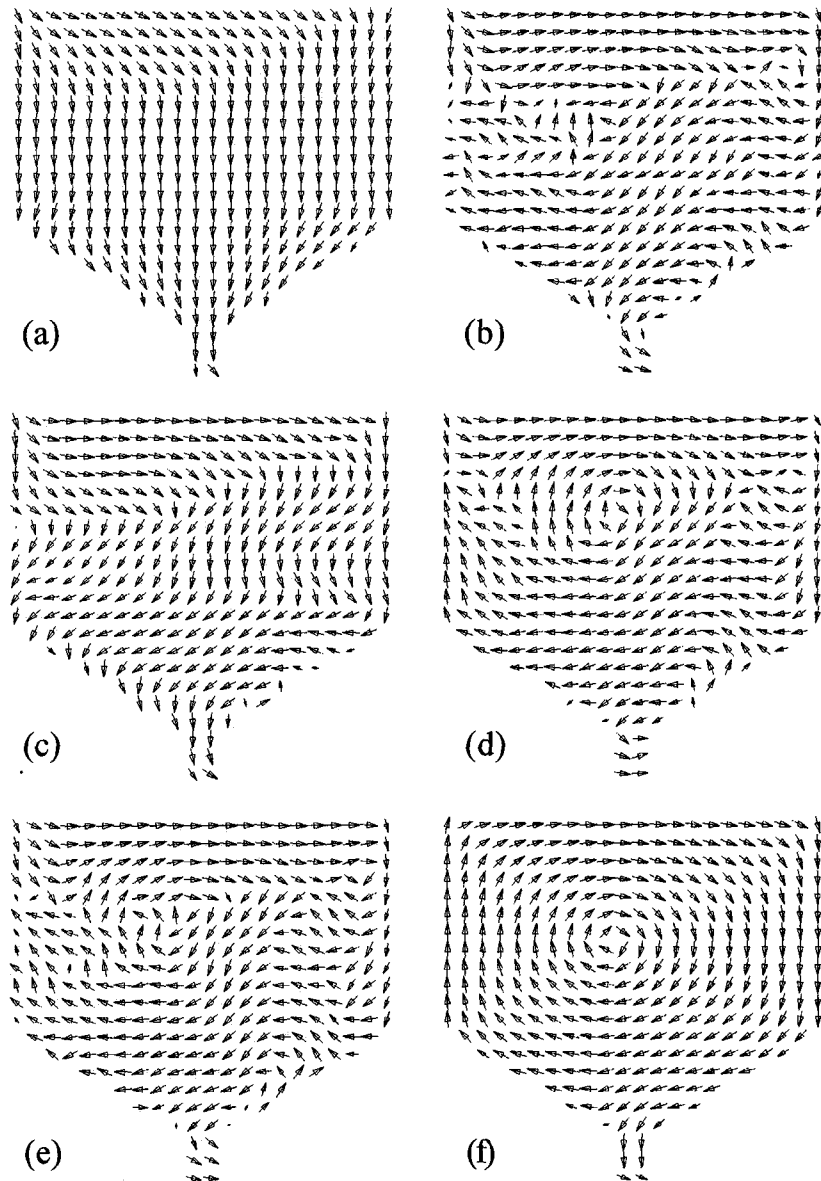


Figure 4.11: The magnetization relaxation process of head B after writing with a large current ( $> 80$  mA). It is sequential in time from (a) to (f).

resulting in the yoke saturation, as shown in Figure 4.11(a), which will in turn require the nucleation of the of the reversed domains during a field reversal, as in the case of head A. In this case, even though the drive current is higher, the field rise time is still slightly longer than that at 80 mA, as for the latter, the vortex center is still in the yoke and, therefore, does not need the nucleation.

It has been found that the domain configurations for head B, both during the dynamic reversal and in the remanent state, are very well repeatable. As shown in Figure 4.11, even though the head yoke was initially saturated during writing, when the driving current is turned off, the yoke magnetization always returns to the single vortex state. This is purely due to the near-square shape of the yoke, as opposed to the elongated yoke for head A that causes significant complications and poor repeatability of the domain structures.

#### 4.2.3 Head C

The dimension and shape of head C is exactly the same as head B. The only thing different is that head C is laminated into two layers equally thick across its thickness, with a very thin layer of non-magnetic material in between. The schematic of head C is shown in Figure 4.12. The idea is to decouple the exchange interaction between the two layers. Therefore, the middle layer could be as thin as below 1 nm, as long as it is a continuous film that can break the exchange coupling between the two lamination layers.

Figure 4.13 shows the temporal profiles of the maximum perpendicular field under three different values of the driving current for head C. The dependence of the head field magnitude and the field rise time upon the drive current amplitude is shown in Figure 4.14. Clearly, the head field rise time is much shorter than both head A and head B at small current. This can be understood by looking

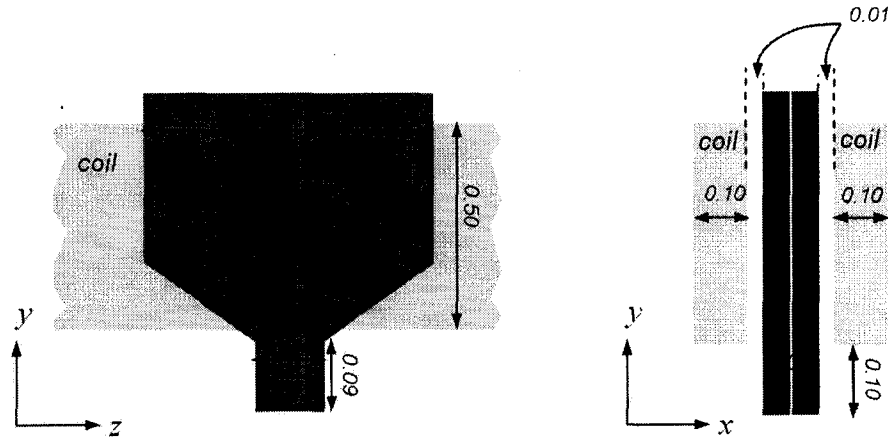


Figure 4.12: Schematic of head C with all dimensions marked in unit of micron. Left: the  $y$ - $z$  plane view. Right: the  $x$ - $y$  plane view.

into Figure 4.15, which shows the magnetization of both lamination layers of the head with a drive current of 40 mA. In the laminated head, if the initial magnetization is a transverse single domain state in both layers, with an edge curling wall at the two sides, as shown in Figure 4.15(b), (which is a stable state for certain aspect ratios of the yoke [58]), for the small driving current, the driving field only causes a magnetization rotation in the yoke that provides the flux to the pole tip, and there is no vortex formed in the yoke. Therefore, the field reversal is achieved by the yoke magnetization rotation upward and downward with respect to the horizontal direction. This rotation yields very fast field reversal, compared to the vortex motion mechanism (head B), not to say the nucleation of reversed domain (head A). Due to this pure magnetization rotation, it is natural that the remanent state magnetization of this head is the same as the one shown in Figure 4.15(b). Notice that the short yoke is important for this magnetization configuration, as with a long yoke, even the lamination does not produce the anti-parallel single domain magnetization in the two layers.

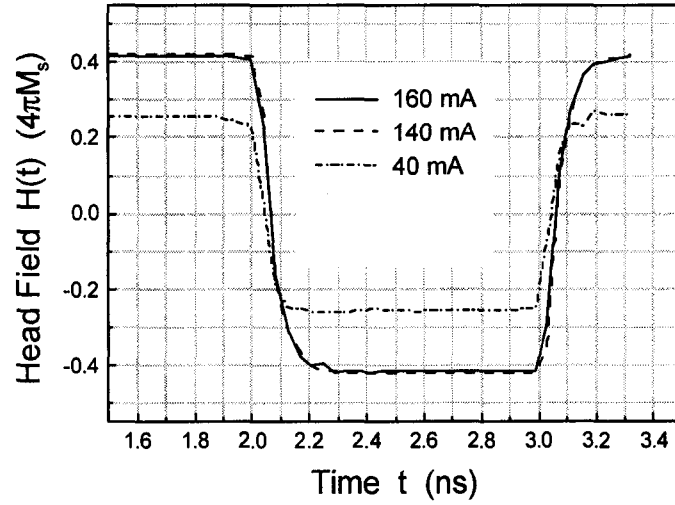


Figure 4.13: Temporal profiles of the maximum perpendicular head field at different driving currents for head C.

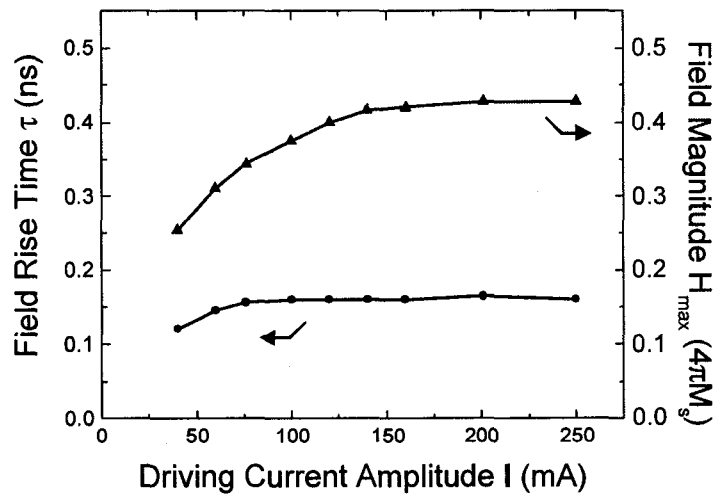


Figure 4.14: Head field rise time and field magnitude vs. driving current for head C.



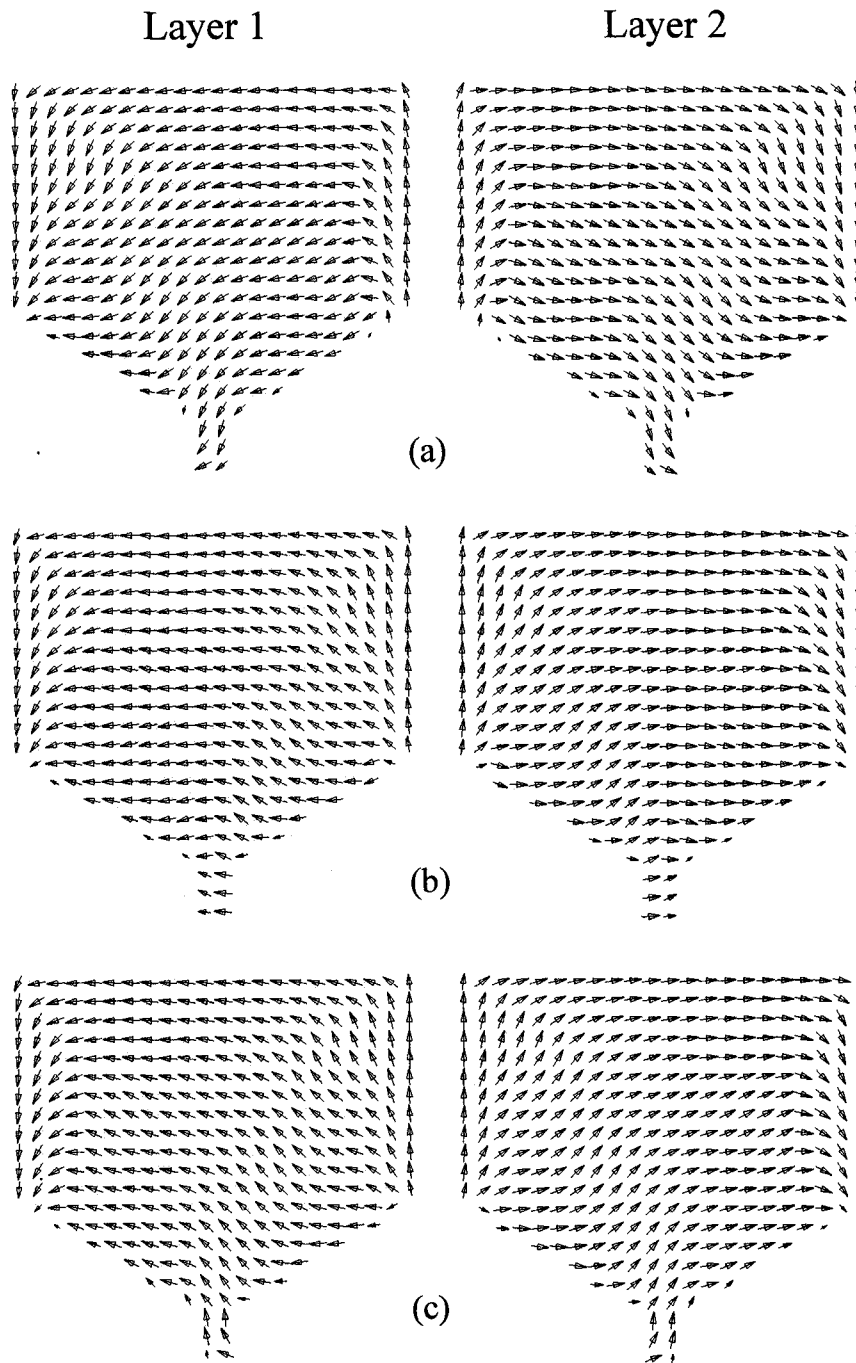


Figure 4.15: Magnetization configurations of head C, (a) before reversal, (b) in the middle of reversal, and (c) after reversal, with a driving current of 40 mA.

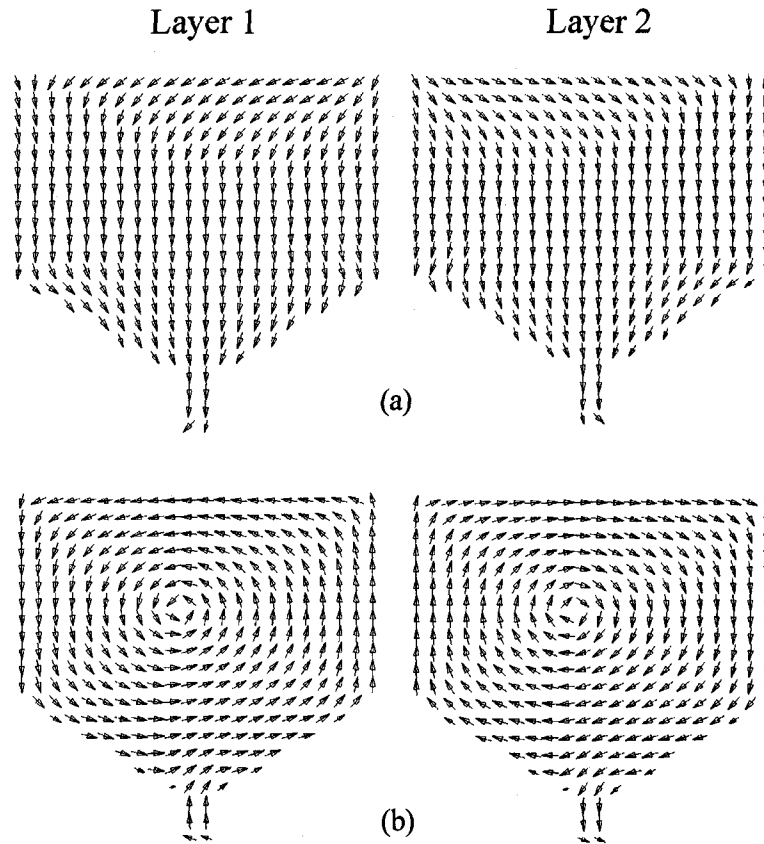


Figure 4.16: Magnetization configurations of head C, (a) with a driving current of 160 mA on, and (b) after the current is off.

It has been noticed that even for head C, with a large driving current, the yoke saturation will still occur, just as in head A and B. In this case, the remanent state magnetization will no longer return to the anti-parallel single domain state as in Figure 4.15(b), instead, two vortices will be formed in the two lamination layers with opposite senses, as shown in Figure 4.16. In this case, each of the two layers behaves the same as head B, thus having similar field rise time performance as head B, which is slightly better than head A.

The comparisons of the head field rise time and the field magnitude versus the driving current for head A, B, and C are shown in Figure 4.17 and Figure

4.18, respectively. The reason for the field rise time performance difference has been explained in detail. In terms of the write efficiency, all the three heads have very similar performance.

#### 4.2.4 Head D

Head D has the same structure and dimension as head C, except that there is a non-magnetic gap introduced between the yoke and the pole tip, which by default is 10 nm, as shown in Figure 4.19. The motivation of doing this is to further decouple the neck region and the pole tip, as it was found that the complication of the magnetic structure in this region may cause variations of the pole tip remanence. The effect of this decoupling can be seen from Figure 4.20. At the remanent state, the magnetization at the bottom of the neck region is antiparallel to that at the top of the pole tip, which is impossible if the pole tip is not detached, due to the exchange coupling. This indicates the independent relaxation of the yoke and the pole tip after writing [59].

The consequence of the independent relaxation is shown in Figure 4.21, which compares a typical head field relaxation process for head A, B, C and D. After driven by a 160 mA current, the amount of time needed for the four heads to reach the final remanent field value is 1.2 ns, 0.6 ns, 0.3 ns and 0.15 ns, respectively. The relaxation process for head D is very well repeatable, due to the independent relaxation made possible by the lamination and the pole tip detachment. Clearly, the domain configurations affects not only the field rise time, but also the head relaxation time. Also notice that, for this dimension, i.e., the pole tip size and the throat height, the remanent field happens to be about the same, regardless of whether the pole tip is laminated or not. This is not always the case for other geometries, as will be discussed in Section 4.2.5.

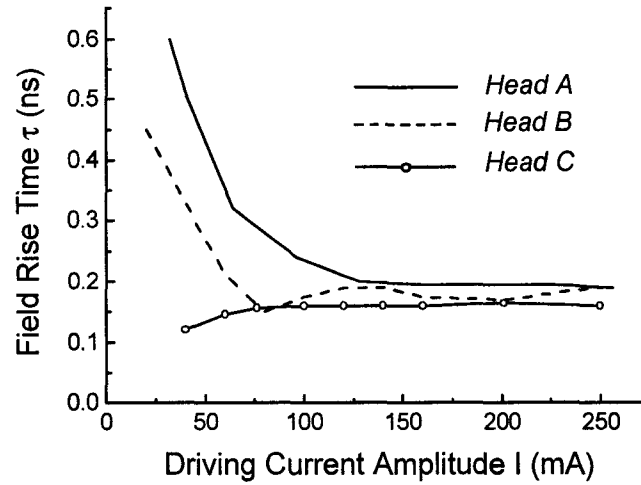


Figure 4.17: Head field rise time vs. the driving current for head A, B and C.

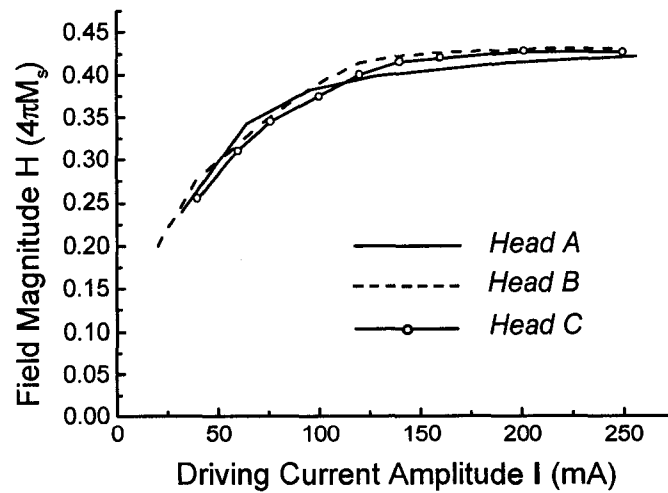


Figure 4.18: Head field magnitude vs. the driving current for head A, B and C.

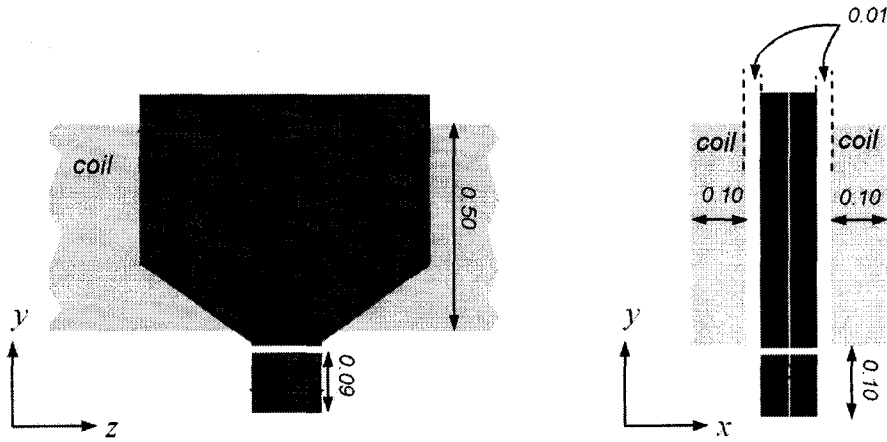


Figure 4.19: Schematic of head D with all dimensions marked in unit of micron. Left: the  $y$ - $z$  plane view. Right: the  $x$ - $y$  plane view.

Due to the same flux reversal mechanism, the field rise time performance of head D is the same as that of head C. However, the gap between the yoke and the pole tip does cause a field loss. Figure 4.22 shows the the maximum head field dependence on the gap length, head D, for two different driving currents. Since the gap does not need to be large to decouple the yoke and the pole tip, as long as it is manufacturable, the field loss could be controlled to within a few percent.

#### 4.2.5 Remanent head field in laminated and detached pole tip heads

It has been pointed out in Chapter 3 that the remanent head field is an issue at high density. Here we show that the pole tip lamination is a very effective way to achieve near-zero remanence. Figure 4.23 shows the remanent head field dependence on the throat height of the pole tip, for a single-layer head and a double-layer laminated head, both with a pole tip footprint of 80 nm by 80 nm. Clearly, with pole tip lamination, a remanent field of less than 800 Oe has been achieved for all throat heights, which is less than 10% of the maximum write field, whereas the unlaminated head still shows strong dependence of remanent

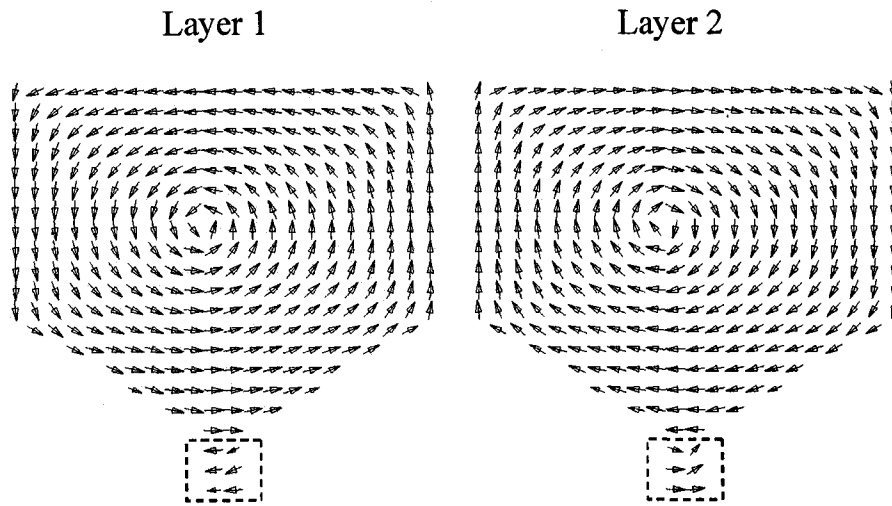


Figure 4.20: Remanent magnetization of head D after driven by a large current.

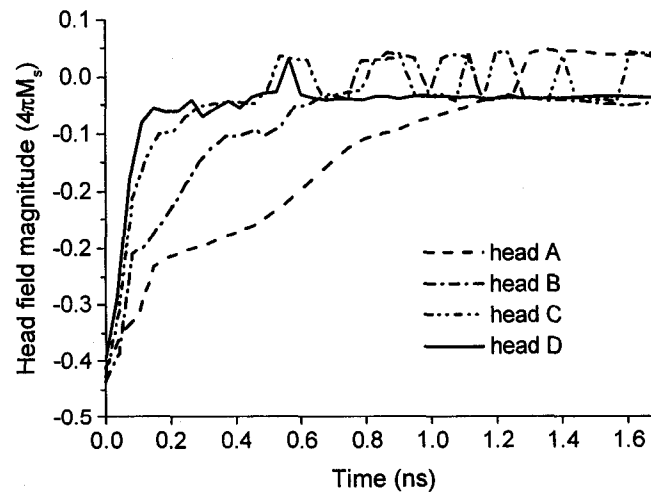


Figure 4.21: The head field relaxation with time for head A, B, C, and D.

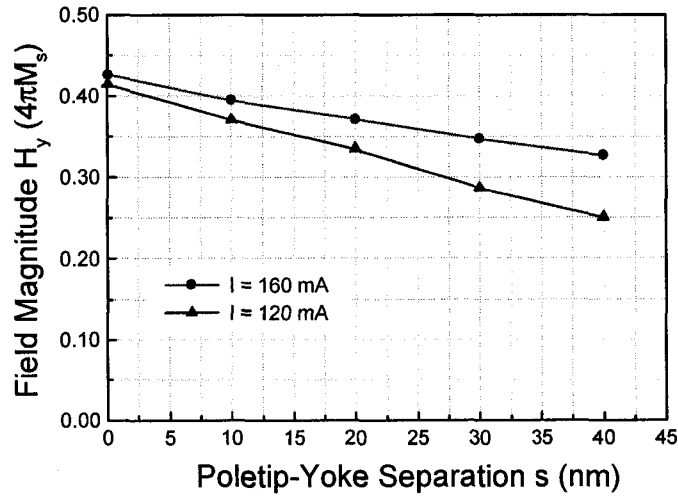


Figure 4.22: Head field magnitude dependence on pole tip-yoke separation for two different driving currents.

field on the throat height.

The reason for the throat height-insensitive robust low remanence is due to the magnetostatic coupling between the lamination layers. As shown in Figure 4.24, at remanent state, the magnetization in the two layers of the laminated pole tip are always anti-parallel, either vertically or horizontally, depending on the throat height. In any case, as a result the flux closure between the two lamination layers, there is little flux leaking into the media, thus a robust low remanent field is always guaranteed.

In fact, the laminated head design has been experimentally tested. In [60], a single pole write head with pole tip lamination was fabricated and tested, which showed significantly improved performance, thanks to the suppressed head-remanence-induced-erasure. In their work, up to 8 layers of lamination of the pole tip has been shown necessary. This is because in their case, the pole tip thickness was about 250 nm, 3 times that of the head we simulated here. Therefore, to assure sufficient flux localization thus low remanence, more

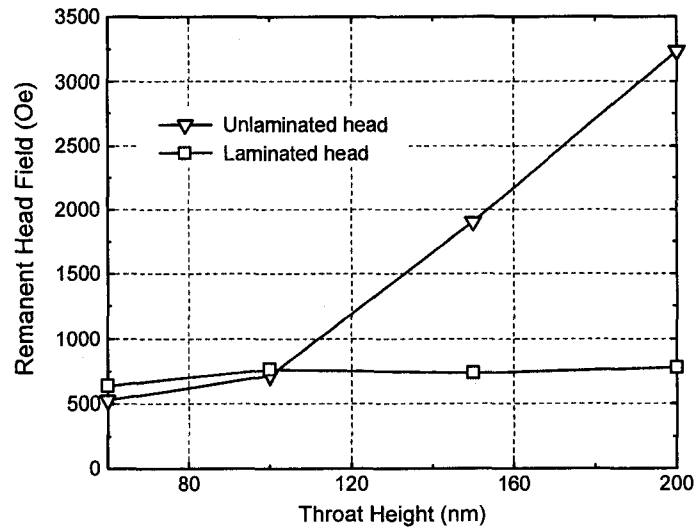


Figure 4.23: Remanent head field dependence on the throat height for an un-laminated head and a laminated head.  $M_s = 1930 \text{ emu/cm}^3$ . The pole tip footprint is 80 nm by 80 nm.

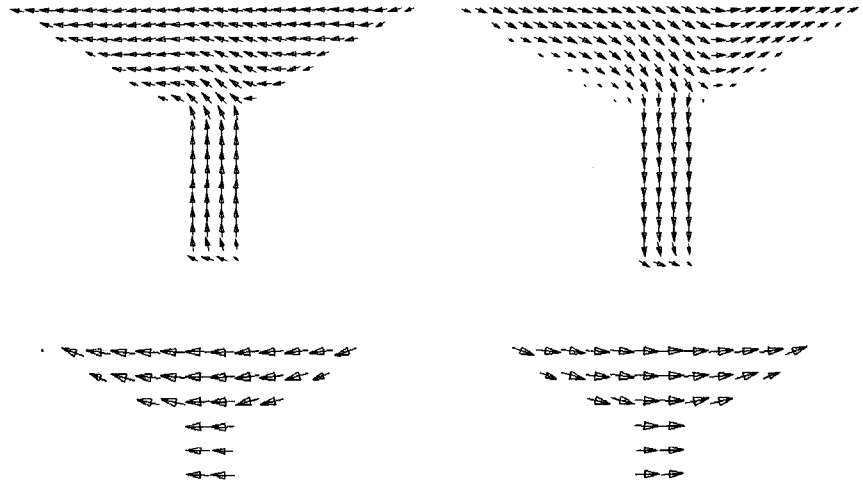


Figure 4.24: Vector plot of the remanent state pole tip magnetization of the two layers of the laminated head with throat heights of 200 nm (top) and 80 nm (bottom), respectively. The pole tip footprint is 80 nm by 80 nm.



lamination layers are needed. In contrast, for the pole tips we present here with a footprint of 80 nm by 80 nm, simulation results showed that a 2-layer lamination is enough. Also to be noticed is that, in actual heads there might be residual flux, which could be from the stray field of the media sucked by the writer shield in a shielded pole head, that may be driving the head after writing. In this case, the head remanence has to have some robustness against this driving flux. A pure magnetostatic coupling between the lamination layers may not be strong enough, and an antiferromagnetic coupling may be needed to enhance the robustness of the low remanence of the pole tip [37].

### 4.3 Stitched Pole Tip Head Design

In Section 4.2, we were mainly dealing with the domain structures in the head, especially for low- and moderate-current cases, and the consequence of those in terms of the head field reversal characteristics and the remanent head field. In this section, we will focus on achieving high field magnitude. As perpendicular recording is expected to extend the recording density to 1 Tbit/in<sup>2</sup>, where a write pole track width of 40 nm with maximum field as high as 2 Tesla is needed [55, 61]. This will be extremely challenging, even with the field from the magnetic charges at the bottom surface of the neck region [62]. Here we propose a stitched pole tip head design that produces enhanced head field compared to a conventional single pole head [63]. The design is not targeting at a particular recording density, as the idea could be used on smaller track widths at higher densities. Various design parameters, such as the throat height, the flare angle  $\theta$  at the neck region, the ABS-SUL separation, and the induced transverse anisotropy field, will be examined.

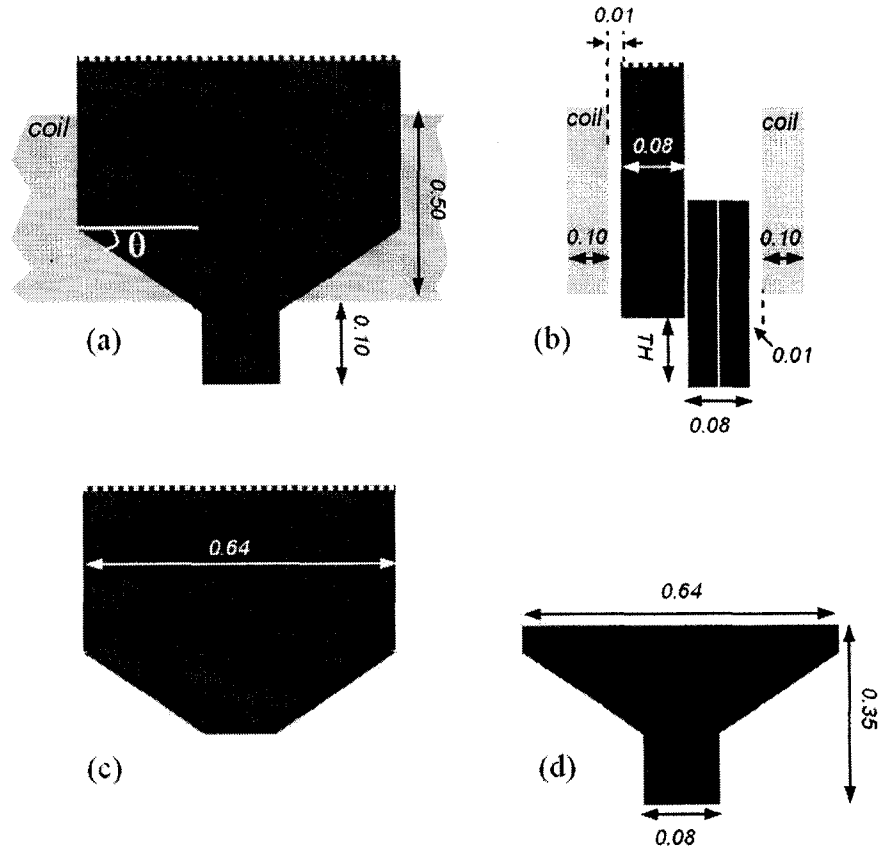


Figure 4.25: Schematic of the stitched pole tip head with all dimensions marked in unit of micron: (a) the  $y$ - $z$  plane view, (b): the  $x$ - $y$  plane view, (c) the  $y$ - $z$  plane view of the yoke layer, and (d) the  $y$ - $z$  plane view of the pole tip layer.

#### 4.3.1 Micromagnetic model and head geometry

In this section, the 3-D micromagnetic model is used for the simulations. A schematic illustration of the stitched pole-tip head is shown in Figure 4.25. The yoke is a single layer slab with a thickness of 80 nm. On the side of the yoke is a stitched pole-tip with a much shorter length. The total pole-tip thickness is also 80 nm, and it is laminated into two layers equally thick, to assure a low remanent head field, as just learned from Section 4.2.5. The yoke and the pole-tip are also exchange decoupled in the contact region. Both the

stitched pole-tip and the side yoke have the same flare angle, but the flat bottom surface of the side yoke is recessed from the ABS by the length of the throat height (TH). The physical track width of the pole-tip is 80 nm. The magnetic material of both the yoke and the pole-tip is assumed to have  $B_s = 2.4$  Tesla. A single turn coil is assumed to drive the head. An ideal SUL with a separation of 30 nm from the ABS is modeled by performing a perfect imaging of the pole-tip and the yoke magnetization dynamically in the simulation. The top boundary of the yoke, denoted by the dashed lines in Figure 4.25, is treated as a flux sink by removing the magnetic charges on that surface, to simulate an ideal flux return path. The 3-D micromagnetic model utilizing LLG equation is used to calculate the head magnetization dynamically under a driving current. Both the yoke and the pole-tip are discretized into cubic cells of 10 nm sides. A damping constant of  $\alpha = 0.05$  in the LLG equation is used in the simulations. The head field is calculated from the resulting magnetization of the head and its image due to the SUL, evaluated at the middle of the recording media, which is 20 nm from the ABS.

#### 4.3.2 Head field

Figure 4.26 shows the down-track head field profile (evaluated at the track center) for the stitched pole-tip head with a driving current  $I = 300$  mA, a flare angle  $\theta = 30^\circ$ , and a throat height of 100 nm. The maximum field value in this case is about 20% higher than that of a traditional single pole head with the same pole-tip dimension but without the side yoke. The field enhancement arises from the magnetic poles at both the bottom surface and the neck region of the side yoke, as shown by the decomposition of the field contributions in Figure 4.26. Note that there is an asymmetry at the two sides of the down-track field

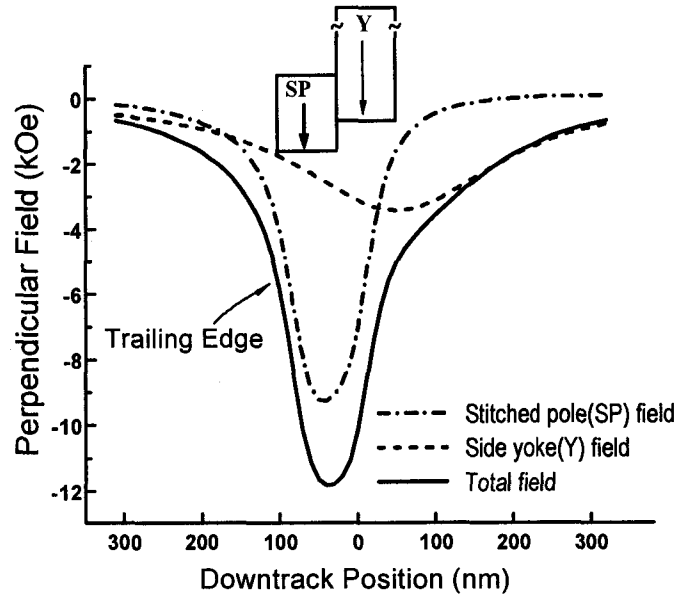


Figure 4.26: The down-track field profile of the stitched-pole-tip head for write current  $I = 300\text{mA}$ , flare angle  $\theta = 30^\circ$ , and throat height = 100 nm.

profile - the field gradient is much poorer at the yoke side of the head, which is not an issue, as long as the other side is chosen as the trailing edge for writing transitions.

The reason to compare the field of the stitched pole with that of a conventional single pole head with the same pole tip dimension is that, although for the same track width, a thick pole does produce higher field, it suffers from the head skewing significantly. Similar structures to the stitched pole tip head actually have been already used in the thin film write heads, although it was mainly for other purposes such as ease of control in fabrication [64], here we have shown that the side yoke actually is essential to produce more field when properly driven by the coil current field.

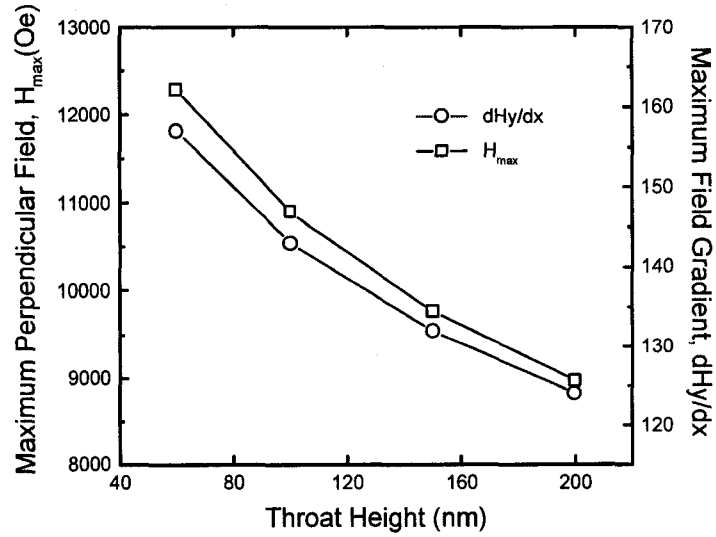


Figure 4.27: Maximum perpendicular head field and maximum down-track field gradient versus the throat height. The driving current is 200 mA, and the flare angle is  $30^\circ$ .

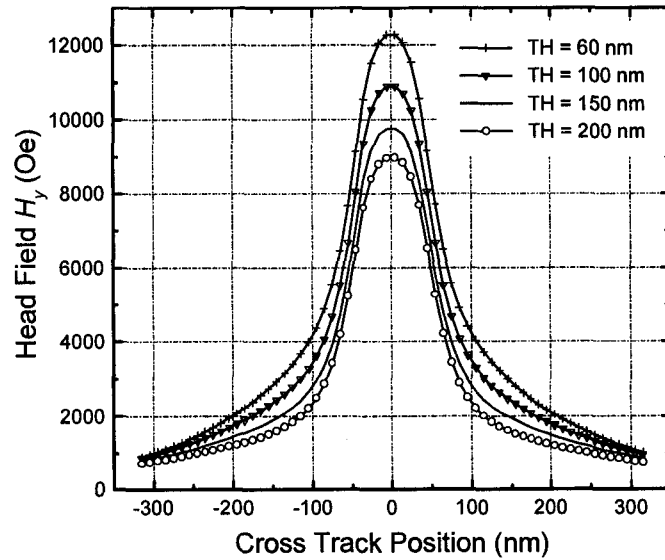


Figure 4.28: Cross-track field profiles for different throat heights. The driving current is 200 mA, and the flare angle is  $30^\circ$ .

### 4.3.3 Throat height

Throat height is a very important design parameter that directly affects the head field magnitude and its spatial distribution, both are crucial for high density recording. Figure 4.27 shows the maximum perpendicular head field and the maximum down-track field gradient for four different throat heights. As the throat height is reduced from 200 nm to 60 nm, the magnetic poles on the bottom surfaces of the flare region become closer to the medium, therefore the effective solid angle (see Section 3.2.1) increases, leading to an increase of the maximum on-track head field from 9 kOe to over 12 kOe. In the mean time, the maximum down-track field gradient also increases by about 25%, from 124 Oe/nm to 157 Oe/nm. Such increases of the head field and the down-track field gradient, however, are accompanied by an increase of the off-track field, as the field from the charges at the side flare region is over a very broad range across the track, as shown in Figure 4.28. In the case of 60 nm throat height, the perpendicular field 100 nm off the track center is about 1/3 of the maximum on-track field, which may cause thermally induced magnetization switching on the adjacent track. Therefore, when choosing the throat height, tradeoffs between on-track field and adjacent track erasure (ATE) has to be made based on the media properties and the thermal stability requirements.

In reality, there are also limitations in terms of processing for extremely low throat heights, as it is determined by the accuracy of the mechanical lapping at the ABS. If this difficulty could be solved, cross-track side shields might be used in conjunction with a low throat height to suppress the off-track field while still maintaining the on-track field magnitude and field gradient [55, 65], although the side shield will make the fabrication of the head very difficult too.

#### 4.3.4 Flare angle

Since part of the head field is from the magnetic charges on the bottom and the flare region of the yoke, it is important to examine the effect of the flare angle on the head field strength and profile. Figure 4.29 shows the cross-track field profiles for various flare angles, evaluated along the line where the maximum on-track field occurs. It is found that a flare angle of  $45^\circ$  yields the maximum on-track peak field. As far as the off-track field is concerned, it decreases with increasing flare angle, and the off-track field for  $45^\circ$  flare angle is only slightly higher than that for  $60^\circ$ . Therefore, a flare angle of  $45^\circ$  is considered optimum for the single pole head design. On the other hand, a zero degree flare angle yields the smallest on-track field and a large off-track field. This is because a flat yoke bottom leads to very poor flux concentration towards the pole tip and much closer distance to the media for the charge at the side.

#### 4.3.5 ABS-SUL separation

It is often believed that perpendicular recording scheme could allow a thick medium for thermal stability. This is in fact not necessarily true. As discussed in Section 3.2.1, the write field magnitude decreases very rapidly with increasing medium thickness, since the ABS-SUL separation increases at the same time, given a fixed head flying height. To show quantitatively the effect of the media thickness, Figure 4.30 plots the dependence of both the maximum perpendicular head field and the maximum down-track field gradient on the medium thickness for the parameters shown in the inset, where the ABS-SUL spacing is assumed to be the sum of the flying height and the media thickness. Since keeping the ABS-SUL separation small is much more effective than increasing the lateral

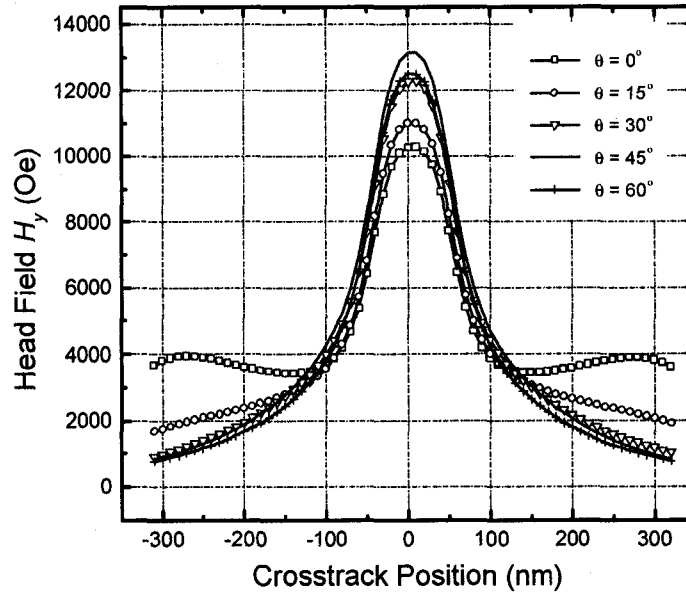


Figure 4.29: Cross-track field profiles for different flare angles. The driving current is 200 mA, and the throat height is 60 nm.

dimension of the head foot print, to maximize the head field magnitude and the field gradient, it is vital to avoid unnecessarily thick medium, as long as reasonable thermal stability and crystalline structure of the medium is obtained.

#### 4.3.6 Induced anisotropy

We have demonstrated that through lamination of the pole tip, robust near-zero remanence could be achieved in single pole heads with extremely narrow track width. In practice, not only is a near-zero remanent field needed, but the time it takes to reach the remanent state after the writing current is turned off also is important [66]. It has been found that in those small pole-tips with deep sub-micron dimensions, an induced longitudinal anisotropy up to several hundred Oersteds has little effect on the remanent field. This longitudinal anisotropy field, however, does help expedite the field relaxation process.



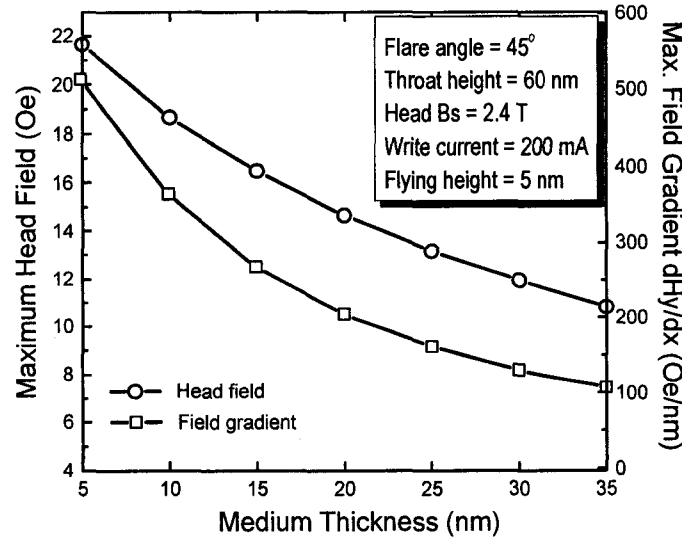


Figure 4.30: Dependence of the maximum perpendicular field and down-track field gradient on the media thickness. The head dimension is the same as in Figure 4.25.

Figure 4.31 shows the field relaxation processes for three different longitudinal anisotropy field values of 0 Oe, 200 Oe and 400 Oe, respectively. Although for all cases the final remanent field is the same, the relaxation is much faster for the cases with longitudinal anisotropy than that without. The reason for this speedup might be that the longitudinal anisotropy provides an initial torque for the magnetization to rotate away from the saturation direction, which is perpendicular to the ABS. Figure 4.32 shows the effect of the longitudinal anisotropy on the writing efficiency. For a typical write current of 200 mA, the write efficiency reduction due to the anisotropy field is essentially negligible.

#### 4.4 Conclusions

In this chapter, three dimensional dynamic micromagnetic modeling has been used to study various head designs, with the focus on the head domain structures and consequently the field rise time performance at low- and

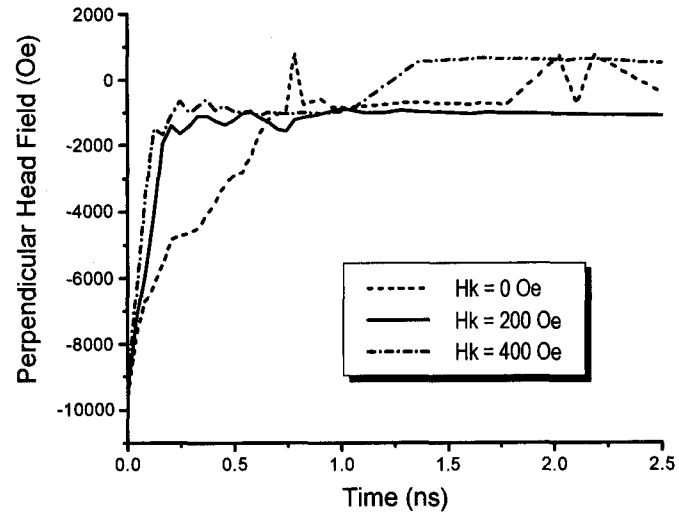


Figure 4.31: Head field relaxation for different longitudinal induced anisotropy fields.

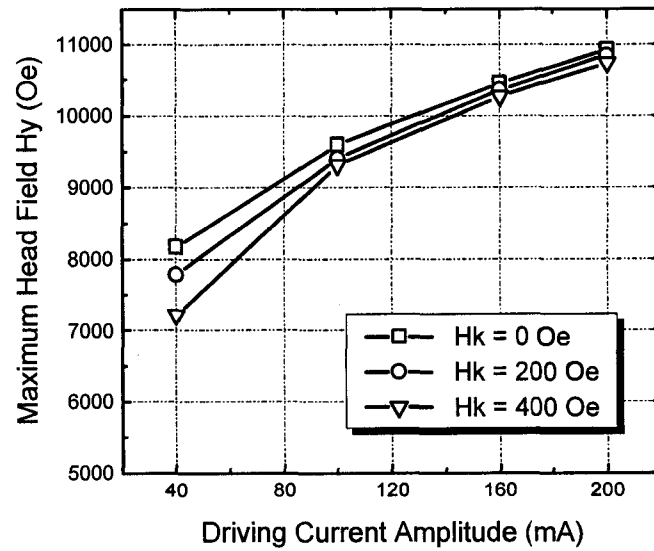


Figure 4.32: Maximum perpendicular head field versus write current for different induced longitudinal anisotropy fields.

moderate-current region, the remanent head field, and the approach to enhancing the head field.

A single pole head with a short yoke and lamination has very fast field rise time in the low driving current region, and the lamination produces negligibly small remanent field. A pole tip detached (exchange decoupled) from the yoke can further improve the remanent field performance, especially the head magnetization relaxation time after the writing process.

A stitched pole-tip head with a recessed side yoke can produce up to 20% more field compared to a conventional single pole head with the same pole tip footprint size. Reducing the throat height increases the on-track field considerably, but the penalty is the possible adjacent track thermal decay due to the high off-track field. A 45° flare angle has been found to yield the optimum on-track field strength and cross track profile. The ABS-SUL separation is extremely important for high field magnitude, which strictly prohibits the use of excessively thick media. A moderate transverse induced anisotropy significantly shortens the field relaxation time after writing without reducing the writing efficiency.

## 5 HIGH FREQUENCY HEAD FIELD DYNAMICS

As discussed in Chapter 1, in addition to high field magnitude for high density recording, a very short field reversal time is also required for high data rate applications. In fact, the increase of the recording density has always been accompanied by the increase of the data rate because, on the one hand, a recorded bit occupies shorter length down the track with increased linear density; on the other hand, the rotation speed of the disk has also been increasing over time. As a result, a data rate of 3 Gbit/sec is expected at an areal recording density of 1 Tbit/in<sup>2</sup> [61, 67]. This means that the head field reversal time has to be within a fraction of a nanosecond, which is getting close to the characteristic time of the gyromagnetic motion of the spins. Therefore, the dynamic micromagnetics of the spin system of the head will play an important role in determining the characteristics of the head field reversal. Furthermore, as such a head is very likely to work at a high driving current, meaning that there will be significant amount of energy being pumped into the head magnetic system, which may in turn affect the magnetization switching speed as the energy dissipation rate also matters, which brings the Gilbert damping constant of the system into the picture as well. In fact, in Chapter 4, we have seen the level-off of the field rise time at large driving current case, which indicates a different magnetization reversal mode than that at low driving current. This phenomenon will be studied in detail in this chapter. Since the dynamic magnetization reversal and the energy damping will be the focus of interest here, the dynamic micromagnetic model is naturally the ideal candidate for the simulation tool here, as it has the full capability of characterizing these features.

In this chapter, we will first present in detail the magnetization reversal processes in the case of hard-driving. Following that we will study the effect of the driving current rise time and the magnetic damping of the system on the field reversal performance of the head. Finally, potential limits of the head magnetization reversal speed is presented, based on the study of the phenomena in this chapter.

### 5.1 Introduction

For a given damping constant, the time of reversing the magnetic moment of a single spin is inversely proportional to the amplitude of the applied field. Therefore, increasing driving current amplitude has been used along with shortening the current rise time to achieve fast head field rise time. Although the behavior of a many-spin system is not exactly the same as that of a single spin, for example, there could be different reversal modes in a many-spin system, the practice of having higher driving field and short current rise time has been so far successful in shortening the field rise time and therefore, raising the data rate to beyond 1 Gbit/sec. However, what we are concerned with here is whether this technique will still work at even higher frequencies. In other words, can the magnetization reversal follow an extremely short current rise with a high drive current? To answer this question, the details of the magnetic damping processes in the head during a reversal has to be studied. Previous micromagnetic simulation studies have shown that, unlike a single spin, a many-spin system such as a ferromagnetic thin film with zero magnetic damping can still reverse its magnetic moment to minimize the Zeeman energy while generating spin waves as an energy reservoir [68, 69, 70, 71]. However, for a write head that is supposed to

produce high field, a complete damping of the exchange energy, hence a full alignment of the magnetization is very important. In fact, as will be shown in this chapter, simply decreasing current rise time and/or increasing current amplitude eventually will not shorten the field rise time, but make it worse.

## 5.2 Micromagnetic modeling

The head used for the simulation in this chapter is the same as the one shown in Figure 4.25, with a throat height of 90 nm and a flare angle of  $45^\circ$ . The driving current was assumed to have a linear ramp rising with the time interval during the transition defined as the current rise time. An ideal soft magnetic underlayer is assumed in the simulation by performing a perfect imaging of the head magnetization dynamically, with spacing between the ABS and the soft underlayer equal to 30 nm. The 3-D dynamic micromagnetic model utilizing the LLG equation is used in the simulation. Both the yoke and the pole-tip are discretized into cubic cells of 10 nm sides. The damping constant is varied from 0 to 0.2. The head field at the center of the recording medium that is 20 nm away from the ABS is calculated from the resulting magnetization configurations from micromagnetic simulations. The field rise time is defined as the time for the field to reverse from  $-90\%$  to  $+90\%$  of the full magnitude. The driving current amplitude used in this chapter was 200 mA, unless otherwise noted.

## 5.3 Results and discussions

### 5.3.1 Magnetization reversal processes

Figure 5.1 shows the calculated head field versus time at 1 Gbit/sec recording data rate for current rise time  $\tau_c = 100$  ps and damping constant  $\alpha = 0.01$ .

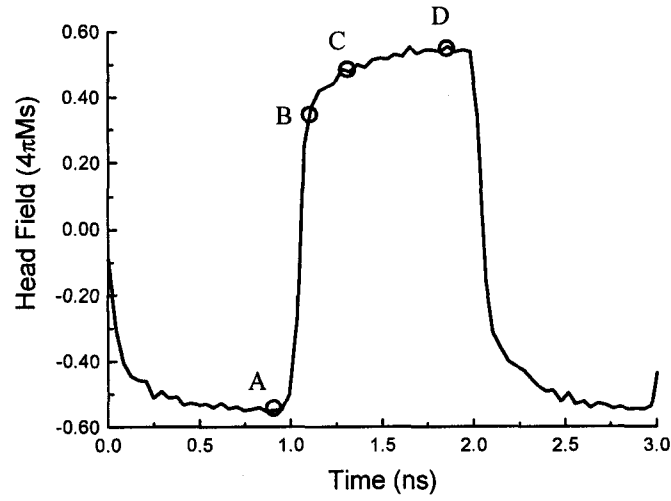


Figure 5.1: Head field versus time for current rise time  $\tau_c = 100$  ps and damping constant  $\alpha = 0.01$ .

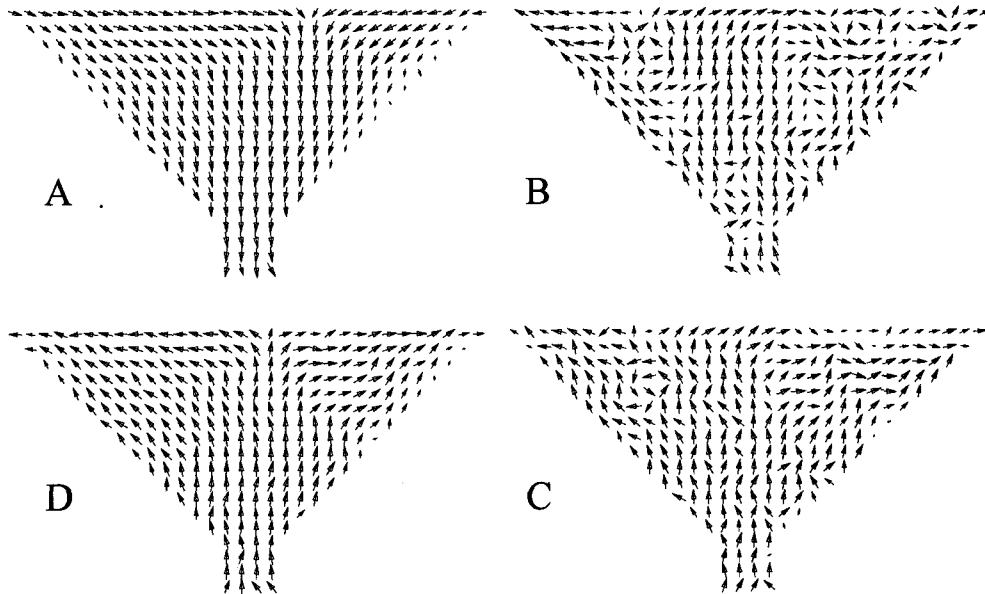


Figure 5.2: Magnetization configurations of the head during the flux reversal corresponding to point A, B, C, and D in Figure 5.2.

The field reversal process can be divided into two stages: stage 1, which is from point A to point B, and stage 2, which is from point B to point D, where the final value of the reversed field is reached. In this case, the initial stage of the reversal, from A to B, takes about 0.1 ns, whereas the second stage is much slower. The distinction between the two stages can be seen from Figure 5.2, which shows a sequence of the transient magnetization configurations corresponding to the points A, B, C, and D in Figure 5.1. The initial stage of the magnetization reversal in both the head yoke and the pole-tip is actually governed by the gyromagnetic motion of the spins around the total local effective magnetic field, which includes the current field, the magnetostatic interaction field (the demagnetizing field) and the ferromagnetic exchange field. During this stage, the Zeeman energy either gets directly damped if the damping constant is relatively large, or stored as the ferromagnetic exchange energy in the resulting spin waves if the damping constant is small. The latter case is more like the case shown here, as shown in state B. Although the majority of the spins were switched in this state, local fluctuations of spins around the driving field direction exist, which stores the initial Zeeman energy in the form of the exchange energy in the spin wave. In this case, a reversal is completed only when the spin wave is damped out through energy dissipation, to reach the final value of the reversed head field. The smaller the damping constant, the slower the completion stage of the reversal becomes.

### 5.3.2 Effect of damping constant

For a given driving current waveform, i.e., amplitude and rise time, the total field rise time should be inversely dependent on the damping constant, because of the time needed to damp out the exchange energy in the second stage of the



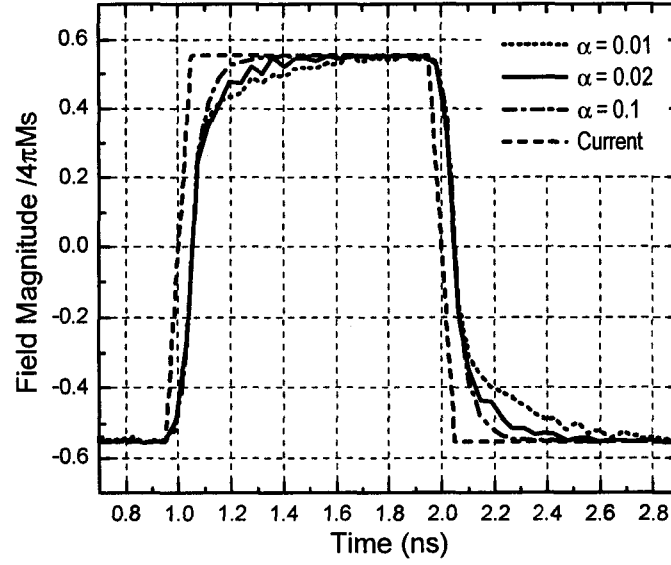


Figure 5.3: Temporal profile of the head field for different damping constants. The current rise time is 100 ps.

reversal. Figure 5.3 shows the head field versus time for two consecutive field reversals with a current rise time of 100 ps. The normalized current waveform is also shown as reference. The field rise time is 0.38 ns, 0.24 ns, and 0.13 ns for damping constant values of 0.01, 0.02, and 0.1, respectively. This monotonic dependence has been found for all driving current rise times, as will be shown later.

### 5.3.3 Effect of current rise time

The end of the initial stage and the beginning of the damping stage of a reversal can be clearly identified by the “knee” in the head field reversal profile. Especially for very short current rise time. The field magnitude at the “knee” depends on the amount of exchange energy stored in the resulting spin waves. Since for a given spin wave wavelength, the more energy the spin wave stores, the larger the precession cone angle and therefore, the smaller the head field at that point. For a given damping constant value, the head field magnitude at the

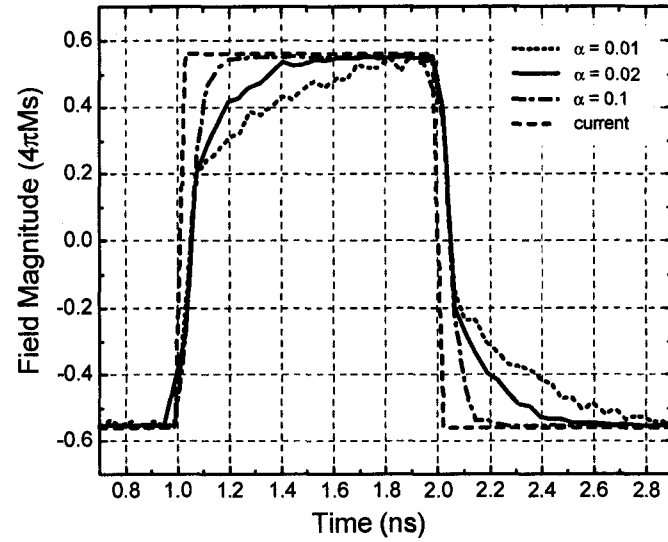


Figure 5.4: Temporal profile of the head field for different damping constants. The current rise time is 20 ps.

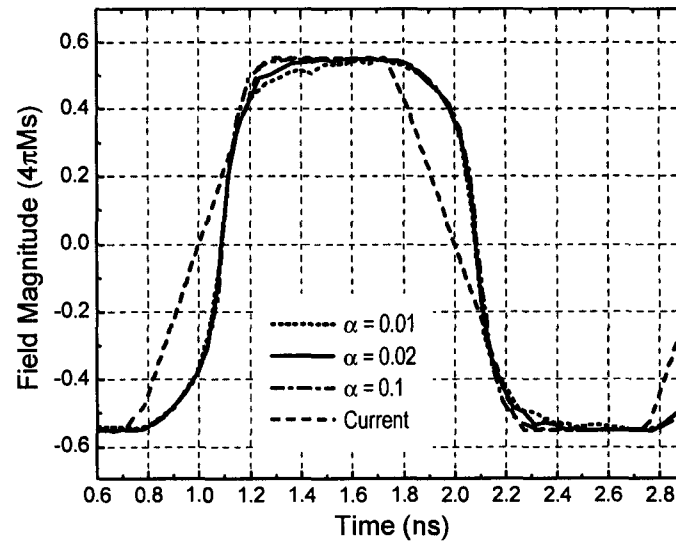


Figure 5.5: Temporal profile of the head field for different damping constants. The current rise time is 500 ps.

“knee” point should be inversely related to the amount of energy pumped in by the driving current field. The latter turns out to be dependent on the current rise time, as shown in Figures 5.4 and 5.5. The head fields at the “knee” point are 36%, 45%, and 58% of the full magnitude, for the current rise time of 20 ps, 100 ps, and 500 ps, respectively. This could be understood as follows.

In the case of an extremely short driving current rise time, e.g., 20 ps, at the end of the initial reversal, or the “knee” point, there is strong spin wave excitation with little energy dissipated, which leads to a lower field magnitude at the “knee” point. On the other hand, if the current rise time is very long, e.g., 500 ps, part of the energy has already been dissipated at the “knee” point, yielding better magnetization alignment and thus higher field. This can be clearly seen from the magnetization patterns at the “knee” point for the current rise time of 20 ps and 500 ps, respectively, shown in Figures 5.6 and 5.7.

This phenomenon could also be understood from another viewpoint. The driving current fields in today’s high-end drives are substantially greater than the quasi-static switching field of the yoke and the pole-tips. In this situation, an extremely short current rise time will actually cause the magnetization of the yoke and the pole-tip to switch at the current field value which is significantly larger than that for a longer current rise time. This is demonstrated in Figure 5.8, which shows the head field as a function of the driving current during field reversals for two different current rise time. Notice that the loops also contains the temporal information, as each of the head field values was measured at the instant at which the corresponding driving current value was measured. Since the head field mainly arises from the magnetization of the pole-tip, the curves effectively represent the hysteresis loops of the head magnetization during switching. The area enclosed in each loop is proportional to the energy pumped into the head spin system for each case.

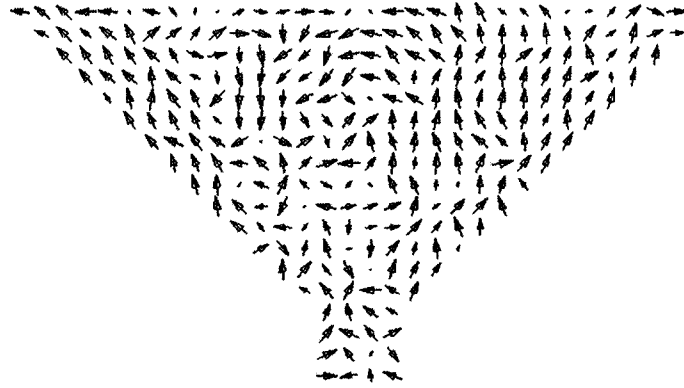


Figure 5.6: The magnetization configuration of the head at the “knee” point of the field reversal for current rise time of 20 ps.

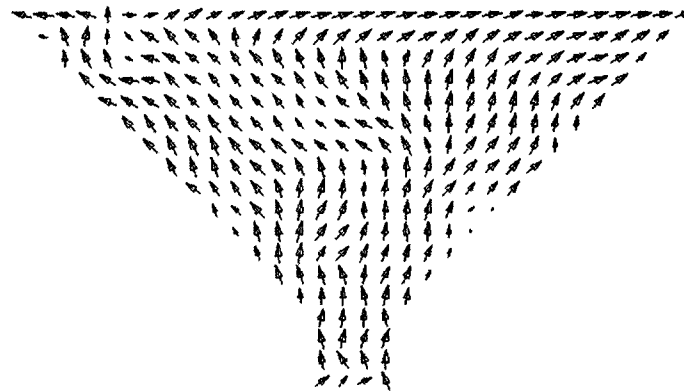


Figure 5.7: The magnetization configuration of the head at the “knee” point of the field reversal for current rise time of 500 ps.

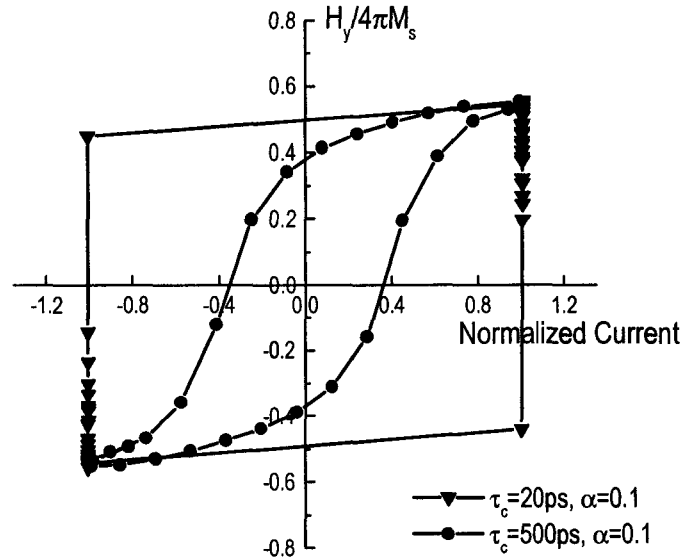


Figure 5.8: Hysteresis loops of the head field versus the normalized driving current for current rise time of 20 ps and 500 ps, respectively.

It is evident from Figure 5.8 that a shorter current rise time can actually cause more energy to be pumped into the spin system of the yoke and the pole-tip, resulting in a longer damping stage in the field reversal, thereby a slower overall field rise time. On the other hand, if the driving current rises slowly relative to the energy damping, the Zeeman energy can be dissipated during the initial stage of the head magnetization reversal. In this case, the field rise time will be essentially governed by the current rise time and the damping stage is of less importance especially with current overshoot, an approach being used in today's drives. This could also be seen from the less sensitivity of the field rise time to the damping constant, as the distinction between the two stages of the reversal is not as clear in this case, and the amount of energy to be dissipated is much smaller. Having known the limiting factors at the two extremes of the current rise time, for a given damping constant, there must exist an optimum current rise time for producing the shortest head field rise time.

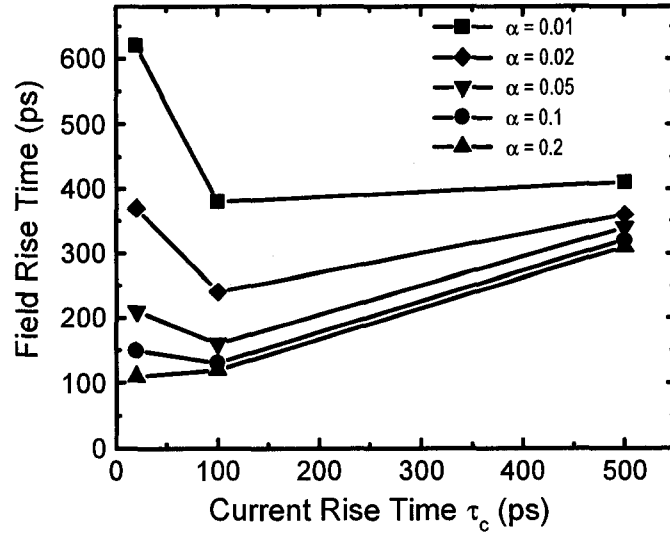


Figure 5.9: Field rise time versus current rise time for different values of damping constant.

Figure 5.9 shows the field rise time ( $-90\%$  to  $+90\%$ ) as a function of the current rise time for different values of the damping constant. When the damping constant is relatively small, the existence of an optimum current rise time becomes evident. In fact, many experimental measurements suggested a damping constant in the range between 0.01 and 0.02 [39, 40]. Therefore, this optimal current rise time effect will very likely exist in practice.

#### 5.3.4 Limit of field reversal speed

The excitation of spin waves and the subsequent energy dissipation process that we just discussed may pose a limitation on how fast the magnetization of the head could be reversed, in the sense of reaching the full magnitude as a working write head. Figure 5.10 shows the temporal profile of the head field for an ideal extreme case of zero damping, where the exchange energy in the spin wave has no way to dissipate. In this case, the head field quickly decays to some

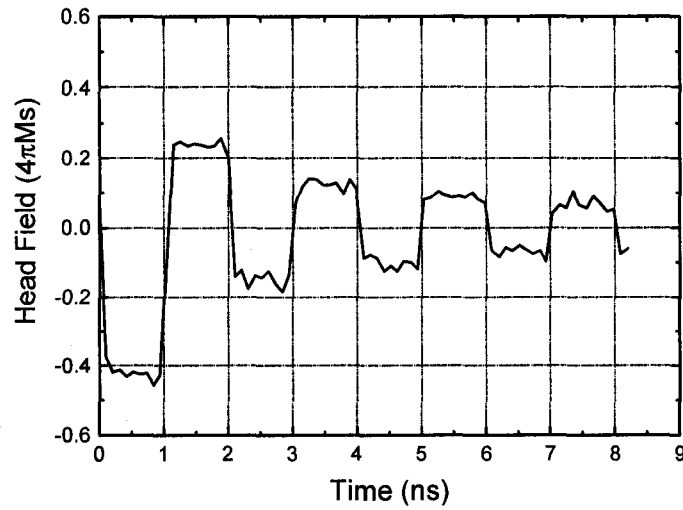


Figure 5.10: Temporal profile of the head field for damping constant  $\alpha = 0$ , current rise time  $\tau_c = 100$  ps, and data rate of 1 Gbit/sec.

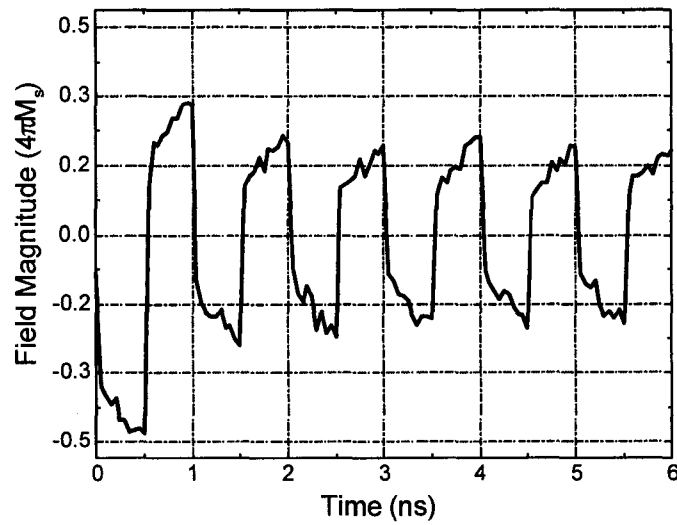


Figure 5.11: Temporal profile of the head field for damping constant  $\alpha = 0.004$ , current rise time  $\tau_c = 20$  ps, and data rate of 2 Gbit/sec.

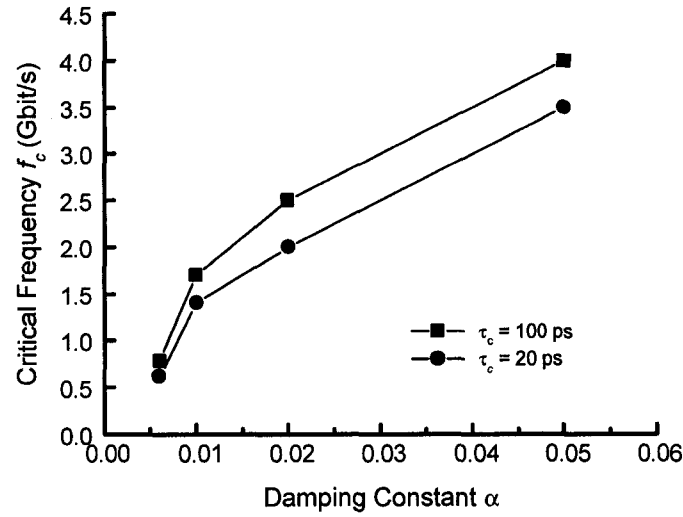


Figure 5.12: The critical frequency versus the damping constant for two different current rise times.

insignificant value, as the spin system is being driven into a severe chaos with the accumulation of the exchange energy pumped in by the driving current.

In a realistic head spin system with very small damping, if the resulting spin waves are not fully dissipated by the time the next current reversal arrives, the remaining undamped spin waves will keep the head magnetization from reaching its maximum amplitude. Such a phenomenon will occur if the cycling frequency of the current field is too high for the given current rise time and the damping constant. Figure 5.11 shows a calculated head field time temporal profile for a driving current cycling at 2 Gbit/second data rate, current rise time of 20 ps, and a damping constant of  $\alpha = 0.004$ . During the beginning cycles, incomplete energy dissipation yields accumulation of the spin wave energy in both the yoke and the pole-tip and the portion of the head magnetization that can be reversed become reduced, resulting in a decrease of the head field amplitude. As the current cycling continues, the head field amplitude will reach a steady value when the energy pumped in by the current field and the



energy dissipated reach a dynamic equilibrium. Therefore, one can define a critical frequency, or data rate, at which the head field can be barely reversed without reduction of the field magnitude. Obviously, the critical frequency will be dependent on both the actual damping constant of the ferromagnetic system and the current rise time, as shown in Figure 5.12.

#### 5.4 Conclusions

The head field reversal under a large driving current field at high frequency can generally be characterized by two stages: the initial stage, which is mainly governed by the gyromagnetic motion and dependent very little on the energy damping; followed by the damping stage, which strongly depends on the energy damping constant. When the damping constant is small, and the current rise time is very short, such that the energy damping is significantly slower than the current rising, spin waves will be excited at the end of the initial stage, acting as a temporal energy reservoir for storing the initial Zeeman energy due to the driving field. At extremely short current rise time, the field rise time is limited by the damping stage due to the strong spin wave excitation, whereas for very slow current rise time, the field reversal is limited by the current reversal time. As a result, there exists an optimum current rise time at which the head field rise time is minimized. When the cycling frequency of the driving current exceeds the rate of energy dissipation, the head field amplitude will decrease. The roll-off frequency reaches the maximum at the optimum current rise time, and it is damping constant dependent.

## 6 SOFT UNDERLAYER IN READ AND WRITE IN PERPENDICULAR RECORDING

In this chapter, we present a micromagnetic modeling study of the soft underlayer (SUL) in both the write and the readback process of perpendicular recording [72]. The effect of the SUL on readback has been investigated via a 2-D micromagnetic model that takes into account the free layer of the spin valve reader, the soft magnetic shields of the reader, and the SUL. 3-D micromagnetic modeling has been performed to evaluate the effect of the SUL in the writing process. It has been found that the SUL imaging effect on the media magnetization enhances the readback signal amplitude differently for high density and low density, making the rolloff of the readback signal faster with the linear density and thus deteriorating the readback performance by lowering down the maximum achievable linear density. Most approaches for increasing the density limit via making the SUL imaging less effective are accompanied by the tradeoff of the write field loss. Reducing the head-medium spacing and the reader gap with an optimized spin valve reader stripe height are found essential for maximizing the linear density limit imposed by the rolloff of the readback.

### 6.1 Introduction

In perpendicular recording, the soft underlayer (SUL) is a very crucial component for achieving high field magnitude. It is essentially part of the write head as it serves as a portion of the write flux path, in addition to the main write pole and the return pole. It turns out that, if only the imaging effect

hence the write field boosting is concerned, it is relatively easy. As long as a soft magnetic material with proper moment, thickness and permeability is used that is sufficient to conduct the flux from the write pole without being saturated (hence flux leakage), this condition is met. A simple quantitative relation between the SUL moment and thickness needed and a given pole tip material, based on flux conservation, is given as follows [53]:

$$t_{min \text{ SUL}} \sim \frac{1}{2} \frac{M_{s \text{ pole tip}}}{M_{s \text{ SUL}}} w_{\text{pole tip}} \quad (6.1)$$

where  $t_{min \text{ SUL}}$  is the minimum thickness of the SUL needed,  $M_{s \text{ pole tip}}$  and  $M_{s \text{ SUL}}$  are the saturation magnetization of the pole tip and the SUL, respectively, and  $w_{\text{pole tip}}$  is the physical track width of the write pole tip, which is smaller than the thickness of the pole tip along the down-track direction.

The above relation seems fairly simple and straightforward. However, there are complications that the SUL brings into the perpendicular recording system. It turns out that most of the complications have to do with the readback process, since after the writing is finished, the SUL is still there underneath the recording layer (hard layer) and it will be magnetized by the fringing field from the recorded bits and hence making the readback performance different from those without SUL. To the first-order approximation, the SUL effectively doubles the thickness of the medium layer, the reader will therefore sense a stronger signal field, as demonstrated by previous studies [73, 74, 75, 76, 77]. Although the SUL will in general boost the readback signal, the boosting actually differs for recorded bits at different frequencies, as will be shown in detail in this chapter. As a result, it in fact degrades the readback performance, since the rolloff of the readback signal becomes faster with increasing linear density. This has been observed both by experiments and by modeling [53].

Other issues associated with the SUL include the complications of the domains that is created during the writing process [78], and consequently, the noise these domains cause during the readback [79, 80]. These issues have brought to the attention of the industry and therefore, active research is being carried out to solve them [81, 82].

In this chapter, we will present a micromagnetic modeling study of the SUL in perpendicular recording, both in writing and in readback, in order to gain a more complete understanding of the effect of the SUL in perpendicular recording. In particular, the effect of the SUL on the linear density limit will be emphasized.

This chapter is organized as follows. In Section 6.2, the micromagnetic model and the simulation parameters, for both read and write, are presented. In section 6.3, we will first show the micromagnetic states of the SUL in the fringing field of the recorded bits in the hard layer, which will provide the fundamentals for the results following up in this chapter. The waveform from an isolated transition, i.e., the transition response, for different SUL parameters will then be presented. Having the above set, rolloff of the readback signal with increasing linear density will be investigated in Section 6.4, based upon which the  $-20\text{dB}$ -density,  $D_{20\text{dB}}$ , will be defined and then used as a major figure of merit throughout the chapter. Various parameters that affect  $D_{20\text{dB}}$  will be investigated in detail in Section 6.5. Since there are usually trade-offs between increasing  $D_{20\text{dB}}$  and maximizing the write field, the effect of SUL on the write field is not discussed as a separate section, it is, instead, mostly presented in this section. Finally, Section 6.6 concludes the chapter.

Table 6.1: Default simulation parameters for Chapter 6.

Variable	Quantity
Head-media mag. spacing (HMS)	10 nm
Reader gap (shield-shield spacing (SSS))	80 nm
Reader stripe height/SSS	1.5
Free layer $M_s$	1100 emu/cm <sup>3</sup>
Shield $M_s$	800 emu/cm <sup>3</sup>
SUL $M_s$	800 emu/cm <sup>3</sup>
Medium $M_r$	400 emu/cm <sup>3</sup>
SUL $H_k$	0 Oe
Free layer thickness	5 nm
Media(hard layer) thickness	20 nm
SUL thickness	100 nm
Interlayer(between media and SUL) thickness	0 nm

## 6.2 Micromagnetic modeling

To simulate the readback process of a spin valve head in the presence of the SUL, we have modified the 3-D micromagnetic model that has been used in previous chapters for the write head into a 2-D readback model. The 2-D readback model includes the modeling of the free layer of the spin valve read head, the soft magnetic shields of the reader, and the SUL. Other layers of the spin valve head was ignored. The model is geometrically two-dimensional by assuming no variation of the magnetization in the cross-track direction. The entire modeled system is discretized into 5 nm by 5 nm square elements. The magnetization of each element is three-dimensional and it can rotate to any direction according the effective field exerting on it, where the effective field here includes the contributions from the magnetostatic interaction, the anisotropy field, the exchange coupling, and the field from the recorded magnetization pattern in the hard layer. The LLG equation is used for calculating the magnetization

states of the free layer, of the soft magnetic shields of the reader, and of the SUL self-consistently. This automatically takes into account the effect of the shields and the SUL on the readback. The magnetization of the hard layer is not included in the model, instead, the field from the recorded bits in the hard layer, assuming infinitely sharp transitions, is computed analytically and used as the input to the model for calculating the magnetization states of the whole system - the free layer, the shields, and the SUL. The output readback voltage is then obtained by averaging the free layer magnetization orientation over the stripe height of the spin valve. Although the LLG equation is used to solve for the magnetization configurations, the model is actually quasi-static. In the model, the way to calculate the readback waveform over a segment of the media is to shift the entire model with respect to the fringing field pattern of the media along the track, and get the static magnetization configuration at each position.

For those results regarding the write field, a 3-D micromagnetic modeling was performed. In those cases, the writer is a single pole head with pole-tip dimension of 80 nm cross-track and 160 nm down-track, throat height of 80 nm with a 45-degree neck region flare angle, and  $B_s$  of 2.4 Tesla. The head-to-SUL spacing is 30 nm and the head field is calculated at a distance of 20 nm away from the head air-bearing surface (ABS). Other simulation parameters are listed in Table 6.1. By default, all the results presented in this chapter are based on these parameters if not otherwise specified.

### 6.3 SUL micromagnetics and transition response

In perpendicular recording, during the writing process, the SUL is magnetized by the field from the pole tip, which in turn produces another field equivalent to that from the “image” pole tip. After the write field is removed

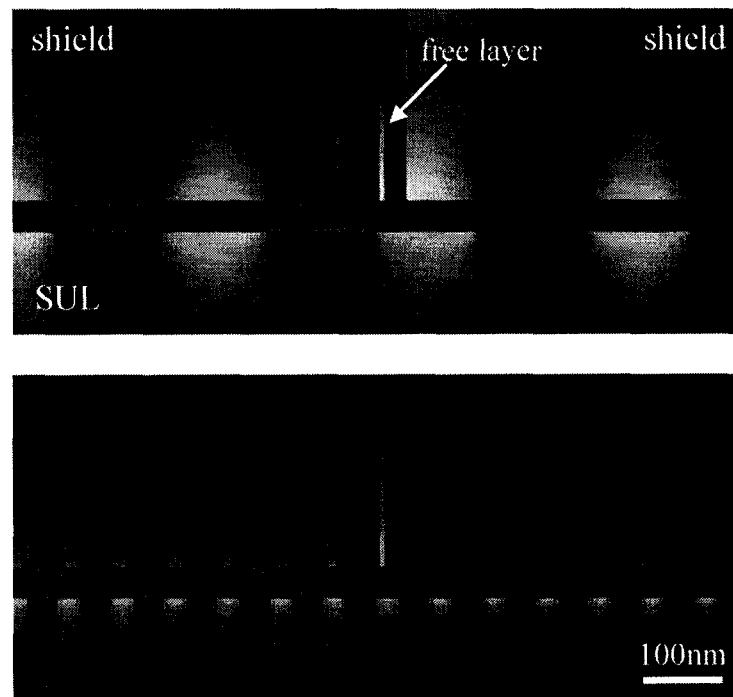


Figure 6.1: The magnetization states of the free layer, the shields, and the SUL, for linear densities of 212 kfc i (top) and 726 kfc i (bottom), respectively. The bright and dark contrasts represent the strength of the magnetization component upward and downward in the vertical direction, respectively. Both images are in the same length scale and gray scale. The medium layer is not shown.

and the bits are recorded, the SUL will be once again magnetized by the field arising from the medium magnetization. Those induced charges in the SUL will again alter the flux from the media into the free layer of the spin valve head during the readback. The flux pattern from the media depends on the linear density - the lower the density, the further the flux goes, whereas for high density bit patterns it is highly localized. The SUL magnetization state basically follows the flux pattern from the media and therefore, strongly depends on the linear density.

Figure 6.1 shows the magnetization states of the SUL, the soft magnetic shields, and the free layer, in the presence of the recorded all-‘1’ pattern in the

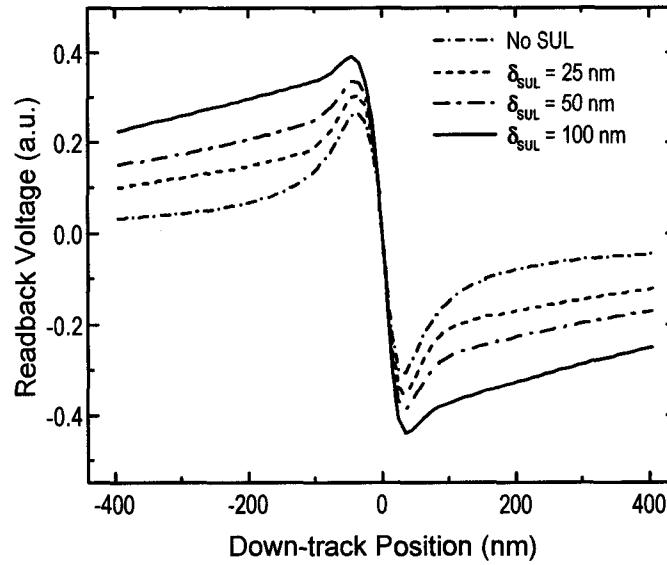


Figure 6.2: Transition response for different values of the SUL thickness. The saturation magnetization of the SUL is  $800 \text{ emu/cm}^3$ .

media, for two different linear densities. Obviously, the flux penetration depth, i.e., the depth through which the SUL is magnetized, is much larger for the low density bit pattern. This is true both underneath the medium (in the SUL) and above the medium (in the free layer). The effect of the SUL magnetization dependence on linear density will be discussed in more details later.

For perpendicular media, the media fringing field that the free layer of the spin valve reader senses can be considered as the sum of the field from the charges on the top surface of the medium and that from the bottom surface of the medium, the latter decreases the total field due to the opposite polarity of the charges. The magnetization of the SUL, to the first order approximation, is effectively doubling the thickness of the medium layer. Consequently, the contribution from the bottom surface charges will be less, as they are further away from the free layer. Therefore, the signal field will be increased. If either the SUL  $M_s$  or thickness is not sufficiently large, SUL saturation will occur.



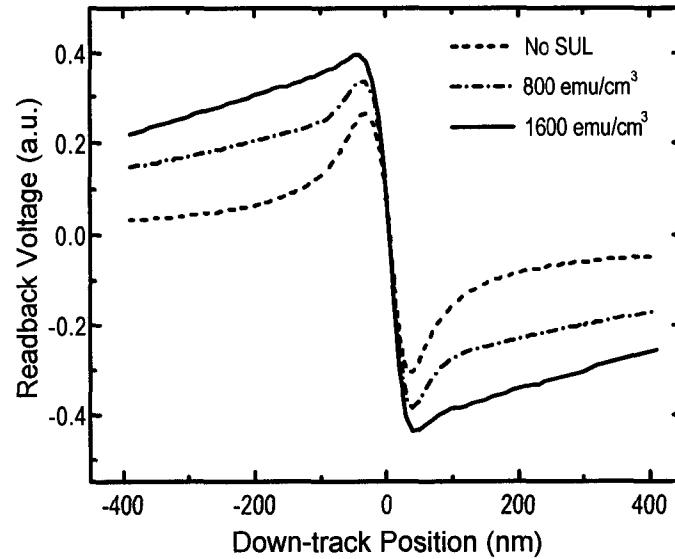


Figure 6.3: Transition response for different values of the SUL saturation magnetization. The thickness of the SUL is 100 nm.

This will reduce the imaging efficiency, same as in the writing process, and in turn reduce the readback signal amplitude.

Figure 6.2 shows the effect of the SUL thickness on the transition response, i.e., the readback waveform for an isolated transition, which is corresponding to the low density extreme. The result without SUL is also shown for comparison. It can be seen that not only does the amplitude of the readback signal increase with increasing SUL thickness, but its shape also changes - the tails of the transition response away from the transition center also become flattened, compared to the rapid drop in the case without SUL. The transition response converges beyond a certain SUL thickness, e.g., 100 nm in this case, at which a full imaging is reached without SUL saturation. Notice that the shape of the transition response still is not arctangent-like or error-function-like with perfectly flat tails, as the latter only occurs when the effective media thickness is infinite. The dependence of the transition response upon the  $M_s$  value of

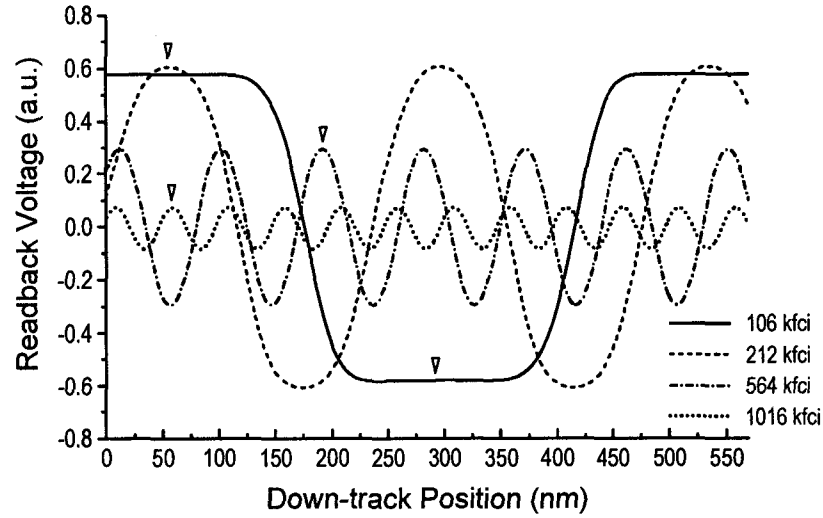


Figure 6.4: Examples of simulated readback waveform at different linear densities. The SUL thickness is 50 nm and  $M_s = 800 \text{ emu/cm}^3$ .

the SUL is shown in Figure 6.3. The same trend as for SUL thickness has been found. In any case, to reach a full imaging, sufficiently large SUL  $M_s$  and/or thickness are needed.

#### 6.4 High density readback rolloff and $-20\text{dB}$ -density $D_{20\text{dB}}$

In this section, we will discuss the simulation results of the readback waveform at different linear densities and compare the amplitude rolloff characteristics of the readback. Figure 6.4 shows the readback waveforms from all-‘1’ patterns for different linear densities. They are plotted together for ease of comparison. The readback voltage amplitude is measured at the center of the bits, i.e., half bit length from the transition center, at each linear density, as marked by the small triangles in the figure. It can be seen that the maximum readback amplitude actually does not occur at the lowest density, which is due to the non-flat tails of the transition response as mentioned earlier. This effect is much more pronounced for the media without SUL, as will be seen later.

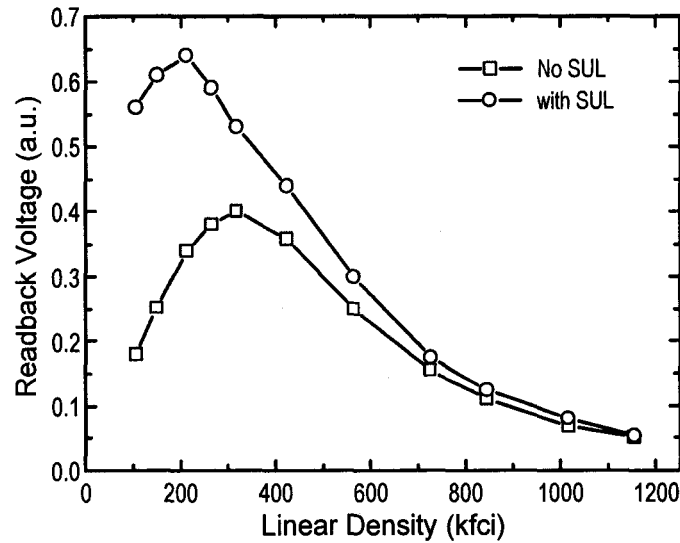


Figure 6.5: A comparison of the rolloff curves of the readback amplitude with linear density for the cases with and without SUL. The SUL thickness is 100 nm and  $M_s = 800 \text{ emu/cm}^3$ .

Figure 6.5 plots the readback voltage as a function of the linear density for the same medium with and without the SUL. In the presence of the SUL, a stronger signal amplitude is found at all densities. However, the signal amplification, i.e., the ratio of the voltage for the case with SUL to that without SUL, is dependent on the linear density. In fact, the readback signal enhancement is mainly at low densities and it drops very quickly with increasing linear density, as plotted in Figure 6.6. This is because at low density, the flux from the charges at the bottom of the hard layer propagates far away into the free layer, cancelling that from the top surface of the hard layer. The SUL imaging effect brings the bottom surface charges further down, thus reducing its contribution and increasing the total field that the reader senses. At high density, however, the flux already is very localized, at both the top surface and the bottom surface of the the hard layer, further bringing down the bottom surface charges only causes very little difference in the signal field at the free layer. The same

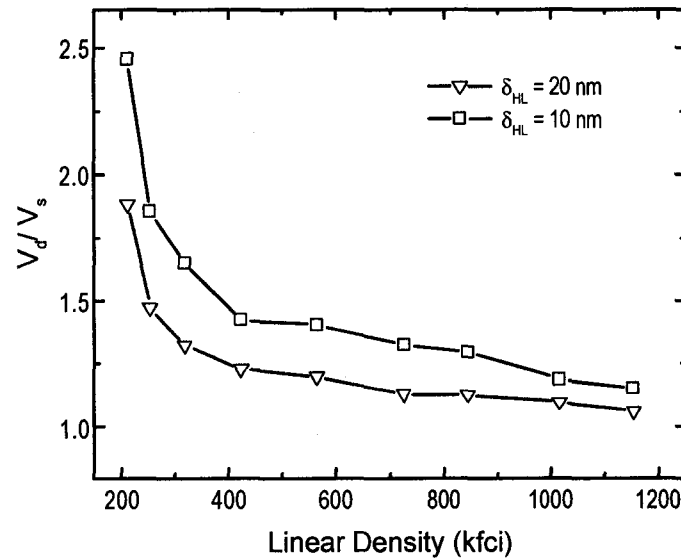


Figure 6.6: The ratio of the readback voltage with SUL,  $V_d$ , to that without SUL,  $V_s$ , as a function of the linear density for two medium thickness values.

argument directly leads to the conclusion that the signal enhancement is larger for a thin media than that for a thick media, as seen from Figure 6.6.

One of the issues associated with high density perpendicular recording is that, to maintain a sufficiently large signal for the maximum density, the signal corresponding to a low density (e.g., for those regions of some consecutive '0's where there is no transition over many bits.) will be very large and the free layer is often saturated, causing nonlinearity of the readback. Due to the linear density-dependent signal amplification just discussed, this problem will be exacerbated by the SUL. To address this issue quantitatively, it is more illustrative to normalize each of the rolloff curves in Figure 6.5 to the maximum signal power of its own, i.e., the square of the readback voltage, and assign that signal level to be one such that the free layer is not yet saturated. Having this set, there will be a minimum acceptable readback power,  $P_{min}$ , for a given noise power and signal-to-noise ratio requirement. The density corresponding to this minimum will be the density limit imposed by the rolloff characteristics

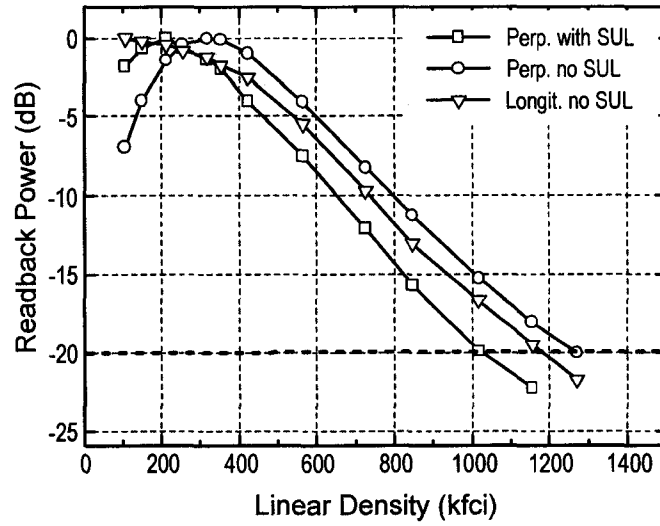


Figure 6.7: Normalized rolloff curves of the readback power with linear density for the cases with and without SUL. The rolloff curve for a longitudinal media is also shown.

of the system. To exactly determine  $P_{min}$ , an analysis of all the noise sources, i.e., medium noise, electronic noise, spin valve reader mag-noise and amplifier noise etc., will be required. Instead of doing that, without losing conceptual generality, we will take the density at which the readback power drops to 20 dB below the maximum, i.e., the voltage is 10% of the maximum, to be a figure of merit of the system performance in terms of the density limit. We will refer to this density as  $-20\text{dB-density}$ , or  $D_{20dB}$ , and use it as a key quantity in the rest of this chapter.

Figure 6.7 shows the normalized rolloff curves for the same data as in Figure 6.5. Clearly, the shallower the rolloff curve, i.e., the less difference between the signal amplitudes at high and low densities, the higher the  $D_{20dB}$ . Unfortunately, the existence of the SUL actually lowers  $D_{20dB}$ . This is consistent with the observation of the different signal enhancement for low and high density discussed above.

In the following sections, various parameters that affect  $D_{20dB}$  will be investigated in detail. Trade-offs between maximizing  $D_{20dB}$  and maximizing write field will be discussed.

### 6.5 $D_{20dB}$ maximization

From the previous section, it suggests that suppressing the SUL imaging effect should actually help increase  $D_{20dB}$ . In Figure 6.8 we plot the dependence of  $D_{20dB}$  on the SUL thickness.  $D_{20dB}$  increases by about 20% as the SUL thickness is reduced from 150 nm to 30 nm. One other reason for avoiding excessively thick SUL is that it is more likely to have complicated domains across the depth of the SUL [78]. Meanwhile, the onset of the write field magnitude reduction (so is the field gradient, not shown) occurs at the SUL thickness of about 30 nm. This indicates that the SUL thickness for the parameters in this case could be as small as 30 nm to maximize  $D_{20dB}$  without appreciable reduction of the write field magnitude and gradient. Similar examination on the effect of the SUL saturation magnetization,  $M_s$ , has also been performed and the result is shown in Figure 6.9. Unlike for the SUL thickness, the dependence of  $D_{20dB}$  on SUL  $M_s$  is much less sensitive; whereas the write field loss is fairly severe with decreasing SUL  $M_s$ . Therefore, given the same imaging capability, a thin layer of SUL with higher moment is preferable to a thick SUL layer with lower moment.

It has been reported that the domain walls in the SUL causes additional noise in the readback [79]. To suppress this noise, various approaches are being explored, including introducing an anisotropy field along the radial (cross-track) direction in the SUL, or using exchange biasing to create a single domain state in the SUL [80, 81, 82]. It is therefore necessary to know the effect of the

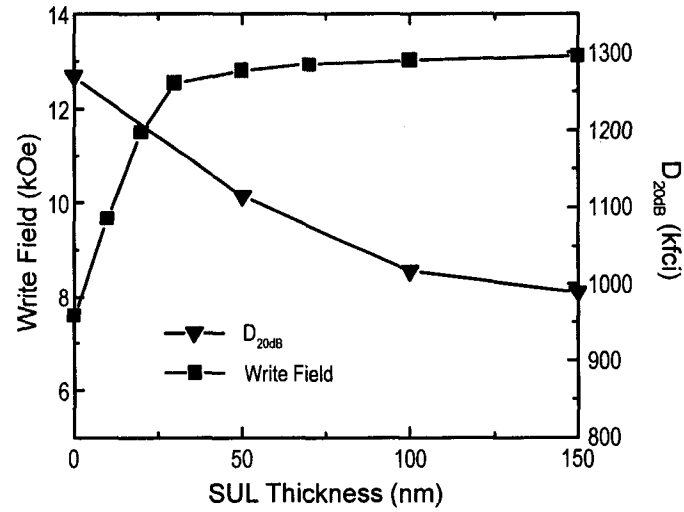


Figure 6.8: Dependence of  $D_{20dB}$  and the write field on the SUL thickness.

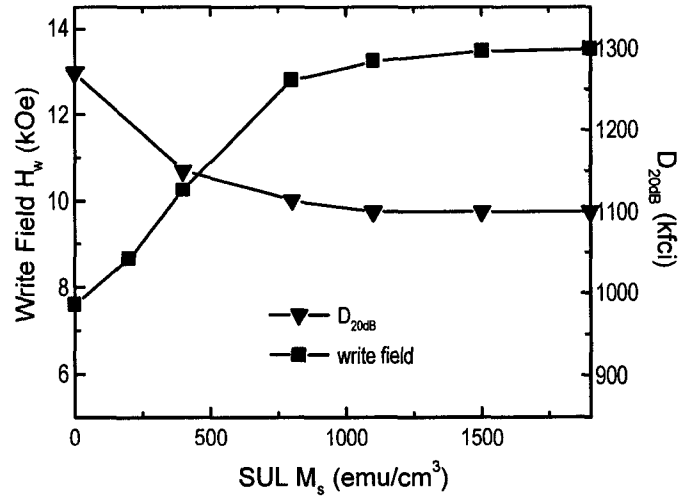


Figure 6.9: The dependence of  $D_{20dB}$  and write field on the SUL saturation magnetization.

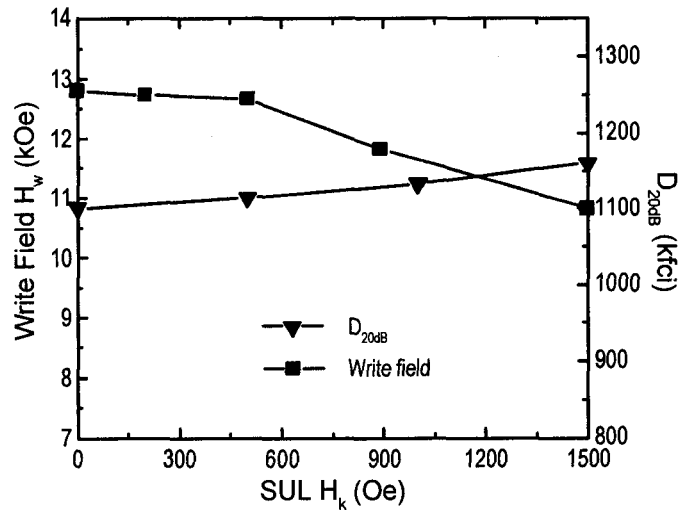


Figure 6.10: The dependence of  $D_{20dB}$  and write field on the anisotropy field of the SUL.

anisotropy field of the SUL on the write field and the readback. It can be seen from Figure 6.10 that the effect of the anisotropy field  $H_k$  of the SUL on the write field is marginal - an  $H_k$  up to 500 Oe causes only insignificant write field loss, since the imaging effect of the SUL is hardly affected. The reason is that the field from the write pole is usually several thousand Oersteds or more at the SUL, much larger than the in-plane anisotropy field. This is also true for the readback because the medium is much closer to the SUL than the writer, although the medium  $M_r$  is smaller than that of the write pole. As a result,  $D_{20dB}$  is also virtually independent of the SUL anisotropy - there is only 3% increase of  $D_{20dB}$  when SUL  $H_k$  increases from 0 Oe to 1000 Oe, as shown in Figure 6.10. This on the other hand suggests that a large SUL anisotropy up to several hundred Oersteds could be used to suppress SUL noise without sacrificing write field magnitude and  $D_{20dB}$ .

The next parameter we will examine is the thickness of the media (hard layer). Figure 6.11 shows the rolloff curves of the readback with SUL for different



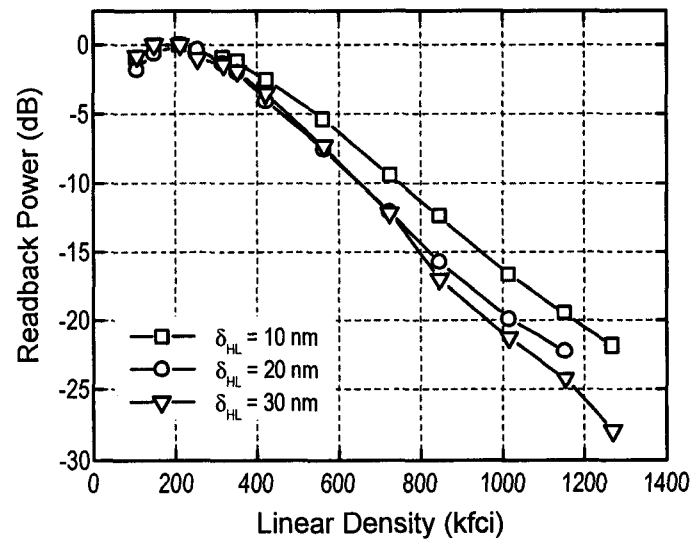


Figure 6.11: Rolloff curves of the readback power with linear density for different values of medium thickness.

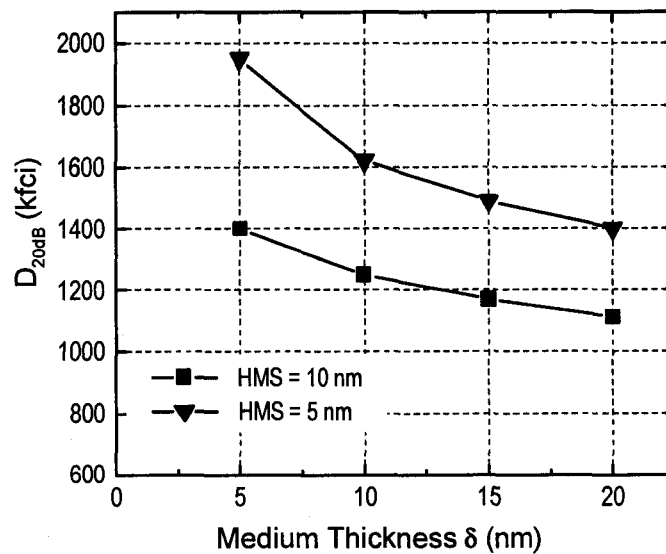


Figure 6.12: Dependence of  $D_{20dB}$  on the medium thickness and the head-medium magnetic spacing HMS.

thickness of the hard layer. Reducing the medium thickness is desirable both for write field due to the smaller head-to-SUL spacing (see Figure 4.30) and for  $D_{20dB}$ . The increase in  $D_{20dB}$  is significant only when the medium is very thin, as seen in Figure 6.12. Notice that the gain through reducing medium thickness should be constrained by the requirement of the medium thermal stability. Since the medium field decays much faster at high linear densities as the flux goes into the free layer, to maintain reasonable signal field at high density, it is essential to keep the head-medium magnetic spacing (HMS), the magnetic spacing from the head ABS to the top surface of the media layer, as small as possible. This is also desirable both for write field and for  $D_{20dB}$ . As evidenced from Figure 6.12, a reduction of HMS from 10 nm to 5 nm increases  $D_{20dB}$  dramatically.

One other important parameter is the reader gap, i.e., the shield-to-shield spacing (SSS) of the read head. It not only affects  $T_{50}$ , the width of the transition response curve at half of the peak magnitude (the counterpart of  $PW_{50}$  in longitudinal recording), therefore the readback resolution [75], but also plays a crucial role in determining  $D_{20dB}$ . As shown in Figure 6.13, for a medium thickness of 10 nm and HMS of 5 nm,  $D_{20dB}$  increases from 1550 kfc i to 2410 kfc i as the reader gap is decreased from 80 nm to 30 nm while a fixed stripe height-to-SSS ratio of 1.5 is maintained for each SSS value.

The explanation of the  $D_{20dB}$  dependence on SSS involves the examination of the signal flux propagation into the free layer of the spin valve reader, which will be discussed below together with the effect of the stripe height of the spin valve reader. Although reducing SSS is quite effective for increasing  $D_{20dB}$ , it may not be arbitrarily shrunk due to the multi-layer thin film structure of the spin valve head. Considering the flux from the medium magnetization that propagates into the free layer of the read head, for an isolated transition or very low density bit patterns, the flux propagation length into the free layer is

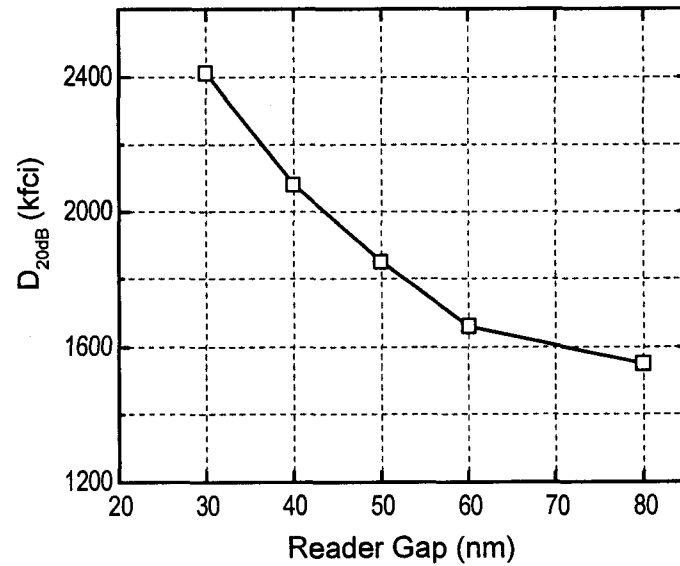


Figure 6.13: Dependence of  $D_{20dB}$  on the reader gap (SSS). The ratio of the stripe height to SSS is 1.5 for all SSS values. HMS = 5 nm, media thickness = 10 nm.

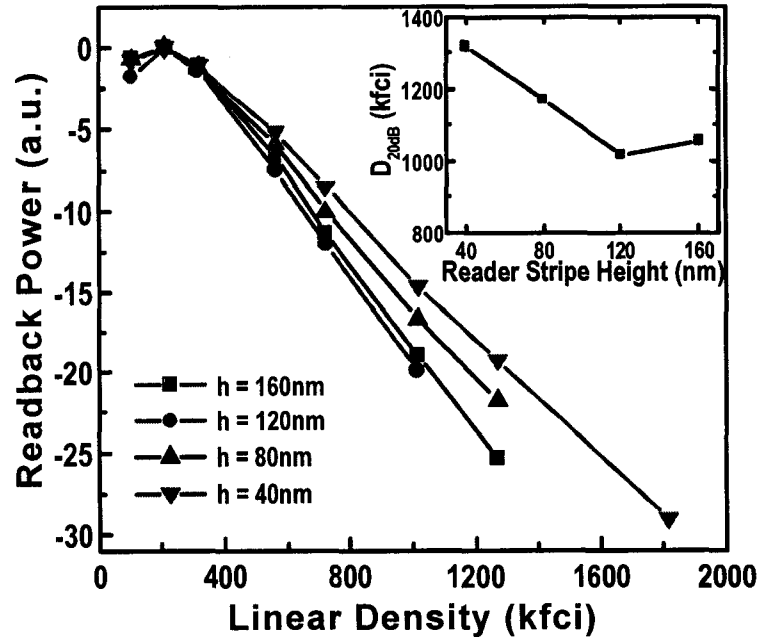


Figure 6.14: Normalized rolloff curves of the readback power with linear density for different spin valve reader stripe heights. The reader gap is 80 nm. Inset: dependence of  $D_{20dB}$  on the stripe height.

roughly the same as the SSS; whereas for high density bit patterns, the signal field decays much faster as it goes up into the free layer. The flux propagation length is defined as the distance from the ABS up to the point where the signal field drops to a certain value, e. g.,  $e^{-1} = 37\%$  of that at the ABS. Therefore, optimizing the stripe height for a given SSS should help increase  $D_{20dB}$ .

Figure 6.14 shows the rolloff curves for different stripe heights with same SSS of 80 nm. The inset of the figure shows  $D_{20dB}$  versus the stripe height. It is noticed that a stripe height of 120 nm yields the minimum  $D_{20dB}$ , namely, in this case, the ratio of the readback signal amplitude for low density to that for high density is maximum. This stripe height actually is approximately equal to the flux propagation length at the low-density limit. As the stripe height gets smaller, since the length over which the free layer magnetization is averaged becomes smaller, the high density readback voltage increases while that for low density does not increase or increases not as much, yielding an increase of the  $D_{20dB}$ . On the other hand, if the stripe height is too large, the low density readback voltage starts decreasing too, resulting in a slower rolloff thus a higher  $D_{20dB}$ , as shown in the inset of Figure 6.14.

Finally, Figure 6.15 shows the effect of the interlayer between the hard layer and the SUL on the write field and  $D_{20dB}$ , respectively. Increasing interlayer thickness from 0 nm to 15 nm does lead to a slight increase of  $D_{20dB}$  from 1100 kfc i to 1200 kfc i. This, however, is overwhelmed by the loss of the write field due to the increased head-to-SUL spacing. On the other hand, it has been shown that a larger interlayer thickness will yield a write field with larger in-plane component, which will reduce the medium switching field and make the medium magnetization switching faster [83]. Therefore, an optimization of the interlayer thickness might be done in practical systems design without significantly affecting  $D_{20dB}$ . In reality, it is actually not trivial

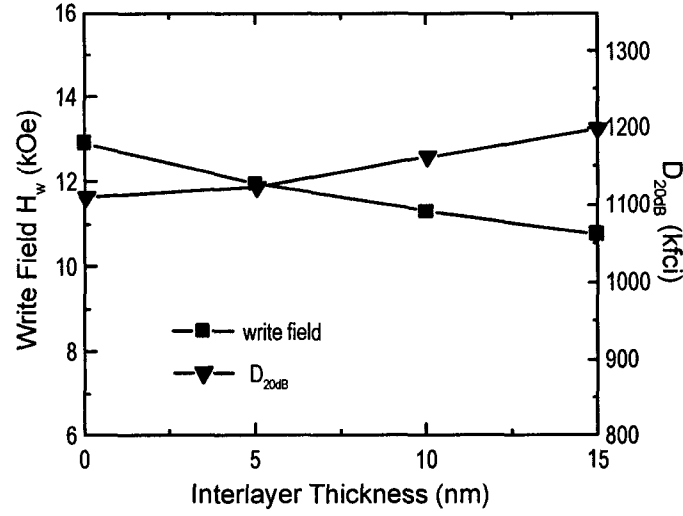


Figure 6.15: Dependence of  $D_{20dB}$  and the write field on the interlayer thickness.

to make the interlayer extremely thin (e.g., several nm) while still maintaining good magnetic properties of both the hard layer and the SUL. Therefore, the challenge today is still how to make the interlayer thinner.

## 6.6 Conclusions

In this chapter, we have studied the effect of the SUL on both the write and the readback process, using micromagnetic modeling. The magnetic imaging effect exists in both the write and the read process, the former is desirable for the write field, whereas the latter lowers the maximum achievable linear density. Reducing the saturation magnetization and/or the thickness of the SUL could increase  $D_{20dB}$ , but it is accompanied by the loss of the write field. In fact, most approaches for increasing  $D_{20dB}$  via making the SUL imaging less effective are accompanied by the tradeoff of the write field loss. A small head-medium spacing, a narrow reader gap with an optimized spin valve reader stripe height are found crucial for maximizing the  $D_{20dB}$ .  $D_{20dB}$  is not sensitive to SUL  $H_k$

and the interlayer thickness. A small medium thickness is desirable for both the write field and the  $D_{20dB}$ .

## 7 EFFECT OF STRESS IN MAGNETIC THIN FILMS

In this chapter, the effect of stress in magnetostrictive soft magnetic thin films, in particular, on the in-plane anisotropy, is studied. A theoretical derivation based on the expression of the magnetoelastic energy associated with the stress has been carried out. The easy axis directions and the effective anisotropy constants have been identified as functions of the stress, the magnetostriction coefficients of the material, and the growth texture of the film. The magnetoelastic energy has been combined into the existing micromagnetic model to take into account the effect of stress on thin film magnetization. Simulation of the micromagnetic states has been done on thin films with various materials, stress states, and growth textures. The resulting simulated static magnetic domain structures are in good agreement with the theoretical predictions. The extended model has also been used for the simulations of a conceptual perpendicular write head design, which utilizes an externally induced stress in the head material to help achieve better performance in terms of the write efficiency and cross-track field profiles.

### 7.1 Introduction

In a magnetic material with non-zero magnetostriction, stress could greatly affect the magnetic properties of the film through the coupling between the stress and the magnetization, which manifests itself through the magnetoelastic energy. Theoretical [84] and experimental [84, 85] studies have shown the stress induced perpendicular anisotropy, i. e., the easy axis is normal to the film plane, and consequently the stripe domains in soft magnetic thin films. These effects

have already been used to experimentally demonstrate a potential application in future magnetic random access memory (MRAM) devices [86, 87].

In general, on the bulk thin film level, the stress typically affects properties such as coercivity and permeability of the film [84]. Whereas at device level, the stress can directly affect the magnetization through the stress-induced anisotropy. This effect has been noticed in both magnetoresistive read heads [88] and in inductive write heads [89, 90] of a hard drive. In many real devices such as a recording head, instead of the perpendicular anisotropy, a particular in-plane anisotropy easy axis is often desired and it could be achieved by careful control of the stress [57].

The stress induced anisotropy depends not only on the magnitude and direction of the stress, but also on the magnetostriction coefficients of the materials, as well as the crystallographic growth texture of the film. In this chapter, the stress-induced in-plane anisotropy in soft magnetic thin films will be first derived in Section 7.2, based on an analytical analysis of the magnetoelastic energy. As far as micromagnetic models are concerned, those including the stress effect for recording media with hexagonal crystal structure have been developed previously [91, 92]. In Section 7.3, we will extend the micromagnetic model that we have been using to model the write heads to include the magnetoelastic effect for cubic structured soft magnetic materials with different crystallographic textures. In Section 7.4, using the extended micromagnetic model, we will present the simulation results of static magnetic domains in soft magnetic thin film elements under various combinations of stress, materials, and growth textures [93]. In Section 7.5, the model is used for the simulations of a conceptual perpendicular head design, which utilizes the stress-induced in-plane anisotropy to help improve the head performance [94]. Finally, Section 7.6 concludes the chapter.



## 7.2 Stress induced in-plane anisotropy: Analytical derivation

In this section, the stress induced in-plane anisotropy in a thin film will be derived analytically. The derivation is similar to that in [84]. Considered here is a soft magnetic polycrystal thin film with a cubic crystal structure and magnetostriction coefficients  $\lambda_{111}$  and  $\lambda_{100}$ . For a cubic structured single grain with uniform magnetization  $\mathbf{M}$  under a uniaxial stress  $\sigma$ , the magnetoelastic energy density is given by (for bi-axial stresses, the energy is simply the sum of the contributions from the two orthogonal stresses):

$$E_\sigma = -\frac{3}{2}\lambda_{100}\sigma (m_x^2\sigma_{x'}^2 + m_y^2\sigma_{y'}^2 + m_z^2\sigma_{z'}^2) - 3\lambda_{111}\sigma (m_x m_y \sigma_{x'} \sigma_{y'} + m_y m_z \sigma_{y'} \sigma_{z'} + m_z m_x \sigma_{z'} \sigma_{x'}) \quad (7.1)$$

where  $(m_{x'}, m_{y'}, m_{z'})$  and  $(\sigma_{x'}, \sigma_{y'}, \sigma_{z'})$  are the directions of  $\mathbf{M}$  and  $\sigma$ , respectively, both with respect to the three primary cubic crystal axes of the grain. In reality, however, the directions of the stress and the magnetization are usually known only with respect to the thin film and specifically, in the derivation here, both will be assumed in the plane. Therefore, two coordinate systems are needed, namely, the global system  $xyz$ , which is fixed to the film; and the local system,  $o'x'y'z'$ , which is local to each of the grains in the film, the latter with three Cartesian axes being  $[100]$ ,  $[010]$ , and  $[001]$  directions of the local crystal grain. It then follows that there will be  $N$  local coordinate systems to be described, because of the different crystallographic orientations, where  $N$  is the total number of grains in the thin film. Shown in Figure 7.1 is an illustration of the two coordinate systems as well as  $\mathbf{M}$  and  $\sigma$ .

In general, for the  $i^{th}$  grain, the two coordinate systems are related by the

following formula:

$$\begin{pmatrix} x \\ y \\ z \end{pmatrix} = A_i \begin{pmatrix} x' \\ y' \\ z' \end{pmatrix} = \begin{pmatrix} l_1 & m_1 & n_1 \\ l_2 & m_2 & n_2 \\ l_3 & m_3 & n_3 \end{pmatrix} \begin{pmatrix} x' \\ y' \\ z' \end{pmatrix} \quad (7.2)$$

and therefore,

$$\begin{pmatrix} x' \\ y' \\ z' \end{pmatrix} = A_i^{-1} \begin{pmatrix} x \\ y \\ z \end{pmatrix} \quad (7.3)$$

where  $A_i$  is the transformation matrix relating the coordinates of a vector in the system local to the  $i^{th}$  grain,  $(x', y', z')$ , to that in the global system,  $(x, y, z)$ . The elements of matrix  $A_i$  are defined as follows:

$$\begin{aligned} l_1 &= \cos \psi \cos \varphi - \cos \theta \sin \psi \sin \varphi \\ l_2 &= -\cos \psi \sin \varphi - \cos \theta \sin \psi \cos \varphi \\ l_3 &= \sin \theta \sin \psi \\ m_1 &= \sin \psi \cos \varphi + \cos \theta \cos \psi \sin \varphi \\ m_2 &= -\sin \psi \sin \varphi + \cos \theta \cos \psi \cos \varphi \\ m_3 &= -\sin \theta \cos \psi \\ n_1 &= \sin \theta \sin \varphi \\ n_2 &= \sin \theta \cos \varphi \\ n_3 &= \cos \theta \end{aligned} \quad (7.4)$$

where  $\theta$ ,  $\psi$ , and  $\varphi$  are the three Euler angles through which the coordinate basis  $o'x'y'z'$  is transformed into  $oxyz$ .

In order to find the stress induced anisotropy constant for a thin film under a stress, one needs an expression of the magnetoelastic energy density, averaged

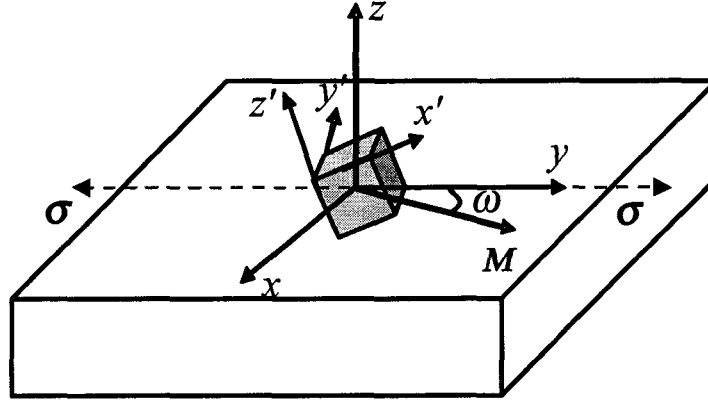


Figure 7.1: Illustration of the two coordinate systems.  $xyz$  is the global system that is fixed to the thin film, and  $x'y'z'$  is the coordinate system local to the grain. Also shown are the relative orientation of the stress and the magnetization of a grain in the thin film, both lying in the plane.

over all the grains, as a function of  $\omega$ , the angle between  $\mathbf{M}$  and  $\sigma$ . Without loss of generality,  $\sigma$  can be assumed in the direction of  $\hat{y}$ , as shown in Figure 7.1. Therefore, in the global coordinate system, the directions of  $\sigma$  and  $\mathbf{M}$  are given by:

$$\hat{\sigma} = (0, 1, 0) \quad (7.5)$$

and

$$\hat{\mathbf{m}} = (\sin \omega, \cos \omega, 0) \quad (7.6)$$

To apply Eq. (7.1),  $\mathbf{M}$  and  $\sigma$  are first transformed into the local systems using Eq. (7.3). For the  $i^{th}$  grain, we have:

$$\begin{pmatrix} m_{x'}^i \\ m_{y'}^i \\ m_{z'}^i \end{pmatrix} = \mathbf{A}_i^{-1} \begin{pmatrix} \sin \omega \\ \cos \omega \\ 0 \end{pmatrix} \quad (7.7)$$

and

$$\begin{pmatrix} \sigma_{x'}^i \\ \sigma_{y'}^i \\ \sigma_{z'}^i \end{pmatrix} = A_i^{-1} \begin{pmatrix} 0 \\ 1 \\ 0 \end{pmatrix} \quad (7.8)$$

Combining Eqs. (7.1), (7.4), (7.7), and 7.8 yields the magnetoelastic energy density of a grain,  $E_\sigma(\theta, \psi, \varphi, \omega)$ , which is a function of the crystal orientation angles of the grain and the angle between  $\mathbf{M}$  and  $\sigma$ , in addition to the magnitude of  $\sigma$  and the magnetostriction coefficients of the material. Finally, to get the average magnetoelastic energy density, one needs to average over all possible grain orientations within the constraints of the crystallographic textures (see Appendix D for details). The averaged magnetoelastic energy density will have the following form:

$$\langle E_\sigma \rangle = K_\sigma \sin^2 \omega + \text{const.} \quad (7.9)$$

This is exactly the expression of the energy density of a uniaxial anisotropy, where  $K_\sigma$  is the stress-induced in-plane anisotropy constant, which, from the above derivations, takes the values for different textures as listed in Table 7.1.

Clearly,  $K_\sigma$  is proportional to the product of  $\sigma$  and a linear combination of  $\lambda_{111}$  and  $\lambda_{100}$ . This means that to achieve same stress-induced anisotropy, lower stress is needed for a material with higher magnetostriction. It can also be seen that except for 100 texture,  $\lambda_{111}$  has more weight than  $\lambda_{100}$  in determining the strength of the anisotropy. In the case of  $\lambda_{111} = \lambda_{100} = \lambda$ , the anisotropy constant becomes:

$$K_\sigma = \frac{3}{2} \lambda \sigma \quad (7.10)$$

which is independent of the film textures. This is consistent with the result of an isotropic magnetostrictive material [95].

Also note that, depending on the sign of the stress (positive is tensile and

negative is compressive) as well as  $\lambda_{111}$  and  $\lambda_{100}$  of the material, which can also be either positive or negative, the value of  $K_\sigma$  in Eq. (7.9) could be either positive or negative. When  $K_\sigma > 0$ , the axis of the stress is the easy axis, whereas when  $K_\sigma < 0$ , Eq. (7.9) can be rewritten as:

$$\begin{aligned}
 \langle E_\sigma \rangle &= K_\sigma(1 - \cos^2 \omega) + \text{const.} \\
 &= -K_\sigma \cos^2 \omega + \text{const.} \\
 &= -K_\sigma \sin^2(90^\circ - \omega) + \text{const.} \\
 &= |K_\sigma| \sin^2(90^\circ - \omega) + \text{const.}
 \end{aligned} \tag{7.11}$$

which means that the direction orthogonal to the axis of the stress in the plane is the easy axis. In other words, changing the stress from tensile to compressive or vice versa while maintaining the magnitude of the stress will turn the easy axis to the perpendicular direction with equal magnitude of  $|K_\sigma|$ .

As an example, Table 7.1 also lists the values of the in-plane anisotropy constants  $K_\sigma$  for  $\text{Fe}_{65}\text{Co}_{35}$  alloy and Fe thin films, respectively, in unit of  $10^4 \text{ erg/cm}^3$  for a 1 GPa uniaxial tensile stress. The magnetostriction coefficients are  $\lambda_{111} = 103.7 \times 10^{-6}$  and  $\lambda_{100} = 17.5 \times 10^{-6}$  for  $\text{Fe}_{65}\text{Co}_{35}$ , and  $\lambda_{111} = -21 \times 10^{-6}$  and  $\lambda_{100} = 21 \times 10^{-6}$  for Fe.

### 7.3 Micromagnetic modeling

Based on the above analysis, we now combine the magnetoelastic energy term into the existing micromagnetic model to simulate the effect of stress on thin film magnetization. Here we have to deal with not only the discretization cells, but also the crystal grains. The crystallographic orientation of the crystallites are assigned according to the desired textures. Therefore, there is a unique coordinate transform matrix associated with each of the crystal grains throughout the entire film, as defined by Eqs. (7.4), (D.2), (D.4), or

Table 7.1: Effective in-plane anisotropy constants for different textures. The numbers in last two columns are the anisotropy constant values, in unit of  $10^4$  erg/cm<sup>3</sup>, for films under a 1 GPa stress.

Texture	$K_\sigma$	Fe <sub>65</sub> Co <sub>35</sub>	Fe
100	$\sigma \left( \frac{3}{4} \lambda_{111} + \frac{3}{4} \lambda_{100} \right)$	90.9	0
110	$\sigma \left( \frac{15}{16} \lambda_{111} + \frac{9}{16} \lambda_{100} \right)$	107	-7.9
111	$\sigma \left( \lambda_{111} + \frac{1}{2} \lambda_{100} \right)$	112	-10.5
Random	$\sigma \left( \frac{9}{10} \lambda_{111} + \frac{3}{5} \lambda_{100} \right)$	103	-6.3

(D.6). The stress and magnetization are first transformed into each of the individual local coordinate systems according to Eq. (7.3), in order to use Eq. (7.1).

### 7.3.1 Effective field due to magnetoelastic energy

We will now start with Eq. (7.1) and derive the effective field due to the magnetoelastic energy. Note that both  $\mathbf{M}$  and  $\sigma$  are now in the local coordinate system. The effective field can be obtained the same way as in Eq. (2.18):

$$\begin{aligned}
 \mathbf{H}_\sigma(\mathbf{r}_i) &= -\frac{\partial E_\sigma(\mathbf{r}_i)}{\partial \mathbf{M}_i} \\
 &= -\frac{\partial E_\sigma(\mathbf{r}_i)}{\partial M_{x'}^i} \hat{\mathbf{e}}_{x'}^i - \frac{\partial E_\sigma(\mathbf{r}_i)}{\partial M_{y'}^i} \hat{\mathbf{e}}_{y'}^i - \frac{\partial E_\sigma(\mathbf{r}_i)}{\partial M_{z'}^i} \hat{\mathbf{e}}_{z'}^i \\
 &= -\frac{1}{M_s} \frac{\partial E_\sigma(\mathbf{r}_i)}{\partial m_{x'}^i} \hat{\mathbf{e}}_{x'}^i - \frac{1}{M_s} \frac{\partial E_\sigma(\mathbf{r}_i)}{\partial m_{y'}^i} \hat{\mathbf{e}}_{y'}^i - \frac{1}{M_s} \frac{\partial E_\sigma(\mathbf{r}_i)}{\partial m_{z'}^i} \hat{\mathbf{e}}_{z'}^i, \quad (7.12)
 \end{aligned}$$

where  $\hat{\mathbf{e}}_{x'}^i$ ,  $\hat{\mathbf{e}}_{y'}^i$ , and  $\hat{\mathbf{e}}_{z'}^i$  are the three unit vectors of the coordinated system local to the  $i^{\text{th}}$  grain. Substituting Eq. (7.1) into Eq. (7.12) gives the three components of  $\mathbf{H}_\sigma(\mathbf{r}_i)$ , omitting the super/subscripts  $i$ :

$$\begin{aligned}
 H_{x'}^\sigma &= \frac{3}{2} \frac{\lambda_{100}\sigma}{M_s} (2m_{x'}\sigma_{x'}) + 3 \frac{\lambda_{111}\sigma}{M_s} (m_{y'}\sigma_{y'} + m_{z'}\sigma_{z'}) \sigma_{x'} \\
 H_{y'}^\sigma &= \frac{3}{2} \frac{\lambda_{100}\sigma}{M_s} (2m_{y'}\sigma_{y'}) + 3 \frac{\lambda_{111}\sigma}{M_s} (m_{z'}\sigma_{z'} + m_{x'}\sigma_{x'}) \sigma_{y'} \\
 H_{z'}^\sigma &= \frac{3}{2} \frac{\lambda_{100}\sigma}{M_s} (2m_{z'}\sigma_{z'}) + 3 \frac{\lambda_{111}\sigma}{M_s} (m_{x'}\sigma_{x'} + m_{y'}\sigma_{y'}) \sigma_{z'} \quad (7.13)
 \end{aligned}$$

So far the effect field due to the magnetoelastic energy has been calculated and expressed in the local coordinate systems. We can now use Eq. (7.2) to convert them back into the global system, and add it to the total effective field obtained from Eq. (2.19), which is defined in the global coordinate system. The rest of the work will be exactly the same as before, i.e., solving LLG equation to get the magnetization of the system.

In all cases, the stress is an input parameter to the model, which could be either from an ideal assumption, or from a distribution simulated by other models such as finite element models. The stress distribution could also be either static or varying with time.

### 7.3.2 Effect field of cubic anisotropy

Although there is a net contribution to the total perpendicular anisotropy from the crystal anisotropy constants  $K_1$  and  $K_2$  for textured films [84], the net in-plane crystal anisotropy, which is the average over all the grains randomly orientated in the plane, will be zero. Nevertheless, in some cases, the cubic crystal anisotropy still needs to be considered. For instance, for a small thin film element with very large grain size hence very few grains in it, the net crystal anisotropy may no longer be zero, and there will be large variation from one device to another [37]. Here we describe how the cubic anisotropy is taken into account in the micromagnetic model. When treating the cubic crystal anisotropy, the orientations of the individual grains need to be tracked, which needs exactly the same crystal orientation data, i.e., the coordinate transform matrices used for the magnetoelastic energy calculation. This is why we leave this topic till this section.

The energy density associated with a magnetization  $\mathbf{M}$  in a cubic crystal,

when only  $K_1$  is considered, is given by:

$$E_{cubicAni} = K_1 (m_x^2 m_{y'}^2 + m_{y'}^2 m_{z'}^2 + m_{z'}^2 m_x^2) \quad (7.14)$$

where  $(m_x, m_{x'}, m_{x'})$  is the direction of  $\mathbf{M}$  in the local coordinate system of the crystallite. The effective field due to the cubic anisotropy can then be obtained the same way as in Eq. (7.12), and the components are given by:

$$\begin{aligned} H_{cubicAni}(x') &= -H_k (m_{y'}^2 + m_{z'}^2) m_{x'} \\ H_{cubicAni}(y') &= -H_k (m_{z'}^2 + m_{x'}^2) m_{y'} \\ H_{cubicAni}(z') &= -H_k (m_{x'}^2 + m_{y'}^2) m_{z'} \end{aligned} \quad (7.15)$$

where  $H_k = 2K_1/M_s$  is the anisotropy field. Same as the case for the magnetoelastic energy, Eq. (7.15) will need to be transformed back to the global system, in order to add the field  $\mathbf{H}_{cubicAni}$  to other terms of the effective field.

#### 7.4 Thin film magnetization rearrangement under stress

In this section, we will apply the extended micromagnetic model with magnetoelastic energy included to simulate the domain structures of a thin film magnetic element. The effect of the stress, the magnetostriction of the material, the growth texture of the film will be discussed.

The thin film element simulated here is a  $1.28 \mu\text{m} \times 0.64 \mu\text{m}$  rectangle with a thickness of 80 nm. The discretization cells are chosen to be  $10 \text{ nm} \times 10 \text{ nm} \times 10 \text{ nm}$  cubes, each of which is also assumed to coincide with a crystal grain. The initial magnetization state is assumed to be two equal-sized antiparallel domains (top and bottom half) along the long axis separated by a  $180^\circ$  domain wall along the center line. The stress is assumed uniform in the film for all cases except Figure 7.4, and also remains unchanged throughout the simulation. The final



converged states of the domain configurations are therefore the static domains for the given stress states.

Figure 7.2 shows the simulated static magnetic domains of a  $\text{Fe}_{65}\text{Co}_{35}$  ( $M_s = 1930 \text{ emu/cm}^3$ ) thin film element under different stress states. When the film is stress-free, the magnetic domains are fully determined by minimizing the demagnetization energy, therefore forming the closure domain structure with four  $90^\circ$  domain walls and a  $180^\circ$  domain wall, with the two horizontal domains being the majority, as shown in Figure 7.2(a). With a 1 GPa uniform uniaxial tensile stress along the vertical direction, according to Table 7.1, the vertical direction will become the easy axis with  $K_\sigma = 1.1 \times 10^6 \text{ erg/cm}^3$ , and therefore an anisotropy field  $H_k = 2K_\sigma/M_s = 590 \text{ Oe}$ . This anisotropy field is strong enough to turn the major domains into the vertical direction, as seen in Figure 7.2(b). From Section 7.2 we learned that, a 1 GPa uniform compressive stress along the horizontal direction should have the same effect as in Figure 7.2(b), and this is confirmed by the simulated domain configurations in Figure 7.2(c). As shown in Table 7.1, the effect of texture is not significant on the stress induced anisotropy for  $\text{Fe}_{65}\text{Co}_{35}$ . This is confirmed by the simulation as well, as the same domain structures are observed on all textures, including the random texture, under the same stress. As an example, Figure 7.2(d) shows the result of a random-textured film, which is almost identical to that in Figure 7.2(b) for 111 texture.

The situation for Fe is, however, quite different, due to the different magnetostriction coefficients, as seen in Table 7.1. The negative sign of  $K_\sigma$  indicates that the easy axis lies along the direction orthogonal to that for  $\text{Fe}_{65}\text{Co}_{35}$  for the same stress. The magnitude of  $K_\sigma$  is also much smaller. Therefore, to see the same effect on the domains, a much higher stress is needed. Figure 7.2(a) shows the simulation results for Fe with 110 texture, the domains show an easy

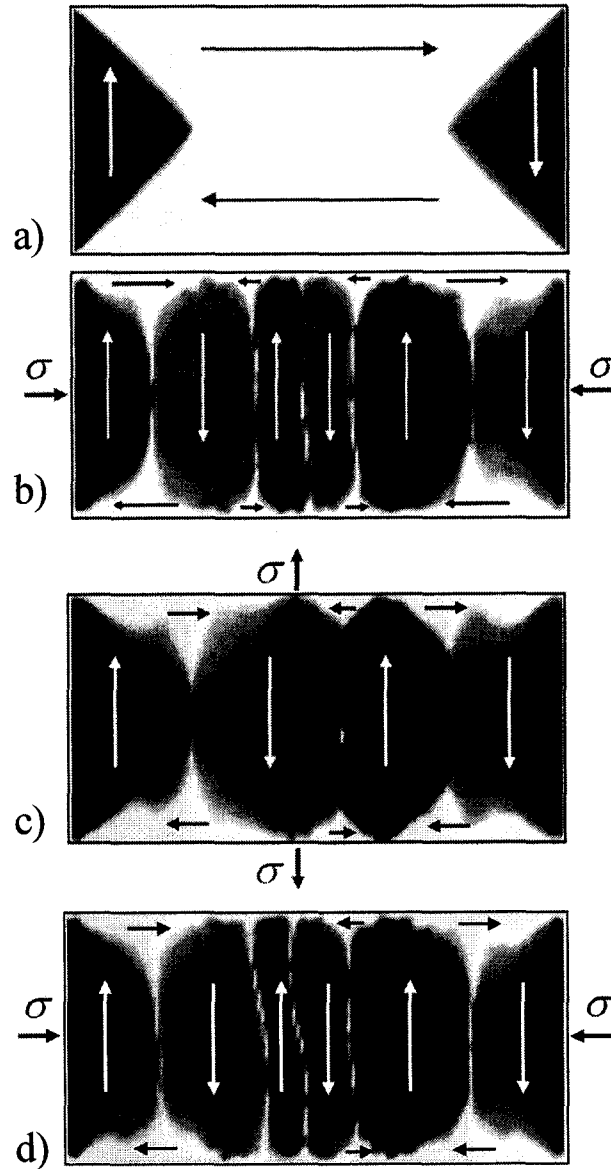


Figure 7.2: The micromagnetic simulation results of the magnetic domains of a  $\text{Fe}_{65}\text{Co}_{35}$  thin film element. From top to bottom: a) stress-free; b) horizontal compressive stress; c) vertical tensile stress; and d) horizontal compressive stress. The magnitude of the stress is all 1 GPa. The film textures are 111 for a) - c) and random for d).

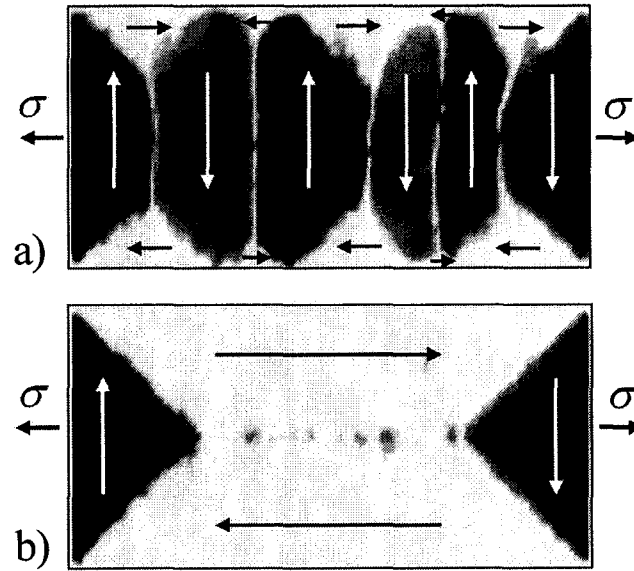


Figure 7.3: The simulated magnetic domains of a Fe thin film element undergoing a 5 GPa uniaxial horizontal tensile stress for a) 110 texture and b) 100 texture, respectively.

axis along the short axis, same as that of Figure 7.2(b) and (d), as expected. In contrast, the domains shown in Figure 7.2b) for Fe with 100 texture clearly indicates no anisotropy effect, which is consistent with the results in Table 7.1.

When an equal biaxial stress exists in the film, the effective in-plane anisotropy is zero. For positive magnetostriction, a biaxial tensile stress makes the film plane an easy plane, whereas a biaxial compressive stress will turn it to a hard plane and the film normal to an easy axis. However, if the stresses along the two perpendicular directions are not equal, the effective anisotropy easy axis will be along that of the stronger one, with the magnitude being the difference of the two [95]. Figure 7.4 shows the magnetization pattern of a  $\text{Fe}_{65}\text{Co}_{35}$  film element on a silicon substrate with a 0.6% uniform strain. The stresses are obtained from a finite element simulation using FEMLAB, which are compressive with mean values of  $-790$  MPa along the long axis and  $-520$  MPa along the

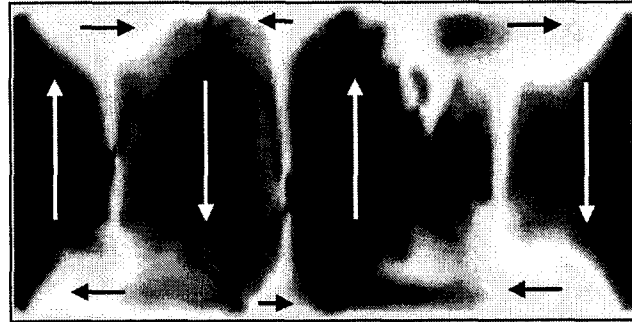


Figure 7.4: The simulated magnetic domains of a  $\text{Fe}_{65}\text{Co}_{35}$  thin film element on a silicon substrate with a uniform strain of 0.6%. The stress distribution was obtained from FEMLAB simulations.

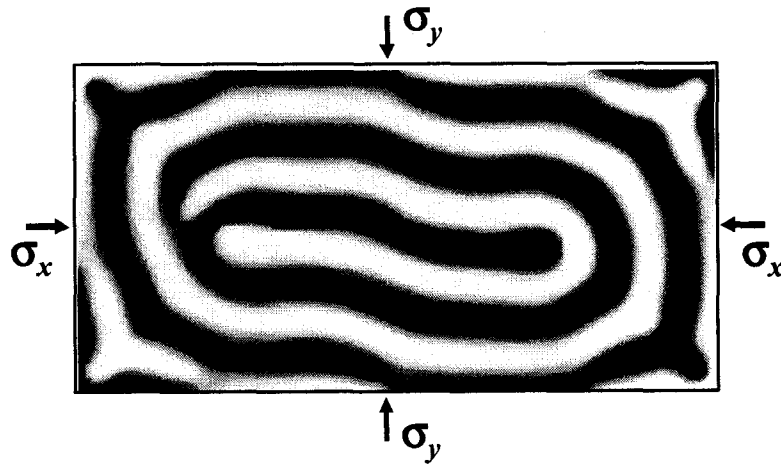


Figure 7.5: The simulated magnetic domains of a  $\text{Fe}_{65}\text{Co}_{35}$  thin film element under a 1 GPa biaxial compressive stress. The contrast represents the magnetization component normal to the film plane.

short axis. As a result, there is a net easy axis along the short axis direction. The relatively irregular shape of the domains is due to the non-uniformity of the stress, and the less volume of the majority domains is due to the lower stress therefore weaker anisotropy.

Although the main interest here is the in-plane anisotropy, the micromagnetic model based on magnetoelastic energy is not limited to only in-plane anisotropy. In fact, the maze-like stripe domains representative of perpendicular anisotropy were also seen from the simulation results for  $\text{Fe}_{65}\text{Co}_{35}$  film elements with equal biaxial compressive stress, as shown in Figure 7.5, consistent with the experimental observations [85].

### 7.5 Conceptual design of a voltage-assisted magnetostrictive perpendicular write head

In this section, we will present the study of a conceptual perpendicular write head design using the extended micromagnetic model. The design utilizes the stress-induced in-plane anisotropy effect to achieve better performance.

Conventional recording heads are purely driven by electrical current and it is necessary that the magnetic materials of the yoke and the pole tip are sufficiently soft to ensure high write efficiency. However, high moment magnetic materials such as  $\text{Fe}_{65}\text{Co}_{35}$  have relatively large magnetostriction, which, coupled with the residual stress in the head, could significantly reduce the write efficiency. The demand of large write field at high density perpendicular recording often requires large write current, causing a lot of issues such as power consumption, head protrusion *etc.*. Furthermore, such a high on-track head field often is accompanied by a high off-track field, which may cause adjacent track erasure problem.

It has been suggested that a perpendicular recording head with a high uniaxial anisotropy in the pole tip along the flux conduction direction can produce high field gradient in the cross-track direction [96]. However, no mechanism of how the anisotropy field can be introduced was given in [96], and more importantly, there will be very severe remanent head field in this head, and the head field reversal will also be very slow.

In the conceptual head design we propose here, the above issues can be avoided while higher write efficiency and better cross-track field profile could be achieved. The next section will discuss the head design.

#### 7.5.1 The head design

Figure 7.6 shows a schematic of the proposed head design. Here we consider a single pole perpendicular write head. Electrodes are placed on both sides of the head yoke and the pole tip and are separated with the latter by a gap that is filled with an electrostrictive material. An alternating voltage, which is synchronized with the write current, is applied across the electrostrictive material to create a stress in the head yoke and pole tip along the cross-track direction. Considering that the magnetostriction coefficient of  $\text{Fe}_{65}\text{Co}_{35}$  is positive, a compressive stress will induce an anisotropy with an easy plane formed by the direction perpendicular to the ABS and the direction down the track ( $x$ - $y$  plane). Due to the thin-film structure of the head, the magnetization will be mostly in the film plane (normal to  $x$  direction), thus the direction perpendicular to ABS, i.e., the flux conduction direction, will be the easy axis.

If a sufficiently large stress ( $\sigma_{max}$  in Figure 7.6) is applied following the rise of the write current, the induced anisotropy will significantly enforce the perpendicular magnetization in the pole tip, as illustrated in Figure 7.7.

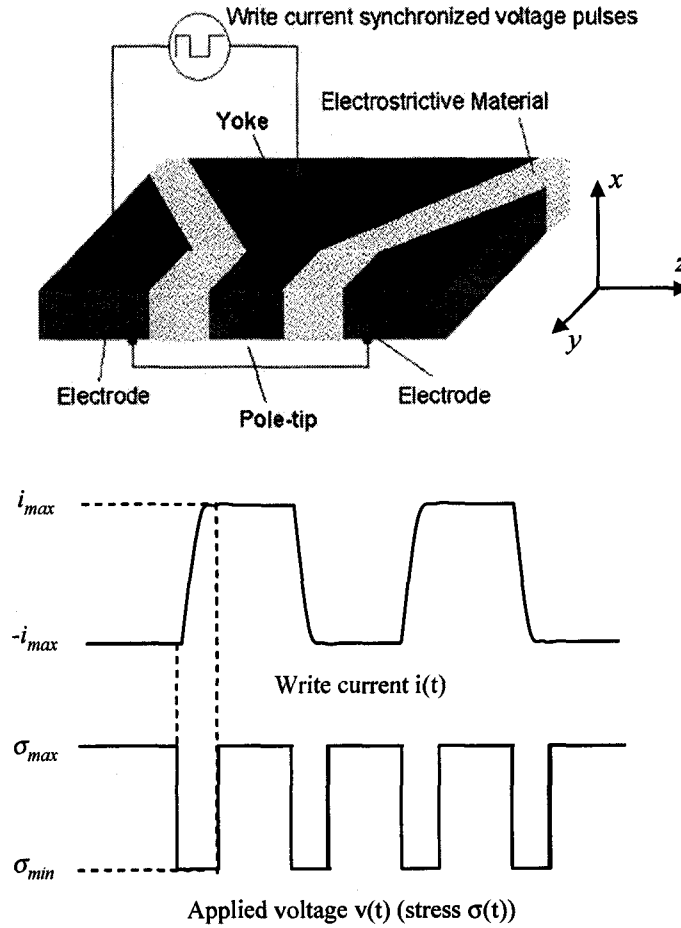


Figure 7.6: Schematic of the voltage-assisted perpendicular write head design (top) and the drive current and voltage waveforms (bottom).

The stress is either released or turned to a tensile one prior to the next current reversal by turning the applied voltage to zero or opposite polarity, to essentially turn the anisotropy off or to  $z$  direction, which used to pin the magnetization in  $y$  direction during the writing. Basically, the stress-induced anisotropy is tuned dynamically in synchronization with the write current, thus solving the difficulty encountered by the fixed anisotropy in [96]. The ideal stress waveform synchronized with the write current waveform is sketched in Figure 7.6. The minimum stress,  $\sigma_{min}$ , can be negative in sign, corresponding

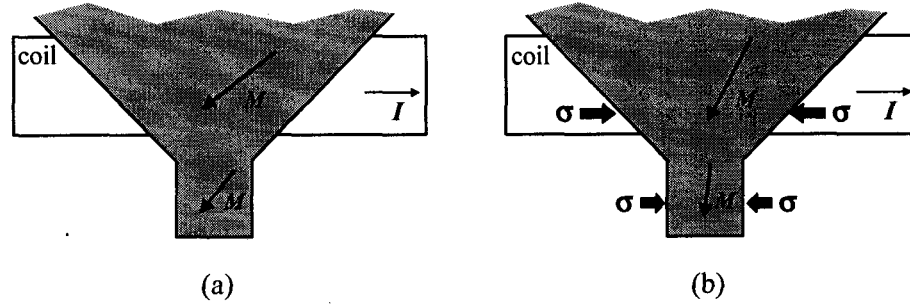


Figure 7.7: Illustration of the head operating mechanism. An application of a lateral stress on the yoke and the pole tip yields a stress-induced anisotropy to assist the magnetization in the perpendicular direction.

to a tensile stress, for assisting the head magnetization reversal, whereas the maximum stress,  $\sigma_{max}$ , is positive, corresponding to a compressive stress, which enforces the reversed magnetization in the direction perpendicular to the ABS.

### 7.5.2 Micromagnetic modeling analysis

In this section, the performance of the proposed head design is analyzed via micromagnetic modeling using the extended model with the magnetoelastic energy term. The model still solves the LLG equation, therefore, it is still a dynamic model. The modeled head yoke has a flare angle of  $45^\circ$ , a thickness of 80 nm, and a total length from the ABS to the back of the yoke of  $0.64 \mu\text{m}$ . The infinitely permeable boundary condition was taken at the back of the yoke to assume an ideal flux return path. The pole tip has a physical track width of 80 nm and its throat height is varied. The head material is  $\text{Fe}_{65}\text{Co}_{35}$  with  $M_s = 1930 \text{ emu/cm}^3$  and magnetostriction coefficients  $\lambda_{111} = 103.7 \times 10^{-6}$  and  $\lambda_{100} = 17.5 \times 10^{-6}$ . The entire head is discretized into cubic cells of  $10 \text{ nm} \times 10 \text{ nm} \times 10 \text{ nm}$  size. Each cell represents a single crystallite and random crystal orientation is assumed from cell to cell. The Gilbert damping constant  $\alpha = 0.02$  is used in the simulation. An ideal SUL was assumed in the simulation by



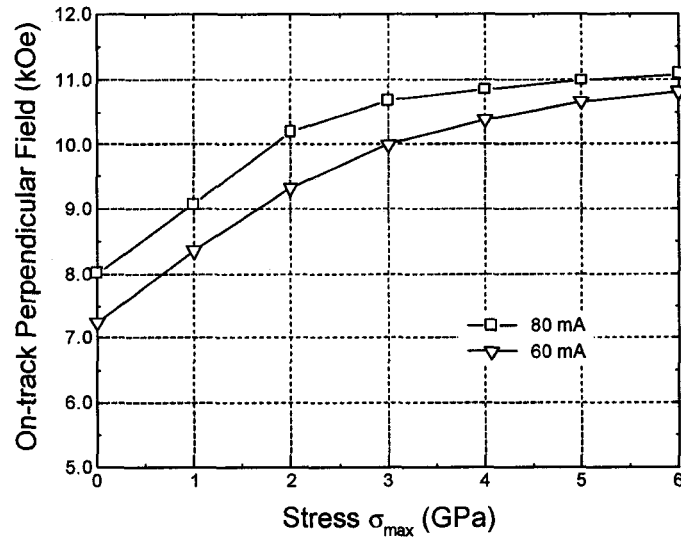


Figure 7.8: Simulated on-track maximum head field as a function of the applied stress to both the yoke and the pole-tip. A throat height of 100 nm was assumed.

taking the imaging effect of it. The ABS-to-SUL separation is 20 nm. The head field is measured at a distance of 15 nm away from the ABS. The modeled head is driven by a single-turn coil.

Figure 7.8 shows the calculated on-track perpendicular head field as a function of the amplitude of the stress  $\sigma_{max}$  for two write current values. A field increase of 35% can be measured at a stress level of 3 GPa compared to the zero-stress case for a drive current of 80 mA. Figure 7.9 shows the on-track head field as a function of the write current amplitude for  $\sigma_{max} = 3$  GPa. At this stress level, the maximum head field is reached at 1/3 of the write current for the zero-stress case. This means that the write current can be reduced by a factor of three and therefore, the power dissipation in the write coil can be reduced by nearly one order of magnitude.

With a 3 GPa lateral compressive stress, the magnetization in the head is better confined along the perpendicular direction. Consequently, the field gradient along the cross-track direction is improved. Figure 7.10 shows two

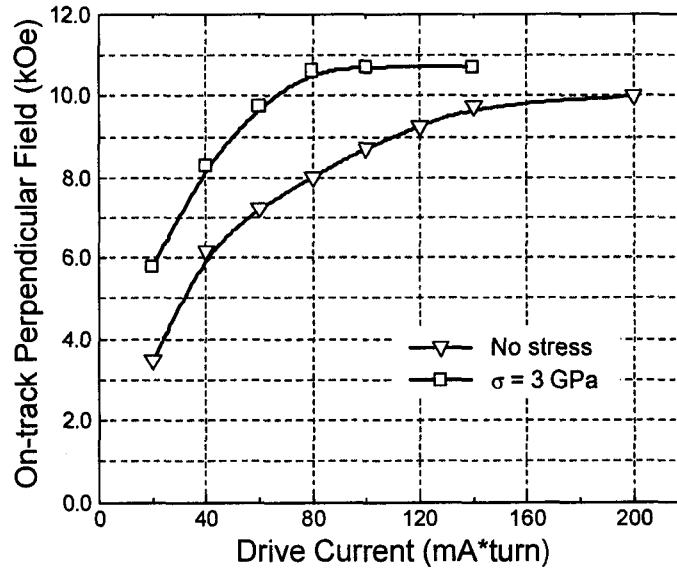


Figure 7.9: Simulated on-track maximum head field as a function of the write current amplitude for a stress amplitude of 3 GPa and zero, respectively.

simulated cross-track field profiles with and without the stress. In the case without the stress, a much larger current amplitude is used to obtain the same on-track field magnitude as that of the case with the stress. At one (physical) track width off the track center, the field magnitude in the case with the stress is about 25% lower than that without.

Figure 7.11 shows an alternative way to improve the cross-track field gradient. The enhancement of the write efficiency through the assistance of stress allows the use of a longer throat height to improve the cross-track field gradient while maintaining the same on-track head field magnitude.

It has also been found that an anisotropy easy axis transverse to the flux conduction direction during the magnetization reversal is very important. It will assist the switching of the magnetization of the yoke and the pole tip, resulting in a rapid reversal. This is crucial in this head design, since if there is still a significant portion of the reversed domain in the yoke by the time of  $\sigma_{max}$

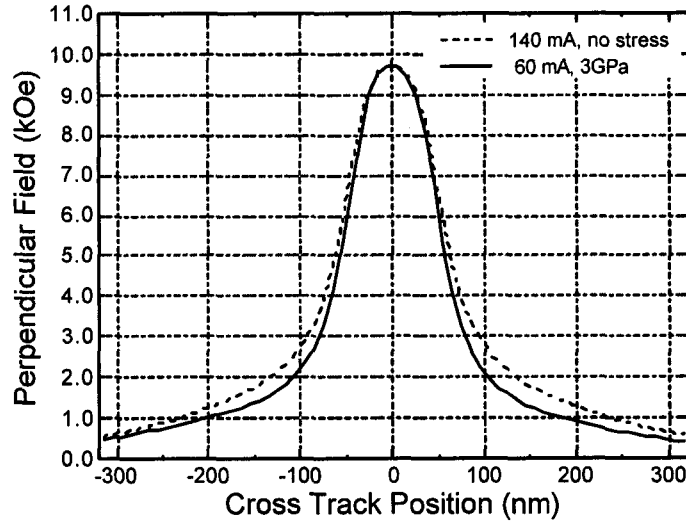


Figure 7.10: Cross-track field profiles of the head with and without stress assist. In the case without stress, the write current is raised so that the two cases have the same on-track field magnitude.

is applied, that portion will be pinned in the direction opposite to the desired direction, yielding much lower field magnitude. This effect is shown in Figure 7.12, the waveform of the dynamic on-track field at a data rate of 1 Gbit/sec. In both cases, a 3 GPa lateral stress is maintained in the bit interval other than the transition period. Clearly, a transverse anisotropy is necessary during the magnetization reversal in this head. This could be achieved by either turning the voltage to the opposite polarity (therefore turn the stress-induced anisotropy easy axis by  $90^\circ$ ) or by a built-in tensile stress in the yoke and the pole-tip introduced in the head fabrication process.

### 7.5.3 Summary and remarks

Using micromagnetic modeling with stress-induced magnetoelastic energy considered, we have investigated a conceptual perpendicular write head design, and shown that with the assistance of the stress-induced anisotropy, better write

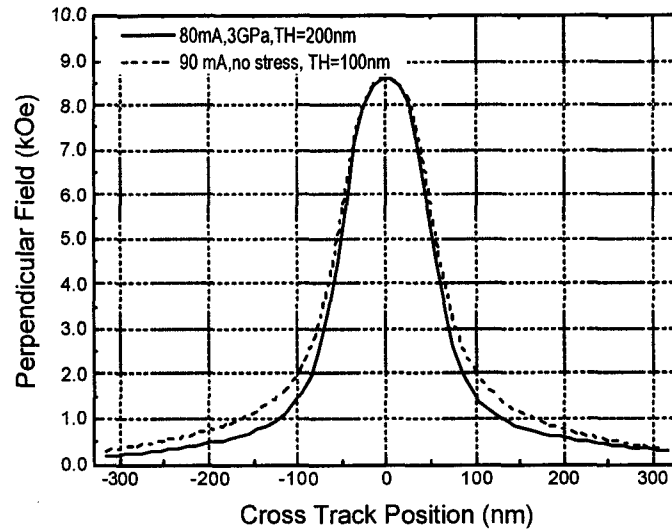


Figure 7.11: Cross-track field profiles of the head with and without stress assist. Similar current amplitudes were used for the two cases. In the 3 GPa stress case, the throat height is doubled to obtain a sharper cross-track field gradient while achieving the same on-track field magnitude as in the zero-stress case.

efficiency and cross-track field gradient can be achieved.

On the other hand, as a conceptual design, we have been focusing on the core of the phenomenon, which is whether a stress-induced anisotropy can bring some improvements to a perpendicular write head's performance. Therefore, the assumption we have taken is that such a stress can be introduced in the head at the desired frequency, which itself needs more validation. There are other aspects to be noticed as well. Just to name a few:

1. The selection of the electrostrictive material and the voltage needed to create a sufficiently high stress in the head magnetic material.
2. The stress needed in the case we modeled is about 3 GPa, which is fairly high. This stress, although might be within the strength of a thin film, which could be as high as an order of magnitude higher than that of the bulk [97], it remains a question whether it will cause other structural

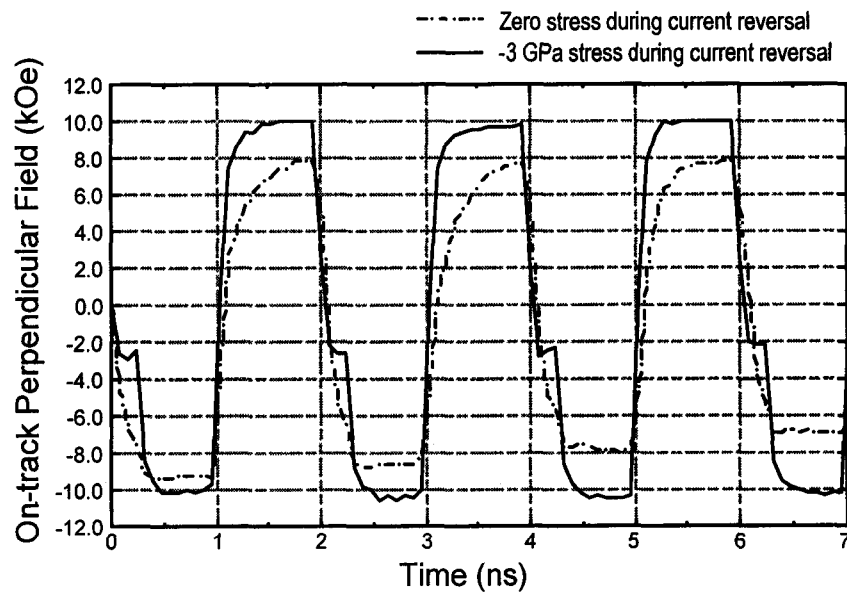


Figure 7.12: Simulated on-track field waveform at 1 Gbit/sec data rate. At each write current transition, the applied lateral stress is changed from +3 GPa to zero(dash-dot line) or -3 GPa (solid line) over a duration of 200 ps. Away from the transitions, a +3 GPa stress is maintained.

failure such as a delamination. Another solution to this issue might be to engineer the high moment head material so that higher magnetostriction could be obtained, hence lowering the stress required.

3. The dynamic response of the mechanic system, the heterostructure of the head, the electrostrictive material, and the leads *etc.*, to the applied voltage, has not been simulated. It is therefore an open question whether a stress cycling at a rate of 1 GHz or higher can be achieved in such a system. A very simple estimation could be made though. The dynamic mechanical relaxation process basically is governed by the acoustic wave propagation in the solid. Therefore, the order of magnitude of the relaxation time should be the dimension of the device, which is at the order of a fraction of a micron, divided by the speed of sound in the solid, which is typically

a few thousand m/s, yielding a time scale at the order of a fraction of a nanosecond. This is at the same order of the time scale of interest. Therefore, it is hard to conclude without further dynamic modeling of the stress/strain relaxation of the mechanical system of thin film solids.

4. There is actually a feedback to the stress due to the change of the magnetization in the head through the magnetostriction effect, which should be considered and added to the externally induced stress, but it was neglected in the model. The validity of this treatment will be discussed in detail in Chapter 8.

## 7.6 Conclusions

In this chapter, we have first derived the expression of the stress-induced in-plane anisotropy in a soft magnetic thin film, based on the the magnetoelastic energy. The easy axis directions and the effective anisotropy constants have been identified as functions of the stress, the magnetostriction coefficients of the material, and the growth texture of the film. The magnetoelastic energy has also been combined into the existing micromagnetic model to enable the simulations of thin film magnetization with the effect of the stress taken into account.

The extended micromagnetic model has been used to simulate thin films with various materials, stress states, and growth textures. The resulting simulated static magnetic domain structures are in good agreement with the theoretical predictions and experimental measurements.

A conceptual perpendicular write head design, which utilizes an externally induced stress in the head material, has been investigated using the extended micromagnetic model with the stress effect. With sufficiently high stress, the

new head design shows much improved write efficiency and cross-track field gradient, both are very important for high density perpendicular write heads.

## 8 MAGNETOELASTIC RELAXATION OF MAGNETIC THIN FILMS

In last chapter, we have extended the micromagnetic model to incorporate the effect of stress on magnetization, where we have assumed that the stress, either induced externally, or intrinsic in the film due to thermal expansion *etc.*, remains unchanged independent of the magnetization evolution. In reality, the inverse effect exists simultaneously in the material, which is the magnetostriction effect, in other words, the strain caused by the magnetization states.

Nevertheless, a simple orders-of-magnitude estimate could be made before actually doing simulation studies. Let us again take  $\text{Fe}_{65}\text{Co}_{35}$  as the example. The strain intrinsically associated with the magnetization states should be on the same order of the magnetostriction coefficient of the material,  $\lambda_{111} = 103.7 \times 10^{-6}$  and  $\lambda_{100} = 17.5 \times 10^{-6}$ , taking the larger one gives a strain at the order of  $10^{-4}$ . The Young's modulus of the FeCo alloy, assuming same order of magnitude as steel, is about 200 GPa. Therefore, the stress due to the magnetostriction should be  $10^{-4} \times 200 \text{ GPa} \simeq 2 \times 10^{-2} \text{ GPa}$ . Notice that the stress level needed for a significant anisotropy is at the order of 1 GPa (Chapter 7). This suggests that the stress due to the intrinsic magnetostriction can be neglected when dealing with the stress-induced anisotropy where a much higher stress is being considered.

Although the simple estimate above suggests that the magnetostriction is not significant in the particular application of the stress-induced anisotropy in the new head design. It needs further proof through more sophisticated analysis or modeling. Furthermore, there might be other circumstances where the



magnetostriction associated with the magnetization configuration in a thin film is of interest. Therefore, in this chapter, we will try to develop a model that can solve for the magnetization and the stress-strain states self-consistently. Qualitative description of the behavior of the stress and strain has been given in [95] for a thin film with a given domain structure. A theoretical derivation of the magnetostriction in a cubic single crystal can be found in [98], in which the magnetoelastic energy and the elastic energy are both considered simultaneously, and the energy minimum is solved analytically to give the solution of the magnetostriction. In this chapter, we will construct a model that takes into account not only the magnetic energy (magnetostatic, anisotropy, exchange, and Zeeman energy if there is an external field), but also the magnetoelastic energy and the elastic energy, in order to solve for the equilibrium state magnetization and the strain-stress state in a self-consistent manner for magnetic thin films.

In section 8.1 we will present the model. Section 8.2 shows some simulation results using the model. Section 8.3 summarizes the chapter.

### 8.1 Model construction/Derivation

In this section, we will show the construction of the model and the derivation of different terms of the energies and the effective forces.

Considered here is a magnetic thin film element, which is discretized into cubic cells with typical size of  $10\text{ nm} \times 10\text{ nm} \times 10\text{ nm}$ . Since not only the magnetic, but also the magnetoelastic and pure elastic energy are considered, the mesh cells are treated to be also the crystal grains. Furthermore, since what are to be solved now include both the magnetization and the stress-strain distribution, the variables needed now include not only the magnetization of each mesh cell, but also the displacement of the cell boundaries in both  $x$  and  $y$  directions in

the film plane, with which the stress and strain are defined.

To make the problem reasonably manageable, certain assumptions need to be made. Here the problem is assumed to be a plane-stress case, which is a condition that prevails in a flat plane in the  $x$ - $y$  plane, loaded in its own plane and without  $z$ -direction restraint [99]. Since there is no constraint in the  $z$ -direction, the only boundary conditions to be set are the boundaries of the planar film, which could be either constrained or unconstrained, and the model is therefore a 2-D model. The thin film structure to be modeled is discretized into  $N_x$  cells, for  $i = 1, \dots, N_x$ , in  $x$ -direction and  $N_y$  cells in  $y$ -direction, for  $j = 1, \dots, N_y$ .

### 8.1.1 Elastic energy and force

The strain components of the cell with coordinate  $(i, j)$  is given by:

$$\begin{aligned}\varepsilon_{i,j}^x &= \Delta x_{i,j} - \Delta x_{i-1,j} \\ \varepsilon_{i,j}^y &= \Delta y_{i,j} - \Delta y_{i,j-1} \\ \varepsilon_{i,j}^z &= -\frac{\nu}{1-\nu} (\varepsilon_{i,j}^x + \varepsilon_{i,j}^y)\end{aligned}\tag{8.1}$$

where  $\Delta x_{i,j}$  is the displacement of the boundary surface element between the cell  $(i, j)$  and the cell  $(i+1, j)$  normalized to  $a_x$ , the cell size in  $x$ -direction, and  $\Delta y_{i,j}$  is the displacement of the boundary surface element between the cell  $(i, j)$  and the cell  $(i, j+1)$  normalized to  $a_y$ , the cell size in  $y$ -direction. The third equation of Eq. (8.1) is due to the condition that there is no out-of-plane stress, i. e.,  $\sigma_z = 0$ , and  $\nu$  is the Poisson's ratio of the material.

The stress at the location of the cell  $(i, j)$  is related to the strain at the cell,

without the shear components, by the following equation [100]:

$$\begin{pmatrix} \sigma_{i,j}^x \\ \sigma_{i,j}^y \\ \sigma_{i,j}^z \end{pmatrix} = \frac{E}{(1+\nu)(1-2\nu)} \begin{pmatrix} 1-\nu & \nu & \nu \\ \nu & 1-\nu & \nu \\ \nu & \nu & 1-\nu \end{pmatrix} \begin{pmatrix} \varepsilon_{i,j}^x \\ \varepsilon_{i,j}^y \\ \varepsilon_{i,j}^z \end{pmatrix} \quad (8.2)$$

therefore

$$\begin{aligned} \sigma_{i,j}^x &= \frac{E}{1+\nu} \left[ \varepsilon_{i,j}^x + \frac{\nu}{1-2\nu} (\varepsilon_{i,j}^x + \varepsilon_{i,j}^y + \varepsilon_{i,j}^z) \right] \\ \sigma_{i,j}^y &= \frac{E}{1+\nu} \left[ \varepsilon_{i,j}^y + \frac{\nu}{1-2\nu} (\varepsilon_{i,j}^x + \varepsilon_{i,j}^y + \varepsilon_{i,j}^z) \right] \\ \sigma_{i,j}^z &= \frac{E}{1+\nu} \left[ \varepsilon_{i,j}^z + \frac{\nu}{1-2\nu} (\varepsilon_{i,j}^x + \varepsilon_{i,j}^y + \varepsilon_{i,j}^z) \right] \end{aligned} \quad (8.3)$$

where  $E$  is the Young's modulus of the material. Combining Eqs. (8.1) and (8.3) gives the stress components at the cell (i, j) as functions of the displacements associated with the cell (i, j) and its neighboring cells:

$$\begin{aligned} \sigma_{i,j}^x &= \frac{E}{1-\nu^2} [\varepsilon_{i,j}^x + \nu \varepsilon_{i,j}^y] \\ &= \frac{E}{1-\nu^2} [(\Delta x_{i,j} - \Delta x_{i-1,j}) + \nu (\Delta y_{i,j} - \Delta y_{i,j-1})] \\ \sigma_{i,j}^y &= \frac{E}{1-\nu^2} [\nu \varepsilon_{i,j}^x + \varepsilon_{i,j}^y] \\ &= \frac{E}{1-\nu^2} [\nu (\Delta x_{i,j} - \Delta x_{i-1,j}) + (\Delta y_{i,j} - \Delta y_{i,j-1})] \\ \sigma_{i,j}^z &= 0 \end{aligned} \quad (8.4)$$

With Eqs. (8.1) and (8.4), the elastic energy density of the cell (i, j) can now be written as:

$$\begin{aligned} E_{i,j}^{el} &= \frac{1}{2} \vec{\varepsilon}_{i,j} \cdot \vec{\sigma}_{i,j} \\ &= \frac{E}{2(1-\nu^2)} [(\Delta x_{i,j} - \Delta x_{i-1,j})^2 + (\Delta y_{i,j} - \Delta y_{i,j-1})^2 + \\ &\quad 2\nu (\Delta x_{i,j} \Delta y_{i,j} + \Delta x_{i-1,j} \Delta y_{i,j-1} - \Delta x_{i-1,j} \Delta y_{i,j} - \Delta x_{i,j} \Delta y_{i,j-1})] \end{aligned} \quad (8.5)$$

By taking the partial derivative of the total elastic energy with respect to  $\Delta x_{i,j}$  one can get the effective force on the boundary surface element whose displacement is  $\Delta x_{i,j}$ :

$$F_{\Delta x_{i,j}}^{el} = -\frac{\partial E_{Tot}^{el}}{\partial \Delta x_{i,j}} \quad (8.6)$$

where  $E_{Tot}^{el}$  is defined as:

$$E_{Tot}^{el} = \sum_{i=1}^{N_x} \sum_{j=1}^{N_y} E_{i,j}^{el} \quad (8.7)$$

From Eq. (8.5) it can be seen that  $F_{\Delta x_{i,j}}^{el}$  only involves  $E_{i,j}^{el}$  and  $E_{i+1,j}^{el}$ . Combining Eqs. (8.5), (8.6), and (8.7) yields:

$$\begin{aligned} F_{\Delta x_{i,j}}^{el} = & -\frac{E}{1-\nu^2} \left[ (2\Delta x_{i,j} - \Delta x_{i-1,j} - \Delta x_{i+1,j}) \right. \\ & \left. + \nu (\Delta y_{i,j} - \Delta y_{i,j-1} + \Delta y_{i+1,j-1} - \Delta y_{i+1,j}) \right] \end{aligned} \quad (8.8)$$

From Eq. (8.6),  $F_{\Delta x_{i,j}}^{el}$  is the driving force to change the displacement of the boundary surface element  $\Delta x_{i,j}$ , whose direction is determined by its sign. Likewise, we can find the force on  $\Delta y_{i,j}$  due to the elastic energy:

$$\begin{aligned} F_{\Delta y_{i,j}}^{el} = & -\frac{E}{1-\nu^2} \left[ (2\Delta y_{i,j} - \Delta y_{i,j-1} - \Delta y_{i,j+1}) \right. \\ & \left. + \nu (\Delta x_{i,j} - \Delta x_{i-1,j} + \Delta x_{i-1,j+1} - \Delta x_{i,j+1}) \right] \end{aligned} \quad (8.9)$$

### 8.1.2 Magnetoelastic energy and force

In this section we deal with the magnetoelastic energy and the effective force on the surface elements due to this energy term. As opposed to Chapter 7 where the magnetoelastic energy is calculated for a given fixed stress, here the stress will be a function of the displacements  $\Delta x_{i,j}$  and  $\Delta y_{i,j}$ . This is how the displacement variables are related to the magnetoelastic energy. We will use

Eq. (7.1) for the magnetoelastic energy of cell (i, j), which, for convenience, is rewritten here:

$$E_{i,j}^{magel} = -\frac{3}{2}\lambda_{100}\sigma_{i,j}(m_{x'}^2\sigma_{x'}^2 + m_{y'}^2\sigma_{y'}^2 + m_{z'}^2\sigma_{z'}^2) - 3\lambda_{111}\sigma_{i,j}(m_{x'}m_{y'}\sigma_{x'}\sigma_{y'} + m_{y'}m_{z'}\sigma_{y'}\sigma_{z'} + m_{z'}m_{x'}\sigma_{z'}\sigma_{x'}) \quad (8.10)$$

where  $(m_{x'}, m_{y'}, m_{z'})$  and  $(\sigma_{x'}, \sigma_{y'}, \sigma_{z'})$  are the directions of the magnetization of the cell (i, j) and the uniaxial stress  $\sigma_{i,j}$ , either along  $x$ -direction or along  $y$ -direction, both defined in the primary crystal axes coordinate system of the cell (i, j). Also note that  $\sigma_{i,j}$  is defined by Eq. (8.4). Combining Eqs. (8.4) and (8.10) should give the expression of the magnetoelastic energy density of a cell (i, j). However, notice that in Eq. (8.10) everything is defined in the local crystal system, whereas in Eq. (8.4) the stress is expressed with respect to the global system that is fixed to the film, exactly the same as the two systems we used in Chapter 7. Therefore, we need to do the coordinate transformation first. Assume that the coordinate transform matrix for cell (i, j) is  $A_{i,j}$ , which means a vector  $\mathbf{v}$  in the global system is converted into  $\mathbf{v}'$  in the local system:

$$\mathbf{v}' = A_{i,j}\mathbf{v} \quad (8.11)$$

where

$$A_{i,j} = \begin{pmatrix} a_{i,j}^{11} & a_{i,j}^{12} & a_{i,j}^{13} \\ a_{i,j}^{21} & a_{i,j}^{22} & a_{i,j}^{23} \\ a_{i,j}^{31} & a_{i,j}^{32} & a_{i,j}^{33} \end{pmatrix} \quad (8.12)$$

can be calculated by Eqs. (7.4), (D.2), (D.4), and (D.6).

Now let's consider a uniaxial stress along  $x$ -direction in the global coordinate system,  $(\sigma_x, 0, 0)$ , which will be represented in the local coordinate system as,

ignoring the subscript (i, j):

$$A \begin{pmatrix} \sigma_x \\ 0 \\ 0 \end{pmatrix} = \begin{pmatrix} a_{11} & a_{12} & a_{13} \\ a_{21} & a_{22} & a_{23} \\ a_{31} & a_{32} & a_{33} \end{pmatrix} \begin{pmatrix} \sigma_x \\ 0 \\ 0 \end{pmatrix} = \begin{pmatrix} a_{11}\sigma_x \\ a_{21}\sigma_x \\ a_{31}\sigma_x \end{pmatrix} = \sigma_x \begin{pmatrix} a_{11} \\ a_{21} \\ a_{31} \end{pmatrix} \quad (8.13)$$

This means that

$$\begin{pmatrix} \sigma_{x'} \\ \sigma_{y'} \\ \sigma_{z'} \end{pmatrix}_x = \begin{pmatrix} a_{11} \\ a_{21} \\ a_{31} \end{pmatrix} \quad (8.14)$$

Substituting Eqs. (8.14) and (8.4) into Eq. (8.10) yields the expression of the magnetoelastic energy of the cell (i, j) due to the  $x$ -component of the stress, as a function of its magnetization and displacements  $\Delta x_{i,j}$  and  $\Delta y_{i,j}$ , ignoring the subscript (i, j) for  $m$ 's and  $a$ 's:

$$E_{i,j}^{magelX} = B_x(i, j) \frac{E}{1 - \nu^2} [(\Delta x_{i,j} - \Delta x_{i-1,j}) + \nu(\Delta y_{i,j} - \Delta y_{i,j-1})] \quad (8.15)$$

where  $B_x(i, j)$  is defined as:

$$\begin{aligned} B_x(i, j) = & -\frac{3}{2}\lambda_{100} (m_x^2 a_{11}^2 + m_y^2 a_{21}^2 + m_z^2 a_{31}^2) \\ & - 3\lambda_{111} (m_x m_y a_{11} a_{21} + m_y m_z a_{21} a_{31} + m_z m_x a_{31} a_{11}) \end{aligned} \quad (8.16)$$

and is independent of the displacements  $\Delta x_{i,j}$  and  $\Delta y_{i,j}$ .

Likewise, for the  $y$ -component of the stress,  $(0, \sigma_y, 0)$  in the global system, the projected components in the local system are given by:

$$\begin{pmatrix} \sigma_{x'} \\ \sigma_{y'} \\ \sigma_{z'} \end{pmatrix}_y = \begin{pmatrix} a_{12} \\ a_{22} \\ a_{32} \end{pmatrix} \quad (8.17)$$

and hence the magnetoelastic energy due to the  $y$ -component of the stress, as a function of its magnetization and displacements  $\Delta x_{i,j}$  and  $\Delta y_{i,j}$ , ignoring the subscript  $(i, j)$  for  $m's$  and  $a's$ :

$$E_{i,j}^{magelY} = B_y(i, j) \frac{E}{1 - \nu^2} [\nu (\Delta x_{i,j} - \Delta x_{i-1,j}) + (\Delta y_{i,j} - \Delta y_{i,j-1})] \quad (8.18)$$

where  $B_y(i, j)$  is defined as:

$$\begin{aligned} B_y(i, j) = & -\frac{3}{2} \lambda_{100} (m_x^2 a_{12}^2 + m_y^2 a_{22}^2 + m_z^2 a_{32}^2) \\ & - 3 \lambda_{111} (m_x m_y a_{12} a_{22} + m_y m_z a_{22} a_{32} + m_z m_x a_{32} a_{12}) \end{aligned} \quad (8.19)$$

The total magnetoelastic energy is

$$E_{Tot}^{magel} = \sum_{i=1}^{N_x} \sum_{j=1}^{N_y} (E_{i,j}^{magelX} + E_{i,j}^{magelY}) \quad (8.20)$$

in which the terms involving  $\Delta x_{i,j}$  are  $E_{i,j}^{magelX}$ ,  $E_{i+1,j}^{magelX}$ ,  $E_{i,j}^{magelY}$  and  $E_{i+1,j}^{magelY}$ . Taking the partial derivative of  $E_{Tot}^{magel}$  with respect to  $\Delta x_{i,j}$  gives the force on  $\Delta x_{i,j}$  due to the magnetoelastic energy:

$$\begin{aligned} F_{\Delta x_{i,j}}^{magel} &= -\frac{\partial E_{Tot}^{magel}}{\partial \Delta x_{i,j}} \\ &= -\frac{\partial}{\partial \Delta x_{i,j}} [E_{i,j}^{magelX} + E_{i+1,j}^{magelX} + E_{i,j}^{magelY} + E_{i+1,j}^{magelY}] \\ &= -\frac{E}{1 - \nu^2} [B_x(i, j) - B_x(i + 1, j)] - \frac{\nu E}{1 - \nu^2} [B_y(i, j) - B_y(i + 1, j)] \end{aligned} \quad (8.21)$$

Similarly, one has the force on  $\Delta y_{i,j}$  due to the magnetoelastic energy:

$$\begin{aligned} F_{\Delta y_{i,j}}^{magel} &= -\frac{\partial E_{Tot}^{magel}}{\partial \Delta y_{i,j}} \\ &= -\frac{\partial}{\partial \Delta y_{i,j}} [E_{i,j}^{magelX} + E_{i,j+1}^{magelX} + E_{i,j}^{magelY} + E_{i,j+1}^{magelY}] \\ &= -\frac{\nu E}{1 - \nu^2} [B_x(i, j) - B_x(i, j + 1)] - \frac{E}{1 - \nu^2} [B_y(i, j) - B_y(i, j + 1)] \end{aligned} \quad (8.22)$$

Finally, the sum of Eqs. (8.8) and (8.21) gives the total force on  $\Delta x_{i,j}$  due

to both the elastic energy and the magnetoelastic energy:

$$\begin{aligned}
 F_{\Delta x_{i,j}}^{Tot} = & -\frac{E}{1-\nu^2} \left[ (2\Delta x_{i,j} - \Delta x_{i-1,j} - \Delta x_{i+1,j}) \right. \\
 & \left. + \nu (\Delta y_{i,j} - \Delta y_{i,j-1} + \Delta y_{i+1,j-1} - \Delta y_{i+1,j}) \right] \\
 & - \frac{E}{1-\nu^2} \left[ (B_x(i,j) - B_x(i+1,j)) + \nu (B_y(i,j) - B_y(i+1,j)) \right]
 \end{aligned} \tag{8.23}$$

and the sum of Eqs. (8.9) and (8.22) gives the total force on  $\Delta y_{i,j}$  due to both the elastic energy and the magnetoelastic energy:

$$\begin{aligned}
 F_{\Delta y_{i,j}}^{Tot} = & -\frac{E}{1-\nu^2} \left[ (2\Delta y_{i,j} - \Delta y_{i,j-1} - \Delta y_{i,j+1}) \right. \\
 & \left. + \nu (\Delta x_{i,j} - \Delta x_{i-1,j} + \Delta x_{i-1,j+1} - \Delta x_{i,j+1}) \right] \\
 & - \frac{E}{1-\nu^2} \left[ \nu (B_x(i,j) - B_x(i,j+1)) + (B_y(i,j) - B_y(i,j+1)) \right]
 \end{aligned} \tag{8.24}$$

### 8.1.3 The solution algorithm

In this section, we describe the algorithm used to solve for the magnetization and the stress-strain distribution in the thin film. As mentioned before, the independent variables are the magnetization and the displacements of the cell boundaries of each cell. The effective magnetic field due to the pure magnetic energy terms  $\mathbf{H}_{eff}^{mag}$  has been derived in Chapter 2 (Eq. (2.19)), so has the the effective magnetic field due to the magnetoelastic energy term in Chapter 7 (Eq. (7.13)). For the latter, the field is the sum of the contribution from both  $x$ -direction stress and  $y$ -direction stress. Therefore, Eqs. (8.4), (8.14) and (8.17) need to be substituted into Eq. (7.13) to get the effective magnetic field due to magnetoelastic energy  $\mathbf{H}_{eff}^{magnet}$ .

The basic idea of this model is to find the minimum of the total energy of the system, including the magnetic energy, the magnetoelastic energy



and the elastic energy. The initial state of the system includes an assumed magnetization distribution, which is typically chosen to be something close to a demagnetized state for ease of converging to the energy minimum. The initial state of the displacements is set to be all zero. At each step of the simulation, the magnetization at the cell  $(i, j)$  changes its direction slightly towards the direction of the total effective magnetic field,  $\mathbf{H}_{eff}^{mag} + \mathbf{H}_{eff}^{magel}$ , at the cell  $(i, j)$ , whereas the displacements  $\Delta x_{i,j}$  and  $\Delta y_{i,j}$  slightly relax according to the magnitude and the direction of the total effective force on them, which are defined by Eqs. (8.23) and (8.24). The system continues to relax while all the energy terms are tracked, the state corresponding to the minimum of the total energy is then defined as the equilibrium.

## 8.2 Simulation results

### 8.2.1 $\text{Fe}_{65}\text{Co}_{35}$ thin film

In this section we will show the simulation results of both the magnetization and the strain-stress relaxation of a magnetic thin film element. The material of the thin film is assumed  $\text{Fe}_{65}\text{Co}_{35}$ , and the thin film element is a rectangle with length 640 nm, width 160 nm, and thickness 10 nm. The parameters used are  $M_s = 1930 \text{ emu/cm}^3$ , Young's modulus  $E = 200 \text{ GPa}$ , Poisson's ratio  $\nu = 0.3$ ,  $\lambda_{111} = 103.7 \times 10^{-6}$  and  $\lambda_{100} = 17.5 \times 10^{-6}$ . The thin film is assumed a single crystal oriented in such a way that the  $x$ - and  $y$ -directions are two  $\langle 100 \rangle$  directions.

Figure 8.1 shows how the different energy terms change during the relaxation for the thin film element with 2-D constraint. For a better view, the values of the magnetic energy and the total energy have been shifted so that they are all

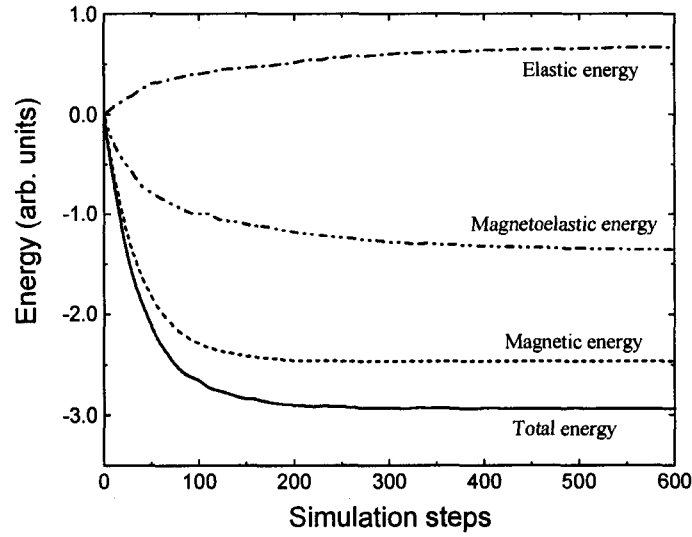


Figure 8.1: Different energy terms in the relaxation process.

zero at the starting point. It can be seen that both the magnetic energy and the magnetoelastic energy decreases as the simulation progresses, while the elastic energy increases as expected, since it has the form of a quadratic of the strain. Nevertheless, the decrease of the magnetoelastic energy overcomes the penalty of the elastic energy increase, and finally all the energy terms settled down at a level, which yields a minimum of the total energy of the system.

The simulation results of the magnetization and the strain-stress distribution of the thin film with 2-D constraint at the equilibrium state are shown in Figure 8.2. The magnetization of the thin film is simply a demagnetized state with the four closure domains as shown in Figure 8.2(a). Figure 8.2(b) is the  $x$ -component of the strain. Clearly, in the area of the two majority horizontal domains,  $\varepsilon_x > 0$ , meaning that the film expands in  $x$ -direction, consistent with the positive magnetostriction. Because the film is constrained, the total strain in either  $x$ - or  $y$ -direction (not shown) should be zero, which is confirmed by the significant larger negative strain at the two ends of the film in Figure 8.2(b)

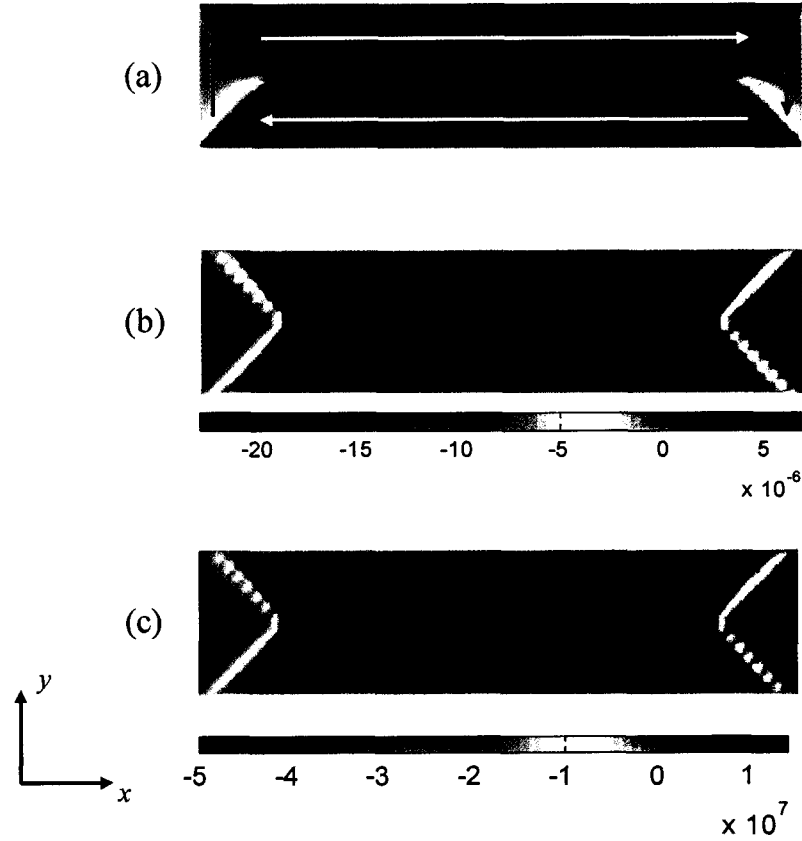


Figure 8.2: Colormaps of the magnetization and the spontaneous strain-stress distribution of a  $\text{Fe}_{65}\text{Co}_{35}$  thin film under 2-D constraint, where all the four boundaries of the rectangle are pinned. (a) The magnetization, (b)  $x$ -component of the strain  $\varepsilon_x$ , (c)  $x$ -component of the stress  $\sigma_x$ . The stress here is in *cgs* units,  $\text{dyne}/\text{cm}^2$ . ( $1 \text{ Pa} = 10 \text{ dyne}/\text{cm}^2$ )

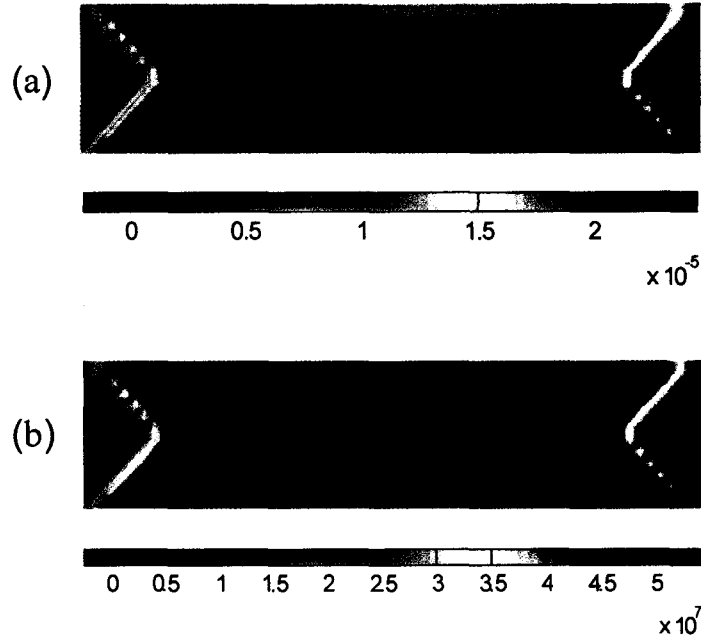


Figure 8.3: Colormap of the spontaneous strain and stress distribution of a  $\text{Fe}_{65}\text{Co}_{35}$  thin film without constraint. (a)  $x$ -component of the strain  $\epsilon_x$ , (b)  $x$ -component of the stress  $\sigma_x$ . The stress here is in *cgs* units, dyne/cm<sup>2</sup>. (1 Pa = 10 dyne/cm<sup>2</sup>)

for  $\epsilon_x$ . The distribution of the  $x$ -component of the stress  $\sigma_x$  is shown in Figure 8.2(c). The stress is conform to the magnetization very well too.

Also noticed is that the order of magnitude of the stress spontaneously generated in the film is only at the order of  $10^7$  dyne/cm<sup>2</sup>, which is the order of MPa, a few orders of magnitude smaller than the stress needed to alter the magnetization states in the thin film as seen in Chapter 7. This validates the assumption of negligible stress due to spontaneous magnetostriction when dealing with the external stress-induced anisotropy in Chapter 7.

Figure 8.3 shows the simulated  $x$ -component of the strain and stress for the same thin film, but without constraint. Although the magnetization configuration is exactly the same as Figure 8.2(a), the strain-stress distribution is quite different from the case with constraint. As seen in Figure 8.3(a), the

$x$ -component of the strain  $\varepsilon_x$  is more uniform than in the constrained case, without the large negative strain at the ends. The magnitude of  $\varepsilon_x$  is about  $23 \times 10^{-6}$  in the film except at the two ends, very close to the value of  $\lambda_{100}$ , which is the magnetostriction along a  $\langle 100 \rangle$  direction when the material is magnetized along the same direction, which is the case here. As a consequence of the uniform strain, the stress is very uniformly distributed as well, as shown in Figure 8.3(b), which is at the same order as that with the 2-D constraint, except at the two ends, where the magnetization is perpendicular to that in the center of the film.

### 8.2.2 Arbitrary materials

In this section, we modeled some cases with arbitrarily chosen material properties, in order to further understand the effect of the magnetoelastic relaxation on the magnetization and the strain-stress state in magnetic thin films. As will be shown in this section, under some conditions, the magnetic domain configuration could be significantly different from its counterpart with very weak magnetoelastic coupling, as a result of minimizing the total system energy.

The material modeled here has the following properties:  $M_s = 200 \text{ emu/cm}^3$ , exchange coupling constant  $A = 1.0 \times 10^{-8} \text{ erg/cm}$ ,  $\lambda_{111} = \lambda_{100} = 10^{-5}$  for low-magnetostriction and  $10^{-3}$  for high-magnetostriction, Young's modulus  $E = 20 \text{ GPa}$ , Poisson's ratio  $\nu = 0.1$ . The thin film element is a square single crystal film element with four edges all being  $\langle 100 \rangle$  directions. The side length of the square element is 320 nm and the thickness is 10 nm. Both the discretization cell and the crystal grains are taken as  $10 \text{ nm} \times 10 \text{ nm} \times 10 \text{ nm}$  cubes. The film is constrained at the four boundaries. The initial magnetization state is chosen to be a four-domain closure structure similar to Figure 8.4, and the initial stress

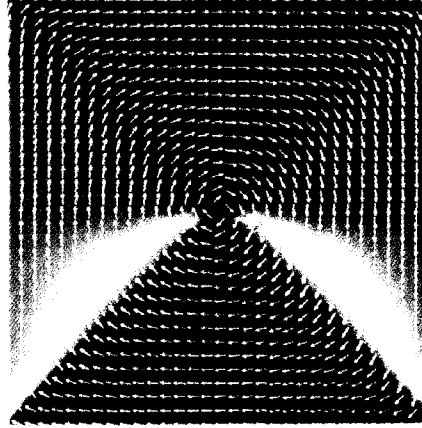


Figure 8.4: The equilibrium state magnetization configuration of the thin film element with low magnetostriction ( $\lambda_{111} = \lambda_{100} = 10^{-5}$ ).

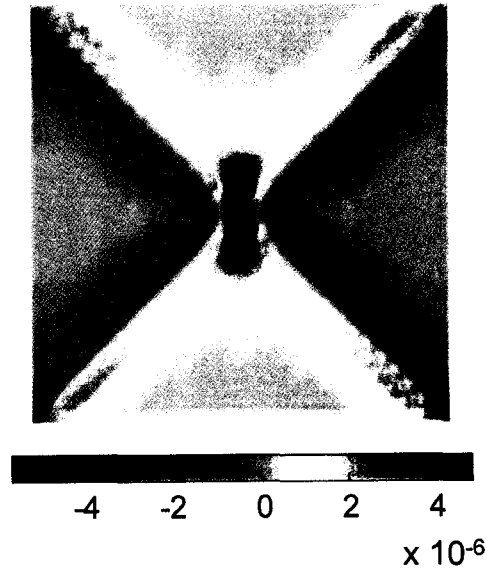


Figure 8.5: The equilibrium state distribution of the horizontal strain component in the film with low magnetostriction ( $\lambda_{111} = \lambda_{100} = 10^{-5}$ ).

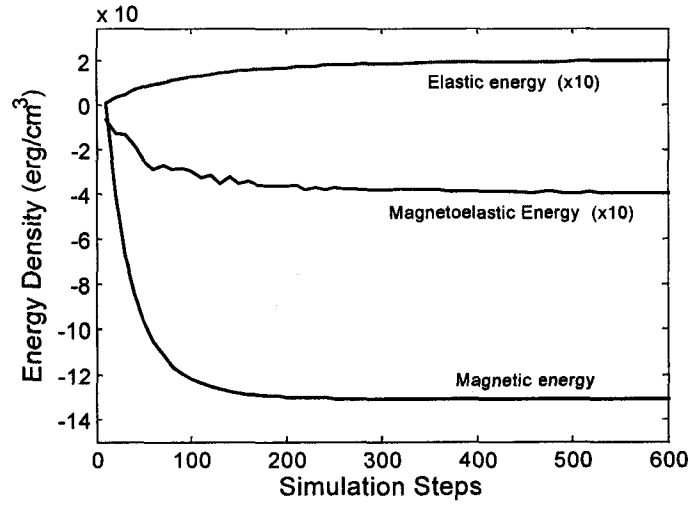


Figure 8.6: Different terms of the energy density averaged over all the cells in the relaxation process for the low-magnetostriction case ( $\lambda_{111} = \lambda_{100} = 10^{-5}$ ).

and strain are set to be zero.

Figures 8.4 and 8.5 show the equilibrium state magnetization and strain distribution for the low-magnetostriction case. In this case, closure domains are formed, which is clearly a consequence of minimizing the magnetic energy. In Figure 8.6, different energy terms are compared as they evolve from the initial state towards the final equilibrium. Since the magnetostriction coefficients are small, the magnetic energy is dominant. Therefore, the domain structure in Figure 8.4 is effectively the demagnetized state without magnetostriction. The strain and stress then relax according to the magnetization configuration to further lower the total energy, which is a relative small effect on top of the magnetic energy term.

Figures 8.7 and 8.8 show the equilibrium state magnetization and strain distribution, respectively, for the high-magnetostriction case. The magnetostriction coefficient here is 100 times that of the previous case, while all other parameters are exactly the same. Quite different from the low-magnetostriction

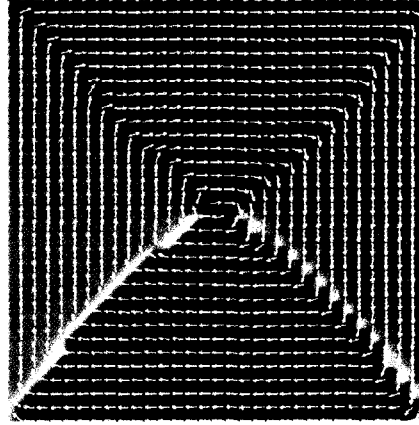


Figure 8.7: The equilibrium state magnetization configuration of the thin film element with high magnetostriction ( $\lambda_{111} = \lambda_{100} = 10^{-3}$ ).

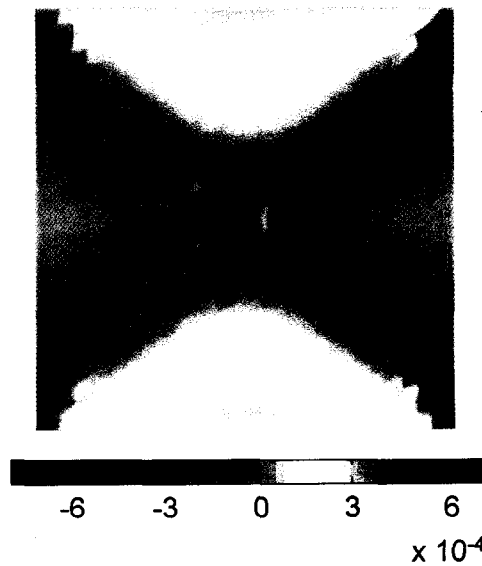


Figure 8.8: The equilibrium state distribution of the horizontal strain component in the film with high magnetostriction ( $\lambda_{111} = \lambda_{100} = 10^{-3}$ ).



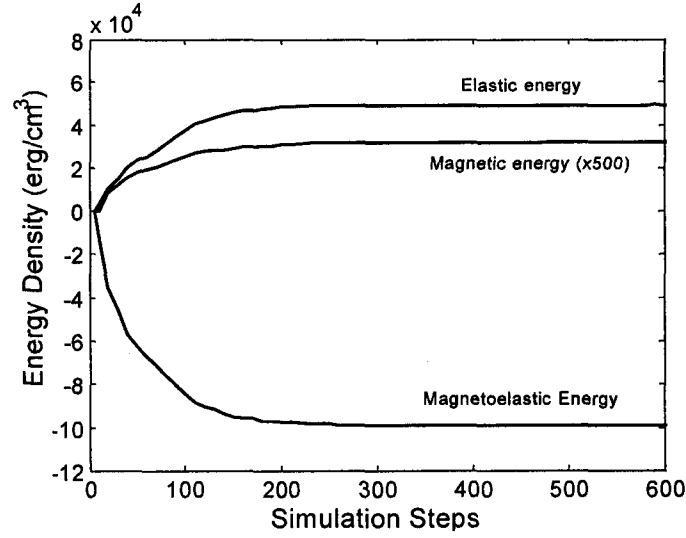


Figure 8.9: Different terms of the energy density averaged over all the cells in the relaxation process for the high-magnetostriction case ( $\lambda_{111} = \lambda_{100} = 10^{-3}$ ).

case, four distinct domains are formed with very sharp domain walls, which conforms very well to that of the strain and stress distribution in the film.

### 8.2.3 Discussions

A qualitative explanation could be given to understand the different magnetization configurations observed above. In general, the domain wall thickness is determined by  $\sqrt{A/K}$ , where  $A$  is the exchange coupling constant, and  $K$  is the anisotropy constant, which could be from the crystal anisotropy ( $K_u$ ), the magnetostatic energy ( $2\pi M_s^2$ ), or that due to the magnetoelastic energy, which, to the first order approximation, is proportional to the square of the magnetostriction times the Young's modulus (detailed discussion follows later). The very last term turns out dominant in this high-magnetostriction case, as can be seen from Figure 8.9. This makes the effective anisotropy much higher, leading to well defined domains and very sharp domain walls.

From another perspective, for the high-magnetostriction case, if the magnetic domain structure and the strain distribution were the same as that of Figures 8.4 and 8.5 with the strain simply 100 times higher, the magnetoelastic energy, which is the dominant term now, will no longer be the minimum. Therefore, the system will be driven further to relax to the state with minimum magnetoelastic energy, as shown in Figures 8.7 and 8.8. Specifically, the stress at the vicinity of the domain walls will be so high that it will realign the magnetization until the configuration in Figures 8.7 is formed. Consequently, the strain and stress will be redistributed as well. Actually, it can be found in Figure 8.8 that the strain is more uniformly distributed compared to Figure 8.5. Quantitatively, the sums of the average magnetoelastic energy density and the elastic energy density, for the two configurations mentioned above, are  $-1.98 \times 10^4$  erg/cm<sup>3</sup> and  $-4.53 \times 10^4$  erg/cm<sup>3</sup>, respectively, which shows the configurations in Figures 8.7 and 8.8 indeed have lower energy.

It is worthwhile exploring explicitly the conditions under which significant domain changes occur. From previous examples one can see that, only when the energy reduction through the deformation,  $E_{magel} + E_{el}$ , overwhelms the change of the magnetic energy, can this happen. The magnetoelastic energy has the form of  $-E\lambda\varepsilon$ , where  $E$  is the Young's modulus,  $\lambda$  the saturation magnetostriction, and  $\varepsilon$  the strain; and the elastic energy has the form of  $E\varepsilon^2$ . The strain at the equilibrium will be determined by

$$\frac{d}{d\varepsilon} (E_{magel} + E_{el}) = 0 \quad (8.25)$$

which yields that at the equilibrium state, the strain  $\varepsilon_o$  is at the order of the magnetostriction  $\lambda$ , and  $E_{magel} + E_{el}$  is a fraction of  $-E\lambda^2$ , which is denoted as  $E_o$ . The negative sign indicates that through straining, the system can always lower its energy, and the amount of the energy reduction, compared to the

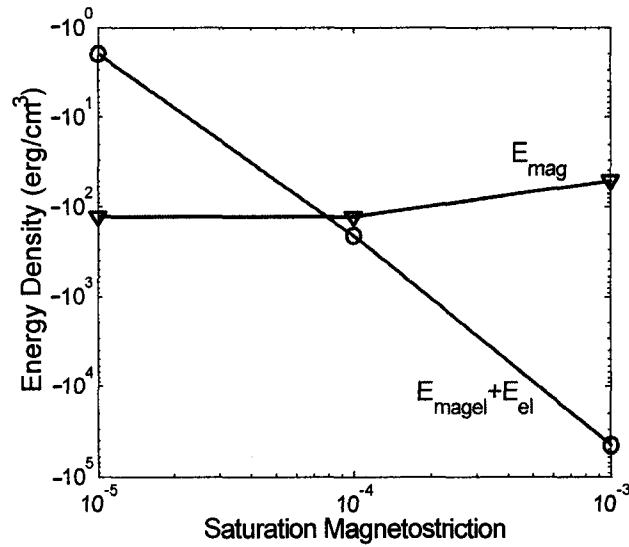


Figure 8.10: Dependence of simulated values of different terms of the energy density at equilibrium state on the saturation magnetostriction of the material. The curve for the magnetic energy is the range this energy term varies during the relaxation.  $M_s = 200 \text{ emu/cm}^3$ , exchange coupling constant  $A = 1.0 \times 10^{-8} \text{ erg/cm}$ , Young's modulus  $E = 20 \text{ GPa}$ , Poisson's ratio  $\nu = 0.1$ .

non-strained state, is  $|E_o|$ .

Figure 8.10 plots the dependence of different equilibrium state energy densities on the magnetostriction, from the simulation results on the thin film element. It can be seen that the sum of the magnetoelastic energy and the elastic energy, which is always negative, depends quadratically on the magnetostriction, and agrees well in orders of magnitude with the above analysis. On the other hand, the range over which the magnetic energy varies stays at the same order of magnitude. Therefore, only when the Young's modulus and/or the magnetostriction are very high, can the magnetization domain pattern deviate from its normal demagnetized state that is corresponding to low-magnetostriction.

According to the above analysis, when the material is magnetically saturated along one direction, there will be an elongation, for positive magnetostriction,

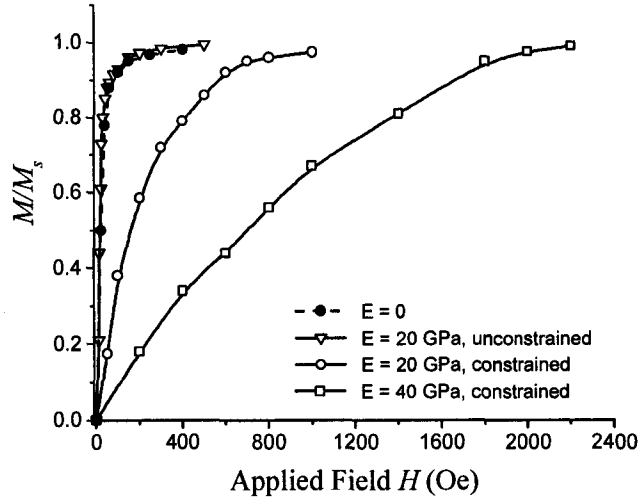


Figure 8.11: Simulated initial magnetization curves for different values of Young's modulus. The initial condition for the magnetization is an AC demagnetized state.  $M_s = 200 \text{ emu/cm}^3$ , exchange coupling constant  $A = 1.0 \times 10^{-8} \text{ erg/cm}$ .  $\lambda_{111} = \lambda_{100} = 10^{-3}$ .

or a shrinkage, for negative magnetostriction, along the saturation direction, if the material is free to deform. An estimate of the energy associated with this deformation has been given above. If, however, the material is constrained such that the boundaries are pinned rigidly, the boundaries are effectively exerting stresses on the material, which is against the tendency of deformation due to the magnetostriction. This will make the film harder to magnetize, since any growth of domains along the applied field direction due to a  $90^\circ$  domain wall motion will tend to elongate (for positive magnetostriction) the material along the field direction, which is not allowed because of the constraint. This is manifested as a compressive stress that is against the magnetization alignment along the field direction. Therefore, in order to bring the material into magnetization saturation, extra energy is needed, which is supplied in the form of Zeeman energy through the applied field. The stronger the magnetoelastic coupling, the more energy, hence the higher the magnetic field is needed. Therefore,

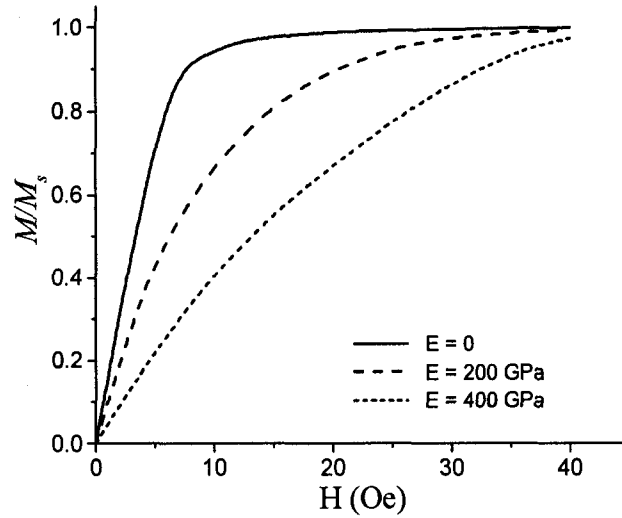


Figure 8.12: Simulated initial magnetization curves for different values of Young's modulus with constraint. Zero Young's modulus means no constraint. The initial condition for the magnetization is an AC demagnetized state. The material is FeCo,  $M_s = 1930 \text{ emu/cm}^3$ ,  $\lambda_{111} = \lambda_{100} = 10^{-4}$ .

the permeability of the film will decrease with increasing magnitude of the magnetoelastic energy, which is proportional to  $E\lambda^2$ .

Figure 8.11 shows the simulated initial magnetization curve for different values of Young's modulus for an arbitrary material with low moment and high magnetostriction. As expected, with the constrained boundary condition, the initial permeability decreases dramatically with increasing Young's modulus. Whereas without constraint, the magnetization curve does not depend on Young's modulus, as the material is free to deform, and no extra energy is needed to magnetize the material. This is evidenced from the two overlapped curves for zero Young's modulus and a 20 GPa Young's modulus without constraint in Figure 8.11.

For realistic materials of interest such as FeCo alloys, however, the increase of the saturation field due to the constraint condition is much smaller, as the magnetoelastic term is much weaker and the magnetic moment is much higher

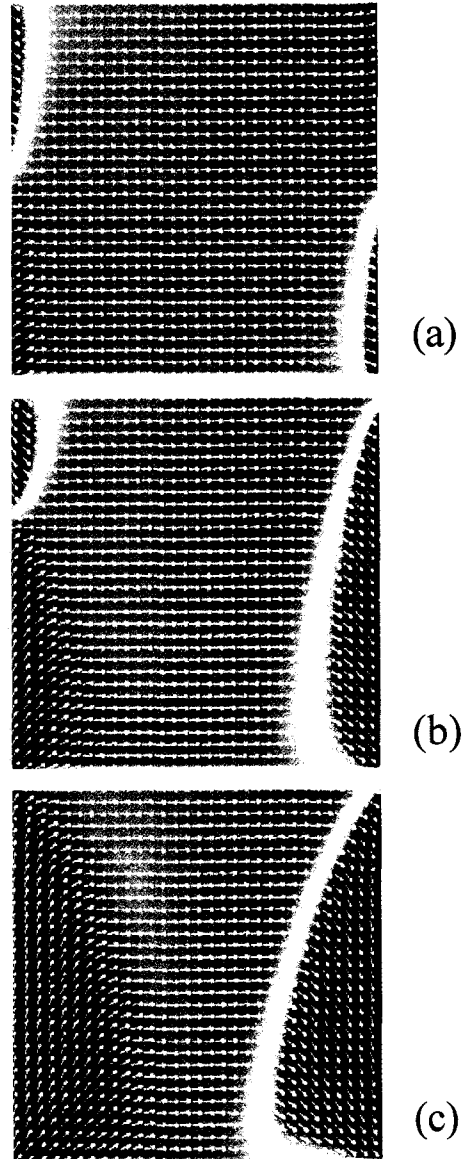


Figure 8.13: Magnetic domain configurations corresponding to 25 Oe field on the three curves in Figure 8.12: The Young's moduli are (a) 0, (b) 200 GPa, and (c) 400 GPa.

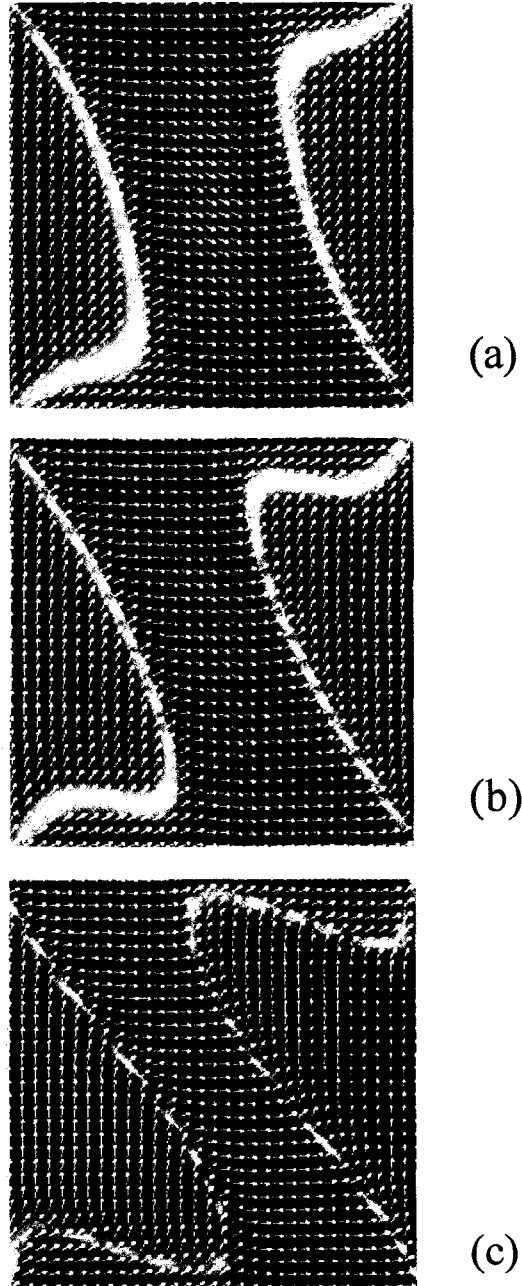


Figure 8.14: Simulated domain configurations of a constrained film with a uniform initial horizontal magnetization for Young's moduli of (a) 0, (b) 10 GPa, and (c) 40 GPa.  $M_s = 200 \text{ emu/cm}^3$ ,  $\lambda_{111} = \lambda_{100} = 10^{-3}$ .

than the previous case (Zeeman energy is the product of the magnetization and the field). Figure 8.12 shows the simulation results for FeCo alloy with the same dimension as before. The saturation field increases by about 15 Oe and 30 Oe, respectively, for Young's modulus values of 200 GPa and 400 GPa. The magnetization configurations under the same field for the three Young's modulus values are shown in Figure 8.13. The net magnetization along the horizontal direction, the applied field direction, is  $0.99M_s$ ,  $0.94M_s$ , and  $0.78M_s$ , respectively.

Figure 8.14 shows a case of zero field relaxation for different strength of magnetoelastic term. The boundary condition is with constraint, and the initial magnetization was uniform horizontal magnetization saturation. It can be seen that, with increase of the magnetoelastic strength, the horizontal domain becomes smaller, as the domain configuration in the zero-magnetoelastic energy case (Figure 8.14(a)) will cause a compressive stress from the two vertical boundaries, suppressing the horizontal magnetization.

### 8.3 Conclusions

In this chapter, we have developed a self-consistent model with magnetic energy, elastic energy and magnetoelastic energy considered altogether. Both the magnetization and the strain-stress distribution in a 2-D magnetic thin film under plane-stress condition are solved simultaneously with the energy minimization method.

Simulations on magnetic thin film elements have shown that spontaneous strain and stress are developed in the thin film. The strain and stress distribution and the magnetization domain configuration are conformed to each other in the thin film to minimize the magnetoelastic energy.



In general, the strength of the inverse effect of magnetostriction on the magnetization, through the internal stress, is characterized by  $E\lambda^2$ , where  $E$  is the Young's modulus, and  $\lambda$  is the saturation magnetostriction. Similar to any other energy terms in a system, it is the relative magnitude that determines whether the effect is significant. Therefore, when this magnetoelastic energy term is comparable to or greater than other magnetic energy terms, this inverse effect should be considered. Otherwise, the system will be solely determined by the magnetic energies.

For a high-moment material such as  $\text{Fe}_{65}\text{Co}_{35}$ , the effect of magnetostriction on magnetization is relatively weak. Nevertheless, it may affect the macroscopic properties such as permeability and coercivity, where of interest are magnetic fields at the order of several tens of Oersteds. Therefore, for applications or devices working in low field range, this inverse effect may not be neglected. On the other hand, in the cases such as the pole tip of a write head, where very high field is in presence and it is mostly demagnetization dominated, this inverse effect can be ignored.

## 9 SUMMARY

In this dissertation, micromagnetic modeling using Landau-Lifshitz equation with Gilbert damping has been used to study the micromagnetic processes in thin film write heads for high density and high data rate perpendicular recording. Both static results, such as the head field magnitude, the remanent head field, the field profiles and gradients *etc.*, and dynamic ones, such as the magnetization reversal processes in the head and hence the head field rise time and their dependence on parameters such as the Gilbert damping constant, have been obtained through systematic micromagnetic simulations. The micromagnetic model has also been used to evaluate various head designs, providing insights into some critical design issues of the perpendicular write heads. In the later part of the thesis, The micromagnetic model has also been extended to include the anisotropy effect induced by stresses in a soft magnetic thin film. The extended model has been used for simulating the magnetic domains in stressed thin films as well as a conceptual head design.

Here we would like to summarize the main results of this thesis work.

1. *Effect of track width reduction on head field.*

At deep submicron track widths, due to the geometric effect, both the head field magnitude and the field gradient degrade rapidly with decreasing track width, as the ABS-to-SUL spacing can not be scaled with the track width of the write pole. At small pole-tip dimensions (around or below 100 nm), significant remanence in the pole-tip will develop after writing, due to the ferromagnetic exchange coupling effect, presenting a danger of erasing previously written bits. The remanent head field also depends on

the throat height of the pole tip as a result of the shape anisotropy, and the micromagnetic state at the neck region between the yoke and the pole tip.

2. *Novel perpendicular write head designs.*

It has been found that a single pole head with a short yoke and lamination has very fast field rise time in the low driving current region, due to a magnetization rotation mechanism during the flux reversal. The lamination of the pole tip produces negligibly small remanent field. A pole tip detached (exchange decoupled) from the yoke can further improve the remanent field performance.

A stitched pole-tip head with a recessed side yoke can significantly enhance the head field compared to a conventional single pole head. A short throat height is desired to produce high field, however, with the potential risk of adjacent track erasure due to high off-track field. A 45° flare angle has been found to yield the optimum on-track field strength and cross track profile.

3. *High frequency head field dynamics.*

The head field reversal at extremely high frequency has been found to be dependent both on the drive current rise time and on the damping constant. A very short current rise time can actually lead to severe excitation of spin waves in the head, which is to be dissipated out in order for the head field to reach its full magnitude. The energy dissipation process depends on the damping constant. Therefore, simply reducing the current rise time may not necessarily yield a faster field reversal, on the contrary, it may make the situation worse. There exists an optimum current rise time at which the head field rise time is minimized. When the cycling

frequency of the driving current exceeds the rate of energy dissipation, the head field amplitude will decrease. The roll-off frequency reaches the maximum at the optimum current rise time, and it is damping constant dependent.

4. *The role of SUL in perpendicular recording.*

We have studied the effect of the SUL on both the write and the read-back process in perpendicular recording via micromagnetic modeling. The magnetic imaging effect exists in both the write and the read process, the former is desirable for write field, whereas the latter lowers the maximum achievable linear density. Most approaches for increasing the linear density limit by making the SUL imaging less effective are accompanied by the tradeoff of the write field loss. A small head-medium spacing, a narrow reader gap with an optimized spin valve reader stripe height have been found crucial for maximizing the linear density limit in the presence of the SUL.

5. *Effect of stress on soft magnetic thin film magnetization.*

An analytical study of the stress-induced in-plane anisotropy has been performed, based on the magnetoelastic energy. The effective anisotropy constants have been identified as functions of the stress, the magnetostriction coefficients of the material, and the growth texture of the film. The magnetoelastic energy has also been combined into a micromagnetic model to enable the simulations of thin film magnetization with the effect of the stress taken into account.

The extended micromagnetic model has been used to simulate thin films with various materials, stress states, and growth textures. The resulting simulated static magnetic domain structures are in good agreement with

the theoretical predictions.

A conceptual perpendicular write head design, which utilizes an externally induced stress in the head material, has been investigated using the extended micromagnetic model with the stress effect. With sufficiently high stress, the new head design shows much improved write efficiency and cross-track field gradient, both are very important for high density perpendicular write head.

#### 6. *Magnetoelastic relaxation of magnetic thin films.*

We have developed a self-consistent model with magnetic energy, elastic energy and magnetoelastic energy considered. Both the magnetization and the strain-stress distribution in a 2-D magnetic thin film under plane-stress condition are solved simultaneously with an energy minimization method. It has been found that, the energy term associated with the magnetostriction is proportional to  $E\lambda^2$ , where  $E$  is Young's modulus, and  $\lambda$  is the saturation magnetostriction. Only when the magnitude of this energy is comparable to or higher than other energies, such as the magnetic energy, will this magnetostriction affect the magnetization through magnetoelastic coupling interactions.

Simulations on magnetic thin film elements have shown that spontaneous strain and stress are developed in the thin film with magnetostriction. The strain and stress are distributed in a way that is conformed with the magnetic domains in the thin film to minimize the magnetoelastic energy. For practical high-moment materials, the inverse effect of the magnetostriction on the magnetization might affect the bulk properties such as permeability and coercivity of a thin film, whereas for those cases such as the pole tip region of a write head, the demagnetization energy

is dominant and therefore, such inverse effect of the magnetostriction is insignificant.

## List of References

- [1] K. Stoev, F. Liu, Y. Chen, X. Dang, P. Luo, J. Chen, K. Kung, M. Mederman, M. Re, G. Choe, and M. Zheng, "Demonstration and characterization of 130 gbit/in<sup>2</sup> recording systems," in *47<sup>th</sup> MMM Conference, Tampa, FL, paper AG-08*, 2002.
- [2] Y. Chen, X. Dang, Y. Liu, H. Jiang, K. Stoev, F. Liu, P. Luo, J. Wang, J. Chen, S. F. Gu, M. Lederman, M. Krounbi, and M. Re, "Inductive write heads using high moment pole materials for ultrahigh areal density demonstrations," in *Intermag, Boston, MA, paper CE-07*, 2003.
- [3] S. H. Charap, P. L. Liu, and Y. J. He, "Thermal stability of recorded information at high densities," *IEEE Trans. Magn.*, vol. 33, pp. 978–983, 1997.
- [4] J. G. Zhu, "New heights for disk drives," *Materials Today*, pp. 22–31, July/August 2003.
- [5] J. G. Zhu, *Micromagnetics of thin-film media*. in Magnetic recording technology, ed. by C.D. Mee and E. D. Daniel, McGraw-Hill, 1996.
- [6] S. Iwasaki, "Perpendicular magnetic recording," *IEEE Trans. Magn.*, vol. MAG-16, pp. 71–76, 1980.
- [7] M. L. Williams and R. L. Comstock, "An analytical model of the write process in digital magnetic recording," vol. Part I, No.5, p. 738, 1971.
- [8] D. Kaiser, H. Dakroub, A. van der Schans, E. Haftek, S. Li, W. Zhu, J. Pro, K. Vorasarn, A. Stankiewicz, R. Cox, Y. Liu, H. Zhang, K. W. Radish, Klarquest, S. Sharma, and E. Champion, "Evaluation of high data rate disk drive recording subsystem," *J. Appl. Phys.*, vol. 93, pp. 6555–6557, 2003.
- [9] P. C. D. Hobbs, D. W. Abraham, and H. K. Wickramasinghe, "Magnetic force microscopy with 25 nm resolution," *Appl. Phys. Lett.*, vol. 55, pp. 2357–2359, 1989.
- [10] G. D. Skidmore and E. D. Dahlberg, "Improved spatial resolution in mfm," *Appl. Phys. Lett.*, vol. 71, pp. 3293–3295, 1997.
- [11] O. Karlqvist, "Calculation of the magnetic field in the ferromagnetic layer of a magnetic drum," *Trans. Roy. Inst. Technol. Stockholm*, vol. 86, p. 3, 1954.

- [12] D. A. Lindholm, "Magnetic fields of finite track width heads," *IEEE Trans. Magn.*, vol. MAG-13, pp. 1460–1462, 1977.
- [13] W. K. Westmijze, "Studies on magnetic recording," *Philips Res. Rep.*, vol. 8(3), p. 161, 1953.
- [14] S. X. Wang and A. M. Taratorin, *Magnetic information storage technology*. London, UK: Academic Press, 1999.
- [15] H. N. Bertram and M. Williams, "Snr and density limit estimates: A comparison of longitudinal and perpendicular recording," *IEEE Trans. Magn.*, vol. 36, pp. 4–9, 2000.
- [16] D. Z. Bai, A. F. Torabi, M. Benakli, M. L. Mallery, and J. G. Zhu, "Micro-magnetic modeling of snr performance of longitudinal and perpendicular media with various head/sul combinations," *IEEE Trans. Magn.*, vol. 40, 2004.
- [17] A. Paton, "Analysis of the efficiency of thin-film magnetic recording heads," *J. Appl. Phys.*, vol. 42, pp. 5868–5870, Dec. 1971.
- [18] J. Jury, A. Gopinath, and J. H. Judy, "Analysis of the efficiency and inductance of multirun thin-film magnetic recording heads," *IEEE Trans. Magn.*, vol. 14, pp. 509–511, May 1978.
- [19] T. C. Arnoldussen, "A modular transmission line/reluctance head model," *IEEE Trans. Magn.*, vol. 24, p. 2482, 1988.
- [20] B. Corb, "High frequency head and playback model for thin-film recording heads," *IEEE Trans. Magn.*, vol. 30, p. 394, 1994.
- [21] E. P. Valstyn and H. Huang, "An extended dynamic transmission line model for thin film heads," *IEEE Trans. Magn.*, vol. 29, p. 3870, 1993.
- [22] E. R. Katz, "Finite element analysis of the vertical multi-turn thin film head," *IEEE Trans. Magn.*, vol. 14, p. 506, 1978.
- [23] M. H. Lean and A. Wexler, "Accurate field computation with the boundary element method," *IEEE Trans. Magn.*, vol. 18, p. 331, 1982.
- [24] W. F. Brown, *Micromagnetics*. John Wiley & Sons, 1963.
- [25] J. G. Zhu, *Interactive phenomena in magnetic thin films*. Ph.D. dissertation, University of California, San Diego, 1989.



- [26] J. G. Zhu and H. N. Bertram, "Micromagnetic studies of thin metallic-films," *J. Appl. Phys.*, vol. 63, pp. 3248–3253, April 1988.
- [27] C. Y. Mao, *Micromagnetic modeling of thin film write heads for magnetic recording*. Ph.D. dissertation, Carnegie Mellon University, Pittsburgh, PA, 2000.
- [28] K. Z. Gao, *Optimization of write heads and media for ultra high density and data rate magnetic recording*. Ph.D. dissertation, University of California, San Diego, 2002.
- [29] L. Landau and E. Lifshitz *Phys. Z. Sowjetunion*, vol. 8, pp. 153–169, 1935.
- [30] C. Kittel, "Theory of the structure of ferromagnetic domains in films and small particles," *Phys. Rev.*, vol. 70, pp. 965–971, 1946.
- [31] H. V. den Berg, *Micromagnetics and domains in soft-ferromagnetic media*. Delft University Press, 1984.
- [32] J. D. Jackson, *Classical Electrodynamics, 3rd Ed.* Wiley Text Books, 1998.
- [33] A. V. Oppenheim, R. W. Schaffer, and J. R. Buck, *Discrete-time signal processing, 2nd Ed.* Prentice Hall, 1999.
- [34] H. Forster, T. Schrefl, R. Dittrich, W. Scholz, and J. Fidler, "Fast boundary methods for magnetostatic interactions in micromagnetics," *IEEE Trans. Magn.*, vol. 39, pp. 2513–2515, Sept. 2003.
- [35] W. Heisenberg *Z. Physik*, vol. 49, p. 619, 1928.
- [36] C. Kittel, "Physical theory of ferromagnetic domains," *Bell Telephone System Technical Publications*, pp. 1–43, 1948.
- [37] D. Z. Bai and J. G. Zhu *Unpublished Data*.
- [38] H. Suhl, "Theory of the magnetic damping constant," *IEEE Trans. Magn.*, vol. 34, pp. 1834–1838, July 1998.
- [39] G. M. Sandler, H. N. Bertram, T. J. Silva, and T. M. Crawford, "Determination of the magnetic damping constant in thin films," *J. Appl. Phys.*, vol. 85, pp. 5080–5082, April 1999.
- [40] C. A. Jr, J. Rantschler, T. J. Silva, and P. Kabos, "Frequency- and time-resolved measurements of thin films with longitudinal bias fields," *J. Appl. Phys.*, vol. 87, pp. 6633–6635, May 2000.

- [41] S. E. Russek, P. Kabos, T. Silva, F. B. Mancoff, D. Wang, Z. Qian, and J. M. Daughton, "High frequency measurements of coefer thin films," *IEEE Trans. Magn.*, vol. 37, pp. 2248–2250, July 2001.
- [42] N. Inaba, Y. Uesaka, A. Nakamura, M. Futamoto, and Y. Sugita, "Damping constants of co-cr-ta and co-cr-pt thin films," *IEEE Trans. Magn.*, vol. 33, pp. 2989–2991, Sept. 1997.
- [43] L. Guan and J. G. Zhu, "Effect of fast head field rise time in perpendicular recording," *IEEE Trans. Magn.*, vol. 38, pp. 2024–2026, Sept. 2002.
- [44] J. G. Zhu and D. Z. Bai, "Understanding field rise time and magnetic damping in thin film recording heads," *J. Appl. Phys.*, vol. 93, pp. 6447–6449, 2003.
- [45] I. Tudosa, C. Stamm, A. B. Kashuba, F. King, H. C. Siegmann, J. Stohr, G. Ju, B. Lu, and D. Weller, "The ultimate speed of magnetic switching in granular recording media," *Nature*, vol. 428, pp. 831–833, April 2004.
- [46] W. H. Press, S. A. Teukolsky, W. T. Vetterling, and B. P. Flannery, *Numerical Recipes: The Art of Scientific Computing*. Cambridge University Press, 2nd Ed., 1993.
- [47] D. Z. Bai and J. G. Zhu *Unpublished Data*.
- [48] H. N. Bertram, *Theory of Magnetic Recording*. Cambridge University Press, 1994.
- [49] D. Z. Bai and J. G. Zhu, "Micromagnetics of perpendicular write heads with extremely small pole tip dimensions," *J. Appl. Phys.*, vol. 91, pp. 6833–6835, May 2002.
- [50] E. B. Svedberg, D. Litvinov, R. Gustafson, C. H. Chang, and S. Khizroev, "Magnetic force microscopy of skew angle dependencies in perpendicular magnetic recording," *J. Appl. Phys.*, vol. 93, p. 2828, 2003.
- [51] B. M. Lairson, S. E. Lambert, H. Nguy, L. Nguyen, A. Wallash, T. Huang, and J. Adler, "Disk drive integration issues for perpendicular recording," *IEEE Trans. Magn.*, vol. 37, p. 12231227, July 2001.
- [52] F. Liu, K. Stoev, P. Luo, Y. Liu, Y. Chen, J. Chen, J. Wang, S. Gu, K. Kung, M. Lederman, M. Krounbi, M. Re, A. Otsuki, and S. Hong, "Perpendicular recording heads for extremely high-density recording," *IEEE Trans. Magn.*, vol. 39, pp. 1942–1948, 2003.

- [53] D. Litvinov, M. H. Kryder, and S. Khizroev, "Recording physics of perpendicular media: Soft underlayers," *J. Magn Magn. Matter.*, vol. 232, p. 84, 2001.
- [54] E. C. Stoner and P. P. Wohlfarth, "A mechanism of magnetic hysteresis in heterogeneous alloys," *Phil. Trans. Roy. Soc.*, vol. A240, pp. 599–642, May 1948.
- [55] M. Mallery, A. Torabi, and M. Benakli, "One terabit per square inch perpendicular recording conceptual design," *IEEE Trans. Magn.*, vol. 38, pp. 1719–1724, July 2002.
- [56] M. Mochizuki, C. Ishikawa, H. Ide, K. Nakamoto, Y. Nakatani, and N. Hayashi, "Remanent head field study of single pole-type head based on micromagnetics," *J. Appl. Phys.*, vol. 93, pp. 6748–6750, May 2003.
- [57] A. Hubert and R. Schafer, *Magnetic Domains: The Analysis of Magnetic Microstructures*. Springer-Verlag Berlin Heidelberg, 1998.
- [58] J. C. Slonczewski, B. Petek, and B. E. Argyle, "Micro-magnetics of laminated permalloy films," *IEEE Trans. Magn.*, vol. 24, pp. 2045–2054, May 1988.
- [59] D. Z. Bai and J. G. Zhu, "A detached pole tip design of perpendicular write heads for high data-rate recording," *IEEE Trans. Magn.*, vol. 38, pp. 2240–2242, Sept. 2002.
- [60] K. Nakamoto, T. Okada, K. Watanabe, H. Hoshiya, N. Yoshida, Y. Kawato, M. Hatatani, K. Meguro, Y. Okada, H. Kimura, M. Mochizuki, K. Kusukawa, C. Ishikawa, and M. Fuyama, "Single-pole/tmr heads for 140-gb/in<sup>2</sup> perpendicular recording," *IEEE Trans. Magn.*, vol. 40, pp. 290–294, Jan. 2004.
- [61] R. Wood, "The feasibility of magnetic recording at 1 terabit per square inch," *IEEE Trans. Magn.*, vol. 36, pp. 36–42, Jan. 2000.
- [62] K. Z. Gao and H. N. Bertram, "Write field analysis in perpendicular recording using three-dimensional micromagnetic simulation," *J. Appl. Phys.*, vol. 91, pp. 8369–8371, May 2002.
- [63] D. Z. Bai and J. G. Zhu, "Stitched pole-tip design with enhanced head field for perpendicular recording," *J. Appl. Phys.*, vol. 93, pp. 6540–6542, May 2003.

- [64] R. E. Rottmayer *Private communication*.
- [65] S. Khizroev and D. Litvinov, "Perpendicular magnetic recording: Writing process," *J. Appl. Phys.*, vol. 95, pp. 4521–4537, 2004.
- [66] W. Cain, A. Payne, M. Baldwinson, and R. Hempstead, "Challenges in the practical implementation of perpendicular magnetic recording," *IEEE Trans. Magn.*, vol. 32, pp. 97–102, January 1996.
- [67] R. Wood, J. Miles, and T. Olson, "Recording technologies for terabit per square inch systems," *IEEE Trans. Magn.*, vol. 38, pp. 1711–1718, July 2002.
- [68] C. Y. Mao, J.-G. Zhu, R. M. White, and T. Min, "Effect of damping constant on the switching limit of a thin-film recording head," *J. Appl. Phys.*, vol. 85, pp. 5870–5872, April 1999.
- [69] C. Y. Mao, J. G. Zhu, and R. M. White, "High speed characteristics of thin film write heads at deep submicron track width," *J. Appl. Phys.*, vol. 87, pp. 5416–5418, May 2000.
- [70] J. G. Zhu, C. Y. Mao, and R. M. White, "Understanding single-turn write head design at narrow track widths," *IEEE Trans. Magn.*, vol. 38, pp. 124–128, Jan. 2002.
- [71] K. Z. Gao and H. N. Bertram, "3-d micromagnetic simulation of write field rise time in perpendicular recording," *IEEE Trans. Magn.*, vol. 38, pp. 2063–2065, Sept. 2002.
- [72] J. G. Zhu, D. Z. Bai, and A. F. Torabi, "The role of sul in readback and effect on linear density performance for perpendicular recording," *IEEE Trans. Magn.*, vol. 39, pp. 1961–1966, July 2003.
- [73] T. A. Roscamp, E. D. Boerner, and G. J. Parker, "Three-dimensional modeling of perpendicular reading with a soft underlayer," *J. Appl. Phys.*, vol. 91, p. 8366, 2002.
- [74] B. Valcu and H. N. Bertram, "3-d analysis of the playback signal in perpendicular recording for an off-centered gmr element," *IEEE Trans. Magn.*, vol. 38, p. 2081, 2002.

- [75] B. Valcu, T. Roscamp, and H. N. Bertram, "Pulse shape, resolution, and signal-to-noise ratio in perpendicular recording," *IEEE Trans. Magn.*, vol. 38, p. 288, 2002.
- [76] Y. Suzuki and Y. Nishida, "Calculation method of gmr head response for double layered perpendicular medium," *IEEE Trans. Magn.*, vol. 37, p. 1337, 2001.
- [77] L. Wang, S. Li, and J. F. de Castro, "Media-to-sensor demagnetization matrix and its applications in micromagnetic simulation of readback process," *IEEE Trans. Magn.*, vol. 38, p. 2078, 2002.
- [78] M. E. Schabes, B. Lengsfeld, and T. Schrefl, "Micromagnetic modeling of soft underlayer magnetization processes and fields in perpendicular magnetic recording," *IEEE Trans. Magn.*, vol. 38, pp. 1670–1675, July 2002.
- [79] N. R. Darragh, D. J. Mapps, T. Donnelly, J. G. Wade, and J. R. Hoinville, "Observation of underlayer domain noise in perpendicular recording disks," *IEEE Trans. Magn.*, vol. 29, p. 3742, 1993.
- [80] K. W. Wierman, C. L. Platt, E. B. Svedberg, J. Yu, R. J. M. van de Veerdonk, W. R. Eppler, and K. J. Howard, "Noise characteristics in exchange-biased soft underlayers for perpendicular media," *IEEE Trans. Magn.*, vol. 37, p. 3956, 2001.
- [81] H. S. Jung and W. D. Doyle, "Cofe-irmn exchange-coupled soft underlayers for perpendicular media," *IEEE Trans. Magn.*, vol. 38, p. 2015, 2002.
- [82] S. Takenoiri, Y. S. K. Enomoto, and S. Watanabe, "Exchange-coupled irmn/cozrnb soft underlayers for perpendicular recording media," *IEEE Trans. Magn.*, vol. 38, p. 1991, 2002.
- [83] R. Gustafson, "Perpendicular recording: Integration challenges," *Joint NAPMRC 2003, Monterey, CA, Talk MA-06*, Jan. 2003.
- [84] P. Zou, W. Yu, and J. A. Bain, "Influence of stress and texture on soft magnetic properties of thin films," *IEEE Trans. Magn.*, vol. 38, pp. 3501–3520, Sept. 2002.
- [85] J. Dho, Y. N. Kim, Y. S. Hwang, J. C. Kim, and N. H. Hur, "Strain-induced magnetic stripe domains in  $\text{La}_{0.7}\text{Sr}_{0.3}\text{MnO}_3$  thin films," *Appl. Phys. Lett.*, vol. 82, pp. 1434–1436, March 2003.

- [86] S. K. Kim, J. W. Lee, S. C. Shin, H. W. Song, C. H. Lee, and K. No, "Voltage control of a magnetization easy axis in piezoelectric/ferromagnetic hybrid films," *J. Magn. Magn. Mater.*, vol. 267, pp. 127–132, 2003.
- [87] S. K. Kim, S. C. Shin, and K. No, "Voltage control of magnetization easy axes: A potential candidate for spin switching in future ultrahigh-density nonvolatile magnetic random access memory," *IEEE Trans. Magn.*, vol. 40, July 2004.
- [88] T. Ishi, T. Suzuki, N. Ishiwata, and K. Yamada, "Stress induced anisotropy effect for sal films in magnetoresistive elements," *IEEE Trans. Magn.*, vol. 32, pp. 3389–3391, Sept. 1996.
- [89] H. Muraoka and Y. Nakamura, "Artificial domain control of a single-pole head and its read/write performance in perpendicular magnetic recording," *J. Magn. Magn. Mater.*, vol. 134, pp. 268–274, 1994.
- [90] H. Koyanagi, R. Arai, K. Mitsuoka, H. Fukui, S. Narishige, and Y. Sugita, "Three-dimensional stress and magnetic anisotropy analyses for thin film heads," *IEEE Translation Journal on Magnetism in Japan*, vol. 5, pp. 185–194, February 1990.
- [91] J. G. Zhu, "Transition noise properties in longitudinal thin-film media," *IEEE Trans. Magn.*, vol. 29, pp. 195–200, 1993.
- [92] G. Khanna, B. M. Clemens, H. Zhou, and H. N. Bertram, "Micromagnetic study of anisotropy sources in textured longitudinal media," *IEEE Trans. Magn.*, vol. 37, pp. 1468–1470, July 2001.
- [93] D. Z. Bai, J. G. Zhu, W. Yu, and J. A. Bain, "Micromagnetic simulation of effect of stress-induced anisotropy in soft magnetic thin films," *J. Appl. Phys.*, vol. 95, pp. 6864–6866, June 2004.
- [94] J. G. Zhu and D. Z. Bai, "Voltage-assisted perpendicular write head design," *IEEE Trans. Magn.*, vol. 40, July 2004.
- [95] B. D. Cullity, *Introduction to Magnetic Materials*. Addison-Wesley Publishing Company, 1972.
- [96] M. S. Patwari, S. Batra, and R. H. Victora, "Effect of pole tip anisotropy on the recording performance of a high density perpendicular head," *J. Appl. Phys.*, vol. 93, pp. 6543–6545, May 2003.

- [97] K. L. Chopra, *Thin Film Phenomena*. McGraw-Hill Book company, 1969.
- [98] S. Chikazumi, *Physics of Ferromagnetism*. Clarendon Press, London, 1997.
- [99] *FEMLAB User's Guide and Introduction, Version 2.3*. COMSOL AB, 2003.
- [100] *FEMLAB Structure Mechanics Module, Version 2.3*. COMSOL AB, 2003.

## A Magnetostatic interaction matrix calculations: for calculating field from magnetization

The magnetic field at a location in the space  $\mathbf{r}_i$  produced by a uniformly magnetized element at location  $\mathbf{r}_j$  is given by (Since for the uniform magnetization there is no body charge, the field is only from the surface charges):

$$\mathbf{H}_{ij} = \int_{s_j} \frac{(\mathbf{r}_i - \mathbf{r}_j) \sigma_j}{|\mathbf{r}_i - \mathbf{r}_j|^3} d^2 r_j \quad (\text{A.1})$$

where  $\sigma_j$  is the magnetic surface charge density at the surfaces of the element at  $\mathbf{r}_j$ , and the integral is over all the surfaces of the element.  $\sigma_j$  can be obtained as:

$$\sigma_j = \mathbf{n}_j \cdot \mathbf{M}_j \quad (\text{A.2})$$

where  $\mathbf{n}_j$  is the surface normal vector that has unity magnitude and pointing outward from inside the element, and  $\mathbf{M}_j$  is the magnetization of the element. Therefore, Eq. (A.1) can be rewritten as:

$$\mathbf{H}_{ij} = \int_{s_j} \frac{(\mathbf{r}_i - \mathbf{r}_j) (\mathbf{n}_j \cdot \mathbf{M}_j)}{|\mathbf{r}_i - \mathbf{r}_j|^3} d^2 r_j \quad (\text{A.3})$$

If we define a magnetostatic interaction matrix,  $\mathcal{D}_{ij}$ , as:

$$\mathcal{D}_{ij} = \int_{s_j} \frac{(\mathbf{r}_i - \mathbf{r}_j) \mathbf{n}_j}{|\mathbf{r}_i - \mathbf{r}_j|^3} d^2 r_j \quad (\text{A.4})$$

since  $\mathbf{M}_j$  is constant and can be taken outside the integral of Eq. (A.3),  $\mathbf{H}_{ij}$  can now be rewritten in the short form:

$$\mathbf{H}_{ij} = \mathcal{D}_{ij} \cdot \mathbf{M}_j \quad (\text{A.5})$$

From Eq. (A.5) it can be seen that the magnetostatic interaction matrix,  $\mathcal{D}_{ij}$ , has the form of a tensor:

$$\mathcal{D}_{ij} = \begin{pmatrix} d_{ij}^{xx} & d_{ij}^{xy} & d_{ij}^{xz} \\ d_{ij}^{yx} & d_{ij}^{yy} & d_{ij}^{yz} \\ d_{ij}^{zx} & d_{ij}^{zy} & d_{ij}^{zz} \end{pmatrix} \quad (\text{A.6})$$



where  $d_{ij}^{xx}$  characterizes the contribution from the  $x$ -component of the magnetization of the element at  $\mathbf{r}_j$  to the  $x$ -component of the field at  $\mathbf{r}_i$ ,  $d_{ij}^{xy}$  the contribution from the  $y$ -component of the magnetization to the  $x$ -component of the field and so on.

Now let's compute  $d_{ij}^{yy}$  and  $d_{ij}^{yz}$ . From the definition in Eq. (A.4), one has:

$$\begin{aligned} d_{ij}^{yy} &= \int_{s_j} \frac{(y_i - y_j)n_j^y}{|\mathbf{r}_i - \mathbf{r}_j|^3} d^2r_j = \int_{v_j} \frac{\partial}{\partial y_j} \frac{(y_i - y_j)}{|\mathbf{r}_i - \mathbf{r}_j|^3} d^3r_j \\ &= \int_{s_j} \frac{2(y_i - y_j)^2 - (x_i - x_j)^2 - (z_i - z_j)^2}{|\mathbf{r}_i - \mathbf{r}_j|^5} d^3r_j \end{aligned} \quad (\text{A.7})$$

where  $x$ ,  $y$  and  $z$  are the three Cartesian components of the vector  $\mathbf{r}$ ,  $n_j^y$  is the  $y$ -component of the surface normal unit vector  $\mathbf{n}_j$ . Similarly we have:

$$\begin{aligned} d_{ij}^{yz} &= \int_{s_j} \frac{(y_i - y_j)n_j^z}{|\mathbf{r}_i - \mathbf{r}_j|^3} d^2r_j = \int_{v_j} \frac{\partial}{\partial z_j} \frac{(y_i - y_j)}{|\mathbf{r}_i - \mathbf{r}_j|^3} d^3r_j \\ &= \int_{s_j} \frac{3(y_i - y_j)(z_i - z_j)}{|\mathbf{r}_i - \mathbf{r}_j|^5} d^3r_j \end{aligned} \quad (\text{A.8})$$

The integrations in Eqs. (A.7) and (A.8) generally have no closed form. However, in the case of our micromagnetic model with rectangular parallelepiped shaped elements, closed form does exist. Suppose the element is centered at  $\mathbf{r}_j = (x_j, y_j, z_j)$ , and has sizes of  $t$ ,  $h$ , and  $w$  in  $x$ -,  $y$ -, and  $z$ -directions, respectively. With the definition of the following quantities:

$$\begin{aligned} x_- &= x_i - x_j - \frac{t}{2} & x_+ &= x_i - x_j + \frac{t}{2} \\ y_- &= y_i - y_j - \frac{h}{2} & y_+ &= y_i - y_j + \frac{h}{2} \\ z_- &= z_i - z_j - \frac{w}{2} & z_+ &= z_i - z_j + \frac{w}{2} \end{aligned} \quad (\text{A.9})$$

the integrations of Eqs. (A.7) and (A.8) yield:

$$\begin{aligned}
 d_{ij}^{yy} = & \\
 & - \arctan \frac{x_+ z_+}{y_+ \sqrt{x_+^2 + y_+^2 + z_+^2}} + \arctan \frac{x_- z_+}{y_+ \sqrt{x_-^2 + y_+^2 + z_+^2}} \\
 & + \arctan \frac{x_+ z_+}{y_- \sqrt{x_+^2 + y_-^2 + z_+^2}} - \arctan \frac{x_- z_+}{y_- \sqrt{x_-^2 + y_-^2 + z_+^2}} \\
 & + \arctan \frac{x_+ z_-}{y_+ \sqrt{x_+^2 + y_+^2 + z_-^2}} - \arctan \frac{x_- z_-}{y_+ \sqrt{x_-^2 + y_+^2 + z_-^2}} \\
 & - \arctan \frac{x_+ z_-}{y_- \sqrt{x_+^2 + y_-^2 + z_-^2}} + \arctan \frac{x_- z_-}{y_- \sqrt{x_-^2 + y_-^2 + z_-^2}} \quad (A.10)
 \end{aligned}$$

and

$$\begin{aligned}
 d_{ij}^{yz} = & \\
 & \ln \left( x_+ + \sqrt{x_+^2 + y_+^2 + z_+^2} \right) - \ln \left( x_- + \sqrt{x_-^2 + y_+^2 + z_+^2} \right) \\
 & - \ln \left( x_+ + \sqrt{x_+^2 + y_-^2 + z_+^2} \right) + \ln \left( x_- + \sqrt{x_-^2 + y_-^2 + z_+^2} \right) \\
 & - \ln \left( x_+ + \sqrt{x_+^2 + y_+^2 + z_-^2} \right) + \ln \left( x_- + \sqrt{x_-^2 + y_+^2 + z_-^2} \right) \\
 & + \ln \left( x_+ + \sqrt{x_+^2 + y_-^2 + z_-^2} \right) - \ln \left( x_- + \sqrt{x_-^2 + y_-^2 + z_-^2} \right) \quad (A.11)
 \end{aligned}$$

Note that  $x_j$ ,  $y_j$ , and  $z_j$  in Eq. (A.9) are the center position of the source element, and are not to be confused with the same symbols used as the integration variables in Eqs. (A.7) and (A.8).

All other components of the magnetostatic interaction matrix,  $\mathcal{D}_{ij}$ , can be calculated the same way as we did above. In fact, they can also be derived from the symmetry considerations. Notice that exchanging the variable  $y$  and  $z$  in Eq. (A.8) yields the same integration, which means:

$$d_{ij}^{yz} = d_{ij}^{zy} \quad (A.12)$$

Similarly, we have:

$$d_{ij}^{xy} = d_{ij}^{yx} \quad (A.13)$$

$$d_{ij}^{xz} = d_{ij}^{zx} \quad (\text{A.14})$$

To make it more clear, let's now write out  $d_{ij}^{yy}$   $d_{ij}^{yz}$  explicitly with the variables:

$$d_{ij}^{yy} = d_{ij}^{yy}(x_i, y_i, z_i, x_j, y_j, z_j, t, h, w) \quad (\text{A.15})$$

$$d_{ij}^{yz} = d_{ij}^{yz}(x_i, y_i, z_i, x_j, y_j, z_j, t, h, w) \quad (\text{A.16})$$

By rotating the coordinate system  $-90^\circ$  around the  $z$  axis, we have  $x \rightarrow -y, y \rightarrow x$ , and therefore  $d_{ij}^{yy} \rightarrow d_{ij}^{xx}$  and  $t \leftrightarrow h$ , which gives:

$$d_{ij}^{xx} = d_{ij}^{yy}(-y_i, x_i, z_i, -y_j, x_j, z_j, h, t, w) \quad (\text{A.17})$$

and similarly:

$$d_{ij}^{zz} = d_{ij}^{yy}(x_i, z_i, -y_i, x_j, z_j, -y_j, t, w, h) \quad (\text{A.18})$$

$$d_{ij}^{yx} = d_{ij}^{yz}(-z_i, y_i, x_i, -z_j, y_j, x_j, w, h, t) \quad (\text{A.19})$$

$$d_{ij}^{xz} = d_{ij}^{yz}(-y_i, x_i, z_i, -y_j, x_j, z_j, h, t, w) \quad (\text{A.20})$$

So far all the nine components of the magnetostatic interaction matrix,  $\mathcal{D}_{ij}$ , have been explicitly calculated, which can give the magnetic field at any point in the space  $\mathbf{r}_i$  due to a rectangular parallelepiped shaped element uniformly magnetized and located at  $\mathbf{r}_j$ .

One final note is that in our model, we are concerned with the magnetostatic interaction between two discrete elements centered at  $\mathbf{r}_i$  and  $\mathbf{r}_j$ , yet what we have done so far only calculates the field due to one element at a point in the space. Therefore a volume average of the field could be done at the element where the field is concerned, which leads to a redefined matrix  $\mathcal{D}_{ij}$ :

$$\mathcal{D}_{ij} = \frac{1}{v_i} \int_{v_i} d^3r_i \int_{s_j} \frac{(\mathbf{r}_i - \mathbf{r}_j)\mathbf{n}_j}{|\mathbf{r}_i - \mathbf{r}_j|^3} d^2r_j \quad (\text{A.21})$$

where the volume integral is done by numerical method. In reality, this average may or may not be needed, as in most cases the field at the center of the cell is already accurate enough.

## B Magnetostatic interaction matrix calculations: for calculating field from surface charge density

The magnetic field in the space can not only be calculated directly from the magnetization of each discretization cell, as shown in Appendix A, but it can also be calculated from the surface magnetic charge densities of the surface elements of the cells. Here we will derive the magnetostatic interaction matrix,  $\mathcal{D}'_{ij}$ , for the calculation of field from the surface charge density.

We will still start with Eq. (A.1) for the expression of the field. However, instead of expressing  $\sigma_j$  in the form of the dot product of the surface normal unit vector and the magnetization, we will treat  $\sigma_j$  as a known constant. With the definition of the matrix  $\mathcal{D}'_{ij}$ :

$$\mathcal{D}'_{ij} = \int_{s_j} \frac{(\mathbf{r}_i - \mathbf{r}_j)}{|\mathbf{r}_i - \mathbf{r}_j|^3} d^2 r_j \quad (\text{B.1})$$

$\mathbf{H}_{ij}$  can be redefined as:

$$\mathbf{H}_{ij} = \mathcal{D}'_{ij} \cdot \sigma_j \quad (\text{B.2})$$

Note that  $\sigma_j$  has three components,  $\sigma_j^x$ ,  $\sigma_j^y$ , and  $\sigma_j^z$ , and the subscript  $j$  means the position with the coordinates  $j_x, j_y, j_z$  in  $x, y$  and  $z$  directions, respectively. For the rectangular parallelepiped shaped elements, the three components of  $\sigma_j$  are defined as:

$$\begin{aligned} \sigma_j^x &= M_{j_x-1, j_y, j_z}^x - M_{j_x, j_y, j_z}^x \\ \sigma_j^y &= M_{j_x, j_y-1, j_z}^y - M_{j_x, j_y, j_z}^y \\ \sigma_j^z &= M_{j_x, j_y, j_z-1}^z - M_{j_x, j_y, j_z}^z \end{aligned} \quad (\text{B.3})$$

which means that the surface charge density of a surface element is equal to the difference of the respective magnetization components of the two neighboring cells sharing the surface element.

Similar to  $\mathcal{D}_{ij}$  in Appendix A,  $\mathcal{D}'_{ij}$  has nine components as well:

$$\mathcal{D}'_{ij} = \begin{pmatrix} d'_{ij}{}^{xx} & d'_{ij}{}^{xy} & d'_{ij}{}^{xz} \\ d'_{ij}{}^{yx} & d'_{ij}{}^{yy} & d'_{ij}{}^{yz} \\ d'_{ij}{}^{zx} & d'_{ij}{}^{zy} & d'_{ij}{}^{zz} \end{pmatrix} \quad (\text{B.4})$$

We will now compute  $d'_{ij}{}^{xx}$  and  $d'_{ij}{}^{yx}$ . From the definition in Eq. (B.1), we have:

$$d'_{ij}{}^{xx} = \int_{z_j^-}^{z_j^+} dz' \int_{y_j^-}^{y_j^+} \frac{(x_i - x_j^-)}{\sqrt{((x_i - x_j^-)^2 + (y_i - y')^2 + (z_i - z')^2)^3}} dy' \quad (\text{B.5})$$

$$d'_{ij}{}^{yx} = \int_{z_j^-}^{z_j^+} dz' \int_{y_j^-}^{y_j^+} \frac{(y_i - y')}{\sqrt{((x_i - x_j^-)^2 + (y_i - y')^2 + (z_i - z')^2)^3}} dy' \quad (\text{B.6})$$

Notice that there is an offset of half the cell size in  $x$  direction in this case for the  $x$  coordinate of the source surface element with respect to  $x_j$ , the  $x$  coordinate of the  $j^{\text{th}}$  cell center, leading to the use of  $x_j^-$  in Eqs. (B.5) and (B.6), which is defined as follows, with the same definition of  $t$ ,  $h$ , and  $w$  as in Appendix A.

$$\begin{aligned} x_j^- &= x_j - \frac{t}{2} & x_j^+ &= x_j + \frac{t}{2} \\ y_j^- &= y_j - \frac{h}{2} & y_j^+ &= y_j + \frac{h}{2} \\ z_j^- &= z_j - \frac{w}{2} & z_j^+ &= z_j + \frac{w}{2} \end{aligned} \quad (\text{B.7})$$

Carrying out the integration in Eq. (B.5) gives:

$$\begin{aligned} d'_{ij}{}^{xx} &= -\frac{x_-}{|x_-|} \frac{y_+}{|y_+|} \arctan \left( \left| \frac{y_+}{x_-} \right| \frac{z_+}{\sqrt{z_+^2 + x_-^2 + y_+^2}} \right) \\ &+ \frac{x_-}{|x_-|} \frac{y_+}{|y_+|} \arctan \left( \left| \frac{y_+}{x_-} \right| \frac{z_-}{\sqrt{z_-^2 + x_-^2 + y_+^2}} \right) \\ &+ \frac{x_-}{|x_-|} \frac{y_-}{|y_-|} \arctan \left( \left| \frac{y_-}{x_-} \right| \frac{z_+}{\sqrt{z_+^2 + x_-^2 + y_-^2}} \right) \\ &- \frac{x_-}{|x_-|} \frac{y_-}{|y_-|} \arctan \left( \left| \frac{y_-}{x_-} \right| \frac{z_-}{\sqrt{z_-^2 + x_-^2 + y_-^2}} \right) \end{aligned} \quad (\text{B.8})$$

where  $x_-$ ,  $y_-$ ,  $z_-$ ,  $x_+$ ,  $y_+$ , and  $z_+$  are defined as:

$$\begin{aligned} x_- &= x_j - x_i - \frac{t}{2} & x_+ &= x_j - x_i + \frac{t}{2} \\ y_- &= y_j - y_i - \frac{h}{2} & y_+ &= y_j - y_i + \frac{h}{2} \\ z_- &= z_j - z_i - \frac{w}{2} & z_+ &= z_j - z_i + \frac{w}{2} \end{aligned} \quad (\text{B.9})$$

Carrying out the integration in Eq. (B.6) gives:

$$\begin{aligned} d'_{ij}{}^{yx} &= \ln \left( z_+ + \sqrt{x_-^2 + y_+^2 + z_+^2} \right) - \ln \left( z_- + \sqrt{x_-^2 + y_+^2 + z_-^2} \right) \\ &\quad - \ln \left( z_+ + \sqrt{x_-^2 + y_-^2 + z_+^2} \right) + \ln \left( z_- + \sqrt{x_-^2 + y_-^2 + z_-^2} \right) \end{aligned} \quad (\text{B.10})$$

Note that the integration for  $d'_{ij}{}^{zx}$  has the same form as that for  $d'_{ij}{}^{yx}$ , therefore, the following exchanges,  $y_+ \leftrightarrow z_+$ , and  $y_- \leftrightarrow z_-$ , in Eq. (B.10) will give the expression of  $d'_{ij}{}^{zx}$ :

$$\begin{aligned} d'_{ij}{}^{zx} &= \ln \left( y_+ + \sqrt{x_-^2 + y_+^2 + z_+^2} \right) - \ln \left( y_- + \sqrt{x_-^2 + y_-^2 + z_+^2} \right) \\ &\quad - \ln \left( y_+ + \sqrt{x_-^2 + y_+^2 + z_-^2} \right) + \ln \left( y_- + \sqrt{x_-^2 + y_-^2 + z_-^2} \right) \end{aligned} \quad (\text{B.11})$$

Multiplying  $d'_{ij}{}^{xx}$ ,  $d'_{ij}{}^{yx}$  and  $d'_{ij}{}^{zx}$  with  $\sigma_j^x$  will give the  $x$ -,  $y$ -, and  $z$ -components of the field produced by the charges on the surface element shared by the two cells shown in the first line of Eq. (B.3), whose normal is in  $x$  direction.

Similarly, we can get other six components of the matrix  $\mathcal{D}'_{ij}$  for the field components from surface elements with normal in  $y$  and  $z$  directions:

$$\begin{aligned} d'_{ij}{}^{xy} &= \ln \left( z_+ + \sqrt{x_+^2 + y_-^2 + z_+^2} \right) - \ln \left( z_- + \sqrt{x_+^2 + y_-^2 + z_-^2} \right) \\ &\quad - \ln \left( z_+ + \sqrt{x_-^2 + y_-^2 + z_+^2} \right) + \ln \left( z_- + \sqrt{x_-^2 + y_-^2 + z_-^2} \right) \end{aligned} \quad (\text{B.12})$$

$$\begin{aligned}
d'_{ij}{}^{yy} = & -\frac{y_-}{|y_-|} \frac{z_+}{|z_+|} \arctan \left( \left| \frac{z_+}{y_-} \right| \frac{x_+}{\sqrt{x_+^2 + y_-^2 + z_+^2}} \right) \\
& + \frac{y_-}{|y_-|} \frac{z_+}{|z_+|} \arctan \left( \left| \frac{z_+}{y_-} \right| \frac{x_-}{\sqrt{x_-^2 + y_-^2 + z_+^2}} \right) \\
& + \frac{y_-}{|y_-|} \frac{z_-}{|z_-|} \arctan \left( \left| \frac{z_-}{y_-} \right| \frac{x_+}{\sqrt{x_+^2 + y_-^2 + z_-^2}} \right) \\
& - \frac{y_-}{|y_-|} \frac{z_-}{|z_-|} \arctan \left( \left| \frac{z_-}{y_-} \right| \frac{x_-}{\sqrt{x_-^2 + y_-^2 + z_-^2}} \right) \quad (B.13)
\end{aligned}$$

$$\begin{aligned}
d'_{ij}{}^{zy} = & \ln \left( x_+ + \sqrt{x_+^2 + y_-^2 + z_+^2} \right) - \ln \left( x_- + \sqrt{x_-^2 + y_-^2 + z_+^2} \right) \\
& - \ln \left( x_+ + \sqrt{x_+^2 + y_-^2 + z_-^2} \right) + \ln \left( x_- + \sqrt{x_-^2 + y_-^2 + z_-^2} \right) \quad (B.14)
\end{aligned}$$

$$\begin{aligned}
d'_{ij}{}^{xz} = & \ln \left( y_+ + \sqrt{x_+^2 + y_+^2 + z_-^2} \right) - \ln \left( y_- + \sqrt{x_+^2 + y_-^2 + z_-^2} \right) \\
& - \ln \left( y_+ + \sqrt{x_-^2 + y_+^2 + z_-^2} \right) + \ln \left( y_- + \sqrt{x_-^2 + y_-^2 + z_-^2} \right) \quad (B.15)
\end{aligned}$$

$$\begin{aligned}
d'_{ij}{}^{yz} = & \ln \left( x_+ + \sqrt{x_+^2 + y_+^2 + z_-^2} \right) - \ln \left( x_- + \sqrt{x_-^2 + y_+^2 + z_-^2} \right) \\
& - \ln \left( x_+ + \sqrt{x_+^2 + y_-^2 + z_-^2} \right) + \ln \left( x_- + \sqrt{x_-^2 + y_-^2 + z_-^2} \right) \quad (B.16)
\end{aligned}$$

$$\begin{aligned}
d'_{ij}{}^{zz} = & -\frac{z_-}{|z_-|} \frac{y_+}{|y_+|} \arctan \left( \left| \frac{y_+}{z_-} \right| \frac{x_+}{\sqrt{x_+^2 + y_+^2 + z_-^2}} \right) \\
& + \frac{z_-}{|z_-|} \frac{y_+}{|y_+|} \arctan \left( \left| \frac{y_+}{z_-} \right| \frac{x_-}{\sqrt{x_-^2 + y_+^2 + z_-^2}} \right) \\
& + \frac{z_-}{|z_-|} \frac{y_-}{|y_-|} \arctan \left( \left| \frac{y_-}{z_-} \right| \frac{x_+}{\sqrt{x_+^2 + y_-^2 + z_-^2}} \right) \\
& - \frac{z_-}{|z_-|} \frac{y_-}{|y_-|} \arctan \left( \left| \frac{y_-}{z_-} \right| \frac{x_-}{\sqrt{x_-^2 + y_-^2 + z_-^2}} \right) \quad (B.17)
\end{aligned}$$

## C Calculation of the driving field from the coil

We calculate here the magnetic field in the space generated by the coil carrying the driving current. Considered here is an infinitely long current sheet running into the paper with a rectangular cross section centered at  $(x_o, y_o)$  with width  $w$  and height  $h$ , as shown in Figure C.1. Assuming the current is flowing out of the paper (a reversed current just reverses the direction of the field) with a current density  $J$ . Because the current sheet is infinite in  $z$ -direction, the magnetic field will be only in the  $x$ - $y$  plane.

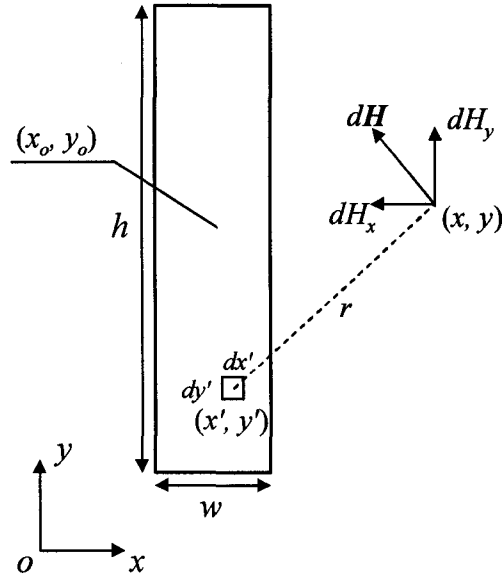


Figure C.1: Illustration of the current coil and the field.

Consider an infinitesimal current element located at  $(x', y')$  in the current sheet with width  $dx'$  and height  $dy'$ . The magnetic field it generates at a point in the space outside the sheet,  $(x, y)$ , can be readily calculated by Ampere's law as below, noticing that the derivation here follows the  $SI$  units:

$$dH = \frac{I}{2\pi r} = \frac{J}{2\pi r} dx' dy' \quad (C.1)$$



The  $x$ - and  $y$ -components of the field  $d\mathbf{H}$  are:

$$\begin{aligned} dH_x &= -\frac{y-y'}{r} dH \\ &= -\frac{J}{2\pi} \frac{y-y'}{(x-x')^2 + (y-y')^2} dx' dy' \end{aligned} \quad (\text{C.2})$$

$$\begin{aligned} dH_y &= \frac{x-x'}{r} dH \\ &= \frac{J}{2\pi} \frac{x-x'}{(x-x')^2 + (y-y')^2} dx' dy' \end{aligned} \quad (\text{C.3})$$

Integrating Eqs. (C.2) and (C.3) will give the  $x$ - and  $y$ -components of the total field at the position  $(x, y)$ :

$$\begin{aligned} H_x &= \oint_{s_{coil}} dH_x \\ &= -\int_{x_o-\frac{w}{2}}^{x_o+\frac{w}{2}} \int_{y_o-\frac{h}{2}}^{y_o+\frac{h}{2}} \frac{J}{2\pi} \frac{y-y'}{(x-x')^2 + (y-y')^2} dx' dy' \end{aligned} \quad (\text{C.4})$$

$$\begin{aligned} H_y &= \oint_{s_{coil}} dH_y \\ &= \int_{x_o-\frac{w}{2}}^{x_o+\frac{w}{2}} \int_{y_o-\frac{h}{2}}^{y_o+\frac{h}{2}} \frac{J}{2\pi} \frac{x-x'}{(x-x')^2 + (y-y')^2} dx' dy' \end{aligned} \quad (\text{C.5})$$

Notice that in Eqs. (C.4) and (C.5),  $x'$  and  $y'$  are the integration variables, not the center position of the current element. Carrying out the above integrations gives the field components:

$$\begin{aligned} H_x &= -\frac{J}{4\pi} \left\{ x_- \ln \left( \sqrt{x_-^2 + y_-^2} \right) + x_+ \ln \left( \sqrt{x_+^2 + y_-^2} \right) \right. \\ &\quad - x_- \ln \left( \sqrt{x_-^2 + y_+^2} \right) - x_+ \ln \left( \sqrt{x_+^2 + y_+^2} \right) \\ &\quad + y_- \left[ \arctan \left( \frac{x_-}{y_-} \right) + \arctan \left( \frac{x_+}{y_-} \right) \right] \\ &\quad \left. - y_+ \left[ \arctan \left( \frac{x_-}{y_+} \right) + \arctan \left( \frac{x_+}{y_+} \right) \right] \right\} \end{aligned} \quad (\text{C.6})$$

From the symmetry of the integrals in Eqs. (C.4) and (C.5), we can easily get

$H_y$  by switching the variables in Eq. (C.6):

$$\begin{aligned}
 H_y = \frac{J}{4\pi} & \left\{ y_- \ln \left( \sqrt{x_-^2 + y_-^2} \right) + y_+ \ln \left( \sqrt{x_-^2 + y_+^2} \right) \right. \\
 & - y_- \ln \left( \sqrt{x_+^2 + y_-^2} \right) - y_+ \ln \left( \sqrt{x_+^2 + y_+^2} \right) \\
 & + x_- \left[ \arctan \left( \frac{y_-}{x_-} \right) + \arctan \left( \frac{y_+}{x_-} \right) \right] \\
 & \left. - x_+ \left[ \arctan \left( \frac{y_-}{x_+} \right) + \arctan \left( \frac{y_+}{x_+} \right) \right] \right\} \quad (C.7)
 \end{aligned}$$

where  $x_-$ ,  $x_+$ ,  $y_-$  and  $y_+$  are defined as:

$$\begin{aligned}
 x_- &= \frac{w}{2} - (x - x_o) & x_+ &= \frac{w}{2} + (x - x_o) \\
 y_- &= \frac{h}{2} - (y - y_o) & y_+ &= \frac{h}{2} + (y - y_o)
 \end{aligned} \quad (C.8)$$

Notice that in Eqs. (C.6) and (C.7), all variables are in the *SI* units. To convert the field components into the *cgs* units, simply multiply the resulting numerical values from Eqs. (C.6) and (C.7) by  $4\pi \times 10^{-3}$ .

## D Coordinate transform matrices and magnetoelastic energy averaging for different textures

Continued from Section 7.2, here we show the coordinate transform matrices for different thin film growth textures and how the averaging of the magnetoelastic energy over all the grains in the film is carried out.

### D.1 Random texture

For a polycrystalline film without texture (random),  $\theta$  varies randomly within  $(0, \pi)$ , whereas both  $\psi$  and  $\varphi$  vary randomly within  $(0, 2\pi)$ , from one grain to another. Therefore, the coordinate transform matrix A is defined simply by Eq. (7.4). The averaging of the magnetoelastic energy density is done as follows:

$$\langle E_\sigma \rangle = \int_0^{2\pi} d\psi \int_0^{2\pi} d\varphi \int_0^\pi E_\sigma(\theta, \psi, \varphi, \omega) \sin \theta d\theta \quad (\text{D.1})$$

### D.2 100 texture

For 100 texture, the film normal  $\hat{z}$  is [001] direction,  $\theta = 0$ ,  $\psi$  and  $\varphi$  vary randomly within  $(0, 2\pi)$ . The matrix A is then given as follows:

$$A_{100} = \begin{pmatrix} \cos \psi \cos \varphi - \sin \psi \sin \varphi & \sin \psi \cos \varphi + \cos \psi \sin \varphi & 0 \\ -\cos \psi \sin \varphi - \sin \psi \cos \varphi & -\sin \psi \sin \varphi + \cos \psi \cos \varphi & 0 \\ 0 & 0 & 1 \end{pmatrix} \quad (\text{D.2})$$

Since  $\theta = 0$ ,  $E_\sigma(\theta, \psi, \varphi, \omega)$  becomes  $E_\sigma(\psi, \varphi, \omega)$ , and the averaging of the magnetoelastic energy density will be only over  $\psi$  and  $\varphi$ :

$$\langle E_\sigma \rangle = \int_0^{2\pi} d\psi \int_0^{2\pi} E_\sigma(\psi, \varphi, \omega) d\varphi \quad (\text{D.3})$$

**D.3 110 texture**

For 110 texture, the film normal  $\hat{z}$  is [110] direction,  $\theta = \pi/2$ ,  $\psi = 3\pi/4$ , and  $\varphi$  varies randomly within  $(0, 2\pi)$ , The matrix A is then given as follows:

$$A_{110} = \begin{pmatrix} -\frac{1}{\sqrt{2}} \cos \varphi & \frac{1}{\sqrt{2}} \cos \varphi & \sin \varphi \\ \frac{1}{\sqrt{2}} \sin \varphi & -\frac{1}{\sqrt{2}} \sin \varphi & \cos \varphi \\ \frac{1}{\sqrt{2}} & \frac{1}{\sqrt{2}} & 0 \end{pmatrix} \quad (D.4)$$

Since both  $\theta$  and  $\psi$  are fixed,  $E_\sigma(\theta, \psi, \varphi, \omega)$  becomes  $E_\sigma(\varphi, \omega)$ , and the averaging of the magnetoelastic energy density will be only over  $\varphi$ :

$$\langle E_\sigma \rangle = \int_0^{2\pi} E_\sigma(\varphi, \omega) d\varphi \quad (D.5)$$

**D.4 111 texture**

For 111 texture, the film normal  $\hat{z}$  is [111] direction,  $\theta = \sin^{-1}(\sqrt{2/3})$ ,  $\psi = 3\pi/4$ , and  $\varphi$  varies randomly within  $(0, 2\pi)$ , The matrix A is then given as follows:

$$A_{111} = \begin{pmatrix} -\frac{1}{\sqrt{2}} \cos \varphi - \frac{1}{\sqrt{6}} \sin \varphi & \frac{1}{\sqrt{2}} \cos \varphi - \frac{1}{\sqrt{6}} \sin \varphi & \frac{2}{\sqrt{6}} \sin \varphi \\ \frac{1}{\sqrt{2}} \sin \varphi - \frac{1}{\sqrt{6}} \cos \varphi & -\frac{1}{\sqrt{2}} \sin \varphi - \frac{1}{\sqrt{6}} \cos \varphi & \frac{2}{\sqrt{6}} \cos \varphi \\ \frac{1}{\sqrt{3}} & \frac{1}{\sqrt{3}} & \frac{1}{\sqrt{3}} \end{pmatrix} \quad (D.6)$$

Since both  $\theta$  and  $\psi$  are fixed,  $E_\sigma(\theta, \psi, \varphi, \omega)$  becomes  $E_\sigma(\varphi, \omega)$ , and the averaging of the magnetoelastic energy density will be only over  $\varphi$ :

$$\langle E_\sigma \rangle = \int_0^{2\pi} E_\sigma(\varphi, \omega) d\varphi \quad (D.7)$$